

ACOUSTIC IMPEDANCE TESTING FOR AEROACOUSTIC APPLICATIONS

By

TODD SCHULTZ

A DISSERTATION PRESENTED TO THE GRADUATE SCHOOL
OF THE UNIVERSITY OF FLORIDA IN PARTIAL FULFILLMENT
OF THE REQUIREMENTS FOR THE DEGREE OF
DOCTOR OF PHILOSOPHY

UNIVERSITY OF FLORIDA

2006

Copyright 2006

by

Todd Schultz

ACKNOWLEDGMENTS

Financial support for the research project was provided by a NASA-Langley Research Center Grant (Grant # NAG-1-2261). I thank Mr. Michael Jones and Mr. Tony Parrot at the NASA-Langley Research Center for their guidance and support. I also thank the University of Florida, Department of Mechanical and Aerospace Engineering, the NASA Graduate Student Research Program Fellowship, and the National Defense Science and Engineering Graduate Fellowship administered by the American Society for Engineering Education for their financial support.

My advisors, Mark Sheplak, Lou Cattafesta, Toshi Nishida, and Tony Schmitz, deserve special thanks. I thank all of the students in the Interdisciplinary Microsystems Group, particularly Steve Horowitz, Fei Liu, Ryan Holman, Tai-An Chen and David Martin, for their assistance and friendship. I thank Paul Hubner for his help with data acquisition systems and LabVIEW programming. I would also like to thank the staff at the University of Florida, including Pam Simon, Becky Hoover, Jan Machnik, Mark Riedy and Teresa Mathia, for helping with the administrative aspects of this project. I also want to thank Ken Reed at TMR Engineering for machining the equipment needed to make this project possible.

TABLE OF CONTENTS

	<u>page</u>
ACKNOWLEDGMENTS	iii
LIST OF TABLES	ix
LIST OF FIGURES	x
ABSTRACT.....	xviii
CHAPTER	
1 INTRODUCTION	1
1.1 Research Goals	10
1.2 Research Contributions.....	12
1.3 Dissertation Organization	12
2 ACOUSTIC WAVEGUIDE THEORY.....	13
2.1 Waveguide Acoustics	13
2.1.1 Solution to the Wave Equation.....	14
2.1.2 Wave Modes.....	16
2.1.3 Phase Speed.....	18
2.1.4 Wave Mode Attenuation.....	22
2.1.5 Reflection Coefficient and Acoustic Impedance	26
2.2 Two-Microphone Method.....	28
2.2.1 Derivation of the TMM	29
2.2.2 Dissipation and Dispersion for Plane Waves	31
3 UNCERTAINTY ANALYSIS FOR THE TWO-MICROPHONE METHOD.....	36
3.1 Multivariate Form of the TMM Data Reduction Equations	37
3.2 TMM Uncertainty Analysis	38
3.2.1 Multivariate Uncertainty Analysis	39
3.2.2 Monte Carlo Method	41
3.2.3 Frequency Response Function Estimate.....	41
3.2.4 Microphone Locations.....	45
3.2.5 Temperature.....	45
3.2.6 Normalized Acoustic Impedance Uncertainty.....	48

3.3	Numerical Simulations	48
3.3.1	Sound-Hard Sample.....	50
3.3.2	Ideal Impedance Model	53
3.4	Experimental Methodology	64
3.4.1	Waveguides	64
3.4.2	Equipment Description.....	66
3.4.3	Signal Processing.....	66
3.4.4	Procedure.....	66
4	MODAL DECOMPOSITION METHOD.....	68
4.1	Data Reduction Algorithm.....	70
4.1.1	Complex Modal Amplitudes	71
4.2.2	Reflection Coefficient Matrix.....	73
4.2.3	Acoustic Impedance	74
4.2.4	Acoustic Power.....	75
4.2	Experimental Methodology	77
4.2.1	Waveguide.....	77
4.2.2	Equipment Description.....	78
4.2.3	Signal Processing.....	80
4.2.4	Numerical Study of Uncertainties	80
5	EXPERIMENTAL RESULTS FOR ACOUSTIC IMPEDANCE SPECIMENS	82
5.1	Ceramic Tubular Honeycomb with 65% Porosity.....	83
5.1.1	TMM Results.....	84
5.1.2	High Frequency TMM Results	87
5.1.3	MDM Results and Comparison.....	89
5.2	Ceramic Tubular Honeycomb with 73% Porosity.....	97
5.2.1	TMM Results.....	98
5.2.2	High Frequency TMM Results	100
5.2.3	MDM Results and Comparison	101
5.3	Rigid Termination.....	109
5.3.1	TMM Results.....	109
5.3.2	High Frequency TMM Results	111
5.3.3	MDM Results and Comparison	113
5.4	SDOF Liner	120
5.4.1	TMM Results.....	121
5.4.2	MDM Results and Comparison	123
5.5	Mode Scattering Specimen	130
5.5.1	MDM Results	130
6	CONCLUSIONS AND FUTURE WORK.....	138
6.1	TMM Uncertainty Analysis.....	138
6.2	Modal Decomposition Method	140

APPENDIX

A	VISCOTHERMAL LOSSES.....	143
A.1	Nondimensionalization and Linearization of the Navier-Stokes Equations.....	144
A.1.1	Continuity	147
A.1.2	x -direction Momentum Equation	147
A.1.3	y -direction Momentum Equation	148
A.1.4	Thermal Energy Equation.....	150
A.1.5	Equation of State for an Ideal Gas.....	151
A.1.6	Summary of the Nondimensional, Linearized Equations	152
A.2	Boundary Layer Solution.....	153
A.2.1	Wall Shear Stress.....	157
A.2.2	Wall Heat Flux.....	158
A.3	Mainstream Flow	158
A.3.1	Axial Momentum.....	159
A.3.2	Energy Equation	161
A.3.3	Summary of the Mainstream Flow Equations	166
A.3.4	Mainstream Flow Wave Equation	167
A.3.5	Dissipation and Dispersion Relations.....	168
B	RANDOM UNCERTAINTY ESTIMATES FOR THE FREQUENCY RESPONSE FUNCTION	173
B.1	Introduction.....	174
B.2	Uncertainty Analysis.....	175
B.2.1	Classical Uncertainty Analysis	176
B.2.2	Multivariate Uncertainty Analysis.....	177
B.2.2.1	Fundamentals.....	178
B.2.2.2	Multivariate uncertainty propagation	181
B.2.2.3	Application: Converting uncertainty from real and imaginary parts to magnitude and phase.....	182
B.3	Frequency Response Function Estimates.....	185
B.3.1	Output Noise Only System Model.....	186
B.3.2	Uncorrelated Input/Output Noise System Model	191
B.4	Application: Measurement of the FRF Between Two Microphones in a Waveguide	200
B.5	Conclusions.....	206
C	FREQUENCY RESPONSE FUNCTION BIAS UNCERTAINTY ESTIMATES..	208
C.1	Bias Uncertainty.....	208
C.2	Conclusions.....	214
D	SOUND POWER FOR WAVES PROPAGATING IN A WAVEGUIDE.....	215

E	MODAL DECOMPOSITION METHOD NUMERICAL ERROR STUDY	219
	E.1 Signal-to-Noise Ratio	222
	E.2 Microphone Phase Mismatch	222
	E.3 Microphone Locations.....	226
	E.4 Speed of Sound.....	228
	E.5 Frequency	229
	E.6 Conclusions	231
F	AUXILIARY GRAPHS	233
	F.1 CT65	233
	F.2 CT73	235
	F.3 Rigid Termination	237
	F.4 SDOF Liner	239
G	COMPUTER CODES	241
	G.1 TMM Program Files	241
	G.1.1 TMM Program Readme File.....	241
	G.1.2 Pulse to MATLAB Conversion Program	242
	G.1.3 TMM Main Program	244
	G.1.4 TMM Subroutine Program	253
	G.1.5 TMM Subroutine for the Analytical Uncertainty in R	255
	G.1.6 TMM Subroutine for the Analytical Uncertainty in Z	257
	G.1.7 TMM Subroutine for the Monte Carlo Uncertainty Estimates.....	258
	G.2 Uncertainty Subroutines	259
	G.2.1 Frequency Response Function Uncertainty	259
	G.2.2 Averaged FRF Uncertainty.....	261
	G.2.3 Effective Number of degrees of Freedom	262
	G.2.4 Numeric Computation of Bivariate Confidence Regions.....	263
	G.2.5 Analytical Propagation of Uncertainty from Rectangular Form to Polar Form.....	265
	G.3 Multivariate Statistics Subroutines	266
	G.3.1 Computation of Bivariate PDF	266
	G.3.2 Numerical Computation of Constant PDF Contours	267
	G.3.3 Multivariate Normal Random Number Generator.....	268
	G.4 Modal Decomposition Programs	268
	G.4.1 Pulse to MATLAB Conversion Program	268
	G.4.2 MDM Main Program	273
	G.4.3 MDM Subroutine to Compute the Decomposition.....	281
	G.4.4 MDM Plotting Subroutine	284
	G.4.5 MDM Mode Scattering Coefficients Plotting Subroutine	290
	LIST OF REFERENCES	294

BIOGRAPHICAL SKETCH300

LIST OF TABLES

<u>Table</u>	<u>page</u>
2-1 Cut-on frequencies in kHz for an 8.5 mm by 8.5 mm waveguide.	17
2-2 Cut-on frequencies in kHz for a 25.4 mm by 25.4 mm waveguide.	18
2-3 Minimum frequencies to keep effects of dispersion and dissipation <5%.....	35
3-1 Elemental bias and precision error sources for the TMM.	43
3-2 Nominal values for input parameters of numeric simulations.	50
4-1 Cut-on frequencies in kHz for the higher-order modes.....	78
4-2 Microphone measurement locations ($a = 25.4$ mm).	79
A-1 Minimum frequency required for series expansion for the two waveguides for air at 20°C.....	170
C-1 Simulation results for the second-order system.	212
E-1 Power in Pa ² for all signals from all simulation sources.....	220

LIST OF FIGURES

<u>Figure</u>	<u>page</u>
1-1 Illustration of the approach, takeoff, and cutback flight segments and measurement points.	2
1-2 Typical noise sources on an aircraft.	4
1-3 Component noise levels during approach, cutback, and take-off for a Boeing 767-300 with GEAE CF6-80C2 engines.	4
1-4 Comparative overall noise levels of various engine types.	5
1-5 Engine cutaway showing the acoustic liner locations.	7
1-6 An example of a SDOF liner showing the atypical honeycomb and the perforate face sheet.	7
1-7 An example of a 2DOF liner.	8
2-1 Illustration of the waveguide coordinate system.	14
2-2 Illustration of the first four mode shapes.	18
2-3 Illustration of the wave front and the incidence angle to the waveguide wall and to the termination.	20
2-4 Phase speed versus frequency for the first four modes.	21
2-5 Angle of incidence to the sidewall versus frequency for the first four modes.	21
2-6 Angle of incidence to the termination versus frequency for the first four modes.	22
2-7 Attenuation of higher-order modes in the large waveguide over a distance of 25.4 mm.	24
2-8 Attenuation of higher-order modes in the small waveguide over a distance of 8.5 mm.	24
2-9 Attenuation of the first higher-order mode ((1,0) or (0,1)) in the large waveguide at the microphone locations used for the TMM experiments.	26

2-10	Reflection and transmission of a wave off an impedance boundary.....	28
2-11	Experimental setup for the TMM.....	29
3-1	Flow chart for the Monte Carlo methods.....	51
3-2	Absolute uncertainty of $R_{00,00}$ due to the uncertainties in l , s , and T for $R_{00,00} = 0.999$ at $f=5$ kHz.....	52
3-3	Absolute uncertainty $R_{00,00}$ due to the SNR for $R_{00,00} = 0.999$ at $f=5$ kHz.....	53
3-4	Estimated value for the (a) reflection coefficient and (b) total uncertainty for the sound-hard boundary.....	54
3-5	Ideal impedance model and estimated values for (a) reflection coefficient and (b) normalized specific acoustic impedance.....	56
3-6	Absolute uncertainty of (a) $R_{00,00}$ and (b) ξ_{spac} due to the uncertainties in l , s , and T for the ideal impedance model at $f=5$ kHz.....	57
3-7	Absolute uncertainty in (a) $R_{00,00}$ (b) ξ_{spac} due to the SNR for the ideal impedance model at $f=5$ kHz.....	58
3-8	Total uncertainty in (a) $R_{00,00}$ and (b) ξ_{spac} as a function of frequency for the ideal impedance model.....	60
3-9	The confidence region contours for the resistance and reactance for the ideal impedance model at 5 kHz.....	62
3-10	Confidence region of the ideal impedance model at 5 kHz with 1% relative input uncertainty and 40 dB SNR.....	63
4-1	Schematic of the experimental setup for the MDM.....	78
4-2	Schematic of the four restrictor plates.....	79
5-1	Photograph of the CT65 material.....	83
5-2	Reflection coefficient for CT65 for the TMM.....	86
5-3	Normalized specific acoustic impedance estimates for CT65 via TMM.....	86
5-4	Reflection coefficient for CT65 for the high frequency TMM.....	88
5-5	Normalized specific acoustic impedance estimates for CT65 via the high frequency TMM.....	89

5-6	Incident pressure field for the MDM for CT65.....	90
5-7	Reflected pressure field for the MDM for CT65.....	90
5-8	Absorption coefficient for CT65.....	91
5-9	Comparison of the reflection coefficient estimates for CT65 via all three methods.....	92
5-10	Mode scattering coefficients for CT65 from the (0,0) mode to the other propagating modes.....	93
5-11	Mode scattering coefficients for CT65 from the (1,0) mode to the other propagating modes.....	93
5-12	Mode scattering coefficients for CT65 from the (0,1) mode to the other propagating modes.....	94
5-13	Mode scattering coefficients for CT65 from the (1,1) mode to the other propagating modes.....	94
5-14	Comparison of the acoustic impedance ratio estimates for CT65 via all three methods.....	96
5-15	Comparison of the normalized specific acoustic impedance estimates for CT65 via all three methods.....	97
5-16	Photograph of the CT73 material.....	98
5-17	Reflection coefficient for CT73 for the TMM.....	99
5-18	Normalized specific acoustic impedance estimates for CT73 via the TMM.....	99
5-19	Reflection coefficient for CT73 for the high frequency TMM.....	100
5-20	Normalized specific acoustic impedance estimates for CT73 via the high frequency TMM.....	101
5-21	Incident pressure field for the MDM for CT73.....	102
5-22	Reflected pressure field for the MDM for CT73.....	103
5-23	Absorption coefficient for CT73.....	103
5-24	Comparison of the reflection coefficient estimates for CT73 via all three methods.....	104
5-25	Mode scattering coefficients for CT73 from the (0,0) mode to the other propagating modes.....	105

5-26	Mode scattering coefficients for CT73 from the (1,0) mode to the other propagating modes.	105
5-27	Mode scattering coefficients for CT73 from the (0,1) mode to the other propagating modes.	106
5-28	Mode scattering coefficients for CT73 from the (1,1) mode to the other propagating modes.	106
5-29	Comparison of the acoustic impedance ratio estimates for CT73 via all three methods.	108
5-30	Comparison of the normalized specific acoustic impedance estimates for CT73 via all three methods.	108
5-31	Photograph of the rigid termination for the large waveguide.	109
5-32	Reflection coefficient for the rigid termination for the TMM.	110
5-33	Standing wave ratio for the rigid termination measured by the TMM.....	111
5-34	Reflection coefficient for the rigid termination for the high frequency TMM.	112
5-35	SWR for the rigid termination calculated from the high frequency TMM.	112
5-36	Triangle restrictor plate.	114
5-37	Incident pressure field for the MDM for the rigid termination.	114
5-38	Reflected pressure field for the MDM for the rigid termination.	115
5-39	Power absorption coefficient for the rigid termination for the MDM.....	115
5-40	Comparison of the reflection coefficient estimates for the rigid termination via all three methods.	117
5-41	SWR for the rigid termination calculated from the MDM.....	117
5-42	Mode scattering coefficients for rigid termination from the (0,0) mode to the other propagating modes.	118
5-43	Mode scattering coefficients for rigid termination from the (1,0) mode to the other propagating modes.	118
5-44	Mode scattering coefficients for rigid termination from the (0,1) mode to the other propagating modes.	119
5-45	Mode scattering coefficients for rigid termination from the (1,1) mode to the other propagating modes.	119

5-46	SDOF liner showing the irregular honeycomb and perforated face sheet.	120
5-47	Reflection coefficient for the SDOF specimen for the TMM.	122
5-48	Normalized specific acoustic impedance estimates for the SDOF specimen via TMM..	122
5-49	Incident pressure field for the MDM for the SDOF specimen.....	124
5-50	Reflected pressure field for the MDM for the SDOF specimen.	124
5-51	Power absorption coefficient for the SDOF specimen for the MDM.	126
5-52	Comparison of the reflection coefficient estimates for the SDOF specimen via the TMM and MDM.....	126
5-53	Mode scattering coefficients for SDOF specimen from the (0,0) mode to the other propagating modes.	127
5-54	Mode scattering coefficients for SDOF specimen from the (1,0) mode to the other propagating modes.	127
5-55	Mode scattering coefficients for SDOF specimen from the (0,1) mode to the other propagating modes.	128
5-56	Mode scattering coefficients for SDOF specimen from the (1,1) mode to the other propagating modes.	128
5-57	Comparison of the acoustic impedance ratio estimates for the SDOF specimen via the TMM and MDM.....	129
5-58	Comparison of the normalized specific acoustic impedance estimates for the SDOF specimen via the TMM and MDM.....	129
5-59	Photograph of the mode scattering specimen.....	130
5-60	Incident pressure field for the MDM for the mode scattering specimen.....	132
5-61	Reflected pressure field for the MDM for the mode scattering specimen.	132
5-62	Power absorption coefficient for the mode scattering specimen for the MDM.	133
5-63	Comparison of the reflection coefficient estimates for the mode scattering specimen via the MDM.	134
5-64	Mode scattering coefficients for the mode scattering specimen from the (0,0) mode to the other propagating modes.	135

5-65	Mode scattering coefficients for the mode scattering specimen from the (1,0) mode to the other propagating modes.	135
5-66	Mode scattering coefficients for the mode scattering specimen from the (0,1) mode to the other propagating modes.	136
5-67	Mode scattering coefficients for the mode scattering specimen from the (1,1) mode to the other propagating modes.	136
5-68	Comparison of the acoustic impedance ratio estimates for the mode scattering specimen via the MDM.	137
5-69	Comparison of the normalized specific acoustic impedance estimates for the mode scattering specimen via the MDM.	137
A-1	Oscillating flow over a flat plate.	145
A-2	Control volume showing the external forces and flows crossing the boundaries. .	161
A-3	Control volume showing the external heat fluxes and flows crossing the boundaries.	166
B-1	A plot of the raw data and estimates for a randomly generated complex variable..	183
B-2	A plot of the raw data and estimates in polar form for a randomly generated complex variable.	185
B-3	System model with output noise only.	187
B-4	System model with uncorrelated input/output noise.	191
B-5	Bode plot of the true FRF and the experimental estimate.	199
B-6	Magnitude and phase plot of the uncertainty estimates.	199
B-7	The experimentally measured FRF between the two microphones.	205
B-8	Comparison for the uncertainty estimated by the multivariate method and by the direct statistics.	205
C-1	FRF for the simulation with random noise.	213
E-1	The rms normalized error for the modal coefficients versus noise power added to the signals.	223
E-2	The rms normalized error for the reflection coefficient matrix versus noise power.	224
E-3	The rms normalized error versus the number of averages for a noise power of 0.01 Pa ²	224

E-4	The rms normalized error for the reflection coefficient versus the number of averages for a noise power of 0.01 Pa^2 .	225
E-5	The rms normalized error for the modal coefficients versus a phase error applied to microphone 4 in group 2 for each source.	225
E-6	The rms normalized error for the reflection coefficient matrix versus a phase error applied to microphone 4 in group 2 for all sources.	226
E-7	The rms normalized error for the modal coefficients versus a microphone location error applied to microphone 1 in group 1 for each source.	227
E-8	The rms normalized error for the reflection coefficient matrix versus a microphone location error applied to microphone 1 in group 1 for all sources.	227
E-9	The rms normalized error for the modal coefficients versus a temperature error.	228
E-10	The rms normalized error for the reflection coefficient matrix versus a temperature error.	229
E-11	The rms normalized error for the modal coefficients versus frequency.	230
E-12	The rms normalized error for the reflection coefficient matrix versus frequency.	230
F-1	Ordinary coherence function for the TMM measurement of CT65.	233
F-2	The measured FRF for CT65 for the TMM.	234
F-3	Ordinary coherence function for the high frequency TMM measurement of CT65.	234
F-4	The measured FRF for CT65 for the high frequency TMM.	235
F-5	Ordinary coherence function for the TMM measurement of CT73.	235
F-6	The measured FRF for CT73 for the TMM.	236
F-7	Ordinary coherence function for the high frequency TMM measurement of CT73.	236
F-8	The measured FRF for CT73 for the high frequency TMM.	237
F-9	Ordinary coherence function between the two microphones for the TMM measurement of the rigid termination.	237
F-10	The measured FRF for the rigid termination for the TMM.	238
F-11	Ordinary coherence function for the high frequency TMM measurement of the rigid termination.	238
F-12	The measured FRF for the rigid termination for the high frequency TMM.	239

F-13 Ordinary coherence function for the TMM measurement of the SDOF specimen.239
F-14 The measured FRF for the SDOF specimen for the TMM.240

Abstract of Dissertation Presented to the Graduate School
of the University of Florida in Partial Fulfillment of the
Requirements for the Degree of Doctor of Philosophy

ACOUSTIC IMPEDANCE TESTING FOR AEROACOUSTIC APPLICATIONS

By

Todd Schultz

August 2006

Chair: Mark Sheplak

Cochair: Louis N. Cattafesta

Major Department: Mechanical and Aerospace Engineering

Accurate acoustic propagation models are required to characterize and subsequently reduce aircraft engine noise. These models ultimately rely on acoustic impedance measurements of candidate materials used in sound-absorbing liners. The standard two-microphone method (TMM) is widely used to estimate acoustic impedance but is limited in frequency range and does not provide uncertainty estimates, which are essential for data quality assessment and model validation. This dissertation presents a systematic framework to estimate uncertainty and extend the frequency range of acoustic impedance testing.

Uncertainty estimation for acoustic impedance data using the TMM is made via two methods. The first employs a standard analytical technique based on linear perturbations and provides useful scaling information. The second uses a Monte Carlo technique that permits the propagation of arbitrarily large uncertainties. Both methods are applied to the TMM for simulated data representative of sound-hard and sound-soft

acoustic materials. The results indicate that the analytical technique can lead to false conclusions about the magnitude and importance of specific error sources. Furthermore, the uncertainty in acoustic impedance is strongly dependent on the frequency and the uncertainty in the microphone locations.

Next, an increased frequency range of acoustic impedance testing is investigated via two methods. The first method reduces the size of the test specimen (from 25.4 mm square to 8.5 mm square) and uses the standard TMM. This method has issues concerning specimen nonuniformity because the small specimens may not be representative of the material. The second method increases the duct cross section and, hence, the required complexity of the sound field propagation model. A comparison among all three methods is conducted for each of the three specimens: two different ceramic tubular specimens and a single degree-of-freedom liner. The results show good agreement between the TMM and the modal decomposition method for the larger specimens, but the methods disagree for the smaller specimen size. The results for the two ceramic tubular materials show a repeating resonant pattern with a monotonic decrease in the resonant peaks of the acoustic resistance with increasing frequency. Also, significant mode scattering is evident in most of the specimens tested.

CHAPTER 1 INTRODUCTION

Modern society has increasingly demanded a safer, more pleasant living environment. Studies have also shown that exposure to noise pollution has adverse health effects such as hearing impairment, reduced speech perception, sleep deprivation, increased stress levels, and general annoyance (Berglund et al. 1999). These results have led to increased noise restrictions on industrial factories, automobiles, and aircraft. The common element of these sources is that they all produce a complex noise spectrum and broad bandwidth. Yet increased noise restrictions have been readily met because of an increased research effort in acoustics, involving sound generation, propagation, and suppression (Golub et al. 2005).

The aerospace industry has been a major focus for increased noise regulations due to community noise concerns around commercial airports (Motsinger and Kraft 1991; Berglund, Lindvall and Schwela 1999). Takeoff, landing and cutback are the flight segments of greatest relevance to community noise concerns because of the relative proximity of the aircraft to the community. These flight segments and reference measurement points are shown in Figure 1-1. During these flight segments, the configuration of the aircraft is altered from the clean cruise configuration via the deployment of high-lift devices and landing gear. Also, during take-off the engines operate at full power, further increasing the noise levels. In order to reduce the fly-over noise, the power to the engines is reduced after take-off, during climb or cutback when the aircraft is still relatively close to the ground near populated areas. The overall noise

level from the aircraft has contributions from many sources as shown in Figure 1-2. These contributions can be separated into two broad categories: airframe noise and engine noise. Examples of airframe noise include noise generated from flaps, slats, landing gear, and vertical and horizontal tails. Engine noise consists of jet noise from the exhaust, combustion noise, turbomachinery noise, and the noise due to the integration of the engines with the airframe. The effective perceived noise levels (EPNL) (Smith 1989) of the component noise sources for the three flight segments are shown in Figure 1-3 for a Boeing 767-300 with GEAE CF6-80C2 engines. The figure shows that the major contributors to the total aircraft noise are jet and fan noise for takeoff, jet noise for cutback, and inlet, fan and airframe noise for approach. Thus, to reduce aircraft noise for takeoff and cutback, engine noise should be reduced, whereas airframe noise must be considered for the approach flight segment.

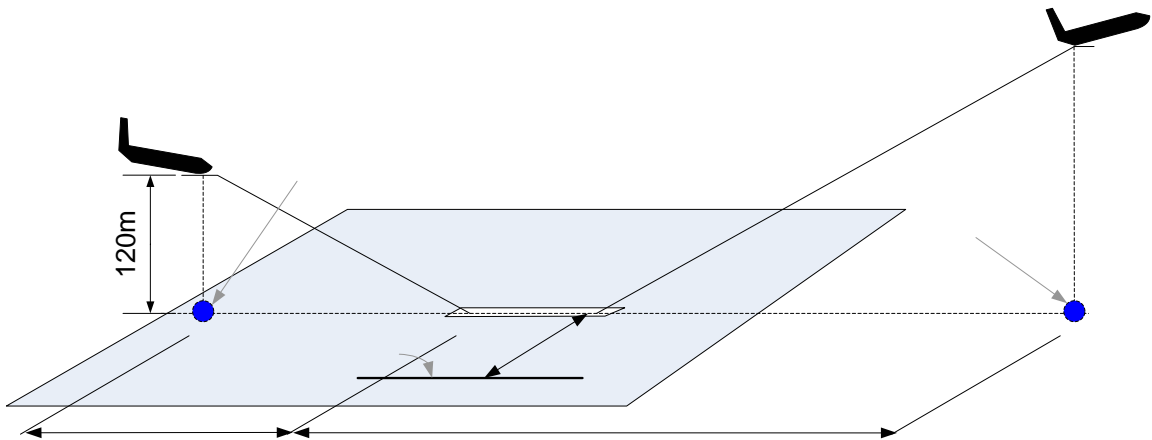


Figure 1-1: Illustration of the approach, takeoff, and cutback flight segments and measurement points (adapted from Smith 1989).

Early commercial aircraft used turbojet engines, and the resulting noise was dominated by the jet noise component. With the advent of ultra high bypass turbofan engines, the dominant noise sources for modern commercial jet aircraft are now engine

noise (during takeoff) and airframe noise (during approach). Because it was the dominant noise source in earlier jet aircraft, jet noise has been studied for many decades. Lighthill's analogy can be used to understand the scaling issues in the evolution of the jet engine noise from the first turbojet engines to modern high-bypass-ratio turbofan engines. Lighthill's analogy relates the mean square value of the radiated density perturbations ($\overline{\rho'^2}$) from a subsonic turbulent jet to the velocity and diameter of the jet as (Dowling and Ffowcs-Williams 1983)

$$\overline{\rho'^2} \sim \rho_0^2 M^8 \frac{D^2}{|r|^2}, \quad (1.1)$$

where ρ_0 is the mean or atmospheric density, M is the exit Mach number of the jet, D is the diameter of the jet and r is the distance from the jet. Equation (1.1) is only valid for subsonic flows and shows that the magnitude of the sound from a jet is more dependent on the velocity of the jet than the size of the jet. In particular, the mean square density perturbations are proportional to the eighth power of the Mach number but only to the second power of the diameter. A comparative chart of the perceived noise levels from various engine types is given in Figure 1-4. The first generation of jet aircraft relied on propulsion from a single, high velocity jet from the aft of the engine (Rolls-Royce 1996). This generated a tremendous amount of noise, as seen from Lighthill's analogy.

Subsequently, noise suppression devices for these engines have been developed to reduce the noise generated from the jets. The devices included suppressor nozzles that promote rapid mixing of the exhaust jet with the ambient fluid (Owens 1979). The overall effect is to quickly reduce the velocity of the jet and thus reduce the noise levels. The next development was the low-bypass-ratio turbofan engine (Rolls-Royce 1996).

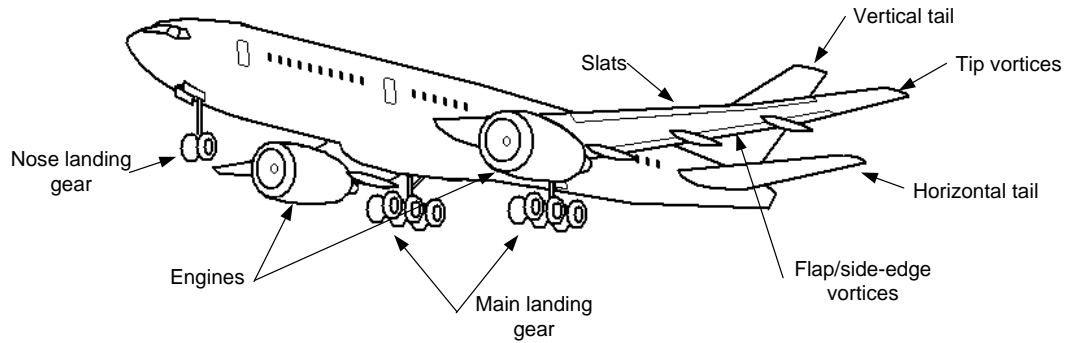


Figure 1-2: Typical noise sources on an aircraft (adapted from Crighton 1991).

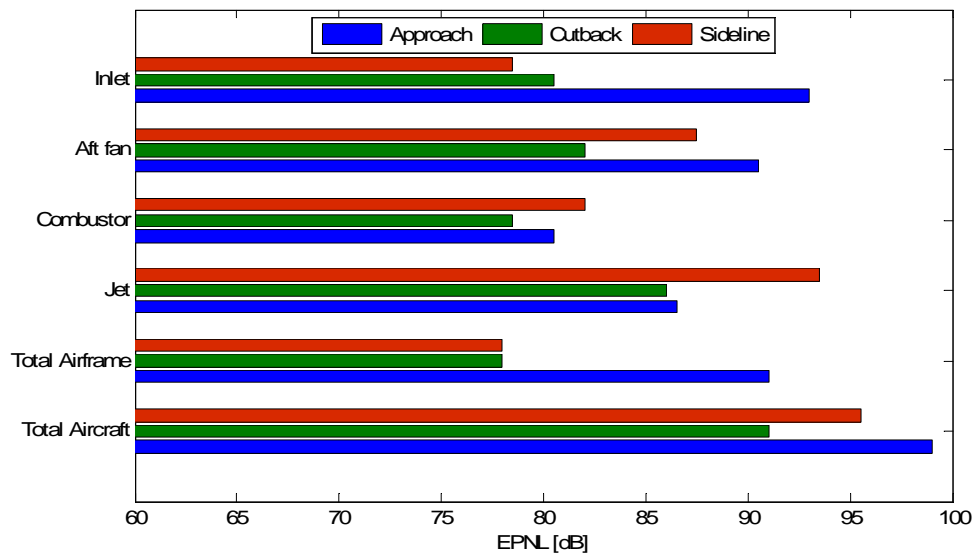


Figure 1-3: Component noise levels during approach, cutback, and take-off for a Boeing 767-300 with GEAE CF6-80C2 engines (adapted from Golub et al. 2005).

For this engine, the majority of the propulsion force is generated by the bypass flow with an increased area, and at the exit the bypass air is mixed with the jet, significantly lowering the exit Mach number. The diameter of the engine and jet was enlarged, but noise levels were significantly reduced because of the lower-velocity jet from the fan and the mixing of the two jets. Modern turbofan engines use high-bypass-ratio inlets, with a bypass ratio of approximately three or greater (Rolls-Royce 1996). The diameter of the fans on these engines can thus be 2.5 m or larger. The diameter of the exiting air flow is increased, the mixing is increased, and the jet velocity is decreased, thus lowering the

propagated noise. The growth of the diameter from these large high-bypass turbofans is now restricted by problems related to the large weight and large frontal area, such as drag (Rolls-Royce 1996).

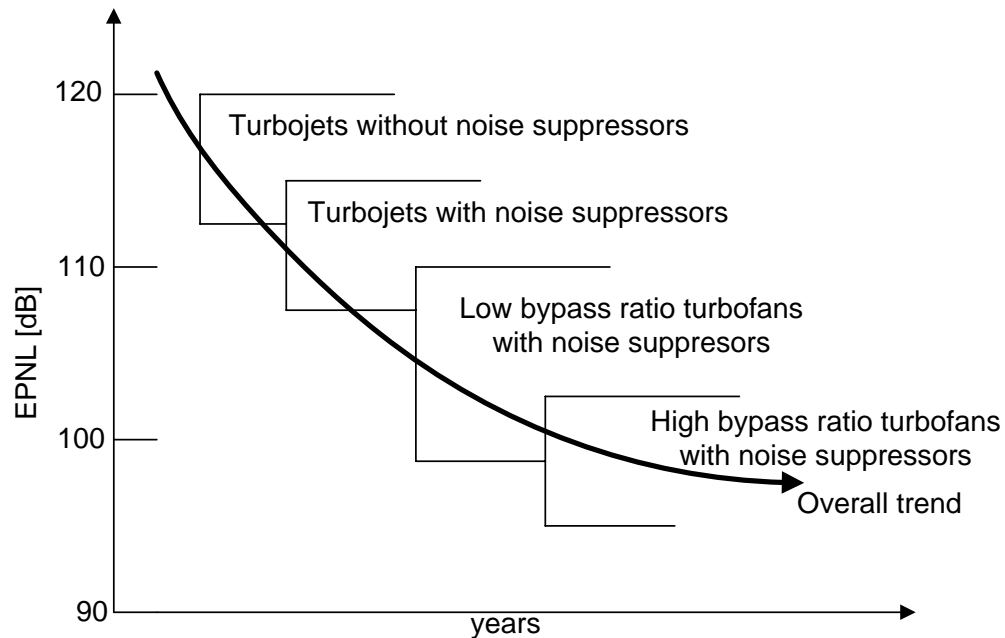


Figure 1-4: Comparative overall noise levels of various engine types (adapted from Rolls-Royce 1996).

Since the use of high-bypass-ratio turbofans has reduced the perceived noise levels from the jet by approximately 20 dB, other noise sources have become important contributors to the overall noise level of the aircraft (Smith 1989). Two such sources are engine noise (other than jet noise) and airframe noise. To reduce the engine noise, designs have focused on acoustic treatments to the interior of the engine nacelles to alter the propagation of the sound and reduce the radiation of noise from the engine into the far-field (Motsinger and Kraft 1991). These nacelle liners are placed at various locations throughout the engine to suppress noise from a particular region, as shown in Figure 1-5. The liners minimize the radiation of sound by altering the acoustic impedance boundary condition along the walls of the nacelle. The acoustic impedance, which is the complex

ratio of the acoustic pressure to the acoustic volume velocity, is a property of the liner configuration and materials. As shown in Figure 1-6, typical single degree-of-freedom (SDOF) liners are a composite structure of a layer of honeycomb support sandwiched between a solid backing sheet and a perforated face sheet. These liners act as Helmholtz resonators and are used to attenuate the noise spectrum (Motsinger and Kraft 1991; Rolls-Royce 1996). The bandwidth over which a SDOF liner is effective is about one octave, centered around its resonant frequency (Motsinger and Kraft 1991). If the liner has two layers of honeycomb separated by a second perforate face sheet, the liner is called a two degree-of-freedom (2DOF) liner as shown in Figure 1-7. The 2DOF liner has two resonant frequencies and a larger bandwidth, about two octaves, of effectiveness relative to the SDOF liner, but weigh more than SDOF liner (Motsinger and Kraft 1991; Bielak et al. 1999). Another type of liner uses a bulk absorber, which is designed to attenuate sound over a broad bandwidth. These liners are less effective at reducing the propagation of engine at a given frequency as compared to the SDOF or 2DOF liners, and usually are not able to provide structural support (Motsinger and Kraft 1991; Bielak, Premo and Hersh 1999). Typical materials used for bulk absorbers include woven wire mesh, ceramic tubular materials, and acoustic foams and fibers such as polyurethane, melamine, fiberglass, etc.

When designing an engine nacelle for noise suppression, semi-empirical analytical models can be used to find the optimal acoustic impedance for acoustic treatment (Motsinger and Kraft 1991). Potential liner candidates must be experimentally tested to determine their acoustic impedance. The experimentally measured values can then be used in new models to predict the noise levels from the engine for that particular

configuration. Scale model and full-size engine testing can be done to verify the noise level predictions and to certify the engine.

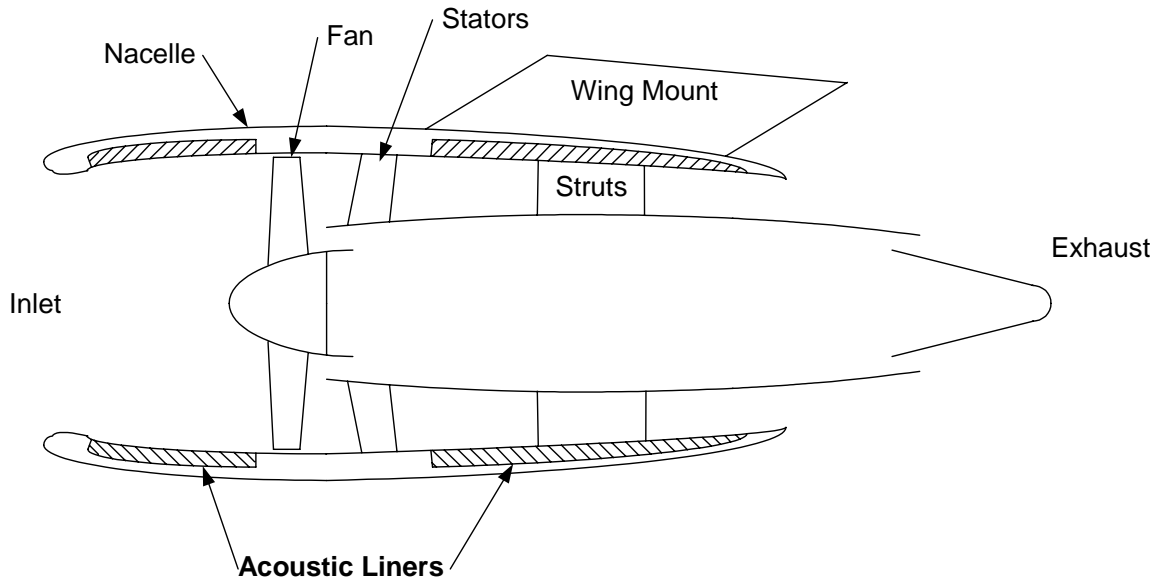


Figure 1-5: Engine cutaway showing the acoustic liner locations (adapted from Groeneweg et al. 1991; Rolls-Royce 1996).

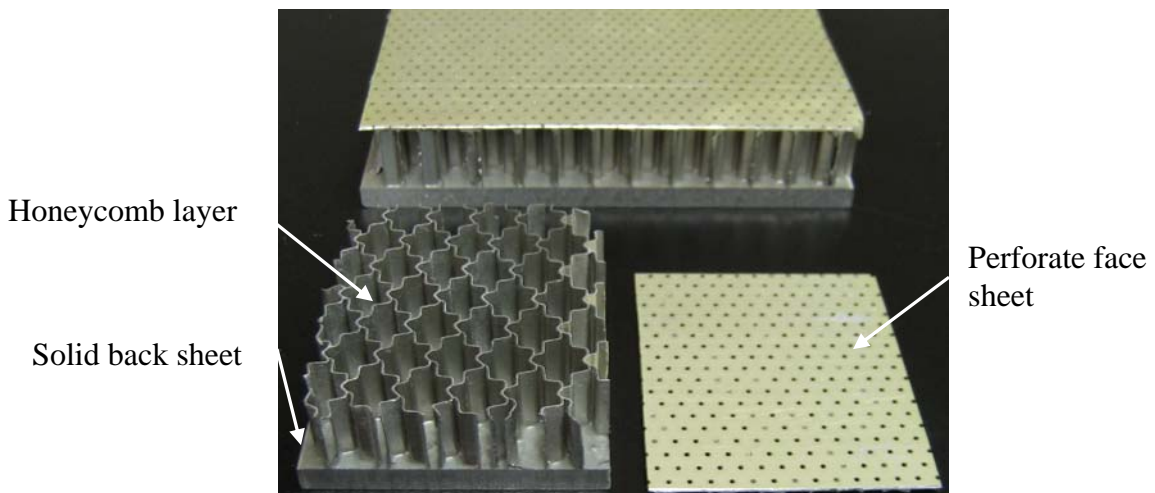


Figure 1-6: An example of a SDOF liner showing the atypical honeycomb and the perforate face sheet (courtesy of Pratt and Whitney Aircraft).

One of the limiting factors for the computational models is the experimental database for the acoustic properties of any material used for noise control (Kraft et al. 1999; Kraft et al. 2003). Current applications require extending the frequency range of

acoustic impedance testing out to 20 kHz to accommodate 1/5th-scale aeroacoustic testing (Kraft, Yu, Kwan, Echternach, Syed and Chien 1999; Kraft, Yu, Kwan, Beer, Seybert and Tathavadekar 2003). Existing methods for measuring normal-incident acoustic impedance have their limitations. Of these, the most noticeable limitation is the frequency range within which the methods are valid. Therefore, existing sound propagation models must extrapolate the acoustic impedance to the frequency range of interest for applications. This introduces a potentially large source of error in the models. Better results could be realized if the actual acoustic impedance of the materials could be measured in the frequency range of interest.

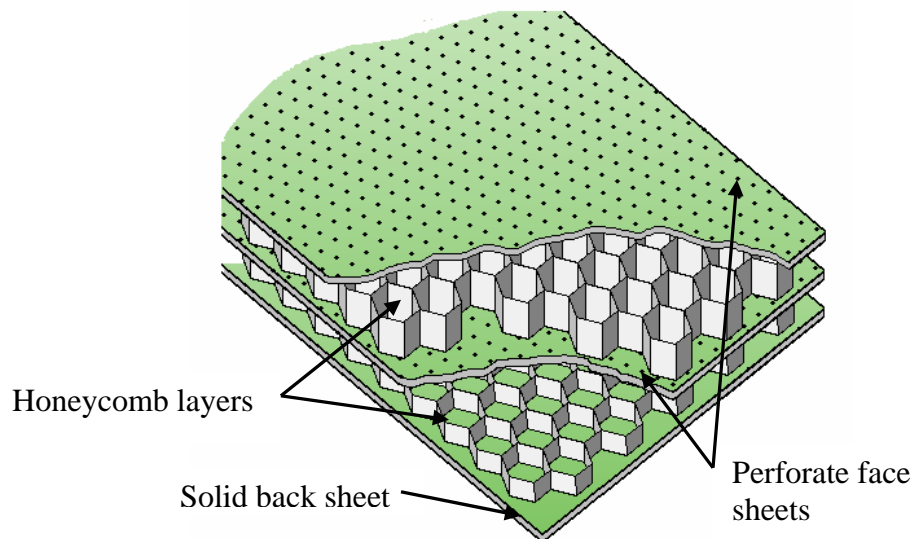


Figure 1-7: An example of a 2DOF liner (adapted from Rolls-Royce 1996).

The Two-Microphone Method (TMM) (Seybert and Ross 1977; Chung and Blaser 1980; ASTM-E1050-98 1998; ISO-10534-2:1998 1998) and the Multi-Point Method (MPM) (Jones and Parrott 1989; Jones and Stiede 1997) are two techniques to determine the normal-incidence acoustic impedance of materials. For the TMM, a compression driver is mounted at one end of a rigid-walled waveguide and the test specimen is mounted at the other end (Figure 2-11). Two microphones are flush-mounted in the duct

wall at two locations along the tube near the specimen to measure the incident and reflected waves with respect to the sample. The data are used to estimate the complex reflection coefficient and the corresponding acoustic impedance of the test specimen. More detailed information on the TMM is presented later in Chapter 2. The test procedure for the MPM is similar to the TMM except the number of microphones is increased and the computations rely on a least-squares approach. However, the MPM still assumes that only plane waves exist in the waveguide. Since the TMM is supported by ISO and ASTM standards, it is the method used in this dissertation.

Both methods have produced results for materials up to a frequency of approximately 12 kHz. The TMM or the MPM can, in theory, be extended to higher frequencies. However, in order to do, the specimen size of the material would need to be reduced to maintain the plane wave assumption, since the upper frequency limit of the method is inversely proportional to the specimen size or waveguide dimensions (ASTM-E1050-98 1998; ISO-10534-2:1998 1998). The size is limited in order to prevent the propagation of higher-order modes and thus maintain the plane wave assumption. For square cross-section of length a , the maximum frequency for plane waves, $f_{plane\ wave}$, is (Blackstock 2000)

$$f_{plane\ wave} < \frac{c_0}{2a}, \quad (1.2)$$

where c_0 is the isentropic speed of sound inside the waveguide. A specimen of 25.4 mm by 25.4 mm is limited to a frequency range up to approximately 6.7 kHz in ambient air using the TMM, but a specimen of 8.5 mm by 8.5 mm has a frequency range up to 20 kHz. Unfortunately, a small specimen size results in installation and fabrication issues and in local material variations that can cause changes in the measured acoustic

impedance. The installation and fabrication issues arise from having to cut a finite specimen, often resulting in damage to its edges. Furthermore, the smaller the specimen size, the larger the percentage of the total area composed of the damaged edges. For the local material variations, testing a large number of specimens can quantify these statistical variations. However, this approach is time consuming and costly.

Another method to increase the frequency range is to permit the propagation of higher-order modes (Åbom 1989; Kraft et al. 2003). This allows large specimens but increases the complexity of the measurement setup and data reduction routine. For a 25.4 mm-square duct, the bandwidth is increased to 13.5 kHz if the first four modes propagate or to 20 kHz if the first nine modes propagate. The advantage to this modal decomposition method (MDM) is that the higher-order modes can also be modeled as plane waves at oblique angles of incidence; thus this method can yield information regarding the effects of angle of incidence. The oblique-incidence information can be used to verify the local reactivity assumption, which states that the acoustic impedance is independent of the angle of incidence (Dowling and Ffowcs-Williams 1983).

Before the frequency range can be extended, the accuracy of the existing methods must be understood. Accurate uncertainty estimates give insight into how errors scale versus frequency and will aid in the design of new measurement techniques and improved liners. Without understanding uncertainty, there is no way to ensure that such measurements will meet the needs of the aeroacoustic application.

1.1 Research Goals

The focus of this dissertation is to increase the frequency range of acoustic impedance measurement technology to the range of interest in aeroacoustic applications and to supply experimental uncertainty estimates with the data. These data will help to

evaluate potential liner candidates and improve the accuracy of models of the sound field. Also, design procedures and codes that predict the acoustic impedance of typical liners can be validated using the acoustic impedance data with corresponding uncertainty estimates. The implementation of improved experimental techniques and corresponding uncertainty analyses with existing design and computational tools will assist in the reduction of time and cost required to meet community noise restrictions.

To meet the goal of extending the frequency range of acoustic impedance measuring technology, two different approaches are used. The first seeks to reduce the size of the cross-section of the waveguide and test specimen to increase the cut-on frequency for the first higher-order mode to 20 kHz, allowing the TMM to be used. This will limit the specimen size to 8.5 mm by 8.5 mm , and thus the above mentioned specimen size issues may affect the results. The second approach is to keep the specimen at 25.4 mm by 25.4 mm and allow for the propagation of higher order modes. A direct Modal Decomposition Method (MDM) is used that allows for and computes the amplitudes of the incident and reflected waves for the higher-order modes. This allows the frequency range to increase. This method will provide a comparison for the data measured with the small specimen to elucidate any issues associated with the specimen size. Also, acoustic impedance data at angles of incidence other than perpendicular to the specimen surface are measured, because higher-order modes can also be thought of as plane waves traveling at an angle with respect to the axis of the duct.

Before either path is pursued, two techniques are first developed to estimate the uncertainty for the complex reflection coefficient. One method is an analytical approach that provides scaling information, and the other is a Monte Carlo method that is not

restricted to small perturbations. The two methods are compared to each other to help determine their strengths and weaknesses.

1.2 Research Contributions

The contributions of this dissertation to the aeroacoustic community are as follows.

- Development of an analytical and a numerical method for the propagation of experimental uncertainty in data reduction routines with complex variables.
- Application of the uncertainty analysis methods to the Two-Microphone Method.
- Application of a Modal Decomposition Method for measuring normal-incident acoustic impedance in the presence of higher-order modes in the waveguide.
- Comparison of experimental data with uncertainty estimates for acoustic impedance from the TMM and the MDM. The specimens compared are a rigid termination and two ceramic tubular materials.

1.3 Dissertation Organization

This dissertation is organized into six chapters. This chapter introduced and discussed the motivation for the research present in this dissertation. The next chapter reviews the theory of acoustic waveguides. The derivation of the TMM is presented there as well. Chapter 3 presents the derivation and application of the uncertainty methods for the TMM and includes a discussion of the issues present when increasing the bandwidth of the TMM up to 20 kHz. Chapter 4 introduces the MDM, a method that accounts for the propagation of higher-order modes through the waveguide. This chapter presents the derivation of this method and a discussion of the requirements for the data acquisition hardware to ensure reasonable accuracy. Chapter 5 presents detailed experimental results for different acoustic impedance specimens. The final chapter offers concluding remarks and future directions.

CHAPTER 2 ACOUSTIC WAVEGUIDE THEORY

This chapter introduces the basic analytical analysis for rectangular duct acoustic waveguides. First, the acoustic wave equation is presented, and its solution is given. Next, a discussion of the solution properties is presented. Then this chapter concludes with a derivation of the TMM.

2.1 Waveguide Acoustics

A waveguide is a device that is used to contain and direct the propagation of a wave. A simple example of an acoustic waveguide is a plastic tube with a sound source at one end. For simple geometries of the internal cross section, the exact sound field in the waveguide can be solved from the linear lossless acoustic wave equation, as long as the wave equation assumptions are not violated (Pierce 1994; Blackstock 2000). The lossy wave equation can also be solved for some simple cases but an ad hoc method will be introduced in a later section in this chapter to account for attenuation. The linear lossless acoustic wave equation assumes that an acoustic wave is isentropic, the pressure perturbations are small compared to the medium's bulk modulus ($\rho_0 c_0^2$), and that there is no mean flow of the medium. Under these conditions, the wave equation for pressure fluctuations is

$$\frac{1}{c_0^2} \frac{\partial^2 p'}{\partial t^2} - \nabla^2 p' = 0, \quad (2.1)$$

where p' is the acoustic pressure, c_0 is the isentropic propagation speed given by $c_0 = \sqrt{\gamma R_{gas} T}$, γ is the ratio of specific heats, R_{gas} is the ideal gas constant, T is the absolute temperature, t is time and ∇^2 is the Laplacian operator. First, let the coordinate system for the waveguide be defined as a Cartesian coordinate system with the z -axis aligned with the axis of the tube, and the origin located at a corner of the tube as shown in Figure 2-1. The d -axis as shown is a useful auxiliary coordinate axis. Note that the d -direction is the direction along the axis of the tube and is the propagation direction for reflected waves.

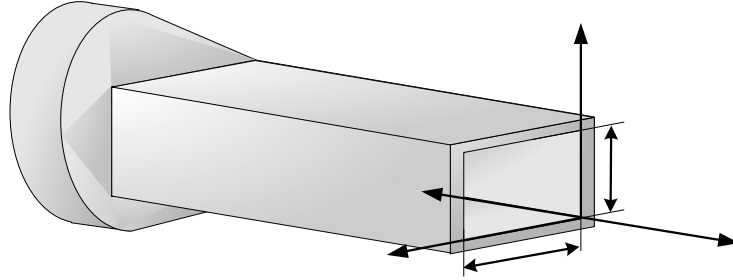


Figure 2-1: Illustration of the waveguide coordinate system.

2.1.1 Solution to the Wave Equation

Solutions to the wave equation are present in many sources such as (Rayleigh 1945), (Dowling and Ffowcs-Williams 1983), (Pierce 1994), (Morse and Ingard 1986), (Kinsler et al. 2000) and (Blackstock 2000). For the solution presented in this section, the acoustic pressure signal is assumed to be time-harmonic which states

$$p' = \text{Re}(\underline{P} e^{j\omega t}), \quad (2.2)$$

where \underline{P} is the complex acoustic pressure amplitude and ω is the angular frequency.

After substituting Equation (2.2) into the acoustic wave equation, it reduces to

$$\nabla^2 \underline{P} + k^2 \underline{P} = 0, \quad (2.3)$$

which is known as Helmholtz's Equation (Pierce 1994; Blackstock 2000). The constant k is the wavenumber, which is defined as

$$k = \frac{\omega}{c_0}. \quad (2.4)$$

The general solution to the Helmholtz equation, assuming propagation in the d -direction, is a summation of normal modes given as

$$\underline{P} = \sum_m \sum_n \psi_{mn}(x, y) (A_{mn} e^{jk_z d} + B_{mn} e^{-jk_z d}) \quad (2.5)$$

where $j = \sqrt{-1}$, A_{mn} and B_{mn} are the complex modal amplitudes of the incident and reflected wave, respectively, m and n are the mode numbers, k_z is the propagation constant, and $\psi(x, y)$ is the transverse factor. The transverse factor is a product of two eigenfunctions determined by the boundary conditions. For the waveguides used in this dissertation, the tube walls are assumed to be sound-hard or rigid and therefore do not vibrate or transmit sound. Practically, the sound-hard boundary condition can be realized for a gaseous medium by utilizing tube walls made of a thick, rigid material, such as steel or aluminum. The only boundary condition provided by a sound-hard boundary for an inviscid flow is that the particle velocity normal to the surface is zero at the walls. From the conservation of momentum (i.e. Euler's Equation), this is represented as the normal gradient component of the acoustic pressure being equal to zero. Hence, the transverse factor for a rectangular duct with rigid walls is

$$\psi_{mn}(x, y) = \cos\left(\frac{m\pi}{a}x\right) \cos\left(\frac{n\pi}{b}y\right) \quad (2.6)$$

where a and b are the side lengths of the waveguide shown in Figure 2-1. The remaining constants, the complex modal amplitudes, A_{mn} and B_{mn} , are determined by

two boundary conditions. The first boundary condition is a given acoustic impedance at $d = 0$. The second boundary condition would be a known pressure or velocity source at the other end of the waveguide at $d = L_{wg}$, where L_{wg} is the length of the waveguide.

Applying the boundary conditions, Equation (2.5) can be solved for each A_{mn} and B_{mn} .

The $A_{mn} e^{jk_z d}$ terms represent waves traveling from the source to the other end of the tube. The $B_{mn} e^{-jk_z d}$ terms represent the reflected waves returning to the source after bouncing off the sample.

The dispersion relation for the rectangular waveguide comes from the separation constant from applying a separation of variables solution to Equation (2.3) and is

$$k_z = \sqrt{\left(\frac{\omega}{c_0}\right)^2 - \left(\frac{m\pi}{a}\right)^2 - \left(\frac{n\pi}{b}\right)^2} \quad (2.7)$$

and, for a normal mode to propagate, k_z must contain a real-valued component.

If k_z has an imaginary component, there will be two solutions to Equation (2.7) that will be complex conjugates. For a waveguide, only the solution that causes the amplitude to exponentially decay is physically valid from conservation of energy. This term will force the acoustic pressure amplitude to zero as the axial distance increases in the direction of propagation, and the wave is deemed an evanescent wave.

2.1.2 Wave Modes

The indices m and n represent the mode numbers and are denoted by (m, n) .

Physically, the indices m and n represent the number of half-wavelengths in the x -direction and y -direction, respectively. The frequency at which a mode makes the transition from evanescent to propagating is known as the cut-on frequency. Below the

cut-on frequency, the mode is evanescent. Above the cut-on frequency, the mode is propagating and present along the entire length of the waveguide. The cut-on frequencies are calculated from the dispersion relation in Equation (2.7) when $k_z = 0$,

$$f_{mn}^{co} = \frac{c_0}{2} \sqrt{\left(\frac{m}{a}\right)^2 + \left(\frac{n}{b}\right)^2}. \quad (2.8)$$

The experiments for this dissertation will use two different waveguides. Both of them have a square cross-section. The length of the sides of the first waveguide is 8.5 mm. For air at 298 K and 101.3 kPa, $c_0 = 343 \text{ m/s}$ and the cut-on frequencies for the different modes are given in Table 2-1. Notice that the cut-on frequency for the first higher-order mode is approximately 20 kHz. This implies that only plane waves are present below this frequency and that the TMM can be used.

Table 2-1: Cut-on frequencies in kHz for an 8.5 mm by 8.5 mm waveguide.

$m \backslash n$	0	1	2	3
0	0	20.2	40.4	60.5
1	20.2	28.5	45.1	63.8
2	40.4	45.1	57.1	72.8
3	60.5	63.8	72.8	85.6

The second waveguide that will be used for this experiment has a square cross-section measuring 25.4 mm on each side. For the same conditions as above, the cut-on frequencies for the different modes are given in Table 2-2. Note that the plane wave mode, mode (0,0), is present for all frequencies. Also note that only the (0,0), (1,0), (0,1) and (1,1) modes are present at frequencies less than 13.5 kHz. The (1,0) and (0,1) modes have one half wavelength in the x -direction and y -direction, respectively. The (1,1) mode has a half wavelength in both the x -direction and the y -direction. The mode shapes are

given in Figure 2-2 as observed from the sound source. The node lines indicate where the acoustic pressure is zero. Also note that the wavenumbers are a function of the mode.

Table 2-2: Cut-on frequencies in kHz for a 25.4 mm by 25.4 mm waveguide.

$m \backslash n$	0	1	2	3
0	0	6.75	13.5	20.3
1	6.75	9.55	15.1	21.4
2	13.5	15.1	19.1	24.4
3	20.3	21.4	24.4	28.7

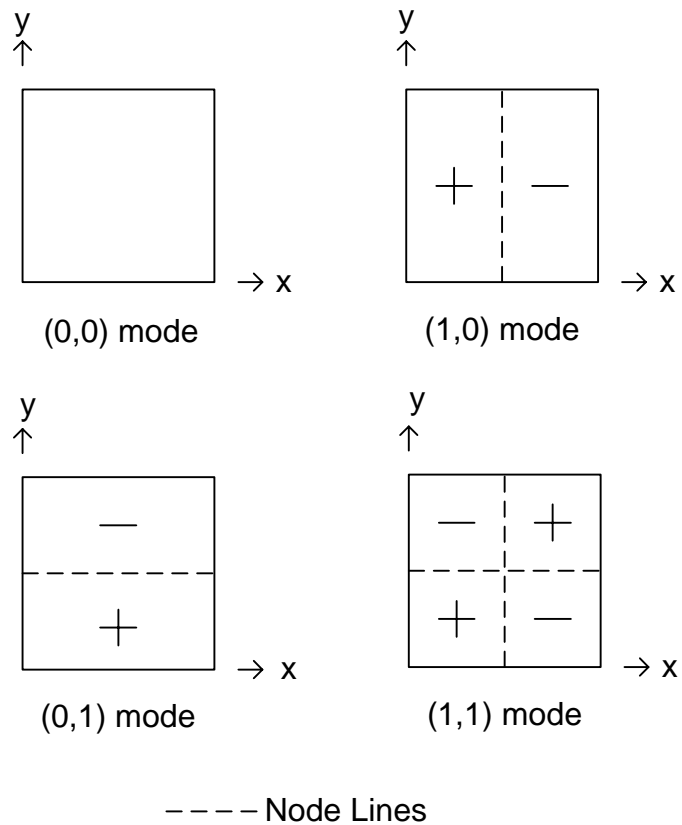


Figure 2-2: Illustration of the first four mode shapes.

2.1.3 Phase Speed

The speed at which a wave front travels down the axis of the waveguide is known as the phase speed. The phase speed, c^{ph} , is defined for a rectangular waveguide as (Blackstock 2000)

$$c^{ph} = \frac{\omega}{k_z}. \quad (2.9)$$

and can be found for each mode:

$$c_{mn}^{ph} = \frac{\omega}{\sqrt{\left(\frac{\omega}{c_0}\right)^2 - \left(\frac{m\pi}{a}\right)^2 - \left(\frac{n\pi}{b}\right)^2}}, \quad (2.10)$$

which can be rewritten as

$$c_{mn}^{ph} = \frac{c_0}{\sqrt{1 - \left(\frac{f_{mn}^{co}}{f}\right)^2}}. \quad (2.11)$$

The concept of the phase speed allows for higher-order modes to be considered as plane waves traveling at an angle inside the waveguide, as shown in Figure 2-3. From Equation (2.11), as the frequency is increased the phase speed approaches the isentropic speed of sound but the phase speed at the cut-on frequencies for each mode tends to infinity. The incidence angle with respect to the waveguide wall normal as seen in Figure 2-3, θ_{mn} , is found from the geometric relationship between the phase speed for that mode and the speed of sound. Thus the incidence angle is found from

$$\theta_{mn} = \sin^{-1}\left(\frac{c_0}{c_{mn}^{ph}}\right) = \sin^{-1}\left(\sqrt{1 - \left(\frac{f_{mn}^{co}}{f}\right)^2}\right). \quad (2.12)$$

Another useful angle that is developed from the concept of phase speed is the angle that the wave makes with the normal to a flat termination at the end of the waveguide ($d = 0$), denoted by ϕ_{mn} . From the geometry given in Figure 2-3 and from specular reflection,

ϕ_{mn} is complementary to θ_{mn} by

$$\phi_{mn} = 90^\circ - \theta_{mn} = \cos^{-1} \left(\frac{c_0}{c_{mn}^{ph}} \right) = \cos^{-1} \left(\sqrt{1 - \left(\frac{f_{mn}^{co}}{f} \right)^2} \right). \quad (2.13)$$

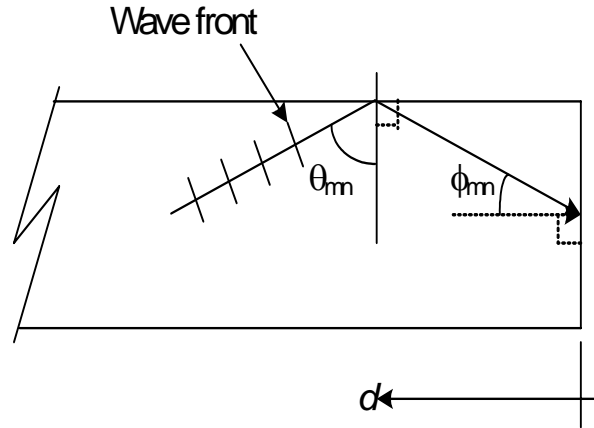


Figure 2-3: Illustration of the wave front and the incidence angle to the waveguide wall, θ_{mn} and to the termination, ϕ_{mn} .

The expressions given above for the phase speed, Equation (2.11) and the two angles of incidence, Equations (2.12) and (2.13), are shown only to depend on the waveguide geometry, the bandwidth of interest, and the mode number. For the waveguide with the 8.5 mm by 8.5 mm cross-section and a bandwidth of 20 kHz, the phase speed is simply the isentropic speed of sound and the wave is normally incident to the termination. Continuing with the example of a waveguide with a square cross-section of 25.4 mm by 25.4 mm, at room temperature and pressure the phase speed and the two angles of incidence are graphed in Figure 2-4, Figure 2-5 and Figure 2-6, respectively. A bandwidth of 13.5 kHz is used for the graphs, thus the included modes are (0,0), (1,0), (0,1) and (1,1). Figure 2-4 shows the phase speed, Figure 2-5 shows the angle of incidence the mode makes to the sidewall of the waveguide, and Figure 2-6 shows the angle of incidence the mode makes to the termination. The plane wave mode is present for all frequencies and is normally incident to the termination for all frequencies as well.

The properties of the other modes vary as a function of frequency. The phase speed approaches infinity asymptotically at the cut-on frequencies, where the angle of incidence to the sidewall approaches zero and the angle of incidence to the termination approaches 90 degrees. This shows that the MDM offers the potential to test the impedance of specimens with oblique incident-waves.

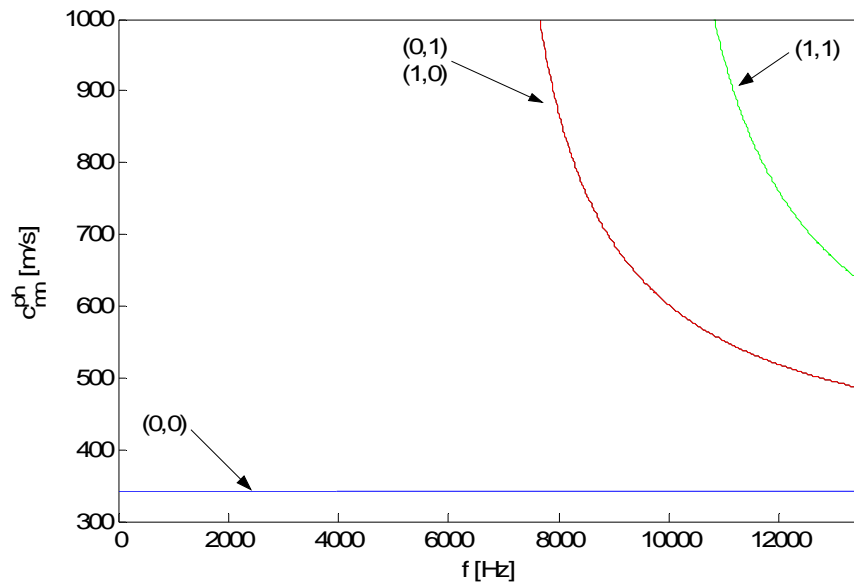


Figure 2-4: Phase speed versus frequency for the first four modes.

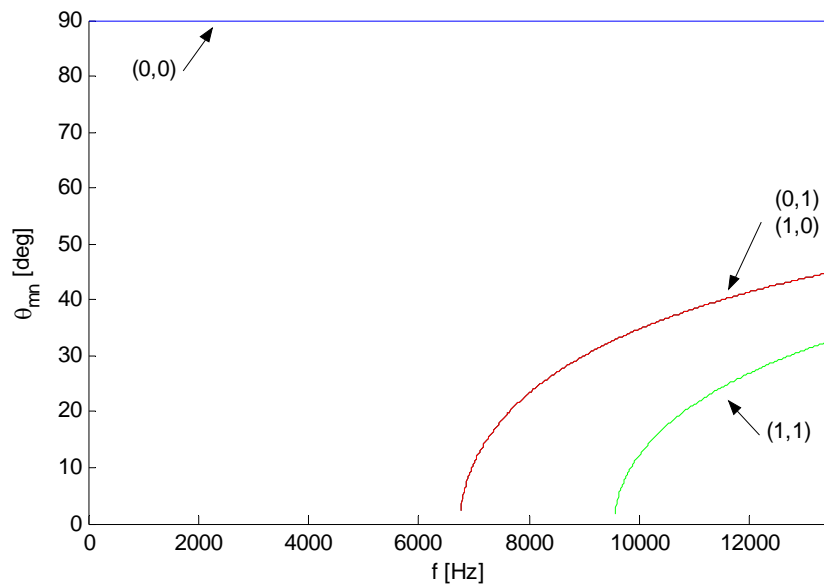


Figure 2-5: Angle of incidence to the sidewall versus frequency for the first four modes.

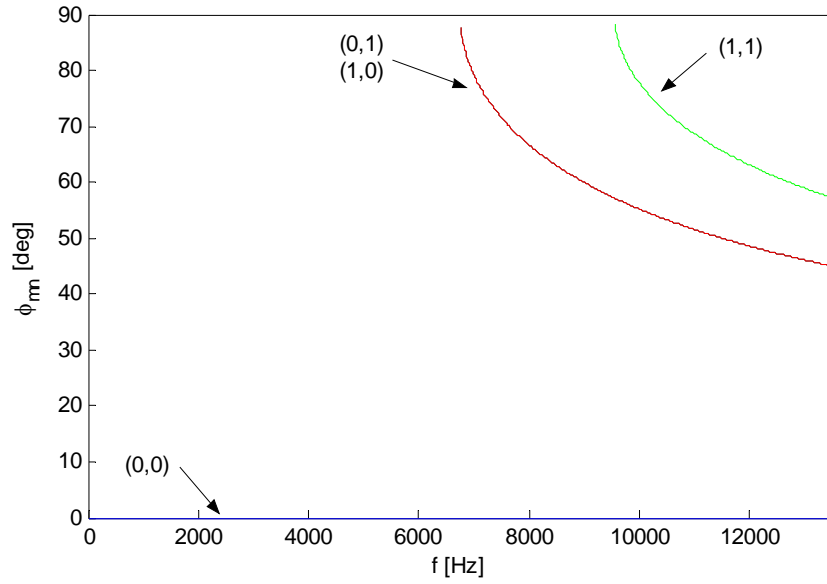


Figure 2-6: Angle of incidence to the termination versus frequency for the first four modes.

2.1.4 Wave Mode Attenuation

The energy in the evanescent wave modes exponentially decays as the wave propagates down the waveguide. The TMM assumes that only the plane wave mode is present at the microphone locations and that all other modes have decayed and can be neglected. To ensure that the evanescent waves have decayed sufficiently, the amplitude of a wave should be measured at two different axial locations in the waveguide.

This analysis of the decay of the amplitude of the evanescent waves assumes only an incident or right-running wave. This allows Equation (2.5) to be simplified for a single mode to

$$P_{mm} = A_{mm} \cos\left(\frac{m\pi}{a} x\right) \cos\left(\frac{n\pi}{b} y\right) e^{jk_c d}. \quad (2.14)$$

To measure the loss in amplitude of the evanescent wave, the ratio of Equation (2.14) is taken for two locations separated by a distance d_e to give

$$\frac{P_{mn}(d+d_e)}{P_{mn}(d)} = \frac{A_{mn} \cos\left(\frac{m\pi}{a}x\right) \cos\left(\frac{n\pi}{b}y\right) e^{jk_z(d+d_e)}}{A_{mn} \cos\left(\frac{m\pi}{a}x\right) \cos\left(\frac{n\pi}{b}y\right) e^{jk_z d}} = e^{jk_z d_e}. \quad (2.15)$$

Recall that for an evanescent wave, the wavenumber is imaginary and thus the amplitude of the evanescent wave will exponentially decay. The loss in amplitude can be defined on a decibel scale by

$$\eta = 20 \log_{10} \left(e^{-|k_z| d_e} \right). \quad (2.16)$$

The decay of the evanescent waves for the two waveguides introduced in Section 2.1.2 can be plotted. The distance traveled by the wave is assumed to be $d_e = 25.4 \text{ mm}$ for the large waveguide which is equal to the length of one of the sides of the cross-section. Figure 2-7 shows the attenuation of the higher-order modes in the large waveguide for modes (0,1), (1,0), up to (3,3) up to their cut-on frequency. The mode can be determined by comparing the cut-on frequency in the figure to those listed in Table 2-2. For the small waveguide, the distance traveled is assumed to be $d_e = 8.5 \text{ mm}$, which is again the length of one of the sides of the cross section. Figure 2-8 shows the attenuation of the higher-order modes in the small waveguide for modes (0,1), (1,0), up to (3,3) up to their cut-on frequency. The mode can be determined by comparing the cut-on frequency in the figure to those listed in Table 2-1. The amplitude of the first evanescent wave ((0,1) and (1,0)) is reduced by -3.8 dB with the frequency lowered from the cut-on frequency by only 16 Hz for the large waveguide and only 25 Hz for the small waveguide. The attenuation of other higher-order modes is larger.

Figure 2-9 shows the attenuation of the first higher-order mode in the large waveguide for two different distances. The two distances chosen are the distances from

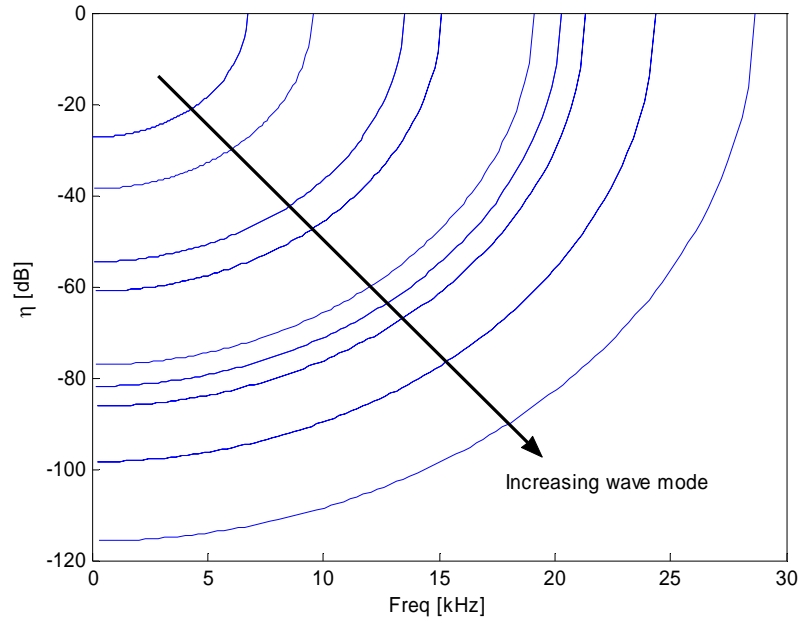


Figure 2-7: Attenuation of higher-order modes in the large waveguide over a distance of 25.4 mm.

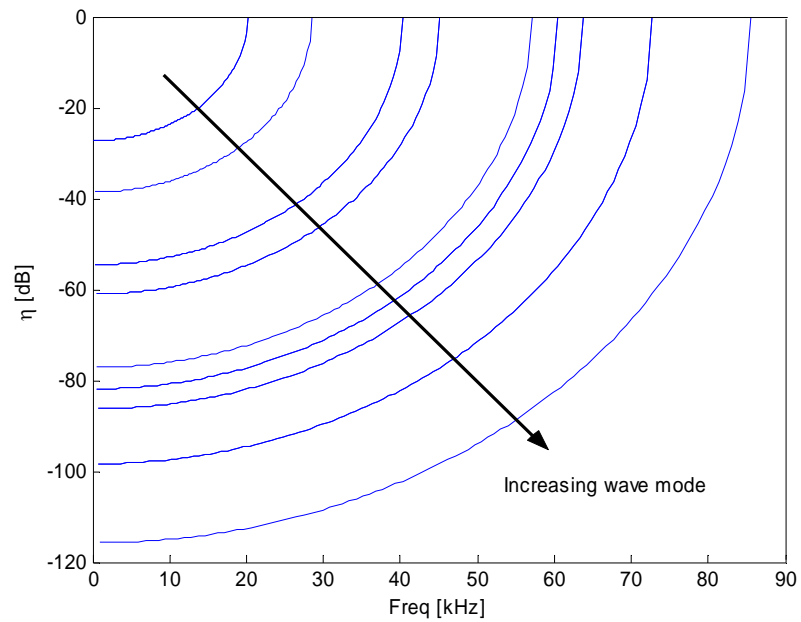


Figure 2-8: Attenuation of higher-order modes in the small waveguide over a distance of 8.5 mm.

the specimen test surface to the two microphones used in the TMM for the large waveguide. The attenuation shown in this figure represents the worst case in terms of contamination of the microphone signals with unmodeled deterministic signals that will

bias the estimates from the TMM. The figure shows that the attenuation approaches -34 dB asymptotically for the closer microphone location and -57 dB for the farther microphone location as the frequency approaches zero, but that the attenuation tends to zero near the cut-on frequencies. The -20 dB point for the closer microphone location is at approximately 5.47 kHz. Above this frequency, the signal measured by this microphone could be affected by the non-negligible amplitude of the higher-order modes propagating from the specimen to the microphone. The absolute amplitude of the first higher-order mode may still be negligible when compared to the absolute amplitude of the plane wave mode, because the overall length of the waveguide provides sufficient attenuation such that only plane waves are incident on the specimen and such that the specimen may not strongly scatter incident energy from the plane wave mode into the higher-order modes upon reflection.

The data shown in the figures in this section demonstrates that the attenuation of the higher-order modes is not an instantaneous effect. At the cut-on frequency, the higher-order modes have an infinite speed and are felt throughout the entire duct. As the frequency decreases away from cut-on, the amplitude of the evanescent mode is decreased, but only by a finite amount. If the initial amplitude of the evanescent mode is sufficiently high, then the attenuation may not be strong enough to reduce the amplitude below the noise floor of the measurement microphones. This may introduce a significant bias error source into the estimates for the TMM or any other method that assumes no amplitude in the evanescent modes. Numerical simulation of the sound field at the microphone locations, including an amplitude component for the higher-order modes, would be required to characterize the impact of the unmodeled evanescent modes. The

relative amplitudes between the microphone locations are known, as shown in Equation (2.15), and the absolute amplitude at one location could be inferred from experimental data. The simulated signals could then be processed as experimental data to gauge the amount of bias error that is introduced into the estimates for the reflection coefficient and acoustic impedance.

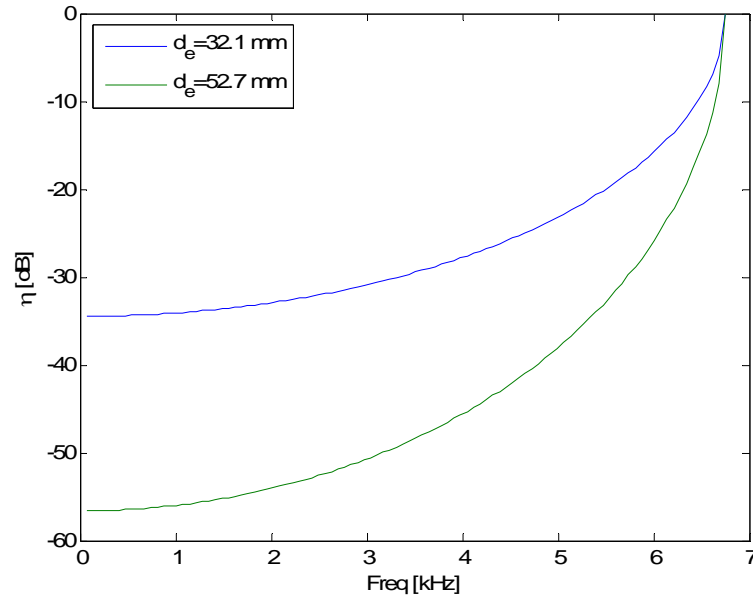


Figure 2-9: Attenuation of the first higher-order mode ((1,0) or (0,1)) in the large waveguide at the microphone locations used for the TMM experiments.

2.1.5 Reflection Coefficient and Acoustic Impedance

For the remainder of this chapter, only plane waves are assumed to propagate, thus restricting the bandwidth for a given waveguide. For this case, the reflection coefficient is the ratio of the acoustic pressure amplitudes of the reflected wave to the incident wave and is a single complex quantity. The plane wave reflection coefficient is defined as

$$R_{00,00} = \frac{B_{00}}{A_{00}}, \quad (2.17)$$

where $R_{00,00}$ is the plane wave reflection coefficient, and A_{00} and B_{00} are the complex modal amplitudes for the incident and reflected wave, respectively. The reflection coefficient indicates the degree to which a material reflects sound. However, the reflection coefficient can also be used to calculate the normalized specific acoustic impedance, ξ_{spac} , of a material. The normalized specific acoustic impedance is defined by the ratio of the acoustic impedance of the material to that of the medium used during the test. For most cases, the medium is air. The acoustic impedance is defined as the complex ratio of the acoustic pressure to the acoustic volume velocity. The specific acoustic impedance is the complex ratio of the acoustic pressure to the acoustic particle velocity. The characteristic impedance is the specific acoustic impedance of that particular medium.

For the purpose of finding the acoustic impedance ratio, consider an incident wave reflecting off the termination of the waveguide as shown in Figure 2-10. The two boundary conditions are applied to the interface (Blackstock 2000):

1. The pressure must be continuous across the interface.
2. The normal component of the particle velocity must be continuous across the interface.

The first boundary condition leads to the following expression

$$1 + R_{00,00} = T_{00,00}, \quad (2.18)$$

where $T_{00,00}$ is the plane wave transmission coefficient defined as the ratio of the amplitude of the transmitted pressure wave to the amplitude of the incident pressure wave. The second boundary condition leads to the following expression

$$\frac{1 - R_{00,00}}{Z_0} \cos(\phi_i) = \frac{T_{00,00}}{Z_1} \cos(\phi_{tr}), \quad (2.19)$$

where Z_0 and Z_1 are the specific acoustic impedances for medium 0 and medium 1, respectively. The terms $Z_0/\cos(\phi_i)$ and $Z_1/\cos(\phi_r)$ represent the acoustic impedance for medium 0 and medium 1, respectively, but under the plane wave assumption the incidence angle and the transmission angle are 0° with respect to the specimen surface normal and the acoustic impedance becomes identical to the specific acoustic impedance.

Thus, Equation (2.19) simplifies to

$$\frac{1 - R_{00,00}}{Z_0} = \frac{T_{00,00}}{Z_1}. \quad (2.20)$$

Equations (2.18) and (2.20) can be combined, and then the resulting expression can be solved for the plane wave specific acoustic impedance ratio, given by

$$\xi_{spac} = \frac{Z_1}{Z_0} = \frac{1 + R_{00,00}}{1 - R_{00,00}}. \quad (2.21)$$

From Equation (2.21), the task of finding the normalized specific acoustic impedance reduces to finding the reflection coefficient of the incident and reflection plane waves.

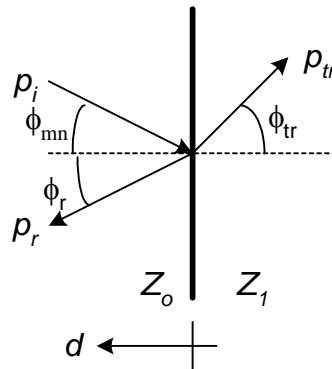


Figure 2-10: Reflection and transmission of a wave off an impedance boundary.

2.2 Two-Microphone Method

The TMM (Seybert and Ross 1977; Chung and Blaser 1980; ASTM-E1050-98 1998; ISO-10534-2:1998 1998) is a standardized technique for determining the normal incident acoustic impedance. A schematic of the test setup for the TMM is given in

Figure 2-11. The notation used here follows the ASTM E1050-98 standard (ASTM-E1050-98 1998). The advantage of the TMM is the simplicity offered by assuming the sound field is only comprised of plane waves. Therefore, only two unknown coefficients are determined and only two microphones are used. The data reduction equation for the TMM is derived in this section, starting from the basic assumptions and the general solution of the wave equation given in Equation (2.5). Afterwards, the effects of dispersion and dissipation are addressed briefly.

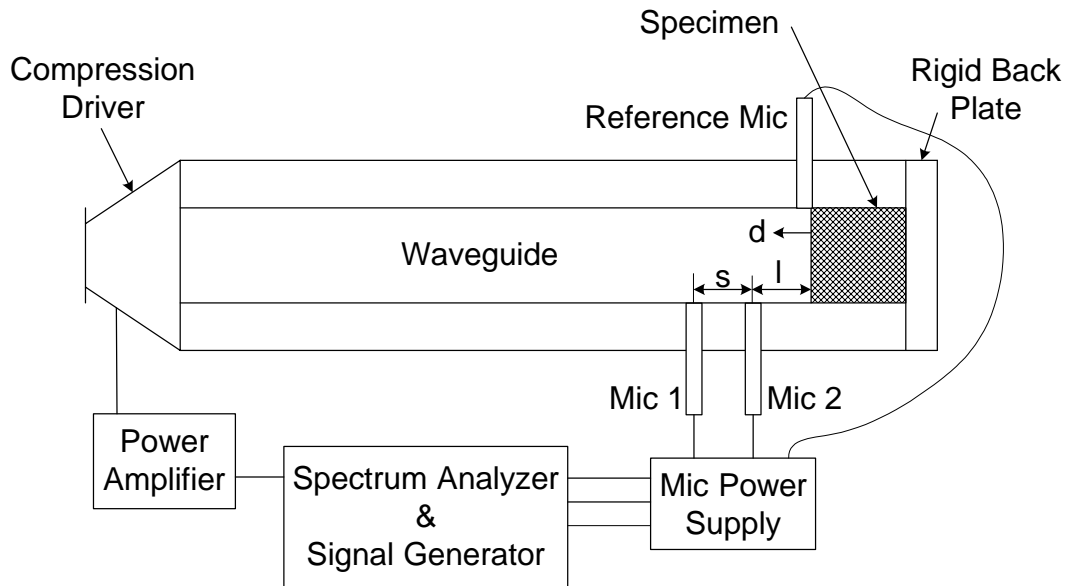


Figure 2-11: Experimental setup for the TMM.

2.2.1 Derivation of the TMM

The TMM assumes that the sound field inside the waveguide is composed solely of plane waves. This simplifies the solution to the wave equation from Equation (2.5) to

$$\underline{P} = A_{00} e^{jk_z d} + B_{00} e^{-jk_z d}. \quad (2.22)$$

This equation can then be recast by using the definition of the reflection coefficient given in Equation (2.17) to

$$\underline{P} = A_{00} \left(e^{jk_z d} + R_{00,00} e^{-jk_z d} \right). \quad (2.23)$$

Now, the two primary unknowns are $R_{00,00}$ and A_{00} . The two unknowns are solved for by taking measurements of the complex pressure amplitude at two different locations along the waveguide. Let l denote the distance between the test specimen and the closest microphone, \underline{P}_2 , and s denote the distance between the two microphones. The system of equations is

$$\underline{P}_1 = A_{00} \left(e^{jk_z(l+s)} + R_{00,00} e^{-jk_z(l+s)} \right), \quad (2.24)$$

$$\underline{P}_2 = A_{00} \left(e^{jk_z l} + R_{00,00} e^{-jk_z l} \right). \quad (2.25)$$

The complex pressure amplitude of the incident wave is eliminated from the system of equations by taking the ratio of \underline{P}_2 to \underline{P}_1 to get

$$H_{12} = \frac{\underline{P}_2}{\underline{P}_1} = \frac{e^{jk_z l} + R_{00,00} e^{-jk_z l}}{e^{jk_z(l+s)} + R_{00,00} e^{-jk_z(l+s)}}, \quad (2.26)$$

where H_{12} is the frequency response function between microphone 1 and microphone 2.

Then this new expression is solved for the reflection coefficient and simplified as

$$R_{00,00} = \frac{\hat{H}_{12} - e^{-jks}}{e^{jks} - \hat{H}_{12}} e^{j2k(l+s)}, \quad (2.27)$$

where $\hat{H}_{12} = E \left[\hat{G}_{12} / \hat{G}_{11} \right]$ is the estimate of the frequency response function between the two microphones, $E[\]$ is the expectation operator, \hat{G}_{12} is the estimated cross spectrum and \hat{G}_{11} is the estimated autospectrum (Bendat and Piersol 2000). The frequency response function is switched from the exact H_{12} to the estimate \hat{H}_{12} in Equation (2.27) because \hat{H}_{12} is an unbiased estimate of H_{12} and reduces to H_{12} in the case of no measurement noise.

The form of the data reduction equation in Equation (2.27) is the same as the form presented in the ASTM E1050-98 standard (ASTM-E1050-98 1998). The only difference between this form and the form presented in the ISO 10534-2:1998 standard (ISO-10534-2:1998 1998) is the definition of the reference length, l . The ISO standard defines l to be the distance from the surface of the specimen to the microphone farther away (ISO-10534-2:1998 1998). The remainder of this document will use the definition of l used in the derivation in this section that is consistent with the ASTM E1050-98 standard, which is the distance from the surface of the specimen to the closest microphone (ASTM-E1050-98 1998). After the reflection coefficient is found from Equation (2.27), the normalized specific acoustic impedance is computed from Equation (2.21).

2.2.2 Dissipation and Dispersion for Plane Waves

A dispersion relation is an expression that shows how the wave speed depends on frequency. An example of a dispersion relation was given in Equation (2.11) for the phase speed of the higher-order modes in the waveguide. Dissipation is the removal of energy from the propagating wave. The main mechanisms for the dissipation of wave propagation in ducts are viscous losses and thermal conduction in the boundary layer (Ingard and Singhal 1974; Blackstock 2000). At high frequencies, molecular relaxation can also be another source of attenuation, but this is neglected in this analysis. The boundary layer is a thin region near the boundary where the effects of viscosity and heat transfer are important. The no-slip boundary condition and viscosity produce a transfer of momentum from the flow to the wall and retards the flow in the boundary layer region. The no-slip boundary condition states that the velocity of the flow must match the velocity of the solid boundaries, which for the cases presented in this dissertation are not

moving. The viscous boundary layer thickness for an oscillatory flow over a stationary plate is

$$\delta(\omega) \approx 6.5 \sqrt{\frac{\nu}{\omega}}, \quad (2.28)$$

where ν is the kinematic viscosity, and δ is defined as the distance from the boundary to the point in the flow where the velocity only differs by 1% from the free stream value (White 1991). As the frequency increases, the viscous boundary layer thickness decreases and the region where the no-slip boundary condition influences the flow is reduced. The thermal boundary layer is the region where heat is transferred from the flow to the boundary. The thermal boundary layer thickness is related to the viscous boundary thickness and the Prandtl number by (White 1991)

$$\delta_t \sim \frac{\delta}{\text{Pr}^2}, \quad (2.29)$$

where $\text{Pr} = \nu/\alpha$ is the Prandtl number and α is the thermal diffusivity. Both the transfer of momentum and the transfer of thermal energy from the flow to the wall work to reduce the amplitude of the pressure wave.

To account for dispersion and dissipation in viscothermal flows, the wavenumber is allowed to be complex and is given by

$$k = \frac{\omega}{c} - j\beta, \quad (2.30)$$

where c is the speed of sound inside the waveguide adjusted for dispersion and β is the dissipation coefficient. The speed of sound corrected for viscothermal effects is (Blackstock 2000)

$$c = c_0 \left[1 - \frac{\sqrt{2}}{S} \left(1 + \frac{\gamma - 1}{\sqrt{\text{Pr}}} \right) \right], \quad (2.31)$$

where S is the Stokes number given by

$$S = \sqrt{\frac{\omega L^2}{\nu}}, \quad (2.32)$$

and $L = 4A/l_{\text{perimeter}}$ is the hydraulic diameter of the waveguide, $l_{\text{perimeter}}$ is the wetted perimeter of the cross section and A is the cross-sectional area. The dissipation coefficient for viscothermal effects for plane waves is (Ingard and Singhal 1974; Blackstock 2000)

$$\beta = \frac{\sqrt{2}}{S} \left(1 + \frac{\gamma - 1}{\sqrt{\text{Pr}}} \right) \left(\frac{\omega}{c_0} \right). \quad (2.33)$$

Both Equations (2.31) and (2.33) contain the Stokes number, which is a nondimensional number that relates a characteristic length, in this case the hydraulic diameter, to the viscous boundary layer thickness for oscillating flows. In the limit of thin acoustic boundary layers (at high frequency), the ratio of the viscous boundary layer thickness to the hydraulic diameter goes to zero, and the Stokes number approaches infinity. Thus as $c \rightarrow c_0$ and $\beta \rightarrow 0$, the lossless wavenumber is recovered. Physically, as the boundary layer becomes smaller, the effects of viscosity and heat transfer become less important and flow should approach the lossless case as shown. Also, Equations (2.30) through (2.33) show that the wavenumber corrected for dispersion and dissipation is a function of the angular frequency, the thermodynamic state, and the geometry of the waveguide. This is in contrast to the wavenumber given in Equation (2.4) for linear lossless acoustic

motion, which was just a function of the angular frequency and the thermodynamic state. The derivations of both Equations (2.31) and (2.33) are given in Appendix A.

To consider the relative importance of the effects of dispersion and dissipation, the propagation constants, kd , are compared for the lossless case and for the case with dispersion and dissipation. The propagation constant for the lossless case is

$$(kd)_{lossless} = \frac{\omega}{c_0} d. \quad (2.34)$$

The propagation constant for the case dispersion and dissipation is

$$(kd)_{thermoviscous} = \left(\frac{\omega}{c} - j\beta \right) d = \frac{\omega}{c_0} d \left(\frac{c_0}{c} - j\beta \frac{c_0}{\omega} \right). \quad (2.35)$$

Simplifying the ratio of $(kd)_{thermoviscous}$ to $(kd)_{lossless}$ yields

$$\frac{(kd)_{thermoviscous}}{(kd)_{lossless}} = 1 + (1-j) \frac{\sqrt{2}}{S} \left(1 + \frac{\gamma-1}{\sqrt{\text{Pr}}} \right). \quad (2.36)$$

In order to neglect the effects of dispersion and dissipation, the ratio in Equation (2.36) must be close to unity. This requires that the last term in the equation is much less than unity and as seen in Equation (2.36), this occurs at high frequencies. For air at standard temperature and pressure with $\gamma = 1.4$, $\nu = 15.7 \times 10^{-6} \text{ m}^2/\text{s}$, $\text{Pr} = 0.708$ (Incropera and DeWitt 2002), Table 2-3 shows the minimum frequency necessary to keep the last term in Equation (2.36) under a value of 0.05 for the two waveguides given in this chapter and for the two ceramic tubular specimens, CT73 and CT65, described in Chapter 5. Notice that dispersion and dissipation are important for the two ceramic tubular materials in the frequency range of interest for acoustic impedance testing.

Table 2-3: Minimum frequencies to keep effects of dispersion and dissipation <5%.

Waveguide cross-section	Frequency [kHz]
25.4 mm x 25.4 mm	0.0067
8.5 mm x 8.5 mm	0.060
CT73 (hydraulic diameter = 1.10 mm)	4.35
CT65 (hydraulic diameter = 0.443 mm)	22.2

CHAPTER 3 UNCERTAINTY ANALYSIS FOR THE TWO-MICROPHONE METHOD

Previous studies on the uncertainty of the TMM have discussed in detail specific error sources due to uncertainties in spectral estimates (Seybert and Soenarko 1981; Bodén and Åbom 1986; Åbom and Bodén 1988) and the microphone spacing and locations (Bodén and Åbom 1986; Åbom and Bodén 1988; Katz 2000) and have provided recommendations to minimize the respective error components. However, these efforts did not provide a method to propagate the estimated uncertainties to the overall uncertainty in the acoustic impedance and reflection factor. The purpose of this chapter is to provide a systematic framework to accomplish this task. In particular, a frequency-dependent 95% confidence interval is estimated using both multivariate uncertainty analysis and Monte Carlo methods.

The multivariate uncertainty analysis is an analytical method that assumes small uncertainties which cause only linear variations in the output quantities, but differs from classical uncertainty methods by allowing multiple, possibly correlated, components to be tracked. As long as the data reduction equation can be cast into a multivariate equation and the derivatives can be found, the multivariate uncertainty method provides a convenient way to propagate the experimental uncertainty. The multivariate technique is required because the measured data and the final output of the TMM are complex variables that are treated as bivariate variables. The input covariance matrix and Jacobian are computed and propagated through the data reduction equation (as shown in Appendix B). The multivariate method thus provides analytical expressions that are used to extract

important scaling information, while the Monte Carlo simulations are used to account for the nonlinear perturbations of the input uncertainties observed in practice.

The remainder of this chapter is organized as follows. First, the TMM data reduction equations are presented in a multivariate form. Next, a general procedure to estimate the complex uncertainty using the multivariate method is outlined, and a brief discussion of the major error sources and their respective frequency scaling follows. The results of numerical simulations to illustrate the relative advantages and disadvantages of the TMM and the multivariate method follow. Specifically, two impedance cases are presented, a sound-hard boundary that is representative of a high-impedance sample, and an “ideal” impedance sample that is representative of an optimum impedance for a ducted turbofan. Monte Carlo simulations are compared with the results of the multivariate method.

3.1 Multivariate Form of the TMM Data Reduction Equations

From Equations (2.27) and (2.21), $R_{00,00}$ and ξ_{00} are complex quantities that are functions of another complex variable \hat{H} , the multivariate uncertainty analysis method is used to propagate the uncertainty (Ridler and Salter 2002; Hall 2003; Hall 2004). To employ the multivariate method, the data reduction equations for the plane wave reflection coefficient and the normalized acoustic impedance given in Equations (2.27) and (2.21), respectively, must be separated into the real and imaginary parts denoted by the subscripts R and I , respectively. For $R_{00,00}$,

$$R_{00,00} = \begin{bmatrix} R_R \\ R_I \end{bmatrix} = \begin{bmatrix} \frac{2\hat{H}_R \cos(k(2l+s)) - \cos(2kl) - (\hat{H}_R^2 + \hat{H}_I^2) \cos(2k(l+s))}{1 + \hat{H}_R^2 + \hat{H}_I^2 - 2\hat{H}_R \cos(ks) - 2\hat{H}_I \sin(ks)} \\ \frac{2\hat{H}_R \sin(k(2l+s)) - \sin(2kl) - (\hat{H}_R^2 + \hat{H}_I^2) \sin(2k(l+s))}{1 + \hat{H}_R^2 + \hat{H}_I^2 - 2\hat{H}_R \cos(ks) - 2\hat{H}_I \sin(ks)} \end{bmatrix}. \quad (3.1)$$

In this form, the two variates of the reflection are functions of five input variates, \hat{H}_R , \hat{H}_I , l , s , and k , where \hat{H}_R and \hat{H}_I are the real and imaginary parts of \hat{H}_{12} , respectively. The FRF is also treated as two variates instead of a single quantity. The corresponding form for the normalized specific acoustic impedance is

$$\xi_{spac} = \begin{bmatrix} \theta \\ \chi \end{bmatrix} = \begin{bmatrix} \frac{1 - R_R^2 - R_I^2}{(1 - R_R)^2 + R_I^2} \\ \frac{2R_I}{(1 - R_R)^2 + R_I^2} \end{bmatrix}. \quad (3.2)$$

3.2 TMM Uncertainty Analysis

Previous studies of the error sources for the TMM have focused on determining general scaling of the error and an experimental design that minimizes such errors with the use of a Gaussian input signal. Seybert and Soenarko found that the bias error in the FRF due to spectral leakage can be minimized by using a small value for the bin width of the spectral analysis (Seybert and Soenarko 1981). Spectral leakage can be eliminated using a periodic input signal. They also found that locating the microphones too close to the specimen introduced bias and random errors that are a function of the measured coherence. To increase the coherence, the microphones should be placed close together relative to the wavelength, but the coherence will always be low when one of the microphone locations coincides with a node in the standing wave pattern. One of the

most important findings was that when the value of s approaches an integer number of half wavelengths, the error increases dramatically.

Bodén and Åbom expanded on these results and found that the bias error of the FRF was impacted by the overall length of the waveguide, the value of the specific acoustic impedance of the specimen, and the location of the microphones relative to the specimen (Bodén and Åbom 1986). The random error was a function of the coherence and was influenced by the value of the reflection coefficient, outside noise sources, and the value of ks . They suggest satisfying $0.1\pi < ks < 0.8\pi$ to keep the overall error low. In combination with their second study (Åbom and Bodén 1988), they concluded that errors in the microphone locations dominated over (1) spatial averaging effects, (2) any offset the acoustic center has from its assumed location at the geometric center, and (3) any effects from the finite impedance of the microphones themselves.

3.2.1 Multivariate Uncertainty Analysis

The results from the previous studies provide the necessary guidance to quantify and minimize component error sources that, together with the multivariate uncertainty and the Monte Carlo methods, can be used to provide 95% confidence intervals. The multivariate method propagates the uncertainty estimates through any data reduction equation (Ridler and Salter 2002; Willink and Hall 2002; Hall 2003; Hall 2004; Schultz et al. 2005) using

$$\mathbf{s}_y = \mathbf{J}\mathbf{s}_x\mathbf{J}^T, \quad (3.3)$$

where \mathbf{s}_y is the sample covariance matrix of the output variable, \mathbf{s}_x is the sample covariance matrix of the input variates, \mathbf{J} is the Jacobian matrix for the data reduction equation, and the superscript T indicates the transpose. With the sample covariance

matrix of the variable, the 95% confidence region is found from the probability statement (Johnson and Wichern 2002)

$$\text{Prob} \left((\mathbf{y} - \bar{\mathbf{y}}) \mathbf{s}_y^{-1} (\mathbf{y} - \bar{\mathbf{y}}) \leq \frac{\nu_{eff} P}{\nu_{eff} + 1 - p} F_{p, \nu_{eff} + 1 - p, \alpha} \right) = 1 - \alpha, \quad (3.4)$$

where \mathbf{y} is a vector representing the multivariate variable, $\bar{\mathbf{y}}$ is the sample mean vector, \mathbf{s}_y is the sample covariance matrix of the mean, $F_{p, \nu_{eff} + 1 - p, \alpha}$ is the statistic of the F distribution with p variates (two for a complex variable), and $\nu_{eff} + 1 - p$ degrees of freedom for a probability $1 - \alpha$, and ν_{eff} is the effective number of degrees of freedom from the measurements (Willink and Hall 2002). If the entire confidence region is not desired, the confidence level estimates of the uncertainty for each variate can be computed from the equation

$$U_n = k_{cf} u_n, \quad (3.5)$$

where u_n is the estimate of the sample standard deviation for the n^{th} output variate (i.e., the square root of the diagonal elements of \mathbf{s}_y), and k_{cf} is the coverage factor given by

$$k_{cf} = \sqrt{\frac{\nu_{eff} P}{\nu_{eff} + 1 - p} F_{p, \nu_{eff} + 1 - p, \alpha}}. \quad (3.6)$$

The Jacobian matrix for the reflection coefficient is

$$\mathbf{J}_{R_{00,00}} = \begin{bmatrix} \frac{\partial R_R}{\partial \hat{H}_R} & \frac{\partial R_R}{\partial \hat{H}_I} & \frac{\partial R_R}{\partial l} & \frac{\partial R_R}{\partial s} & \frac{\partial R_R}{\partial T} \\ \frac{\partial R_I}{\partial \hat{H}_R} & \frac{\partial R_I}{\partial \hat{H}_I} & \frac{\partial R_I}{\partial l} & \frac{\partial R_I}{\partial s} & \frac{\partial R_I}{\partial T} \end{bmatrix}, \quad (3.7)$$

where, in this model, the wavenumber is treated solely as a function of temperature and thus, the uncertainty in the wavenumber is solely due to the uncertainty in the

temperature measurement. The Jacobian matrix for the normalized specific acoustic impedance is

$$\mathbf{J}_{\xi_{spac}} = \begin{bmatrix} \frac{\partial \theta}{\partial R_R} & \frac{\partial \theta}{\partial R_I} \\ \frac{\partial \chi}{\partial R_R} & \frac{\partial \chi}{\partial R_I} \end{bmatrix}. \quad (3.8)$$

3.2.2 Monte Carlo Method

A Monte Carlo method is also used to compute the uncertainties of the reflection coefficient and the acoustic impedance ratio. The Monte Carlo method involves assuming distributions for all of the input uncertainties and then randomly perturbing each input variable with a perturbation drawn from its uncertainty distribution (Coleman and Steele 1999). The assumed distributions will be multivariate distributions if the input variates are correlated. Now, the perturbed input variates are used to compute the outputs, in this case $R_{00,00}$ and ξ_{spac} . This is repeated until the statistical distribution of the output variable has converged, and then the output distribution is used to estimate the 95% confidence regions. A summary of the uncertainty sources is given in Table 3-1.

3.2.3 Frequency Response Function Estimate

Estimates of the uncertainty and error sources in the FRF are documented in the literature (Seybert and Hamilton 1978; Seybert and Soenarko 1981; Schmidt 1985; Bendat and Piersol 2000; Pintelon and Schoukens 2001b; Pintelon et al. 2002). For this paper, two uncorrelated noise sources are assumed to affect a single-input/single-output system with a periodic and deterministic input signal, as described in Appendix B. Also from Appendix B, the FRF estimate is

$$\begin{bmatrix} \hat{H}_R \\ \hat{H}_I \end{bmatrix} = \begin{bmatrix} \sqrt{\frac{\hat{G}_{22}}{\hat{G}_{11}(\hat{C}_{12}^2 + \hat{Q}_{12}^2)}} \hat{C}_{12} \\ \sqrt{\frac{\hat{G}_{22}}{\hat{G}_{12}(\hat{C}_{12}^2 + \hat{Q}_{12}^2)}} \hat{Q}_{12} \end{bmatrix}, \quad (3.9)$$

where \hat{G}_{11} and \hat{G}_{22} are the estimated autospectral densities of the signals from microphones 1 and 2, respectively, and \hat{C}_{12} and \hat{Q}_{12} are the co- and quad-spectral density functions (i.e., $\hat{G}_{12} = \hat{C}_{12} + j\hat{Q}_{12}$). Equation (3.9) is commonly called the \hat{H}_3 estimate. Any phase bias can be eliminated using a switching technique, described in Appendix B. The final estimate of the FRF is computed from the geometric average of the two interchanged measurements as

$$\hat{H} = \sqrt{\frac{\hat{H}^o}{\hat{H}^s}}, \quad (3.10)$$

where \hat{H}^o and \hat{H}^s are the FRF between the microphones in their original and their interchanged locations, respectively.

The details on computing the estimate of the FRF for this system model are given in Appendix B. The sample covariance matrix for \hat{H}_3 and the Jacobian matrix needed to propagate the uncertainty to the averaged FRF are also given in Appendix B. The uncertainty estimation requires an additional measurement with the pseudo-random source turned off to estimate the noise power spectrum.

Table 3-1: Elemental bias and precision error sources for the TMM.

<u>Variable or Origin</u>	<u>Error Source</u>	<u>Error Estimator</u>
T	RTD accuracy	Manufacturer's specifications or calibration accuracy
	Ambient temporal variations	Minimize by conducting the test in limited amount of time
	Spatial variations	Estimate by measuring the temperature at different locations along the waveguide
	Random variations	Statistical methods
s, l	Caliper accuracy	Manufacturer's specifications or calibration accuracy
	Acoustic centers	Calibration or estimate as half microphone diameter
	Random variation	Statistical methods
Microphones	Spatial averaging	Minimize by using microphones with a diameter much smaller than the wavelength
	Impedance change of waveguide wall	Minimize by using microphones with a diameter much smaller than the wavelength
\hat{H}	Phase mismatch	Correct for by using microphone switching
	Magnitude mismatch	Correct for by calibrating each microphone and microphone switching
	A/D limitations	Minimize by maximizing the significant bits
	Finite frequency resolution	Not present for a periodic random input signal
	Random error	Sample covariance matrix given in (Schultz, Sheplak and Cattafesta 2005)

The reflection coefficient's sensitivity to uncertainty in the FRF is described by

$$\frac{\partial R_R}{\partial \hat{H}_R} = 2 \frac{\cos(k(2l+s)) - \hat{H}_R \cos(2k(l+s)) + R_R (\cos(ks) - \hat{H}_R)}{1 + \hat{H}_R^2 + \hat{H}_I^2 - 2\hat{H}_R \cos(ks) - 2\hat{H}_I \sin(ks)}, \quad (3.11)$$

$$\frac{\partial R_R}{\partial \hat{H}_I} = 2 \frac{-\hat{H}_I \cos(2k(l+s)) + R_R (\sin(ks) - \hat{H}_I)}{1 + \hat{H}_R^2 + \hat{H}_I^2 - 2\hat{H}_R \cos(ks) - 2\hat{H}_I \sin(ks)}, \quad (3.12)$$

$$\frac{\partial R_l}{\partial \hat{H}_R} = 2 \frac{\sin(k(2l+s)) - \hat{H}_R \sin(2k(l+s)) + R_l (\cos(ks) - \hat{H}_R)}{1 + \hat{H}_R^2 + \hat{H}_l^2 - 2\hat{H}_R \cos(ks) - 2\hat{H}_l \sin(ks)}, \quad (3.13)$$

and

$$\frac{\partial R_l}{\partial \hat{H}_l} = 2 \frac{-\hat{H}_l \sin(2k(l+s)) + R_l (\sin(ks) - \hat{H}_l)}{1 + \hat{H}_R^2 + \hat{H}_l^2 - 2\hat{H}_R \cos(ks) - 2\hat{H}_l \sin(ks)}. \quad (3.14)$$

Consider the case when $ks = n\pi$, which leads to $\hat{H} = (-1)^n$. As a result, the common denominator in Equations (3.11)-(3.14) equals zero, resulting in a singularity so that any uncertainty in the FRF will result in a large uncertainty in the reflection coefficient. This result agrees with previous studies (Seybert and Soenarko 1981; Bodén and Åbom 1986; Åbom and Bodén 1988).

Equations (3.11)-(3.14) indicate that the sensitivity to the uncertainty in \hat{H} is dependent on the value of \hat{H} and $R_{00,00}$. As \hat{H} approaches the limiting values of zero or infinity (i.e., when one of the microphones is located at a node), or as the magnitude of $R_{00,00}$ approaches the limit of unity, the sensitivity will increase. This implies that the accurate measurement of the two extremes, sound-hard ($R_{00,00} = 1$) and pressure release ($R_{00,00} = -1$) boundaries, which possess cusps in the standing wave patterns, will show the largest sensitivities to uncertainty. The equations also show a periodic element to the uncertainty estimates that is dependent on the wavenumber and the locations of the microphones. Thus for a fixed set of microphone locations, the uncertainty estimates may vary versus frequency. The actual periodicity is complex to analyze because of the combinations of trigonometric functions present in the partial derivatives.

3.2.4 Microphone Locations

This section addresses the effects of the uncertainty of the microphone locations on the reflection coefficient. The respective sensitivity coefficients for the distance between the specimen and the closest microphone l and for the microphone spacing s are

$$\frac{\partial R_R}{\partial l} = -2kR_I, \quad (3.15)$$

$$\frac{\partial R_I}{\partial l} = 2kR_R, \quad (3.16)$$

$$\frac{\partial R_R}{\partial s} = -2k \frac{\hat{H}_R \sin(k(2l+s)) - (\hat{H}_R^2 + \hat{H}_I^2) \sin(2k(l+s)) + R_R (\hat{H}_R \sin(ks) - \hat{H}_I \cos(ks))}{1 + \hat{H}_R^2 + \hat{H}_I^2 - 2\hat{H}_R \cos(ks) - 2\hat{H}_I \sin(ks)}, \quad (3.17)$$

and

$$\frac{\partial R_I}{\partial s} = 2k \frac{\hat{H}_R \cos(k(2l+s)) - (\hat{H}_R^2 + \hat{H}_I^2) \cos(2k(l+s)) - R_I (\hat{H}_R \sin(ks) - \hat{H}_I \cos(ks))}{1 + \hat{H}_R^2 + \hat{H}_I^2 - 2\hat{H}_R \cos(ks) - 2\hat{H}_I \sin(ks)}. \quad (3.18)$$

The sensitivity coefficients for l and s are both directly proportional to the frequency via the wavenumber, emphasizing the difficulty of making accurate measurements at high frequency. Equations (3.17) and (3.18) have the same denominator as Equations (3.11)-(3.14), again showing that half-wavelength spacing $ks = n\pi$ should be avoided. Again, the equations also show a periodic element to the uncertainty estimates that is dependent on the wavenumber and the locations of the microphones as shown with the frequency response function derivatives and that analyzing the periodicity would be even more involved because of the increased number of trigonometric terms.

3.2.5 Temperature

The random uncertainty in the temperature measurement can be handled using standard statistical procedures. The effects of temporal variations in the atmospheric

conditions can be minimized by limiting the duration of the test. The spatial variation in the temperature of the waveguide can be characterized by measuring the temperature at various locations and computing the standard deviation of the measurements, but this will be a crude estimate since the entire temperature is not measured. The temperature sensor for this study is mounted on the exterior wall to avoid undesired reflections and scattering of the sound field inside the waveguide, and is found to give reliable estimate of the gas temperature if the wall is highly conductive. This was confirmed by comparing the measured temperature inside the waveguide to the outside surface metal temperature while the sound source was on for one experimental run. The total uncertainty in temperature is estimated from the root-sum-square of the individual uncertainties.

The sensitivity coefficients of the reflection coefficient with respect to temperature are computed using the chain rule

$$\frac{\partial R_R}{\partial T} = \frac{\partial R_R}{\partial k} \frac{\partial k}{\partial T}, \quad (3.19)$$

and

$$\frac{\partial R_I}{\partial T} = \frac{\partial R_I}{\partial k} \frac{\partial k}{\partial T}, \quad (3.20)$$

where

$$\frac{\partial R_R}{\partial k} = 2s \frac{-A \sin(k(2l+s)) + \frac{l}{s} \sin(2kl) + B \sin(2k(l+s)) - C}{1 + \hat{H}_R^2 + \hat{H}_I^2 - 2\hat{H}_R \cos(ks) - 2\hat{H}_I \sin(ks)}, \quad (3.21)$$

$$\frac{\partial R_I}{\partial k} = 2s \frac{A \cos(k(2l+s)) - \frac{l}{s} \cos(2kl) - B \cos(2k(l+s)) - C}{1 + \hat{H}_R^2 + \hat{H}_I^2 - 2\hat{H}_R \cos(ks) - 2\hat{H}_I \sin(ks)}, \quad (3.22)$$

$$A = \left(1 + 2\frac{l}{s}\right) \hat{H}_R, \quad (3.23)$$

$$B = \left(1 + \frac{l}{s}\right) (\hat{H}_R^2 + \hat{H}_I^2), \quad (3.24)$$

and

$$C = R_R (\hat{H}_R \sin(ks) - \hat{H}_I \cos(ks)). \quad (3.25)$$

Equations (3.19)-(3.25) reveal that the uncertainty in $R_{00,00}$ is approximately proportional to the microphone spacing. Reducing the spacing between the microphones will reduce the sensitivity of the uncertainty in the reflection coefficient with respect to the wavenumber and temperature. Also, Equations (3.21) and (3.22) possess the same singularity as the other derivatives at $ks = n\pi$. Again, the equations also show a periodic element to the uncertainty estimates that is dependent on the wavenumber and the locations of the microphones as shown before with the same difficulties.

For the case with dispersion and dissipation, the complex wavenumber is a function of the thermodynamic state (ambient temperature and pressure), the frequency, and the waveguide geometry (Morse and Ingard 1986; Blackstock 2000). The scaling of the uncertainty in $R_{00,00}$ accounting for these effects is difficult to examine analytically. If dissipation and dispersion are neglected and an ideal gas is assumed, the wavenumber is given by Equation (2.4) and is only a function of temperature. Thus, the derivative of the wavenumber with respect to temperature is

$$\frac{\partial k}{\partial T} = -k \frac{(\gamma R_{gas})}{2c_0^2} \quad (3.26)$$

Equation (3.26) shows that the uncertainty will increase with frequency via the wavenumber and that the uncertainty is inversely proportional to the square of the speed of sound.

3.2.6 Normalized Acoustic Impedance Uncertainty

For the uncertainty analysis, the normalized specific acoustic impedance is treated as solely a function of the reflection coefficient. The Jacobian matrix is

$$\mathbf{J}_{\xi_{spac}} = \begin{bmatrix} \frac{2((1-R_R)^2 - R_I^2)}{((1-R_R)^2 + R_I^2)^2} & \frac{-4R_I(1-R_R)}{((1-R_R)^2 + R_I^2)^2} \\ \frac{4R_I(1-R_R)}{((1-R_R)^2 + R_I^2)^2} & \frac{2((1-R_R)^2 - R_I^2)}{((1-R_R)^2 + R_I^2)^2} \end{bmatrix}. \quad (3.27)$$

Notice that each term has the same denominator and a singularity exists (i.e. when $(1-R_R)^2 + R_I^2 = 0$) for a sound-hard boundary, $R_{00,00} = 1$. This situation will be studied further in the section below.

3.3 Numerical Simulations

Much of the observations in Section 3.2 have been previously reported in the literature (Seybert and Soenarko 1981; Bodén and Åbom 1986; Åbom and Bodén 1988). The main contribution of this chapter is to demonstrate how these uncertainty sources *propagate* and contribute to the overall uncertainty in $R_{00,00}$ if they remain linear. But for typical experimental situations, the uncertainties cause *nonlinear* perturbations in the reflection coefficient and acoustic impedance. In order to demonstrate the uncertainty propagation, numerical experiments on a sound-hard boundary and an “ideal” impedance sample are carried out using the analytical method outlined in Section 3.2 for the overall uncertainty estimate.

Time-series data are simulated using Equations (2.2) and (2.23) by choosing a desired value of $R_{00,00}$, and the resulting data are processed using the algorithms

described in Section 3.2. The nominal values for the input parameters are given in Table 3-2. The test frequency of 5 kHz ($ks = 0.60\pi$) is chosen because the uncertainties are bounded for this set of microphone locations. A parametric study of the effects of sensor signal-to-noise ratio (SNR) and uncertainties in temperature, microphone location, and spacing is completed in isolation, assuming the perturbations remain linear. The relative uncertainties in the temperature, microphone location, and spacing are independently varied from 0.1% to 10% at a single frequency, while the other uncertainties are set to zero and the input signal is noise-free. The effect of the SNR is studied by varying the SNR from 30 dB to 70 dB while holding the other uncertainties to zero. The SNR for the numerical simulations is based on the power in the incident wave only at that frequency compared to the power in the noise signal at that frequency and is kept constant across the entire bandwidth. Next, the total uncertainty in $R_{00,00}$ as a function of frequency is estimated from the case with the relative input uncertainties of 0.01% and 1% for a SNR of 40 dB. The estimated 95% confidence intervals are then compared to the results of the Monte Carlo simulation using 25,000 iterations. All the variables are assumed to be normally distributed for the Monte Carlo simulation outlined in Figure 3-1 and the real and imaginary parts of the FRF are assumed to be correlated, as shown in Appendix B.

The simulations used either a zero-mean periodic random signal for a broadband periodic source or a sinusoid for single-frequency excitation. The bandwidth chosen for the broadband simulations is 0 to 20 kHz. Spectral analysis is carried out using a sampling frequency of 51.2 kHz, with 1,024 samples per block and 1,000 blocks, yielding a frequency resolution of 50 Hz. In these simulations, the microphone spacing is not designed to avoid the situation where $ks = n\pi$ or to maintain the inequality $ks < n\pi$

(Åbom and Bodén 1988). This is acceptable since the goal of the simulations is to demonstrate that the uncertainty analysis methods presented earlier capture the correct behavior. In an actual experiment, multiple microphone spacings can be used to avoid the regions where $ks \approx n\pi$.

Table 3-2: Nominal values for input parameters of numeric simulations.

Parameter	Value
l	32.1 mm
s	20.6 mm
T	23.8 °C

3.3.1 Sound-Hard Sample

The first specimen studied is a sound-hard boundary. To avoid the singularity present in the data reduction and uncertainty expressions, the assumed value of the reflection coefficient is $R_{00,00} = 0.999$, which gives a standing wave ratio (the ratio of the maximum to the minimum pressure amplitude along the axis of the waveguide) of greater than 60 dB. Figure 3-2 shows the absolute uncertainty in the reflection coefficient as a function of the uncertainty in l , s , and T at 5 kHz. Figure 3-3 shows the absolute uncertainty in the reflection coefficient as a function of the SNR. The results in these figures suggest that the dominant source of uncertainty in the magnitude of the reflection coefficient is the random uncertainty in the FRF measurement for signal-to-noise ratios of 50 dB or lower. The dominant source of uncertainty in the phase of the reflection coefficient is in the measurement of the distance between the specimen and the nearest microphone. Improvements in the measurement of the reflection coefficient could be obtained from improvements in the accuracy of the FRF measurements (reducing the noise in the system, increasing the number of averages) and the measurement of the distance between the specimen and the nearest microphone.

The estimated value of the reflection coefficient for the relative uncertainty in the measurement of the microphone location, the microphone spacing, and the temperature each set to 1% and with a SNR of 40 dB is given in Figure 3-4(a) as a function of frequency. The uncertainty results for the multivariate method and the Monte Carlo simulation are shown in Figure 3-4(b). Note that the peaks in the uncertainty are at frequencies 8.4 and 16.7 kHz, where $ks = n\pi$, and the frequencies where one of the microphones is at a node in the standing wave pattern are 1.6, 2.7, 4.9, 8.1, 8.2, 11.5, 13.5, 14.7, 18.0, and 18.8 kHz. The multivariate method agrees with the Monte Carlo simulation within 5% for all frequencies except those corresponding to a node in the standing wave at a microphone location or the singularity where $ks \approx n\pi$, validating the multivariate method for very small component errors. The true value only fell outside the estimated 95% confidence region for both the multivariate method and the Monte Carlo

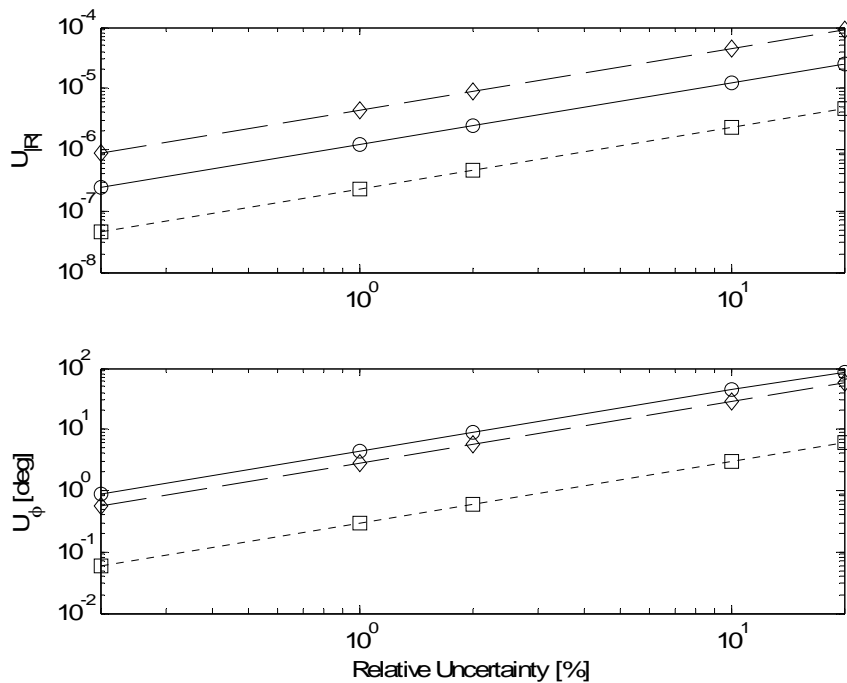


Figure 3-2: Absolute uncertainty of $R_{00,00}$ due to the uncertainties in l , s , and T for $R_{00,00} = 0.999$ at $f=5$ kHz. —○— l , —◇— s , ---□--- T .

simulation five times for the magnitude and zero times for the phase out of the total 400 frequency bins. The two methods also match at lower values of the input uncertainty, but such agreement is not universal for all acoustic materials, which is shown in the next section. Figure 3-4(a) shows that the estimate of the reflection coefficient becomes non-physical, i.e. $|R_{00,00}| > 1$, at the two frequencies where the singularity occurs. The uncertainty in the estimate also increases to account for the singularity and the confidence interval for $|R_{00,00}|$ does include physical values for the estimate.

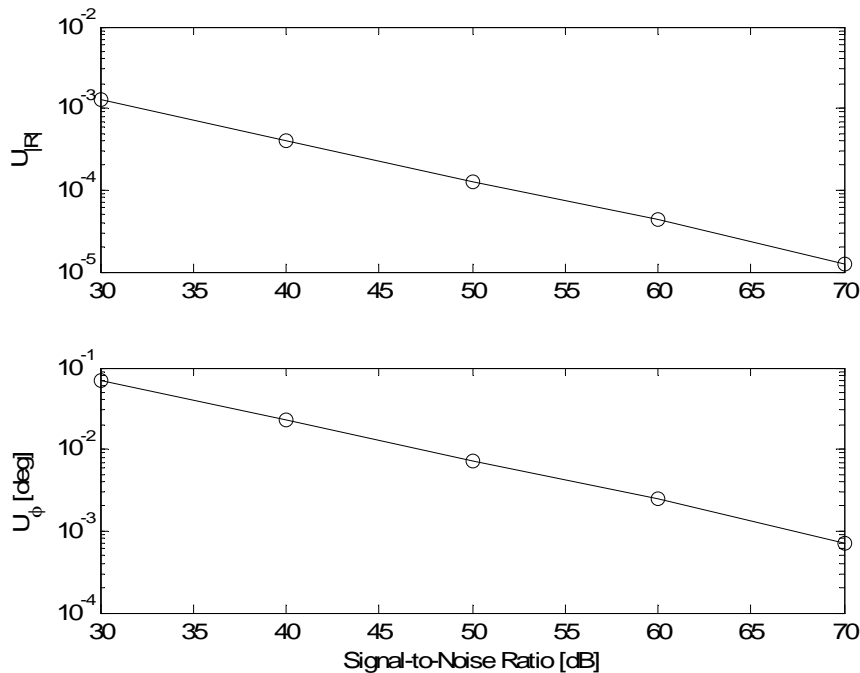
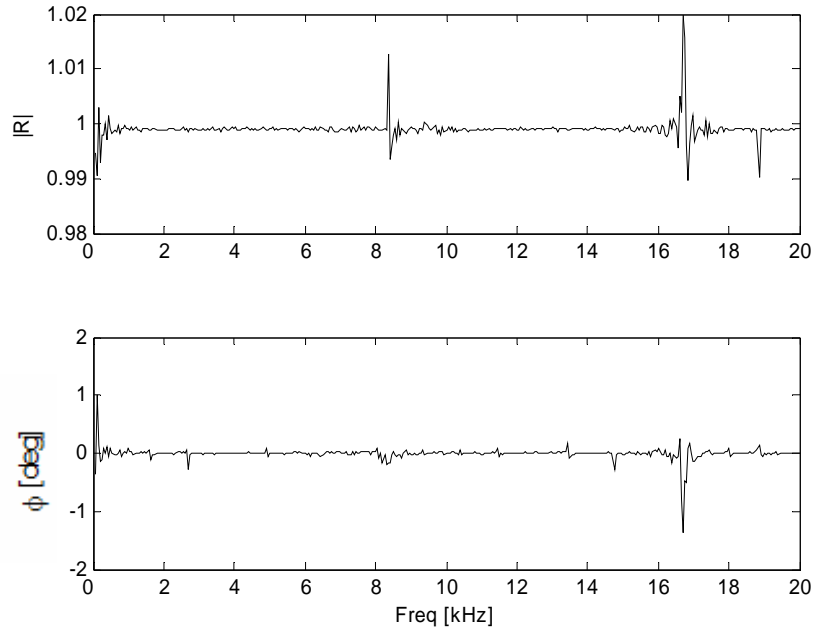


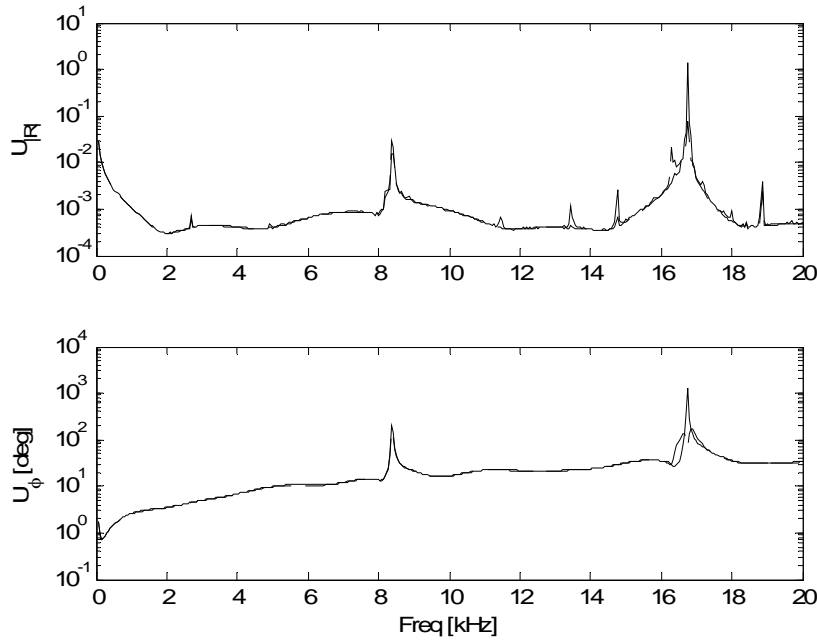
Figure 3-3: Absolute uncertainty $R_{00,00}$ due to the SNR for $R_{00,00} = 0.999$ at $f=5$ kHz.

3.3.2 Ideal Impedance Model

The second simulation corresponds to the ideal impedance model given in Figure 37 of the NASA CR-1999-209002 (Bielak, Premo and Hersh 1999), designed using Boeing's Multi-Element Lining Optimization (MELO) program. The data provided in the NASA CR is limited to a frequency range of 500 Hz to 10 kHz and is extended to the



(a)



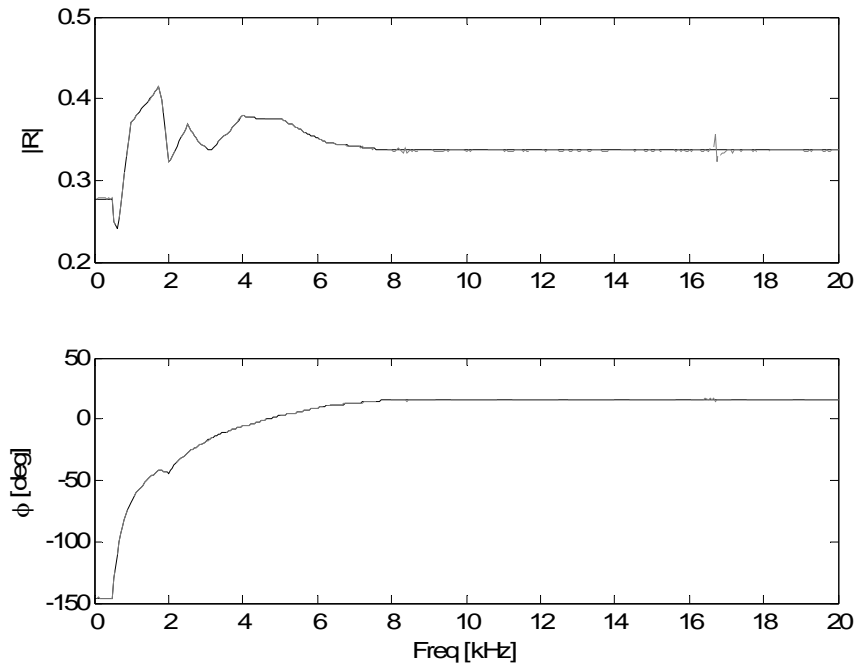
(b)

Figure 3-4: Estimated value for the (a) reflection coefficient and (b) total uncertainty for the sound-hard boundary with 1% relative uncertainty for l , s , and T and 40 dB SNR. — Multivariate Method, — Monte Carlo simulation. The two lines are indistinguishable at most frequencies.

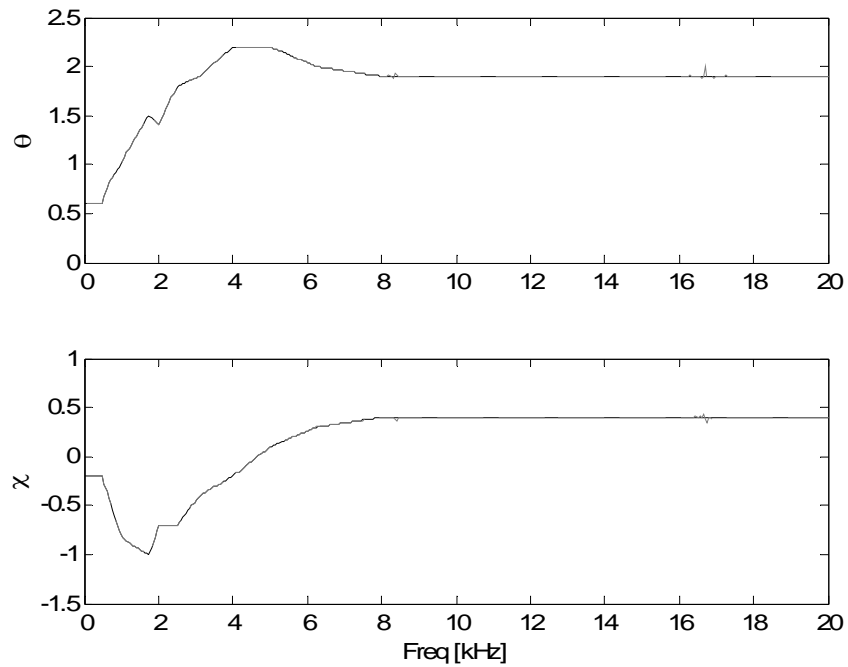
frequency range needed for this simulation by assuming that the first and last values are constant for the ranges of 0 to 500 Hz and 10 to 20 kHz, respectively. The exact reflection coefficient and normalized impedance data are given in Figure 3-5. This specimen is chosen to determine the extent to which the uncertainties in a typical liner specimen scale in a manner similar to that of a sound-hard boundary. The primary distinction between the two cases is that there are no nodes in the standing wave pattern for this impedance sample. As a result, the coherence between the two microphone signals is expected to be near unity for all frequencies assuming a reasonable SNR.

Figure 3-6(a) shows the absolute uncertainty in the reflection coefficient as a function of the uncertainty in l , s , and T at 5 kHz and Figure 3-6(b) shows the absolute uncertainty in the normalized specific acoustic impedance. Figure 3-7(a) shows the absolute uncertainty in the reflection coefficient as a function of the SNR, and Figure 3-7(b) shows the absolute uncertainty in the normalized specific acoustic impedance. The results in these figures suggest that the dominant sources of uncertainty in the magnitude and the phase of the reflection coefficient are the microphone location and spacing. In contrast to the sound-hard boundary, there is no dominating uncertainty source for the total uncertainty in the ideal impedance model data.

The estimated value of the reflection coefficient for the case with a SNR of 40 dB is included in Figure 3-5(a). The estimates for the normalized specific acoustic impedance are included in Figure 3-5(b). The uncertainty results for the multivariate method and the Monte Carlo simulation are shown in Figure 3-8(a) for the reflection coefficient and in Figure 3-8(b) for the normalized specific acoustic impedance. The peaks in the uncertainty are at frequencies 8.4 and 16.7 kHz, where $ks = n\pi$. The

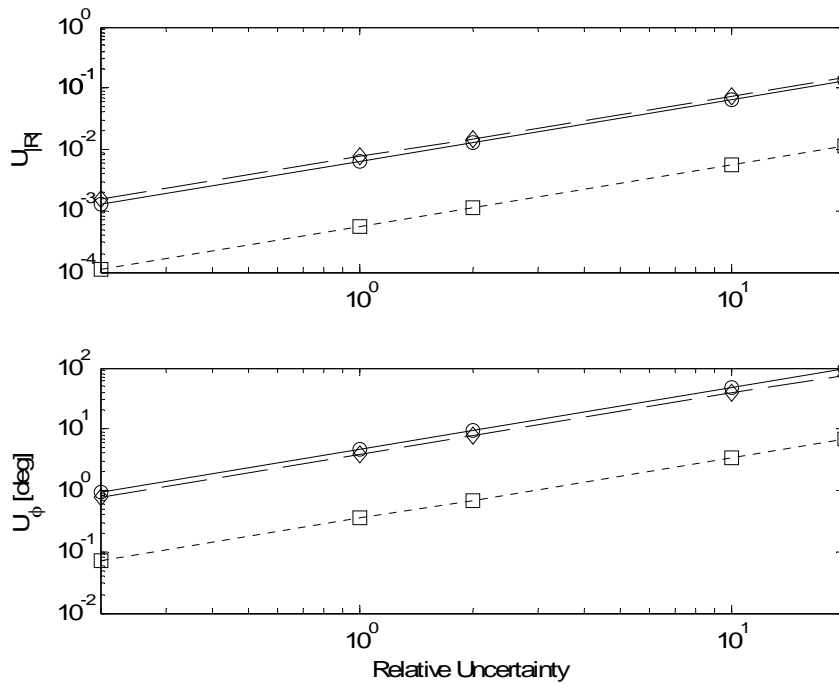


(a)

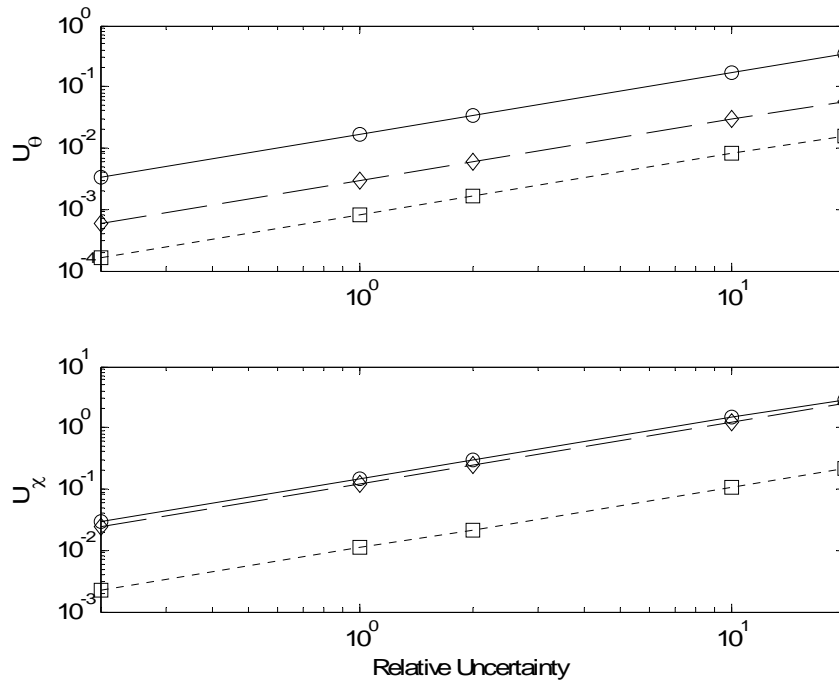


(b)

Figure 3-5: Ideal impedance model and estimated values, adapted from (Bielak, Premo and Hersh 1999), for (a) reflection coefficient and (b) normalized specific acoustic impedance. — Model value, - - - Estimated value (40 dB SNR). The two lines are indistinguishable.

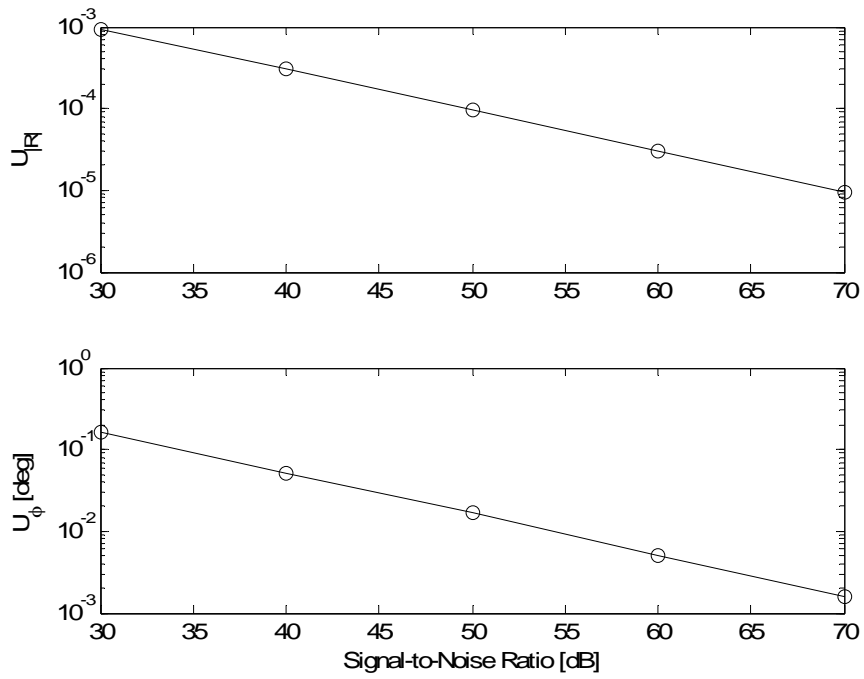


(a)

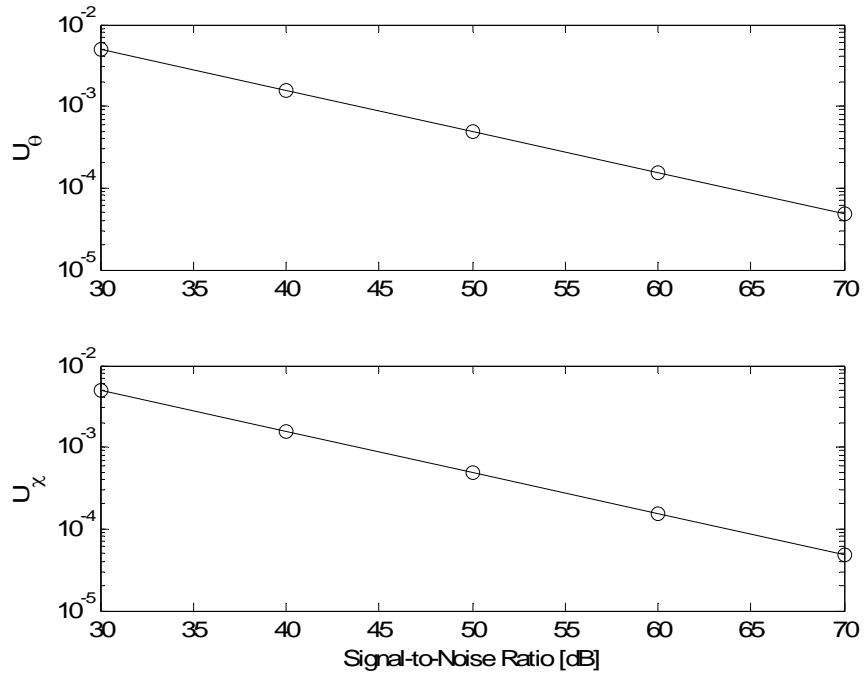


(b)

Figure 3-6: Absolute uncertainty of (a) $R_{00,00}$ and (b) ξ_{spac} due to the uncertainties in l , s , and T for the ideal impedance model at $f=5$ kHz. \circ — l , \diamond — s , \square — T .



(a)

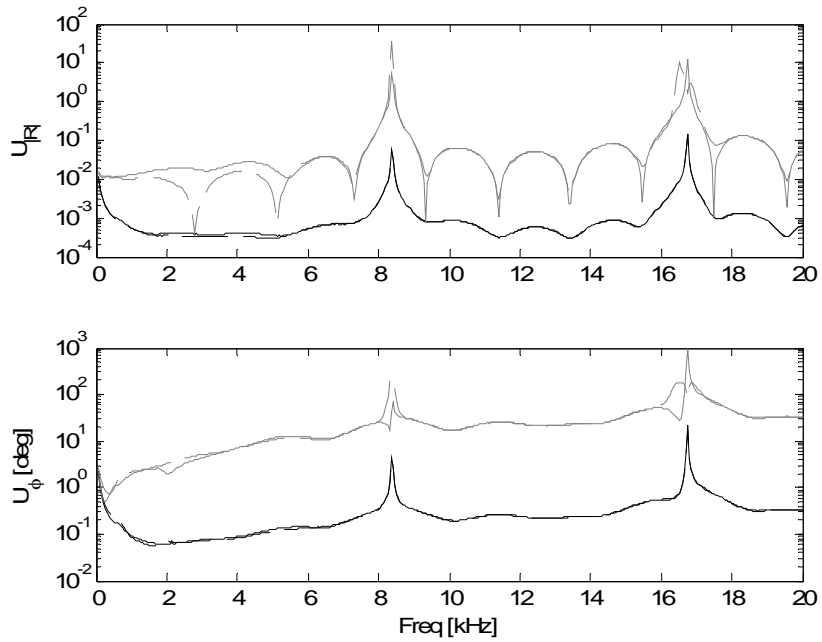


(b)

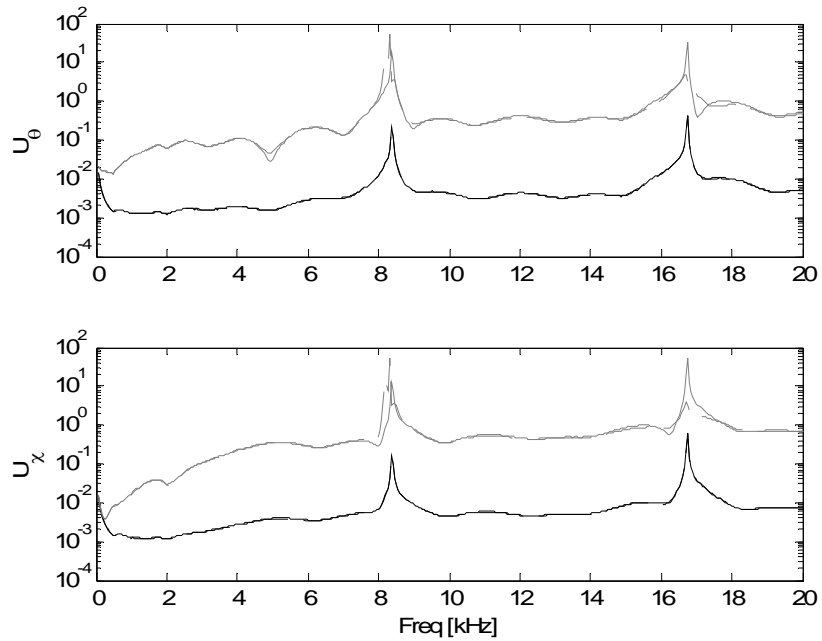
Figure 3-7: Absolute uncertainty in (a) $R_{00,00}$ and in (b) ξ_{spac} due to the SNR for the ideal impedance model at $f=5$ kHz.

average percent difference between the two methods is 5% for both the magnitude and phase for the reflection coefficient for the case with only 0.01% relative uncertainty in l , s , and T , and the average percent difference is 2% for the normalized resistance and reactance. For the case with 1% relative uncertainty in l , s , and T , large differences can be seen in the estimate of the uncertainty in the magnitude of the reflection coefficient at frequencies below 6 kHz. The multivariate method does not reproduce the local minima that the Monte Carlo simulations reveal, but the multivariate method estimates are conservative for this case. The average percent difference between the two methods increases to 75% for the magnitude of the reflection coefficient, 14% for the phase of the reflection coefficient, 13% for the normalized resistance, and 16% for the normalized reactance. These increases demonstrate that uncertainties in l , s , and T are causing nonlinear perturbations in both the reflection coefficient and the normalized acoustic impedance for the case with only 1% relative uncertainty. Thus, the multivariate method fails to give accurate values of the true uncertainty estimates. To increase the accuracy of the multivariate method, the multivariate Taylor series used in the derivations could be expanded to include as many terms as needed for the desired accuracy. The best option is to use numerical techniques such as the Monte Carlo simulations used in this dissertation to propagate the uncertainty.

The probability density function is plotted to further investigate the differences between the multivariate method and the Monte Carlo simulations for large uncertainties. This is done for the normalized specific acoustic impedance data and for a frequency of 5 kHz , since there is a large difference between the two methods and it avoids complications due to the microphone spacing (see Figure 3-8). Figure 3-9(a) shows the



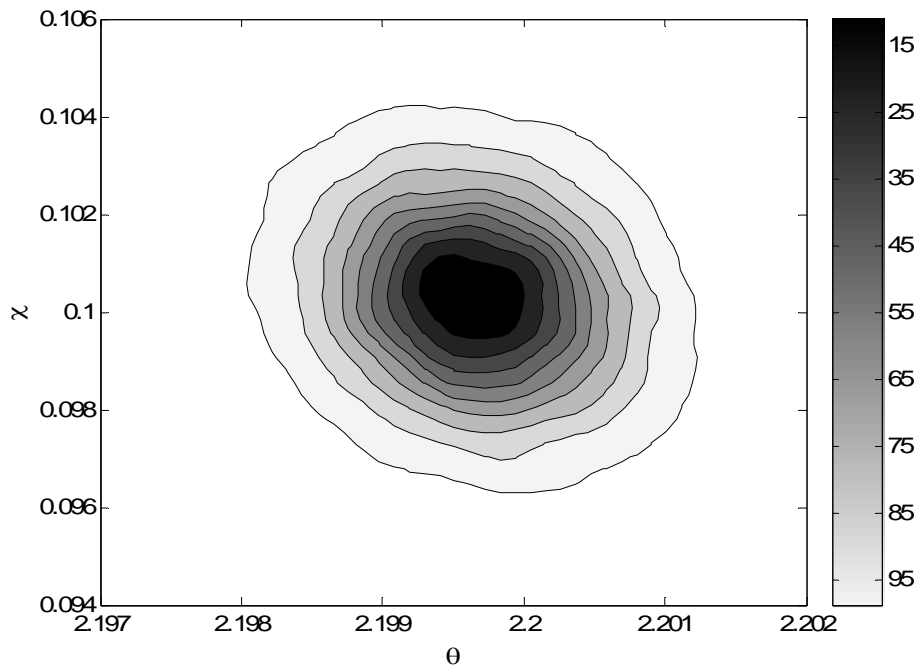
(a)



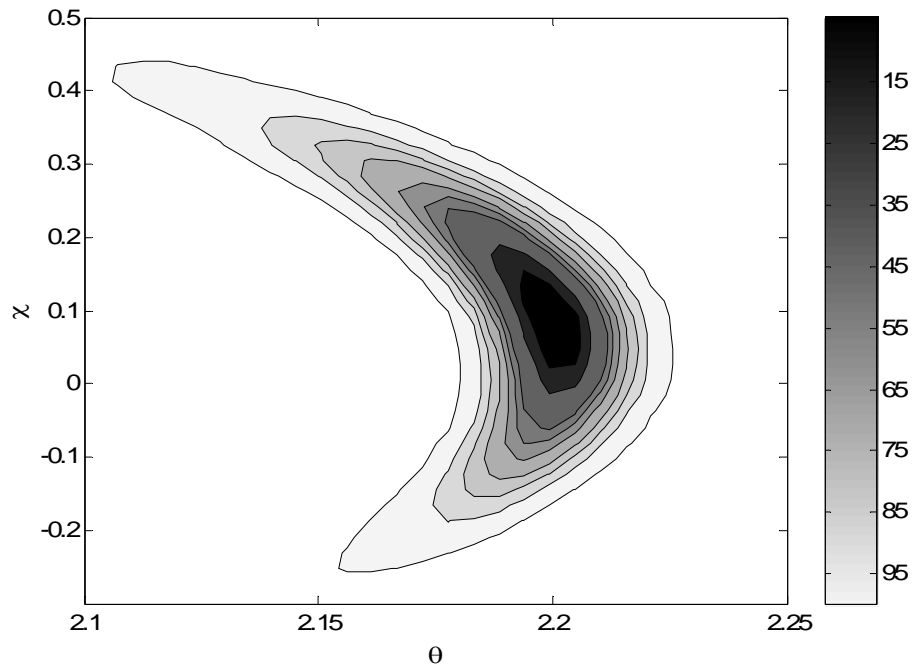
(b)

Figure 3-8: Total uncertainty in (a) $R_{00,00}$ and (b) ξ_{spac} as a function of frequency for the ideal impedance model. — 0.01% Multivariate Method, — — 0.01% Monte Carlo simulation, — — 1% Multivariate Method, — — 1% Monte Carlo simulation. The two lines for the 0.01% relative uncertainty are indistinguishable at most frequencies.

confidence region contours for the case with only 0.01% relative uncertainties in l , s , and T , whereas Figure 3-9(b) is for the case with 1% relative uncertainties. The figures show that as the uncertainties become larger and cause nonlinear perturbations in the data reduction equation, the confidence region contours change from a normal distribution to an irregular “boomerang-shaped” distribution. Thus, the nonlinear effect invalidates the normal distribution assumption and the uncertainty must be found from the actual computed distribution resulting from the Monte Carlo simulation. In general, the uncertainty cannot be summarized by the sample mean vector and the sample covariance matrix. The contour line in the joint probability density function (pdf) that represents a probability of 0.95 should be found and used as the 95% confidence region estimate for the uncertainty. To find the uncertainty in the resistance and reactance due to 1% relative uncertainty in each input variable, 25,000 iterations from the Monte Carlo simulation are used to estimate the joint pdf. The joint pdf is approximated by discretizing the range of the resistance and reactance into 40 bins each, for a total of 1,600 bins, and is smoothed using a $2 \text{ bin} \times 2 \text{ bin}$ kernel. Next, 100 contours of constant joint probability density are found, and the joint pdf is integrated within each contour to find the total probability within that contour. Next, the contour corresponding to 95% coverage is found via interpolation. The quoted uncertainty is then taken as the maximum and minimum values of the contour for each component, such as the real and imaginary parts of the reflection coefficient or the resistance and reactance. The uncertainty estimates of the magnitude and phase of the reflection coefficient are found from the maximum and minimum values of the magnitude and phase for the contour computed from the real and imaginary parts of the reflection coefficients. For the case of the ideal impedance model with 1% relative



(a)



(b)

Figure 3-9: The confidence region contours for the resistance and reactance for the ideal impedance model at 5 kHz with only (a) 0.01% relative uncertainties and (b) 1% relative uncertainties in l , s , and T .

uncertainty and a SNR of 40 dB for a frequency of 5 kHz, the 95% confidence region is given in Figure 3-10, along with the estimated 95% confidence region from the multivariate method and estimated and true values of the normalized impedance. This figure illustrates the difference in the predicted uncertainty regions between the two methods and how much larger the Monte Carlo region is. The quoted uncertainty for this case is best given as a range since it is asymmetrical about the estimate. The estimate of the normalized resistance is 2.20 with a 95% confidence interval of $[2.11, 2.23]$ and the estimate of the reactance is 0.1 with a 95% confidence interval of $[-0.3, 0.4]$. For comparison, the uncertainty estimates from the multivariate method are ± 0.03 for the resistance and ± 0.4 for the reactance.

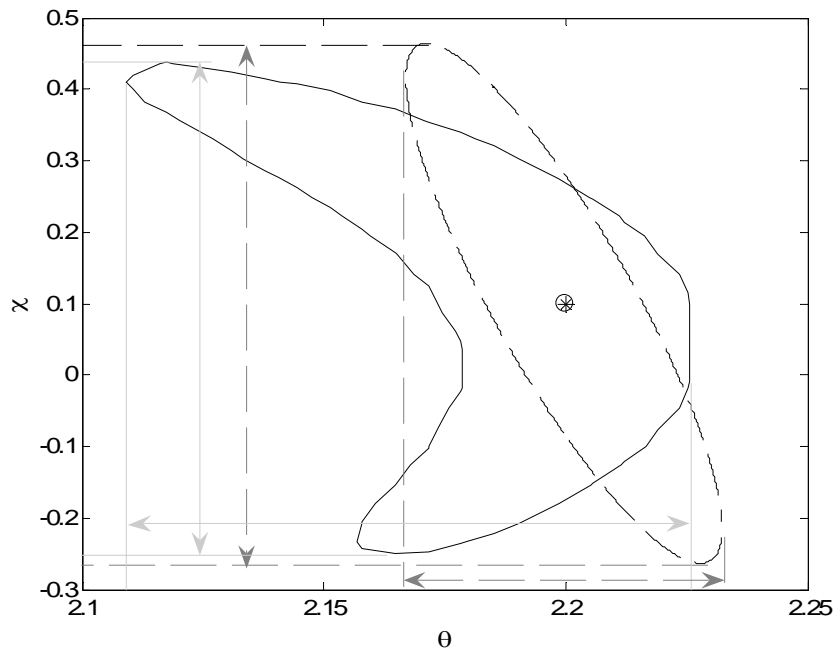


Figure 3-10: Confidence region of the ideal impedance model at 5 kHz with 1% relative input uncertainty and 40 dB SNR. — Monte Carlo confidence region, — — Multivariate confidence region, \odot estimated impedance, $*$ true impedance, — Monte Carlo method simultaneous confidence interval estimates, — — Multivariate method simultaneous confidence interval estimates.

3.4 Experimental Methodology

To demonstrate the multivariate method and the Monte Carlo method on experimental data, two experimental setups are developed, using two different size waveguides. The larger waveguide has a plane wave operating bandwidth up to 6.7 kHz, whereas the small waveguide has a plane wave operating bandwidth up to 20 kHz. A schematic of the experimental setup is shown in Figure 2-11. Each component of the experimental setup and the data acquisition and analysis routine will be discussed in turn.

3.4.1 Waveguides

The larger waveguide is approximately 96 cm long and has a square cross-section measuring 25.4 mm on a side. The walls of the waveguide are constructed of 22.9 mm-thick aluminum (type 6061-T6). The cut-on frequencies for the higher-order modes, given in Table 2-2, show that the limiting bandwidth for the TMM is 6.7 kHz for this waveguide. The location of the microphone, l , and the microphone spacing, s , is measured before the experiment using digital calipers (with an accuracy of $\pm 0.05 \text{ mm}$). The measurement is repeated 45 times and the data are used to compute the best estimates of the microphone location and spacing and the random uncertainty of the geometric center of the microphones. A bias uncertainty due to the difference between the geometric center and the acoustic center is neglected since over the entire operational frequency range of the large waveguide, the microphone diameter is assumed to be small compared to the wavelength and thus the microphones represent point measurements. The total uncertainty in the locations of the microphones is taken as the root-sum-square of the random uncertainty and the accuracy of the calipers. The microphone located closest to the specimen with a 95% confidence interval estimate is located $32.0 \pm 0.8 \text{ mm}$

from the specimen. The spacing between the two microphones with a 95% confidence interval estimate is $20.7 \pm 1.1 \text{ mm}$.

The smaller waveguide is approximately 87 cm long and has a square cross-section measuring 8.5 mm on a side. The walls of the waveguide are constructed out of at least 12.7-mm thick aluminum (type 6061-T6). The cut-on frequencies for the higher-order modes, given in Table 2-1, show that the limiting bandwidth for the TMM is 20 kHz for this waveguide. The location of the microphone, l , and the microphone spacing, s , is measured before the experiment using digital calipers. The measurement is repeated 45 times and the data are used to compute the best estimates of the microphone location and spacing and the random uncertainty. The uncertainty in the acoustic centers of the microphones is estimated ad hoc to be $\pm 1.5 \text{ mm}$, which is considered here because of the increased frequency range as compared to the other waveguide. For this waveguide, the diameter of the microphones can no longer be considered small compared to the wavelength and the microphone measurements no longer represent a point measurement. The Helmholtz number (kd) is on the order of unity at approximately 10 kHz . The total uncertainty is taken as the root-sum-square of the random uncertainty, the accuracy of the calipers, and the bias due to the acoustic centers. The microphone located closest to the specimen with a 95% confidence interval estimate is located $38.1 \pm 2.0 \text{ mm}$ from the specimen. The spacing between the two microphones with a 95% confidence interval estimate is $12.7 \pm 2.0 \text{ mm}$. The majority of the uncertainty in the microphone locations is due to the uncertainty in the acoustic centers of the microphones.

3.4.2 Equipment Description

The compression driver is a BMS 4590P, with an operating frequency range of 0.2 to 22 kHz, powered by a Techron 7540 power amplifier. The drive signal is generated by a Brüel and Kjær Pulse Analyzer System, which also acquired and digitized the two microphone signals with a 16-bit digitizer. The measurement microphones are Brüel and Kjær Type 4138 microphones (3.18 mm diameter) and are installed into the waveguide with their protective grids attached to the microphone. The microphones are calibrated only for magnitude before mounting in the waveguide using a Brüel and Kjær Type 4228 Pistonphone. Atmospheric temperature is measured using a surface-mounted, 100- Ω platinum resistive thermal device (Omega SRTD-1) with an accuracy of ± 2 K.

3.4.3 Signal Processing

For the large waveguide, the two microphone signals are sampled at a rate of 16.4 kHz with a record length of 62.5 ms for a total of 1,000 spectral averages. The frequency resolution is 16 Hz. For the small waveguide, the two microphone signals are sampled at a rate of 65.5 kHz with a record length of 31.3 ms for a total of 1,000 spectral averages. The frequency resolution is 32 Hz. A periodic pseudo-random signal is used as the excitation signal is to the compression driver.

3.4.4 Procedure

The microphones are first calibrated. The excitation signal is applied, and the amplifier gain is adjusted such that the sound pressure level at the reference microphone is approximately 100-120 dB (ref. 20 μ Pa) for all frequency bins. Then the full-scale voltage on the two measurement channels of the Pulse Analyzer System is adjusted to maximize the dynamic range of the data system. The excitation signal is turned off and

the microphone signals are measured to estimate the noise spectra (see Appendix B). The input and output signals for FRF estimation are assumed to contain uncorrelated noise and there the real and imaginary parts of the FRF may be correlated as shown in Appendix B. Next, the excitation signal is turned on and the two microphone signals are recorded with the microphones in their original positions and switched positions. The time-series data are used to compute the required spectra and ultimately \hat{H} , $R_{00,00}$, and ξ_{spac} via Equations (3.10), (2.27), and (2.21), respectively.

For the temperature measurement, the random uncertainty is estimated from the standard deviation of at least 100 measurements, and the bias uncertainty is estimated by the accuracy of the RTD (2 K). The total uncertainty in temperature is computed from the root-sum-square of the random and bias uncertainties.

The uncertainties in the reflection coefficient and the measured normalized acoustic impedance are estimated using both the multivariate method and a Monte Carlo simulation (see Figure 3-1). The input distributions for l , s , and T are assumed to be independent Gaussian distributions and the input distribution for \hat{H} is assumed to be a bivariate normal distribution computed from Appendix B. A specific form for the output distribution of the Monte Carlo simulation is not assumed as described previously at the end of Section 3.3.2. This approach is chosen because of its ability to handle the large perturbations that the uncertainties in the temperature and the microphone locations represent. Results for four specimens are presented in Chapter 5.

CHAPTER 4 MODAL DECOMPOSITION METHOD

Modal decomposition methods presented in the literature can be separated into two different schemes: correlation and direct methods (Åbom 1989). Correlation approaches determine the modal amplitudes by measuring the temporal and spatial correlation of acoustic pressure inside the waveguide. Direct methods, however, use point measurements to compute the modal amplitudes from a system of equations derived from an analytical propagation model. Accurate propagation models exist for rectangular, square, or cylindrical ducts with rigid walls. However, multiple independent sources are required to resolve the acoustic properties of the test specimen, such as the reflection coefficients, mode scattering coefficients, and acoustic impedances. This dissertation uses the latter approach and computes the modal amplitudes by solving a system of linear equations. This method is also amenable to a least-squares solution for added robustness.

Focusing now on prior research on direct methods, early work by Eversman (1970) investigated the energy flow of acoustic waves in rectangular ducts but did not consider the decomposition of modal components. Moore (1972) was one of the first to investigate direct methods to determine the source distribution for ducted fans but limited his results to estimates of the sound pressure levels for each circumferential mode and neglected radial modes. Following this, Zinn et al. (1973) investigated measuring acoustic impedance for higher-order modes by adapting the standing-wave method. Yardley (1974) then added the effects of mean flow and reflected waves to determine the source distribution of a fan but did not expand the method to compute the reflection

coefficient matrix. Yardley also suggested that the microphones should all be mounted flush to the waveguide or duct. Pickett et al. (1977) continued to improve the direct method by adding a discussion of optimum microphone locations but limited their algorithms to a deterministic system of equations. Only results at the fan blade passage frequency were reported. Moore (1979) continued the analysis evolution by comparing integral algorithms for the solution of the deterministic set of equations to the least-squares approach. He concluded that the deterministic system was susceptible to measurement noise, and the least-squares solution provided robustness and approached the integral method solution in the limit of infinite measurement points. Again, his results were limited to estimates of the modal amplitudes.

Subsequently, Kerschen and Johnston (1981) developed a direct technique for random signals, but restricted the method to only incident waves. Pasqualini et al. (1985) concentrated their efforts on a transform scheme for a direct method for circular or annular ducts only. A method for use with transient signals was then developed by Salikuddin and Ramakrishnan (Salikuddin 1987; Salikuddin and Ramakrishnan 1987). Continuing this line of work, Åbom (1989) extended the direct method to any type of signal by measuring the frequency response function between microphone pairs. Åbom noted difficulties associated with generating the necessary independent sources to calculate the reflection coefficient matrix. Akoum and Ville (1998) then developed and applied a direct method based on a Fourier-Lommel transform to the measurement of the reflection coefficient matrix at the baffled end of a pipe. They developed an apparatus for generating the necessary independent sources by mounting a compression driver to the side of a circular waveguide on a rotating ring. Their results were in good agreement

with theoretical predictions for the normal mode, but they stated that discrepancies existed for the higher-order modes since all of the data were near the cut-on frequency. Most recently, Kraft et al. (2003) discussed the development of a modal decomposition experiment using four microphones but did not provide any results.

The contribution of this chapter is to adapt a direct MDM based on a least-squares scheme to a square duct and to use simple sources to acquire the data necessary to estimate the entire reflection coefficient matrix and the acoustic impedance at frequencies beyond the cut-on frequency of higher-order modes. The outline of the chapter is as follows. The next section derives the data reduction procedure for estimating the complex modal amplitudes, the reflection coefficient matrix, and the acoustic impedance values from the measured data. Section 4.2 outlines the experimental procedure and analysis parameters. This section concludes with a brief discussion concerning the sources of error.

4.1 Data Reduction Algorithm

The MDM developed here is restricted to time-harmonic, linear, lossless acoustics without mean flow governed by the Helmholtz equation. The solution is given in Equation (2.5) in Chapter 2, but is repeated here for convenience as

$$\underline{P} = \sum_m \sum_n \psi_{mn}(x, y) (A_{mn} e^{jk_z d} + B_{mn} e^{-jk_z d}), \quad (4.1)$$

where

$$\psi_{mn}(x, y) = \cos\left(\frac{m\pi}{a}x\right) \cos\left(\frac{n\pi}{b}y\right), \quad (4.2)$$

for a rigid-walled square duct. The dispersion relation and an expression for the cut-on frequencies are given in Section 2.1.1 in Equation (2.8).

4.1.1 Complex Modal Amplitudes

The experimental procedure flush-mounts a number of microphones in the sides of the waveguide, as in the TMM. The number and locations of the microphones are selected to observe the desired modes. A test frequency is selected and the total number of propagating modes, σ , is found from the equation for the cut-on frequency, Equation (2.8). The minimum number of microphone measurements required to uniquely determine the acoustic pressure is for this test frequency is 2σ (Åbom 1989). Next, Equation (4.1) is written for each microphone measurement, summing only over the propagating modes for that frequency, to form a system of equations

$$\begin{aligned} \underline{P}_1 &= \sum_m \sum_n \psi_{mn}(x_1, y_1) (A_{mn} e^{jk_z d_1} + B_{mn} e^{-jk_z d_1}) \\ \underline{P}_2 &= \sum_m \sum_n \psi_{mn}(x_2, y_2) (A_{mn} e^{jk_z d_2} + B_{mn} e^{-jk_z d_2}), \\ &\quad \text{M} \\ \underline{P}_\eta &= \sum_m \sum_n \psi_{mn}(x_\eta, y_\eta) (A_{mn} e^{jk_z d_\eta} + B_{mn} e^{-jk_z d_\eta}) \end{aligned} \quad (4.3)$$

where the subscript on \underline{P} represents the microphone location and η is the number of microphone measurements, which must be equal to or larger than 2σ . To decompose the sound field, the microphones should be located with some transverse separation and some axial separation. A simple way to configure the microphone locations is to group the microphones into two groups and locate each group at a separate axial location. The system of equations can be compactly expressed in matrix form as

$$\{\underline{P}\} = \mathbf{L}\{W\}, \quad (4.4)$$

where $\{\underline{P}\}$ is the $\eta \times 1$ vector of measured complex acoustic pressure amplitudes, $\{W\}$ is the $2\sigma \times 1$ vector of the complex modal amplitudes given by

$$\{W\} = \begin{Bmatrix} \{A\} \\ \{B\} \end{Bmatrix}, \quad (4.5)$$

and \mathbf{L} is the $\eta \times 2\sigma$ matrix of the coefficients from Equation (4.3), composed of the transverse function and the propagation exponential.

The coefficient matrix has a special form; it is composed of two sub-matrices that are complex conjugates. As a result of this structure, the determinant of the \mathbf{L} matrix has an imaginary part that is identically equal to zero. To avoid this problem, the matrix equation is transformed into a system of two real-valued matrix equations, each with a coefficient matrix that has a non-zero determinant

$$\{\underline{P}_R\} + j\{\underline{P}_I\} = (\mathbf{L}_R + j\mathbf{L}_I)(\{W_R\} + j\{W_I\}), \quad (4.6)$$

where the subscripts “ R ” and “ I ” denote the real and imaginary parts, respectively (Rao 2002). The expression is rearranged by carrying out the multiplication and collecting the real and imaginary parts

$$\begin{Bmatrix} \{\underline{P}_R\} \\ \{\underline{P}_I\} \end{Bmatrix} = \begin{bmatrix} \mathbf{L}_R & -\mathbf{L}_I \\ \mathbf{L}_I & \mathbf{L}_R \end{bmatrix} \begin{Bmatrix} \{W_R\} \\ \{W_I\} \end{Bmatrix}. \quad (4.7)$$

The solution to Equation (4.7) is found, for example, via Gaussian elimination for the deterministic case in which $\eta = 2\sigma$. For the overdetermined case in which $\eta > 2\sigma$, a least-squares solution to Equation (4.7) is desired for a robust solution, and this can be found by solving the normal equations (Chapra and Canale 2002)

$$\begin{bmatrix} \mathbf{L}_R & -\mathbf{L}_I \\ \mathbf{L}_I & \mathbf{L}_R \end{bmatrix}^T \begin{Bmatrix} \{\underline{P}_R\} \\ \{\underline{P}_I\} \end{Bmatrix} = \begin{bmatrix} \mathbf{L}_R & -\mathbf{L}_I \\ \mathbf{L}_I & \mathbf{L}_R \end{bmatrix}^T \begin{bmatrix} \mathbf{L}_R & -\mathbf{L}_I \\ \mathbf{L}_I & \mathbf{L}_R \end{bmatrix} \begin{Bmatrix} \{W_R\} \\ \{W_I\} \end{Bmatrix}, \quad (4.8)$$

where the superscript \mathbf{T} represents the transpose of the matrix (Chapra and Canale 2002).

4.2.2 Reflection Coefficient Matrix

With the existence of higher-order propagating modes, an incident acoustic mode now may reflect as the same mode and scatter into different modes. This increases the complexity of characterizing the specimen, as a single reflection coefficient no longer describes the acoustic interaction. Instead, a reflection coefficient matrix is defined as

$$\{B\} = \mathbf{R} \{A\}, \quad (4.9)$$

where the size of \mathbf{R} is $\sigma \times \sigma$ and the vectors $\{A\}$ and $\{B\}$ are $\sigma \times 1$ (Åbom 1989; Akoum and Ville 1998). The elements of \mathbf{R} are represented by $R_{mn,qr}$, where the first index, mn , is the mode number for the reflected mode and the second index, qr , is the mode number for the incident mode. The diagonal elements, $R_{mn,mn}$, represent same-mode reflection coefficients, while the off-diagonal elements, $R_{mn,qr}$, represent the mode scattering coefficients. To determine the unknown reflection coefficient matrix, a minimum of σ linearly independent source conditions must be measured (Åbom 1989; Akoum and Ville 1998). The additional vectors of the incident and reflected complex modal amplitudes are combined together to form matrices such that

$$\begin{bmatrix} \{B\}_1 & \{B\}_2 & \text{L} & \{B\}_\sigma \end{bmatrix} = \mathbf{R} \begin{bmatrix} \{A\}_1 & \{A\}_2 & \text{L} & \{A\}_\sigma \end{bmatrix}, \quad (4.10)$$

which can then be solved for the reflection coefficient matrix. The approach in this work, described below, to generate multiple independent sources is to place various restrictor plates between the waveguide and the compression driver, the purpose of which is to emphasize one of the modes. Previous researchers placed the compression drivers perpendicular to the waveguide on a rotating ring and varied the location of the

compression drivers relative to the microphones (Pasqualini, Ville and Belleval 1985; Akoum and Ville 1998; Blackstock 2000).

4.2.3 Acoustic Impedance

The acoustic impedance ratio is defined only for same-mode reflections as (Blackstock 2000)

$$\xi_{mn} = \frac{\frac{Z_{specimen}}{\cos(\phi_{mn}^{tr})}}{\frac{Z_0}{\cos(\phi_{mn})}} = \frac{1 + R_{mn,mn}}{1 - R_{mn,mn}}, \quad (4.11)$$

where $Z_{specimen}$ and Z_0 are the characteristic impedances of the specimen and medium, respectively, and ϕ_{mn}^{tr} is the angle of transmission for the m, n mode. The acoustic impedance ratio is also called the ratio of oblique incidence wave impedance by (Dowling and Ffowcs-Williams 1983). The normalized specific acoustic impedance or the normalized characteristic impedance is obtained from Equation (4.11) as

$$\xi_{spac} = \frac{Z_{specimen}}{Z_0} = \frac{\cos(\phi_{mn}^{tr})}{\cos(\phi_{mn})} \frac{1 + R_{mn,mn}}{1 - R_{mn,mn}}. \quad (4.12)$$

Without further information concerning ϕ_{mn}^{tr} , only the acoustic impedance ratio can be computed from the results of the MDM. However, locally reactive materials are desired for aeroacoustic applications as engine nacelle liners (Motsinger and Kraft 1991), and therefore are commonly tested (Jones et al. 2003; Jones et al. 2004). A locally reactive material is a material whose impedance is independent of the angle of incidence and therefore is assumed to have a transmission angle of approximately zero (Morse 1981).

In this case, Equation (4.12) simplifies to

$$\frac{Z_{specimen}}{Z_0} = \frac{1}{\cos(\phi_{mn})} \frac{1 + R_{mn,mn}}{1 - R_{mn,mn}}, \quad (4.13)$$

which represents the normalized surface response impedance (Dowling and Ffowcs-Williams 1983) and can be estimated from the MDM. To check the validity of the locally reactive assumption, the normalized specific acoustic impedances, from Equation (4.13), for all modes at a given frequency should be equal.

For the TMM, only plane waves are present and, hence, only the normal-incident specific acoustic impedance is determined. The angle of incidence for the (0,0) mode acoustic impedance is seen from Equation (2.13) have normal incidence. Thus, the (0,0) mode acoustic impedances from Equations (4.11)-(4.13) are identical to the estimate from the TMM and the two estimates can be compared. The higher-order modes assumed in the MDM can be thought of as plane waves at an oblique angle of incidence, as discussed in Section 2.1.3. The effect of angle of incidence causes the acoustic impedance value to differ from the specific acoustic impedance value, and thus both estimates of impedance must be considered to fully characterize the specimen.

4.2.4 Acoustic Power

In addition to the acoustic impedance ratio, the absorption coefficient is an important parameter to characterize acoustic materials. The absorption coefficient, α , is defined as the amount of acoustic power absorbed by the specimen normalized by the incident power (ISO-10534-2:1998 1998) and is given as

$$\alpha = \frac{W_i - W_r}{W_i} = 1 - \frac{W_r}{W_i}, \quad (4.14)$$

where W_i and W_r represent the power in the incident and reflected acoustic fields, respectively. In the case of the TMM, the absorption coefficient only considers the

power contained in the plane wave mode, but in the MDM, the absorption coefficient will encompass the total power absorbed in all the propagating modes. Equation (4.14) assumes that no acoustic power is transmitted through the waveguide into the surrounding environment, hence demonstrating the need for terminating the specimen with a rigid back plate and for insuring proper sealing of the waveguide. In this case, all the acoustic energy that is not absorbed by the specimen and dissipated as heat is sent back down the waveguide. Expressions for the incident and reflected powers are derived from integrating the acoustic intensity in the d -direction over the cross-section of the waveguide to obtain the total power, W , given by

$$W(f) = \iint_S I_d dS = \int_{y=0}^a \int_{x=0}^a \frac{1}{2} \text{Re}[\underline{P}\underline{U}_d^*] dx dy, \quad (4.15)$$

where \underline{U}_d is the acoustic velocity perturbation along the d -axis in the frequency domain and is found from Euler's equation (Blackstock 2000) as

$$\underline{U}_d = \frac{j}{\rho c_0 k} \frac{\partial \underline{P}}{\partial d}, \quad (4.16)$$

where $k = \omega/c_0$. The orthogonal properties of the normal modes in the acoustic pressure solution given in Equation (4.1), and in the acoustic velocity perturbation solution, given in Equation (4.16), allow for the expression of the total power to be simplified and ultimately separated into two parts. Each part only contains the modal amplitudes for either the incident waves or the reflected waves. The resulting expressions for the incident and reflected powers are

$$W_i = \frac{a^2}{8\rho c_0 k} \sum_{m=0}^M \sum_{n=0}^N k_{z,mn} |A_{mn}|^2 \quad (4.17)$$

and

$$W_r = \frac{a^2}{8\rho c_0 k} \sum_{m=0}^M \sum_{n=0}^N k_{z, mn} |B_{mn}|^2. \quad (4.18)$$

The full derivation is given in Appendix D. The absorption coefficient not only provides an estimate of the sound absorption capabilities of a material, but also provides a check on the measurement. The absorption coefficient is bounded between zero and unity, and values outside this range indicate a problem with the experimental setup and procedure.

4.2 Experimental Methodology

To verify the data reduction routine outlined above and obtain acoustic impedance data beyond the cut-on frequency, an experimental apparatus is developed. The actual results are presented in the next chapter along with the results for the TMM. The experimental procedure to acquire and reduce the data is similar to the TMM. A compression driver is mounted at one end of a waveguide, and the test specimen is mounted at the other end. For the MDM, eight microphones are flush-mounted in the duct wall at two axial locations near the specimen to resolve the incident and reflected waves. Fourier transforms of the phase-locked, digitized pressure signals at each location are used to estimate the complex acoustic pressure and thus the modal coefficients and reflection coefficient matrix. A schematic of the experimental setup is shown in Figure 4-1, with eight microphones flush-mounted in the waveguide. Each component of the experimental setup and the data acquisition and analysis routine will be discussed in turn.

4.2.1 Waveguide

The waveguide used in the measurements presented is approximately 96 cm long and has a square cross-section measuring 25.4 mm on a side. The walls of the waveguide are constructed of 22.9 mm-thick aluminum (type 6061-T6). The cut-on frequencies for the higher-order modes, given in Table 4-1, show that the limiting bandwidth for the

TMM is 6.7 kHz for this waveguide, as opposed to 13.5 kHz when the MDM is used with the first four modes. To resolve these four modes, eight microphones are placed in two groups of four microphones at two axial locations. The placement is chosen such that each microphone is not located at the node line of any of the modes of interest and to achieve a sufficient signal-to-noise ratio. The locations of the eight microphones are provided in Table 4-2. The independent sources for the MDM are generated via the four different restrictor plates shown in Figure 4-2, each one designed to emphasize one or more of the first four modes.

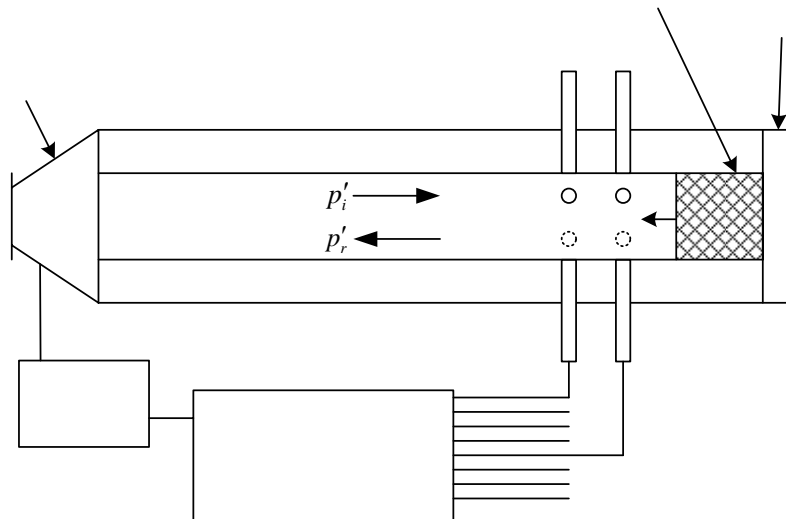


Figure 4-1: Schematic of the experimental setup for the MDM (some microphone connections are left out for clarity).

Table 4-1: Cut-on frequencies in kHz for the higher-order modes.

$m \setminus n$	0	1	2	3
0	0	6.75	13.5	20.3
1	6.75	9.55	15.1	21.4
2	13.5	15.1	19.1	24.4
3	20.3	21.4	24.4	28.7

4.2.2 Equipment Description

The compression driver is a BMS 4590P, with an operating frequency range of 0.2 to 22 kHz, powered by a Techron 7540 power amplifier. The drive signal is generated by

Table 4-2: Microphone measurement locations ($a = 25.4$ mm).

Microphone	x,y,d Location [mm]	Microphone	x,y,d Location [mm]
1	$0.25a, 0, 1.6a$	5	$0.25a, 0, 1.1a$
2	$a, 0.25a, 1.6a$	6	$a, 0.25a, 1.1a$
3	$0.75a, a, 1.6a$	7	$0.75a, a, 1.1a$
4	$0, 0.75a, 1.6a$	8	$0, 0.75a, 1.1a$

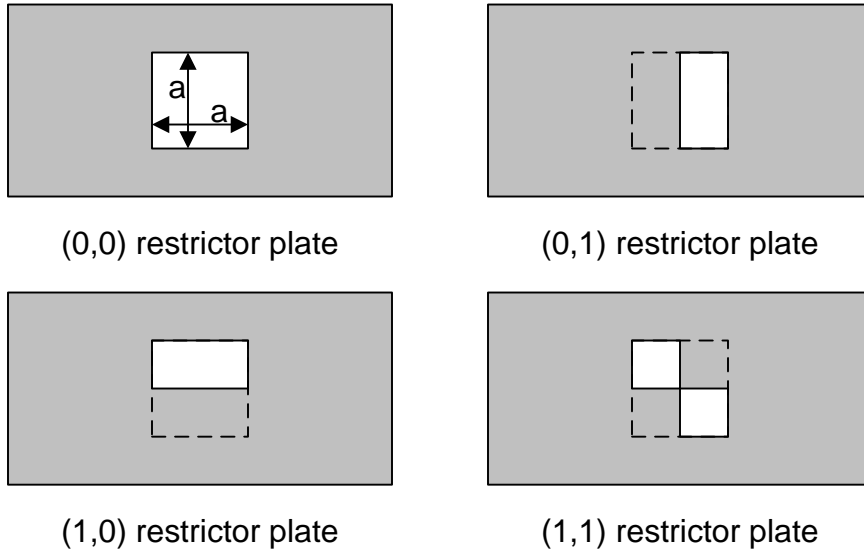


Figure 4-2: Schematic of the four restrictor plates. (The dotted line represents the waveguide duct cross-section.)

a Brüel and Kjær Pulse Analyzer System, which also acquired and digitized the eight microphone signals with a 16-bit digitizer. The measurement microphones are Brüel and Kjær Type 4138 microphones (3.18 mm diameter) and are installed into the waveguide with their protective grids attached to the microphone. The microphones are calibrated only for magnitude before mounting in the waveguide. The phase mismatch between the eight microphones was measured in previous experiments, with each microphone flush mounted at the end of the large waveguide with a reference microphone, up to 6.7 kHz and was found to be no greater than $\pm 5^\circ$. This error is found to be acceptable (less than 10 % uncertainty for the modal amplitudes and reflection coefficients) from the results of

the numerical uncertainty studies in Section 4.2.4. Atmospheric temperature is measured using a 100- Ω platinum resistive thermal device with an accuracy of ± 2 K.

4.2.3 Signal Processing

All eight microphone signals are measured and subsequently processed with a fast Fourier transform algorithm. The frequency resolution is 16 Hz with a frequency span from 0.3 to 13.5 kHz. The 1,000 linear averages are processed using a uniform window with no overlap. Leakage is eliminated by the use of a pseudo-random periodic signal to excite the compression driver. To ensure synchronous data acquisition, the sampling is triggered by the start of the generator signal in a phase locked acquisition mode. The data are then processed using the MDM described above.

4.2.4 Numerical Study of Uncertainties

The main sources of error for the MDM are the signal-to-noise ratio, microphone phase mismatch, uncertainties in the measurements of the microphone locations, and the temperature. The frequency scaling of the uncertainty in the computed values from the MDM is also important, as the goal of the MDM is to extend the frequency range of acoustic impedance testing. Numerical studies have been conducted concerning the effects of the individual error sources and the frequency scaling of the total error, and are only summarized here for brevity; the results are given in Appendix E. These studies were performed for an approximate sound-hard termination, with four different vectors of incident complex modal amplitudes. The reflected modal amplitudes are computed from Equation (4.9) and the data are then used to calculate time-series data. The time-series data are then processed using the MDM described above. The root-mean-square (rms) normalized error between the elements of the calculated reflection coefficient matrix and

the modeled reflection coefficient matrix is used to gauge the uncertainty of the MDM. The numerical studies are performed at a frequency of 12 kHz to avoid pressure nodes for the microphone locations listed in Table 4-2. The simulations varied the error introduced into the simulated input signals to the MDM and computed the perturbed output reflection coefficient matrix for each of the error sources individually. These results showed that the MDM gives reliable and accurate estimates (with ~10% uncertainty) for the complex modal coefficients and the reflection coefficient matrix. The influence of evanescent modes can be simulated to determine the magnitude of the bias error they cause if the amplitudes of the incident and reflected evanescent waver are known.

CHAPTER 5 EXPERIMENTAL RESULTS FOR ACOUSTIC IMPEDANCE SPECIMENS

Previous chapters have described two methods, the TMM and the MDM, for measuring acoustic impedance in detail, including discussions about uncertainty sources. This chapter focuses on presenting the data from these methods when applied to various specimens. Five specimens are tested and presented, but some specimens are only tested with certain methods because of sample size issues described in Chapter 2. The five specimens are listed below with the methods used to test them.

1. Ceramic tubular honeycomb with 65% porosity* (CT65) (TMM, High frequency TMM, and MDM).
2. Ceramic tubular honeycomb with 73% porosity (CT73) (TMM, High frequency TMM, and MDM).
3. Rigid termination (TMM, High frequency TMM, and MDM).
4. SDOF liner (TMM and MDM).
5. Mode scattering specimen (MDM only).

The first two specimens are chosen to represent a typical sound-soft boundary that consists of simple structures that can be easily modeled and does not represent a particularly hard measurement to make accurately in terms of its uncertainty and are tested first to gain confidence in the methods. The rigid termination is chosen to shake down the experiment rig since the uncertainty analysis has show that this specimen is the most sensitive to input uncertainties and errors. The SDOF liner is representative of

* Porosity is the percentage of the open area in the test surface versus the area of the entire test surface.

actual flight hardware and the mode scattering specimen is design to maximum the scattering of incident energy to investigate what values of the mode scattering coefficients are possible. The rest of the chapter presents the results for each specimen, one at a time, in the order presented in the list above. All estimates are computed neglecting the effects of dissipation and dispersion and all uncertainty estimates are the 95% confidence interval estimates made via the Monte Carlo method assuming an arbitrary distribution.

5.1 Ceramic Tubular Honeycomb with 65% Porosity

The specimen chosen for the analysis is a ceramic tubular specimen with 65% porosity (CT65) shown in Figure 5-1 and each ceramic tubular cell has an estimate hydraulic diameter of approximately 0.443 mm . The specimen is 56 mm long for both waveguides and is encased in at least 12.7 mm-thick aluminum, except for the test face, to prevent the loss of acoustic energy from the sides of the specimen. Approximately 10% of the test face of the large waveguide specimen is damaged due to cutting the material and placing the specimen in the mounting fixture, whereas only approximately 2% of the small waveguide test face is damaged. The results for the same material are given in Jones et al. (Jones, Watson and Parrott 2004), but for a different depth of 77.5 mm.

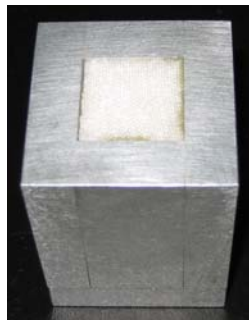


Figure 5-1: Photograph of the CT65 material.

5.1.1 TMM Results

The results from the standard TMM are presented in Figure 5-2 for the reflection coefficient and Figure 5-3 for the normalized specific acoustic impedance, both with uncertainty estimates. The graphs for the coherence and the FRF are given in Appendix F. The coherence between the two microphones for the original and switched positions is above 0.99 for the entire bandwidth. The uncertainty estimates of the magnitude of the reflection coefficient show a periodic increase and decrease in the confidence intervals along with an overall increase with frequency. The minimums are separated by the repeating pattern of approximately 600, 1,000, and 1,000 Hz. The periodic structure suggests there are test conditions where the uncertainty in the magnitude of the reflection coefficient is only a weak function of the input uncertainties. The uncertainty estimates for the phase of the reflection coefficient and for the resistance and reactance show the same general increase in the confidence interval with frequency. The uncertainty in the phase of the reflection coefficient around 1.25 and 4.25 kHz, where phase wrapping occurs, appears unreliable, probably because the numerical techniques with the current discretization setting for approximation of the probability density function could not resolve the phase wrapping. Another discretization resolution issue is also apparent between 5.3 and 5.4 kHz in the reactance. In this narrow frequency range, the uncertainty estimate is jagged, unlike the estimates over the remainder of the bandwidth. Also, the asymmetrical uncertainty estimates at higher frequencies in the presented Monte Carlo simulation results are easily seen in Figure 5-3. For example, at 5.996 kHz the normalized specific acoustic impedance estimate is $4.5 - j0.6$, but the uncertainty estimate for the normalized resistance is $[2.7, 5.1]$ and $[-2.7, 1.6]$ for the normalized

reactance. Also, the maximum uncertainty in the normalized specific acoustic impedance is at anti-resonance at 2.61 and 5.50 kHz and the minimum uncertainty appears at the resonance at 1.26 and 4.24 kHz.

At anti-resonance, the specimen acts as a high impedance specimen, like a sound-hard boundary, and the results in Chapter 3 showed that this condition is then most sensitive to the input uncertainties. At resonance, there is a maximum of particle velocity in the ceramic tubes and thus, increased dissipation. This makes the specimen appear to be sound-soft and again from Chapter 3, less sensitive to input uncertainties. This supports the conclusion from the multivariate uncertainty analysis of the TMM that the uncertainty is a function of the specific acoustic impedance value of the specimen. The periodic structure of the uncertainty estimate of the magnitude of the reflection coefficient shows that there are frequencies where the estimate is insensitive to the input uncertainties. This follows the trends displayed in the derivatives of the reflection coefficient from Sections 3.2.2-3.2.4, where the derivatives contained a sine function. This could be used to an advantage in the design of future waveguide to minimize the uncertainty in the estimates. The uncertainty estimates for the normalized resistance and reactance again show the maximum and minimum at anti-resonance and resonance but the periodic structure is diminished and barely detectable. This suggests that the uncertainty estimates for the normalized resistance and reactance are less dependent on the input uncertainties that produced this structure.

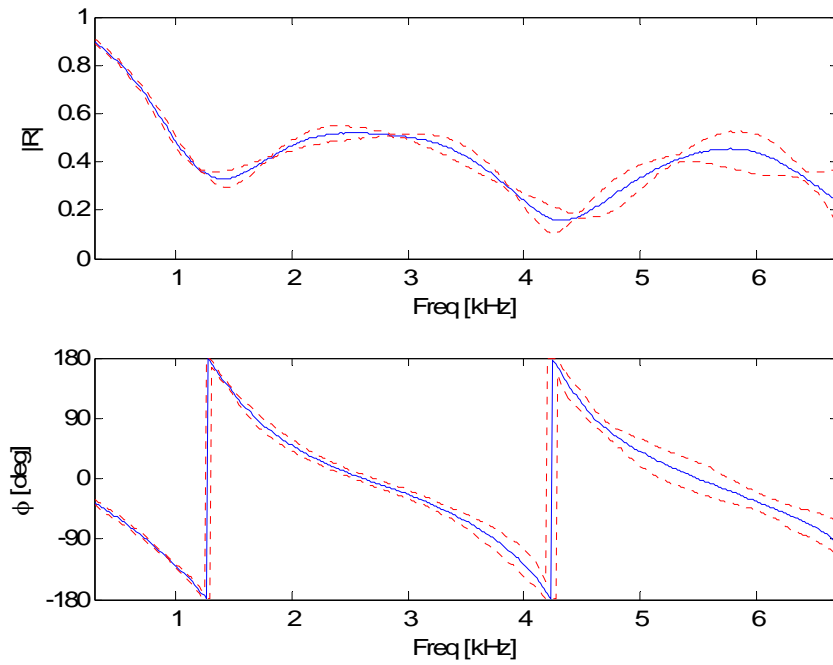


Figure 5-2: Reflection coefficient for CT65 for the TMM. — Estimated value, - - - Uncertainty estimates.

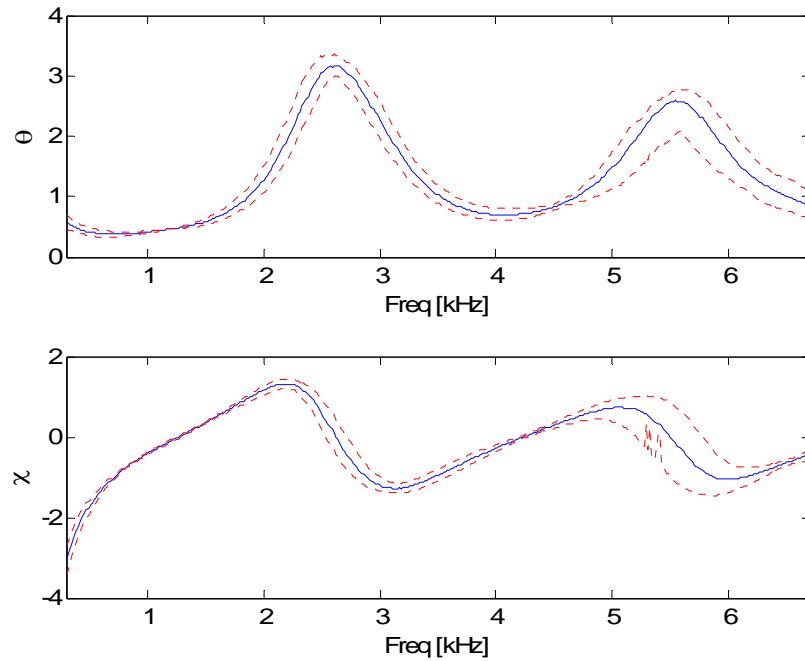


Figure 5-3: Normalized specific acoustic impedance estimates for CT65 via TMM. — Estimated value, - - - Uncertainty estimates.

5.1.2 High Frequency TMM Results

The results from the high frequency TMM for a single specimen are presented in Figure 5-4 for the reflection coefficient and Figure 5-5 for the normalized specific acoustic impedance, both with uncertainty estimates. The graphs for the coherence and the FRF are given in Appendix F. The coherence between the two microphones for the original and switched positions is above 0.9999 for the entire bandwidth. The uncertainty estimates of the magnitude of the reflection coefficient show a periodic increase and decrease in the confidence intervals along with an overall increase with frequency, the same as with the standard TMM results. The uncertainty estimates for the phase of the reflection coefficient and for the resistance and reactance show the same general increase in the confidence interval with frequency, again the same as with the standard TMM results. The difference is apparent for frequencies above 10 kHz, where the uncertainty estimates become extremely unpredictable and large. In this high frequency range, the numerical technique can no longer resolve the confidence region, as the output uncertainty has become extremely sensitive to the input uncertainties. The uncertainty in the phase of the reflection coefficient covers the entire phase space from +180 to -180 degrees. The major contributor to the large and unpredictable confidence regions is the uncertainty in the microphone locations. At 10 kHz, the wavelength is 34.4 mm and an uncertainty of 1 mm has become approximately 3% of the wavelength. The percentage increases to approximately 6% at 20 kHz. To improve the measurement of the location of the two microphone centers, the distance could be measured with an advanced technique, such as describe in literature (Katz 2000).

The estimated values for the magnitude of the reflection coefficient and normalized specific acoustic impedance show an anomaly in a small frequency range centered at 13.5 kHz. At this frequency, the microphone spacing is exactly equal to $\frac{1}{2}$ a wavelength and the TMM is subjected to a known singularity, as shown in Chapter 3. The uncertainty estimates at this frequency tends towards infinity to help reveal the singularity and show the deficiency of the TMM. The data in this range should be replaced by data from an additional measurement of the TMM with a different microphone spacing, but this is not done since the goal of this dissertation is to illustrate the strengths and weaknesses of the TMM.

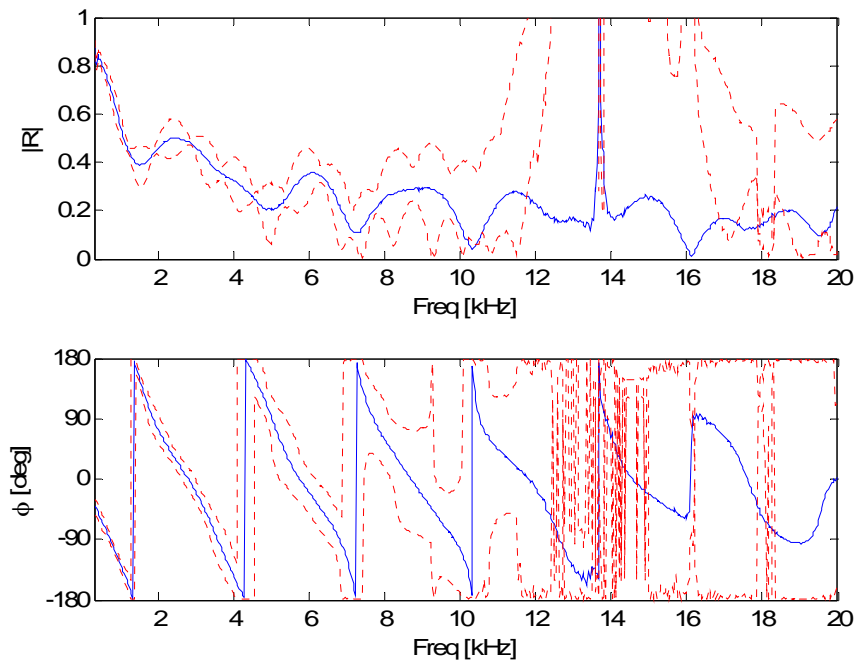


Figure 5-4: Reflection coefficient for CT65 for the high frequency TMM. — Estimated value, - - - Uncertainty estimates.

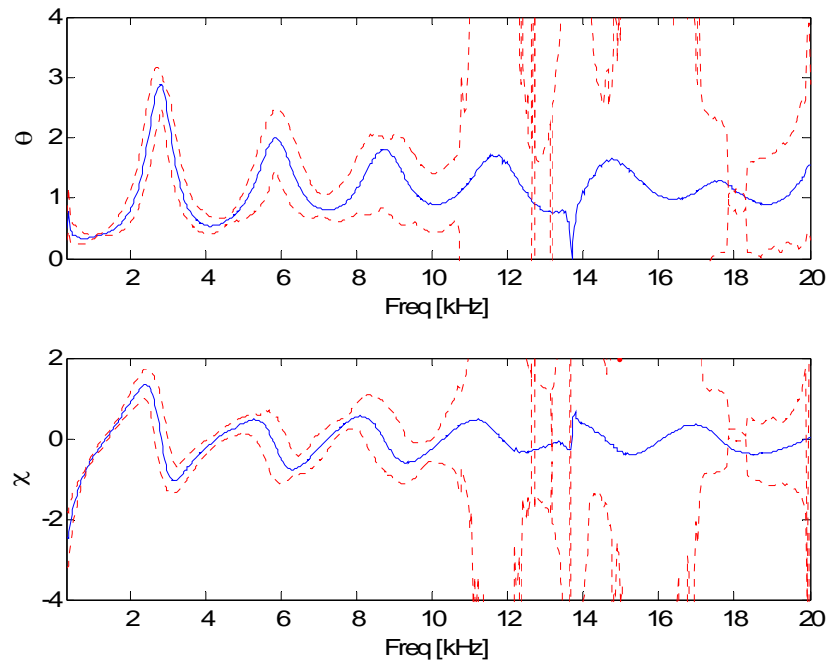


Figure 5-5: Normalized specific acoustic impedance estimates for CT65 via the high frequency TMM. — Estimated value, - - - Uncertainty estimates.

5.1.3 MDM Results and Comparison

The standard TMM, the high frequency TMM and the MDM experimental results for the CT65 specimen are compared in this section, but first the MDM results for the incident and reflected pressure field and the power absorption coefficient are presented. The cut-on frequencies for the higher-order modes are 6.83 kHz for the (1,0) and (0,1) modes and 9.66 kHz for the (1,1) mode, based on the measured temperature during the MDM measurements. Figure 5-6 shows the incident pressure field measured near the specimen for each of the restrictor plates and reveals that one of the sources generates a pressure level approximately 5-10 dB higher than the other three sources for the higher-order modes. The exception is the plane wave mode, where the restrictor plate produces pressure levels only marginally higher than the others. The data for the reflected pressure fields for each of the restrictor plates are presented in Figure 5-7, and this figure shows

evidence of mode scattering, since there is no longer the same difference between the pressure amplitude of each of the sources, as shown in the incident pressure field.

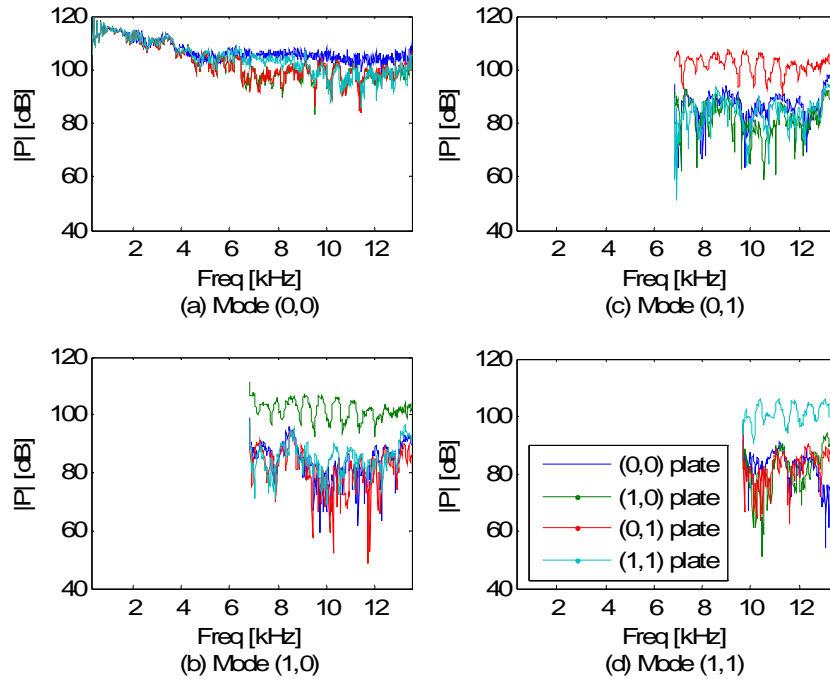


Figure 5-6: Incident pressure field for the MDM for CT65.

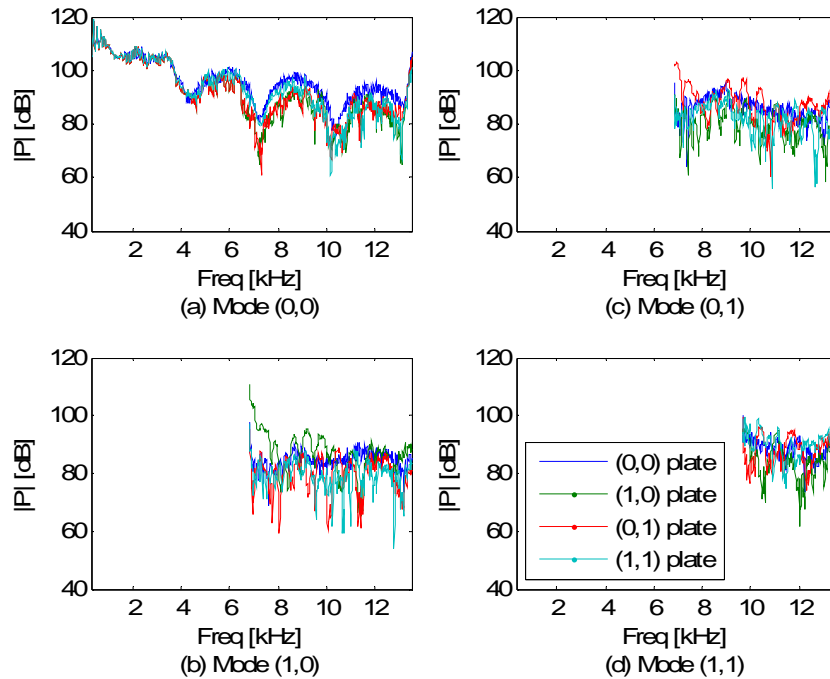


Figure 5-7: Reflected pressure field for the MDM for CT65.

The absorption coefficient is shown in Figure 5-8 for all four restrictor plates. The data show that the total power absorbed is dependent on the modal content of the acoustic field, since the absorption coefficient varies between the sources after the cut-on frequency for the first higher-order mode. The data also confirms the experimental setup and measurement, since the computed value for the absorption coefficient remains bounded between zero and unity.

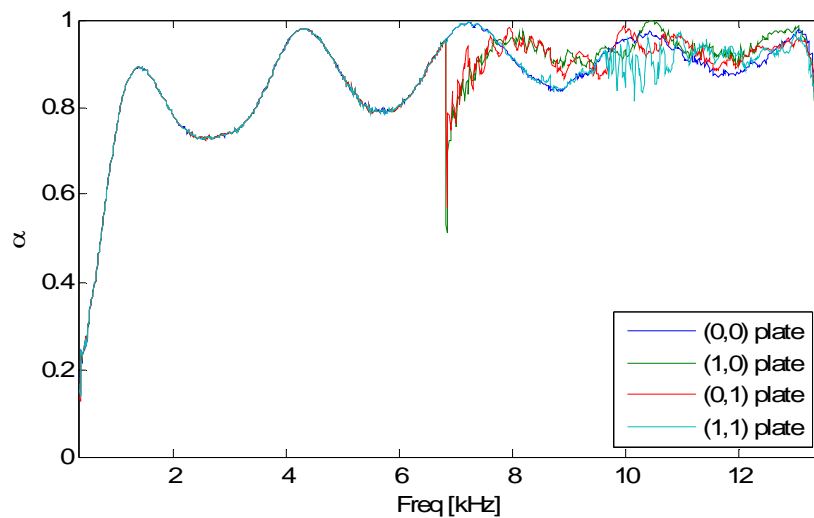


Figure 5-8: Absorption coefficient for CT65.

The magnitude and phase of the reflection coefficients are shown in Figure 5-9 along with results from both TMM measurements. The estimate of the plane wave reflection coefficient provided by the MDM agrees with the TMM of the large waveguide to within its 95% confidence interval estimates, which are not shown in the figures for clarity. The estimates from the small waveguide do not agree with the estimates from the large waveguide over the entire frequency range to within their 95% confidence intervals. A definite shift of the estimate of the small waveguide can be seen from the estimates for the large waveguide in both the reflection coefficient and the normal-incident normalized specific acoustic impedance values. The figure also shows that the estimate of the plane

wave reflection coefficient by the MDM is affected by the same singularity that affects the high frequency TMM at 13.5 kHz. Figure 5-10 through Figure 5-13 show the mode scattering coefficients estimated by the MDM. The magnitude of the mode scattering coefficients is less than 0.2 for all frequencies, except for the frequencies near the (1,1) mode cut-on or for coefficients going into the plane wave mode near 13.5 kHz. Both of these exceptions are unreliable due to either the cut-on phenomenon or the microphone spacing issue.

The results for the acoustic impedance ratio are shown in Figure 5-14, and Figure 5-15 shows the normalized specific acoustic impedance. The test specimen is assumed to be a locally reactive material and thus the transmission angle is assumed to be normal to the surface. The data show a number of resonant frequencies monotonically decaying in

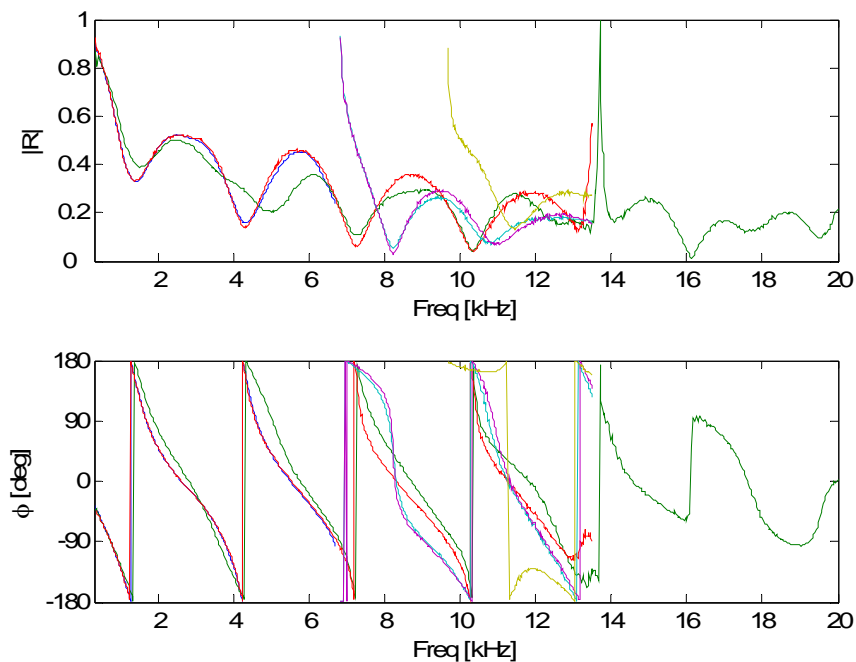


Figure 5-9: Comparison of the reflection coefficient estimates for CT65 via all three methods. — TMM, — high frequency TMM, — MDM (0,0) mode, — MDM (1,0) mode, — MDM (0,1) mode, and — MDM (1,1) mode.

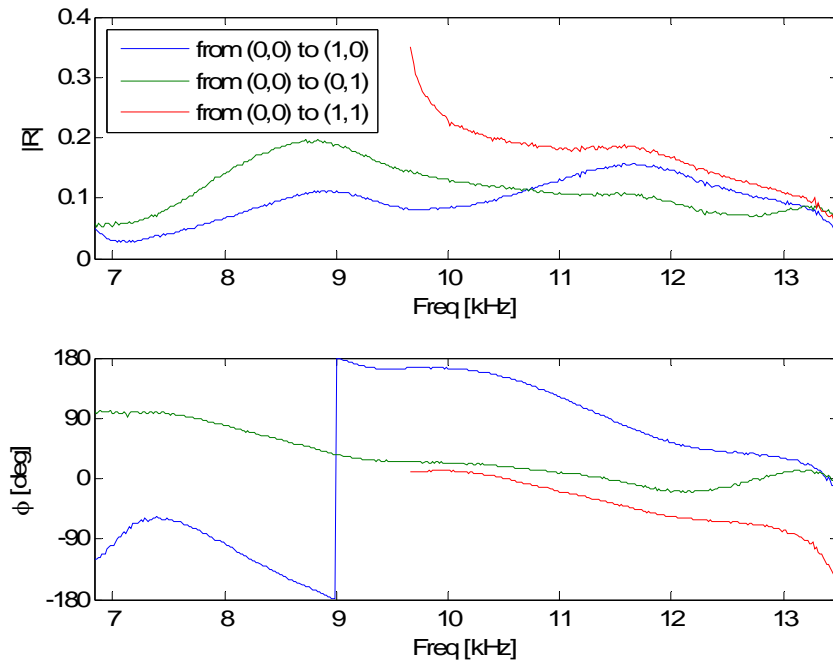


Figure 5-10: Mode scattering coefficients for CT65 from the (0,0) mode to the other propagating modes.

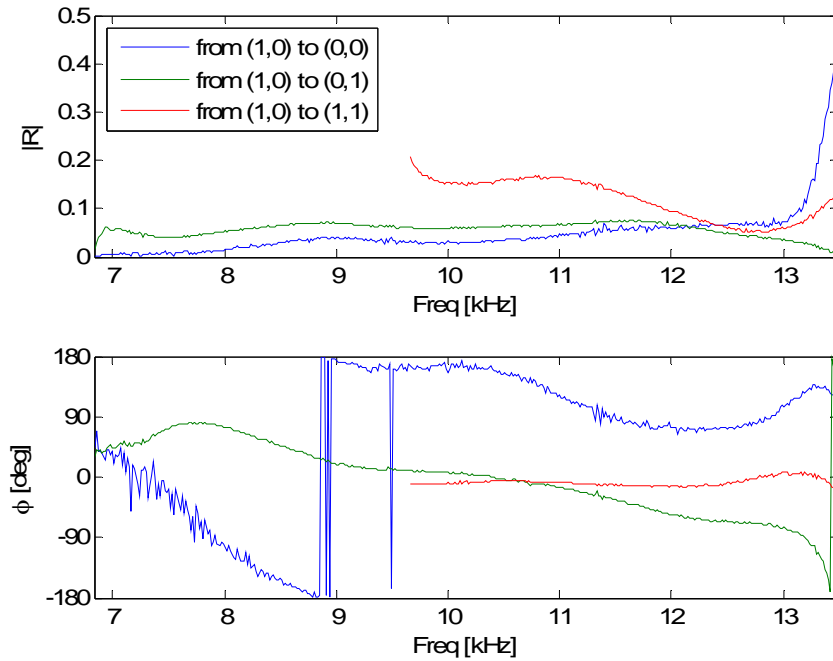


Figure 5-11: Mode scattering coefficients for CT65 from the (1,0) mode to the other propagating modes.

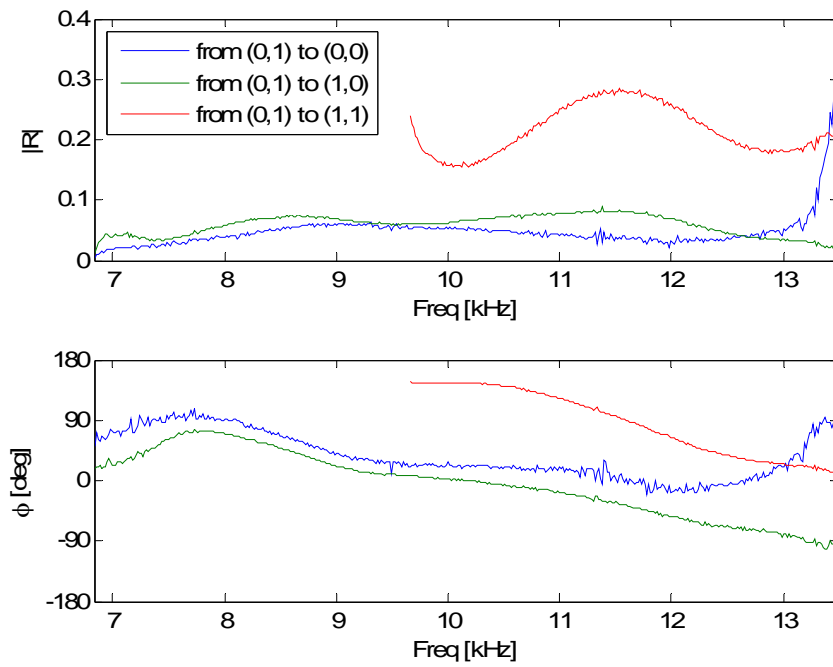


Figure 5-12: Mode scattering coefficients for CT65 from the (0,1) mode to the other propagating modes.

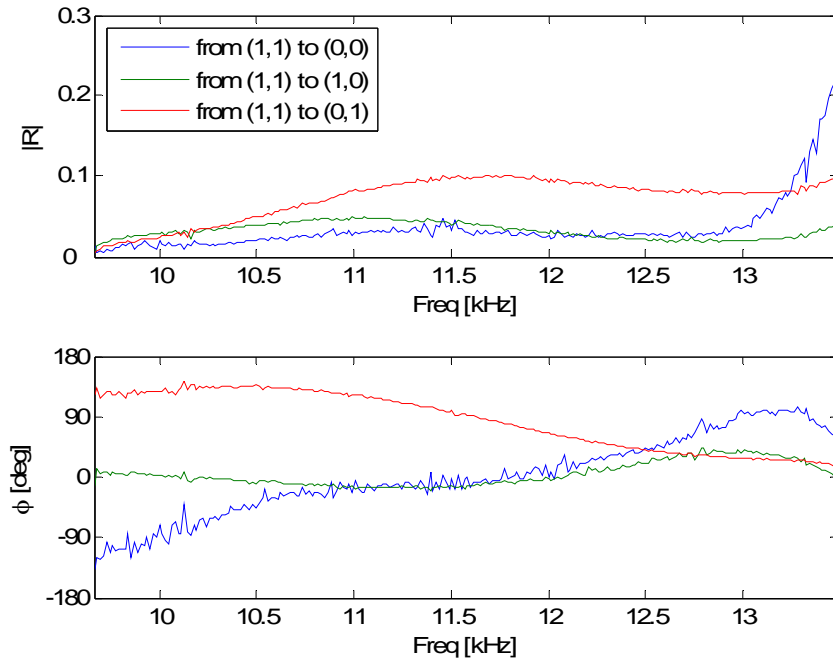


Figure 5-13: Mode scattering coefficients for CT65 from the (1,1) mode to the other propagating modes.

amplitude, which are 1.26, 4.24, 7.20, and 10.3 kHz, as identified from the standard TMM and MDM results. If each ceramic cell is modeled as a rigid-wall waveguide with a rigid termination, the normalized specific acoustic impedance can be calculated at the entrance to the ceramic cells from (Kinsler, Frey, Coppens and Sanders 2000)

$$\xi_{spac} = -j \frac{\omega}{kc_0} \cot(kl_{cell}), \quad (5.1)$$

where l_{cell} is the length of the specimen and the complex wavenumber, k , is given by Equation (2.30) and accounts for boundary layer dissipation and dispersion. The calculated ξ_{spac} from Equation (5.1) is shown in Figure 5-15. The comparisons between the experimental measured normalized specific acoustic impedance and the calculated normalized specific acoustic impedance are reasonable and provide physical insight into the mechanics of the ceramic tubular material as an acoustic liner. The estimate of the resonances between the model and the TMM in the large waveguide and the MDM match well, but the model underestimates the normalized resistance possibly due to heat conduction within the specimen material. For the locally reactive assumption to be valid, the estimates for the normalized specific acoustic impedance should be identical, regardless of the mode. Uncertainty estimates of the normalized specific acoustic impedance are needed to fully evaluate this assumption, but the results show reasonable agreement, except at the cut-on for the (0,1), (1,0), and (1,1) modes and for frequencies above 13 kHz. These frequency ranges should be investigated further, but these results suggest that the locally reactive assumption is reasonable. The unreliable results at the cut-on frequencies are affected by theoretical phase and angle of incidence for the mode cutting on. At the cut-on frequency, the phase speed of the newly propagating mode

approaches infinity and the incident angle approaches normal incidence. Physically, this situation is unrealizable and results in the irregular behavior at the cut-on frequencies. Furthermore, even beyond the cut-on frequency the incidence angle is quite large; it is 67° for the (1,1) mode at 10.5 kHz, where in Figure 5-15 the data for the different modes appear to match. The MDM estimates of the plane wave reflection coefficient and the normal-incidence acoustic impedance agree with the standard TMM estimate within the 95% confidence interval for the standard TMM in the large waveguide. Again, the TMM uncertainty estimates are not shown for clarity.

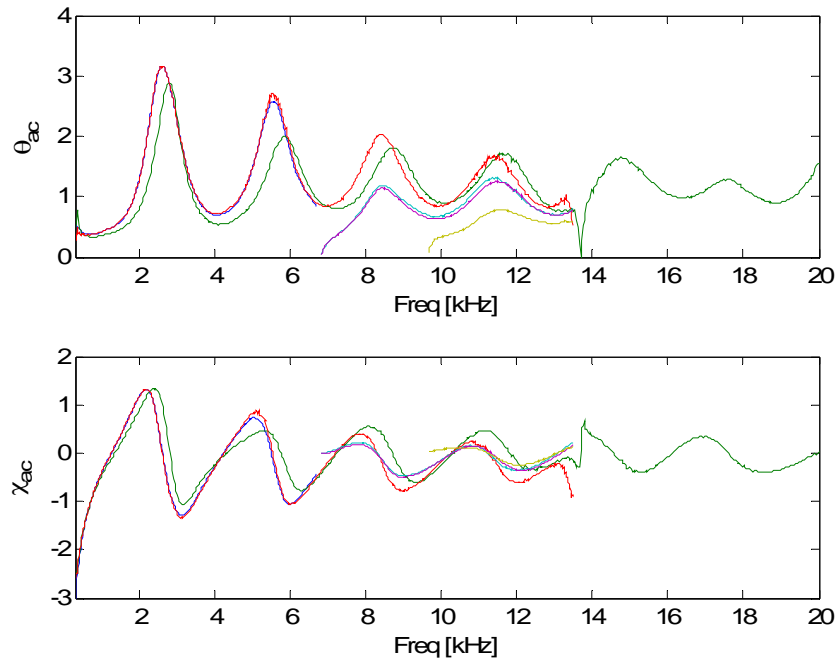


Figure 5-14: Comparison of the acoustic impedance ratio estimates for CT65 via all three methods. — TMM, — high frequency TMM, — MDM (0,0) mode, — MDM (1,0) mode, — MDM (0,1) mode, and — MDM (1,1) mode.

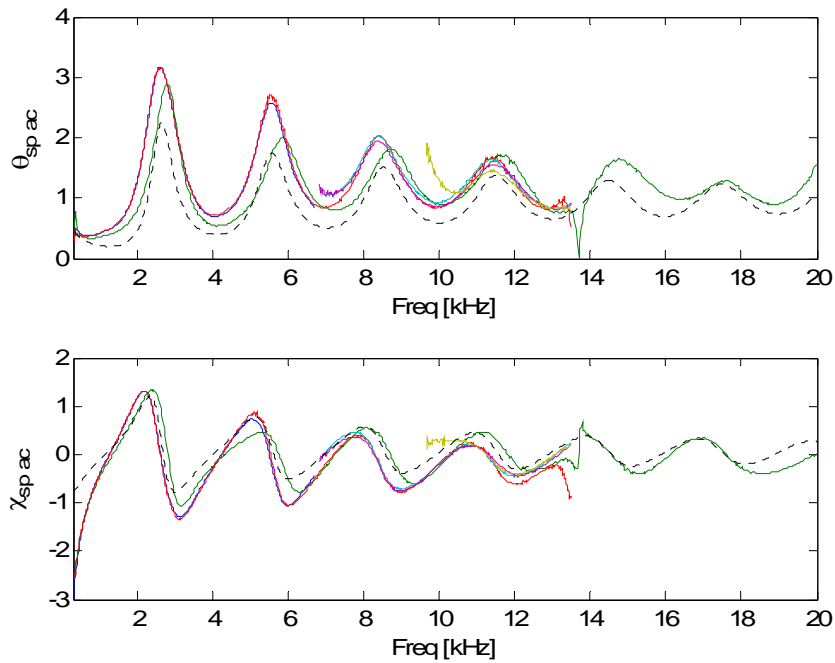


Figure 5-15: Comparison of the normalized specific acoustic impedance estimates for CT65 via all three methods. — TMM, — high frequency TMM, — MDM (0,0) mode, — MDM (1,0) mode, — MDM (0,1) mode, — MDM (1,1) mode, - - - model.

5.2 Ceramic Tubular Honeycomb with 73% Porosity

The multivariate method and the Monte Carlo method are now demonstrated on experimental data for a ceramic honeycomb test specimen with a porosity of 73% shown in Figure 5-16 and each ceramic tubular cell has an estimate hydraulic diameter of approximately 1.1 mm . The specimen is 51 mm long for both waveguides and is encased in 12.7 mm-thick aluminum, except for the 25.4 mm-by-25.4 mm test face, to prevent the loss of acoustic energy from the sides of the specimen. Approximately 15% of the test face of the large waveguide specimen is damaged due to cutting the material and placing the specimen in the mounting fixture, whereas approximately 12% of the small waveguide test face is damaged.

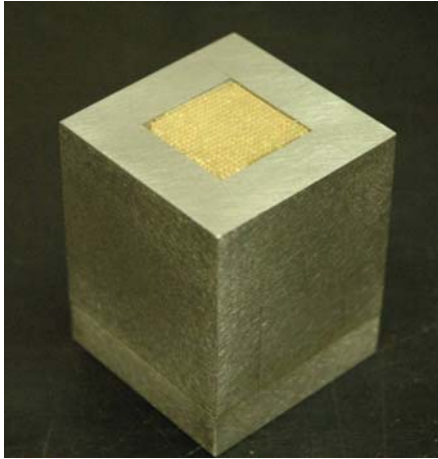


Figure 5-16: Photograph of the CT73 material.

5.2.1 TMM Results

The results from the standard TMM are presented in Figure 5-17 for the reflection coefficient and Figure 5-18 for the normalized specific acoustic impedance, both with uncertainty estimates. The graphs for the coherence and the FRF are given in Appendix F. The coherence between the two microphones for the original and switched positions is above 0.98 for the entire bandwidth. The uncertainty estimates of both the reflection coefficient and normalized specific acoustic impedance show the same trends as the CT65 specimen results, such as a periodic structure with approximately the same frequency spacing between the minimums, increasing uncertainty with frequency, and asymmetrical uncertainty intervals. The uncertainty estimates for the CT73 specimen appear smoother than the estimates for the CT65 specimen and are thus not impacted by discretization errors. Again, the maximum uncertainty in the normalized specific acoustic impedance occurs at anti-resonance.

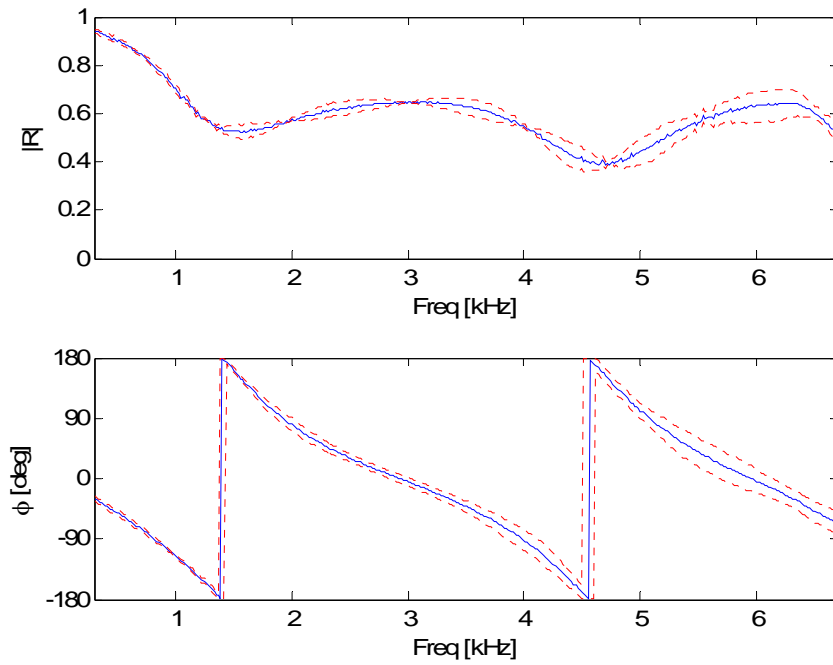


Figure 5-17: Reflection coefficient for CT73 for the TMM. — Estimated value, - - - Uncertainty estimates.

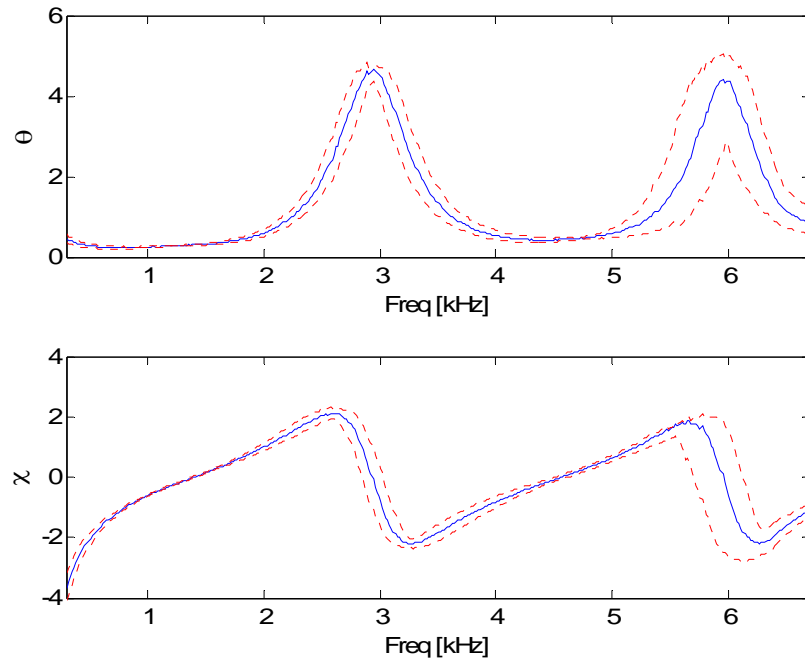


Figure 5-18: Normalized specific acoustic impedance estimates for CT73 via the TMM. — Estimated value, - - - Uncertainty estimates.

5.2.2 High Frequency TMM Results

The results from the high frequency TMM for a single specimen are presented in Figure 5-19 for the reflection coefficient and Figure 5-20 for the normalized specific acoustic impedance, both with uncertainty estimates. The graphs for the coherence and the FRF are given in Appendix F. The coherence between the two microphones for the original and switched positions is above 0.9999 for the entire bandwidth. The uncertainty estimates of the reflection coefficient and normalized acoustic impedance show the same behavior as with the CT65 specimen. The uncertainty estimates below 10 kHz appear reasonable, but beyond 10 kHz the uncertainty estimates are unpredictable because of the large input uncertainties in the location of the microphones as before with the CT65 high frequency TMM results. Again, a singularity in the TMM is present around 13.5 kHz, where the microphone spacing is equal to a half wavelength.

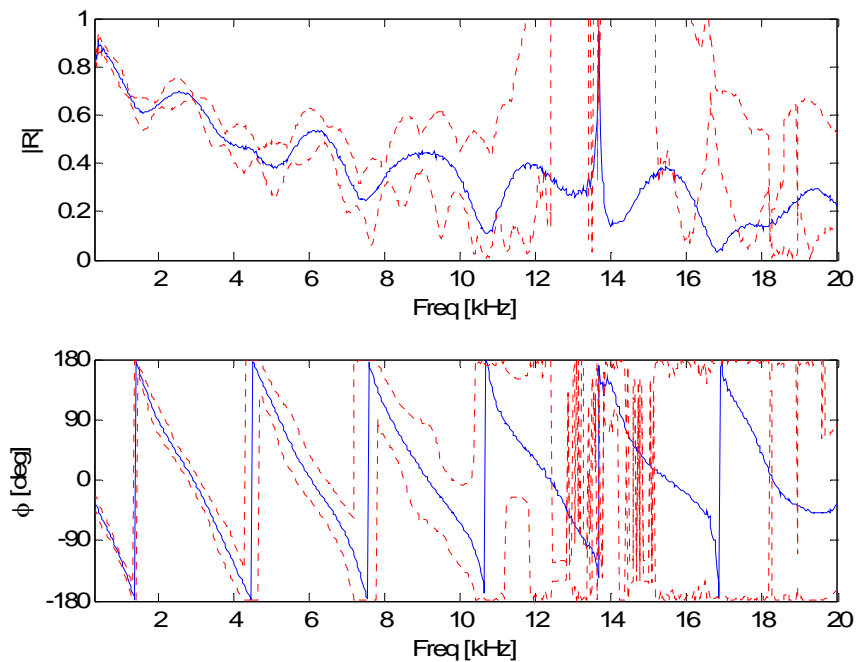


Figure 5-19: Reflection coefficient for CT73 for the high frequency TMM. — Estimated value, - - - - - Uncertainty estimates.

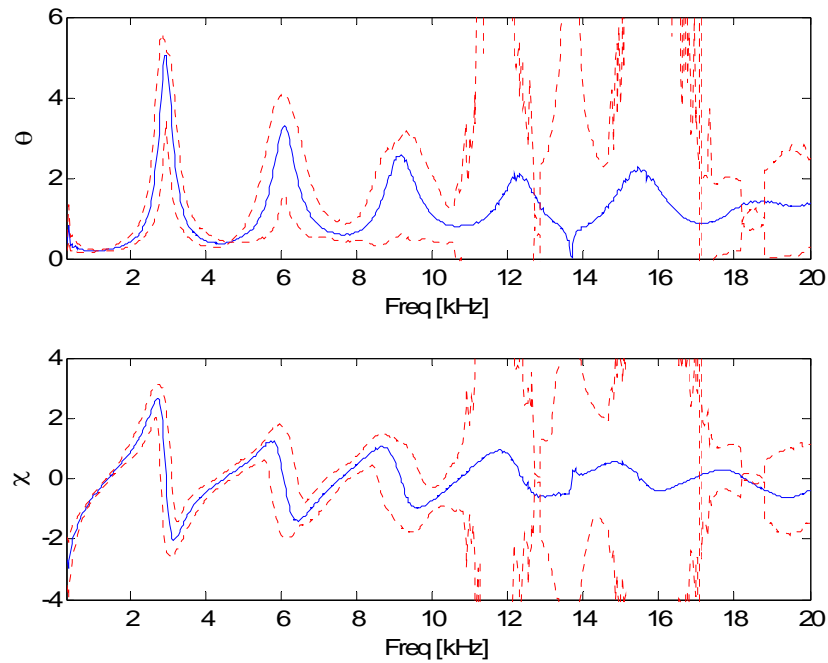


Figure 5-20: Normalized specific acoustic impedance estimates for CT73 via the high frequency TMM. — Estimated value, - - - Uncertainty estimates.

5.2.3 MDM Results and Comparison

The standard TMM, the high frequency TMM, and the MDM experimental results for the CT73 specimen are compared in this section, but first the MDM results for the incident and reflected pressure field and the power absorption coefficient are presented. The cut-on frequencies for the higher-order modes are 6.83 kHz for the (1,0) and (0,1) modes and 9.66 kHz for the (1,1) mode, based on the measured temperature during the MDM measurements. Figure 5-21 shows the incident pressure field measured near the specimen for each of the restrictor plates and again, reveals that one of the sources generates a pressure level approximately 5-10 dB higher than the other three sources for the higher-order modes. The exception is the plane wave mode, where the restrictor plate produces pressure levels only marginally higher than the others. The data for the reflected pressure field for each of the restrictor plates are presented in Figure 5-22, and

again this figure shows evidence of mode scattering, since there is no longer the same difference between the pressure amplitude of each of the sources as shown in the incident pressure field.

The absorption coefficient is shown in Figure 5-23 for all four restrictor plates. Again, the data show that the total power absorbed is dependent on the modal content of the acoustic field, since the absorption coefficient varies between the sources after the cut-on frequency for the first higher-order mode. The data also confirms the experimental setup and measurement, since the computed value for the absorption coefficient remains bounded between zero and unity.

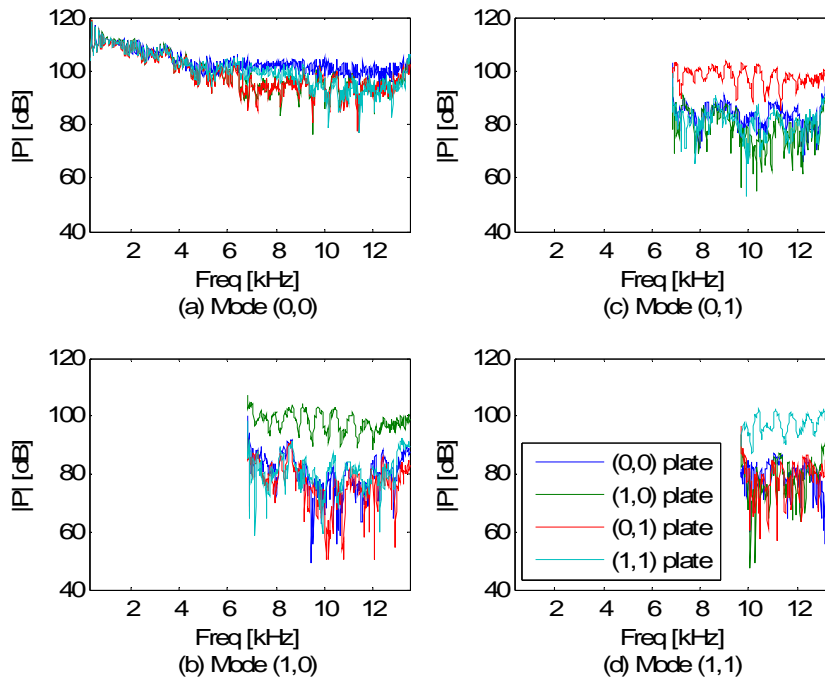


Figure 5-21: Incident pressure field for the MDM for CT73.

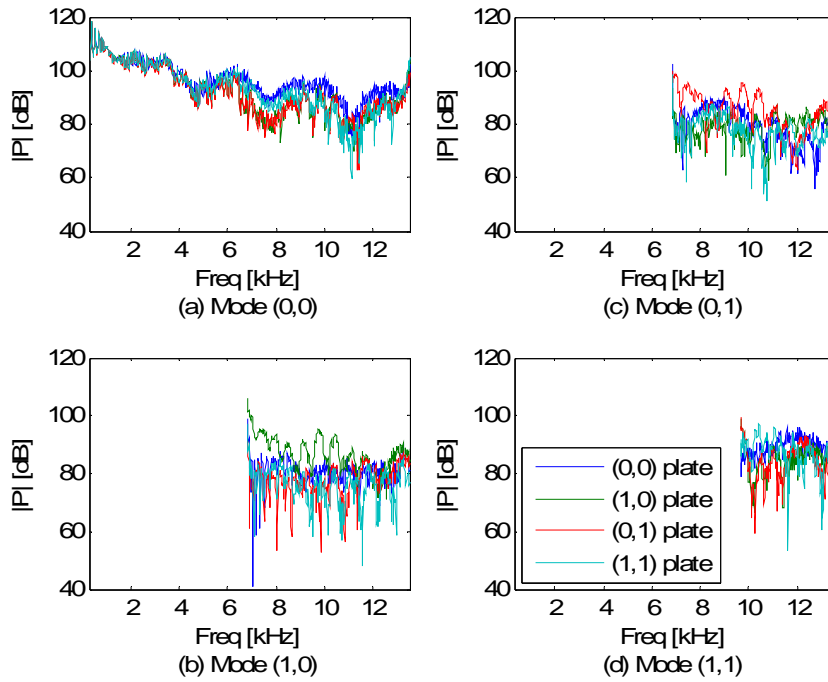


Figure 5-22: Reflected pressure field for the MDM for CT73.

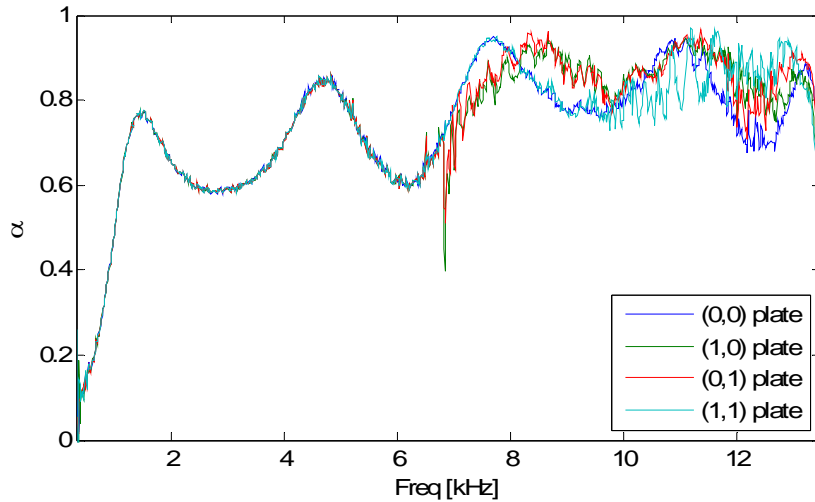


Figure 5-23: Absorption coefficient for CT73.

The magnitude and phase of the reflection coefficients are shown in Figure 5-24 along with results from both TMM measurements. The estimate of the plane wave reflection coefficient provided by the MDM agrees with the TMM in the large waveguide to within its 95% confidence interval estimates, which are not shown in the figures for clarity. The figure also shows that the estimate of the plane wave reflection coefficient

by the MDM is affected by the same singularity that affect the high frequency TMM at 13.5 kHz. Figure 5-25 through Figure 5-28 show the mode scattering coefficients estimated by the MDM. The magnitude of the mode scattering coefficients is less than 0.25 for all frequencies except for the frequencies near the (1,1) mode cut-on or for coefficients going into the plane wave mode near 13.5 kHz. Both of these exceptions are unreliable due to either the cut-on phenomenon or the microphone spacing issue. The figures also show that the most efficient scattering is from the plane wave mode into the (1,1) mode, with a maximum magnitude of approximately 0.4.

The results for the acoustic impedance ratio are shown in Figure 5-29, and Figure 5-30 shows the normalized specific acoustic impedance. The test specimen is assumed to be a locally reactive material, and thus the transmission angle is assumed to be normal to

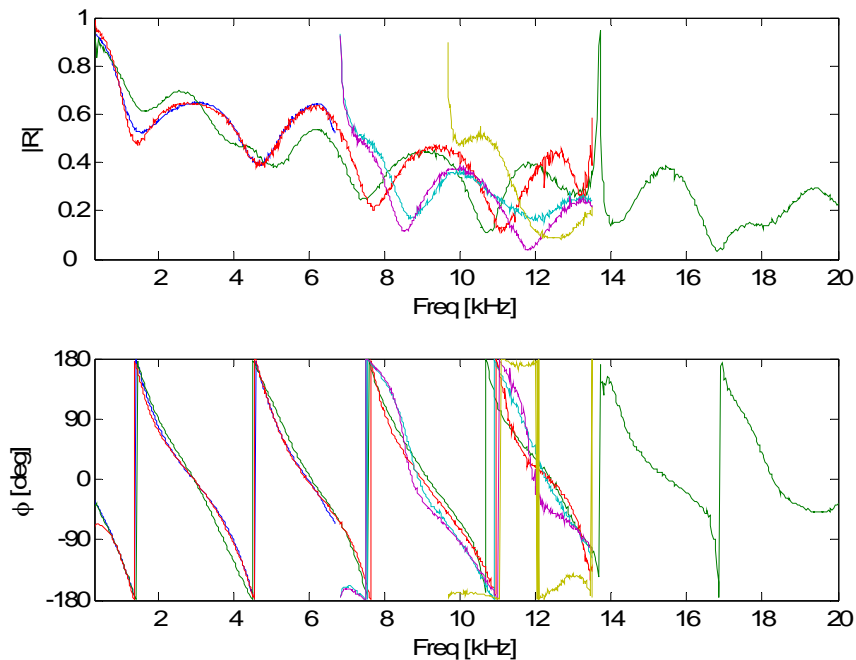


Figure 5-24: Comparison of the reflection coefficient estimates for CT73 via all three methods. — TMM, — high frequency TMM, — MDM (0,0) mode, — MDM (1,0) mode, — MDM (0,1) mode, and — MDM (1,1) mode.

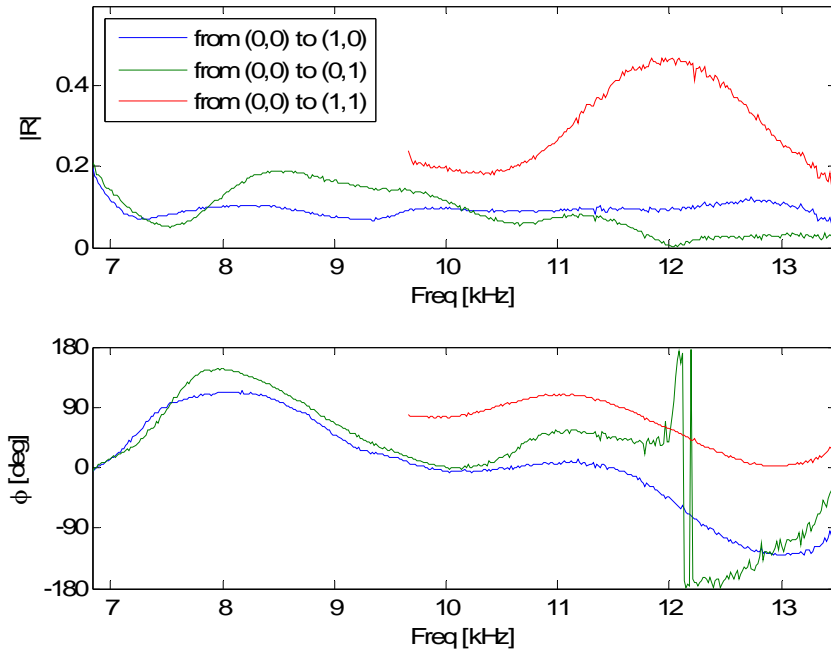


Figure 5-25: Mode scattering coefficients for CT73 from the (0,0) mode to the other propagating modes.

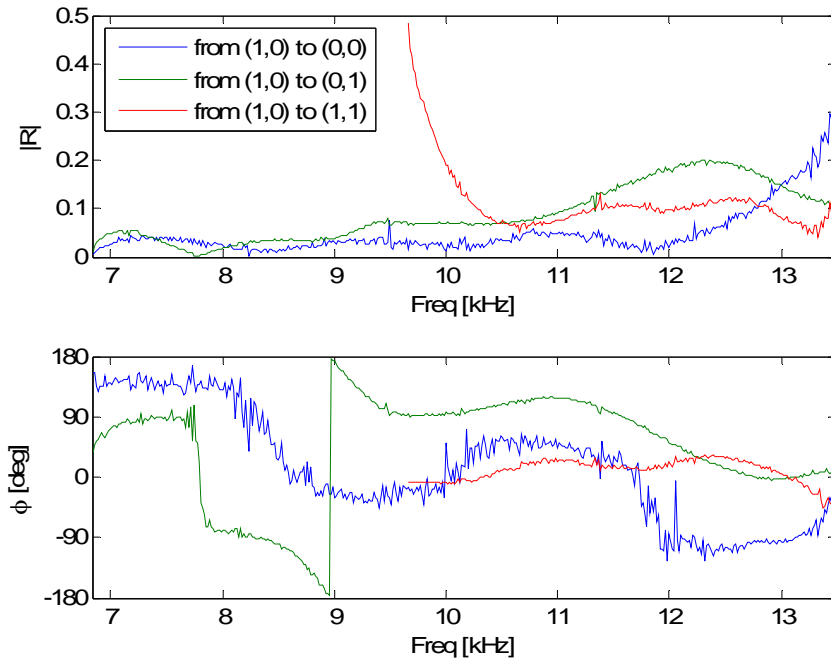


Figure 5-26: Mode scattering coefficients for CT73 from the (1,0) mode to the other propagating modes.

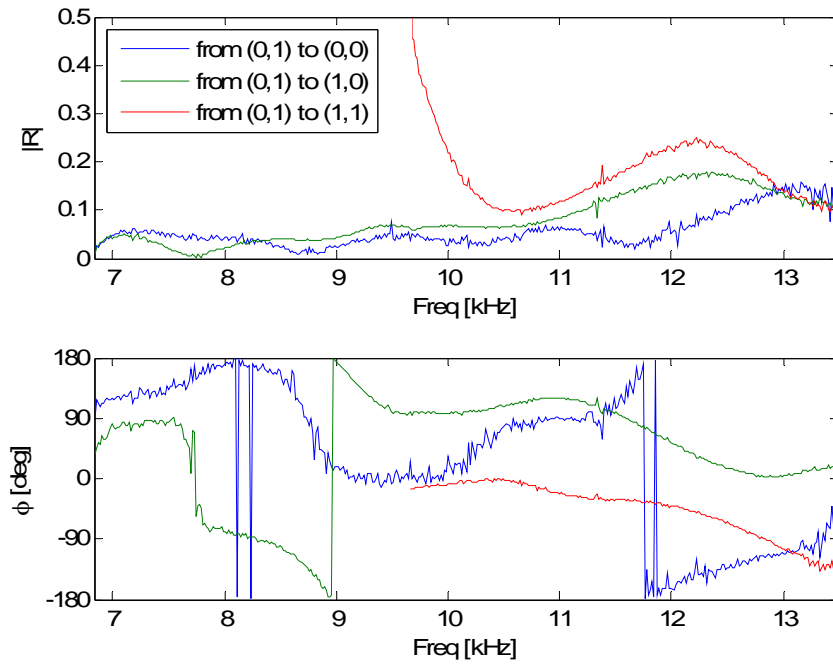


Figure 5-27: Mode scattering coefficients for CT73 from the (0,1) mode to the other propagating modes.

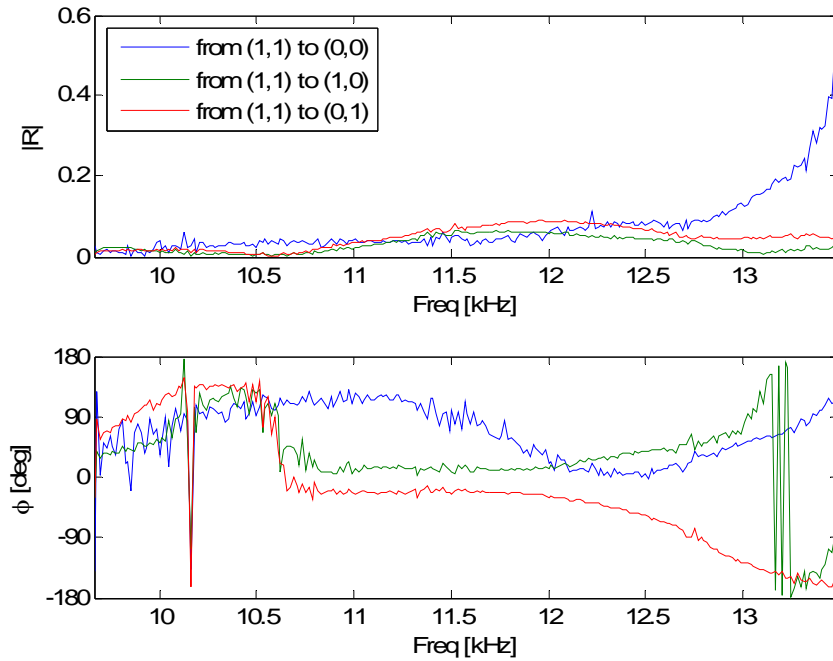


Figure 5-28: Mode scattering coefficients for CT73 from the (1,1) mode to the other propagating modes.

the surface. The normalized specific acoustic impedance model given in Equation (5.1) is not used to model this specimen. The model is inadequate in capturing the physics of the specimen possibility due to either strong interactions between the ceramic cells at the test surface or due to inadequate sealing between the cells and the rigid termination. Still, the data in the two figures show a number of resonant frequencies monotonically decaying in amplitude, which are 1.36, 4.55, 7.62, and 10.9 kHz, as identified from the standard TMM and MDM results. If the ceramic cells are modeled as an ideal quarter-wave resonator, the first four resonant frequencies are 1.69, 5.06, 8.43, and 11.8 kHz. The comparisons between the experimental resonant frequencies and the calculated resonant frequencies are reasonable, and provide physical insight into the mechanics of the ceramic tubular material as an acoustic liner. The results for the normalized specific acoustic impedance show reasonable agreement, except at the cut-on for the (0,1), (1,0), and (1,1) modes and for frequencies above 10 kHz. These frequency ranges should be investigated further for the reasons described in Section 5.1.3, but these results suggest that the locally reactive assumption is reasonable within the bandwidth up to 10 kHz. The MDM estimates of the plane wave reflection coefficient and the normal incidence specific acoustic impedance agree with the standard TMM in the large waveguide estimate to within the 95% confidence interval for the standard TMM as shown in Figure 5-18. Again, the TMM uncertainty estimates are not shown here for clarity.

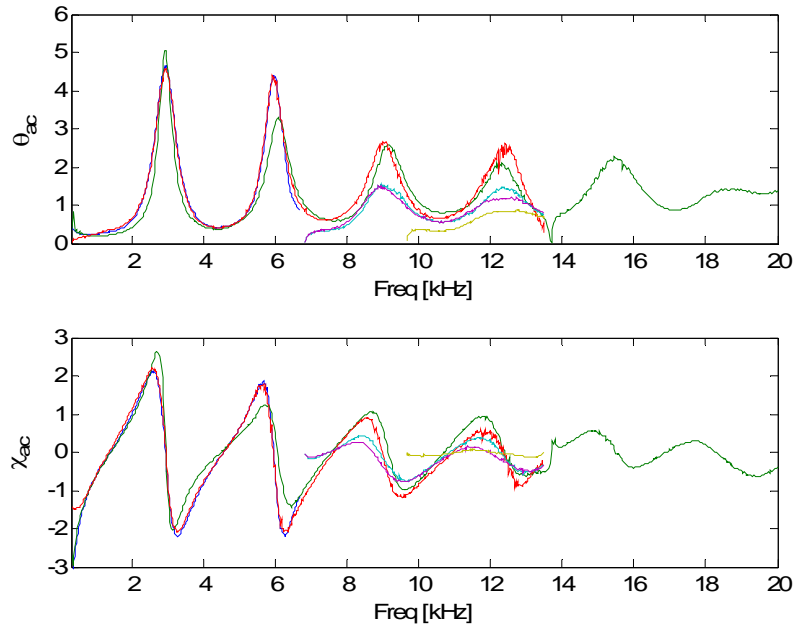


Figure 5-29: Comparison of the acoustic impedance ratio estimates for CT73 via all three methods. — TMM, — high frequency TMM, — MDM (0,0) mode, — MDM (1,0) mode, — MDM (0,1) mode, and — MDM (1,1) mode.

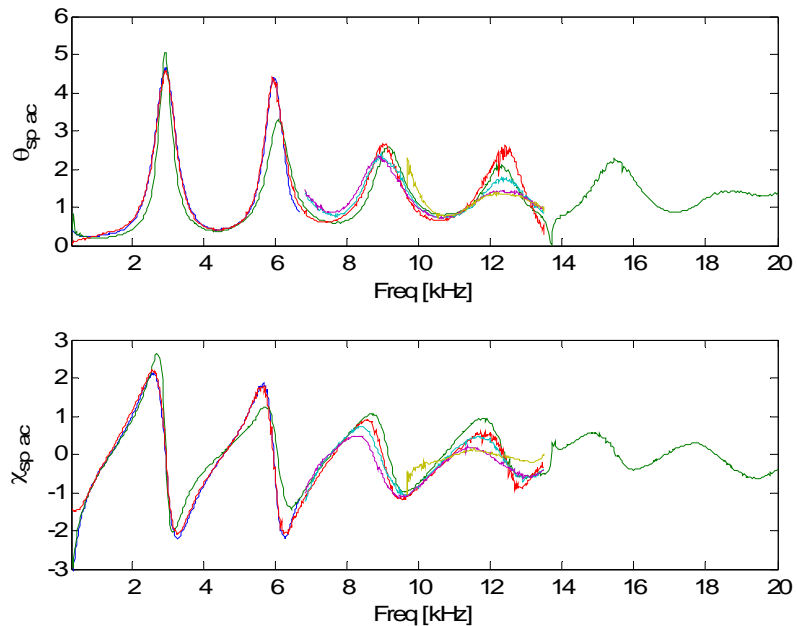


Figure 5-30: Comparison of the normalized specific acoustic impedance estimates for CT73 via all three methods. — TMM, — high frequency TMM, — MDM (0,0) mode, — MDM (1,0) mode, — MDM (0,1) mode, and — MDM (1,1) mode.

5.3 Rigid Termination

The next specimen tested is a rigid termination designed to simulate a sound-hard boundary. This is done by using a solid block of aluminum (type 6061-T6) with a polished test surface as shown in Figure 5-31. The specimen is approximately 31 mm thick for both waveguides. Only the reflection coefficient is considered for this specimen since the impedance should tend towards infinity for a rigid termination.

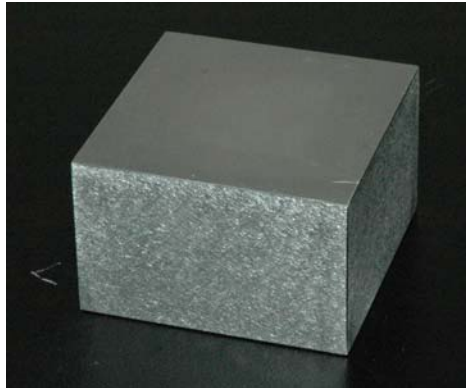


Figure 5-31: Photograph of the rigid termination for the large waveguide.

5.3.1 TMM Results

The results from the standard TMM are presented in Figure 5-32 for the reflection coefficient with uncertainty estimates. The graphs for the coherence and the FRF are given in Appendix F. The coherence between the two microphones for the original and switched positions is above 0.99 for the entire bandwidth, except at 1.63, 2.72, and 4.92 kHz. At these frequencies one of the microphones is located at a node in the standing wave and is only measuring noise. The uncertainty estimates of the magnitude of the reflection coefficient do not strongly show a periodic increase and decrease in the confidence intervals, but still show an overall increase with frequency. The uncertainty estimates for the phase of the reflection coefficient show an almost linear relationship between the confidence interval and frequency. The uncertainty estimates for the phase

of the reflection coefficient and for the resistance and reactance show the same general increase in the confidence interval with frequency. At some frequencies the confidence interval can be seen as asymmetric, but not as much as in the results for the CT65 and CT73 specimens. The value for the magnitude for the reflection coefficient drops to a minimum of 0.96 at approximately 5 kHz, but no changes in the phase are apparent. This suggests that acoustic waves are sensing a dissipation effect not included in the model of the sound field inside the waveguide. The standing wave ratio (SWR) is the ratio of the maximum amplitude in the pressure standing wave pattern to the minimum amplitude and can be computed in decibels from the reflection coefficient by

$$SWR = 20 \log_{10} \left(\frac{1 + |R_{00,00}|}{1 - |R_{00,00}|} \right). \quad (5.2)$$

Physically, the SWR will tend to infinity for an ideal rigid or sound hard termination.

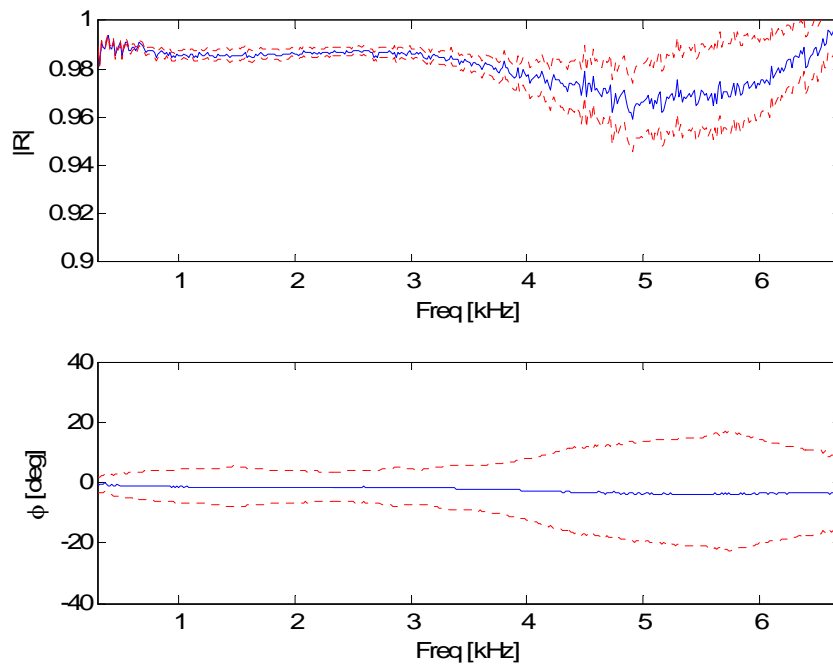


Figure 5-32: Reflection coefficient for the rigid termination for the TMM. — Estimated value, - - - Uncertainty estimates.

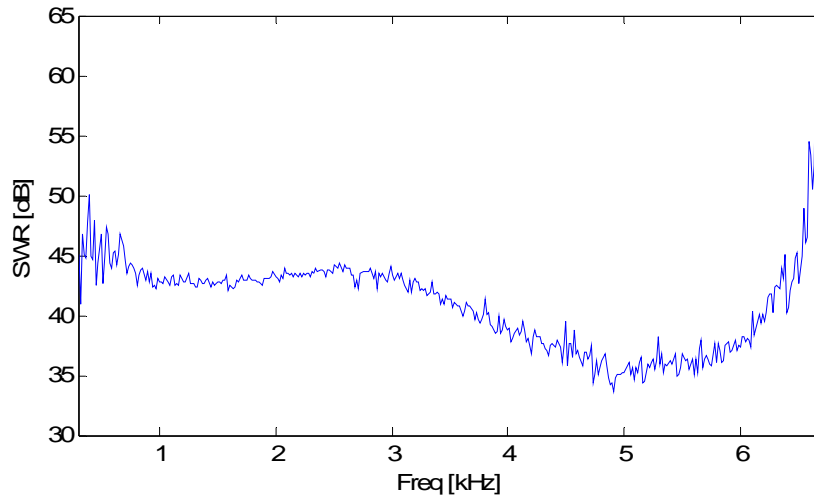


Figure 5-33: Standing wave ratio for the rigid termination measured by the TMM.

The SWR results are given in Figure 5-33 and show that the SWR is approximately 45 dB, except in the frequency range around 5 kHz where the magnitude of the reflection coefficient drops as well.

5.3.2 High Frequency TMM Results

The results from the high frequency TMM are presented in Figure 5-34 for the reflection coefficient with uncertainty estimates. The graphs for the coherence and the FRF are given in Appendix F. The coherence between the two microphones for the original and switched positions is above 0.9999 for the entire bandwidth, but there are drops in the coherence at discrete frequencies. The frequencies are 1.70, 2.27, 6.82, 8.51, 11.4, 12.0, 15.4, 16.0, 18.5, and 20 kHz. Again, these frequencies correspond to frequencies where one of the microphones is located at a node in the standing wave pattern. The uncertainty estimates for the reflection coefficient show the same trends as with the standard TMM and the high frequency TMM of the other specimens. There is a periodic structure, and a general increase in the confidence intervals with frequency. Above 10 kHz, the uncertainty estimates appear unpredictable due to the large

uncertainty in the microphone locations and again at 13.5 kHz the singularity is present. Overall, the uncertainty estimates for this specimen are larger than for the CT65 or CT73 specimens, confirming the analytical multivariate scaling prediction. The SWR is shown in Figure 5-35, and again the drop in the SWR around 5 kHz is present.

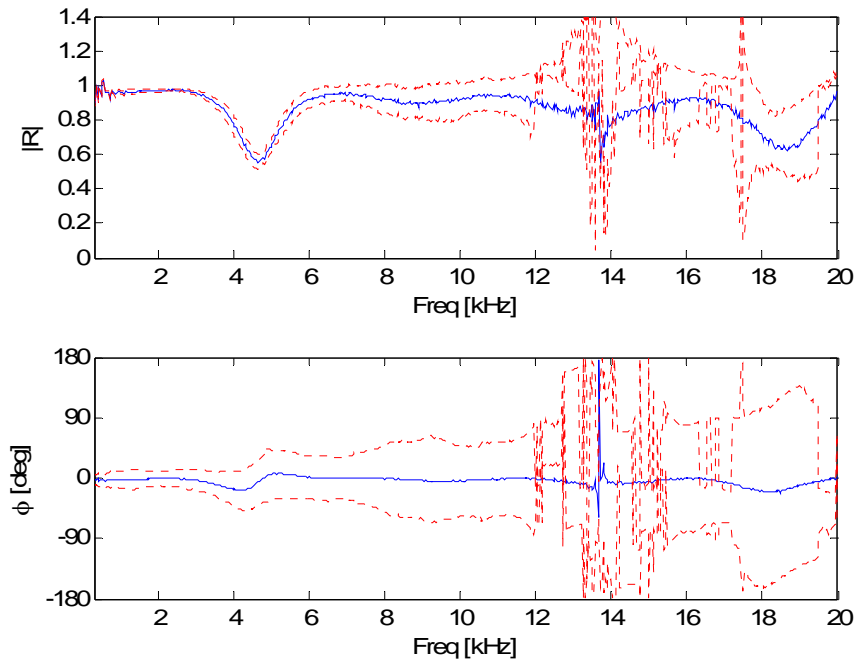


Figure 5-34: Reflection coefficient for the rigid termination for the high frequency TMM.
 — Estimated value, - - - Uncertainty estimates.

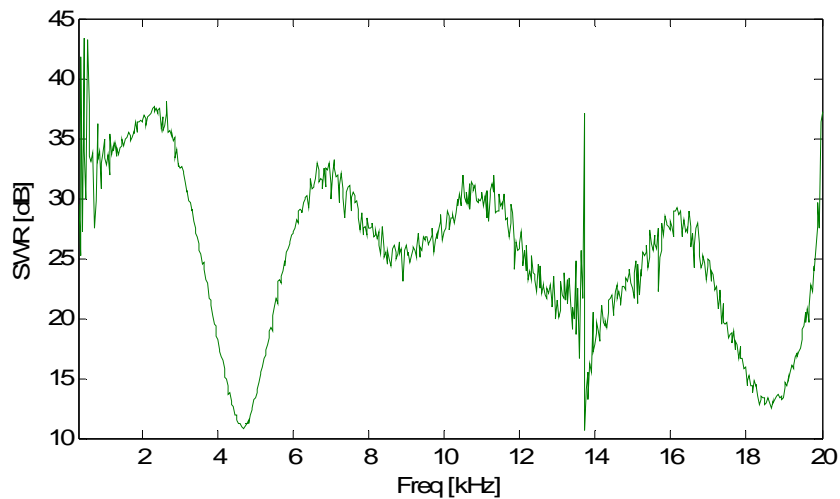


Figure 5-35: SWR for the rigid termination calculated from the high frequency TMM.

5.3.3 MDM Results and Comparison

The standard TMM, the high frequency TMM and the MDM experimental results for the rigid specimen are compared in this section, but first the MDM results for the incident and reflected pressure field and the power absorption coefficient are presented. The cut-on frequencies for the higher-order modes are 6.83 kHz for the (1,0) and (0,1) modes, and 9.66 kHz for the (1,1) mode, based on the measured temperature during the MDM measurements. Figure 5-37 shows the incident pressure field measured near the specimen for each of the restrictor plates. For this measurement, the combination of the (0,0), (1,0), (0,1), and (1,1) restrictor plates did not yield an augmented matrix of the incident and reflected pressure amplitudes with a low condition number, the ratio of the largest to the smallest singular value in the singular value decomposition of a matrix (Chapra and Canale 2002). A condition number of unity would represent a well condition matrix that can be inverted easily. The condition number was greater than 20 for all frequencies beyond the cut-on frequency for the first higher-order mode. To accurately solve for the reflection coefficient matrix, another restrictor plate is designed and used to replace the (1,0) restrictor plate. It is shown in Figure 5-36. The results reveals that one of the sources generates a pressure level approximately 5-10 dB higher than the other sources for the higher-order modes, except for during the use of the triangle restrictor plate, where the levels of both the (1,0) and (0,1) modes are higher. Still, for the plane wave mode, the restrictor plates produce pressure levels only approximately equal. The data for the reflected pressure fields for each of the restrictor plates are presented in Figure 5-38, and this figure shows evidence of mode scattering since there is no longer the same difference between the pressure amplitude of each of the sources as shown in the incident pressure field.

The absorption coefficient is shown in Figure 5-39 for all four restrictor plates. The data show that the total power absorbed is approximately zero for all frequencies and all restrictor plates. The results also show regions where the absorption coefficient is negative, indicating power generation. Physically this is impossible, since the termination is reactive only. Also, the majority of the negative power absorption coefficients are in the frequency range where the data are affected by the singularity created when the microphone spacing is equal to half a wavelength, and thus are

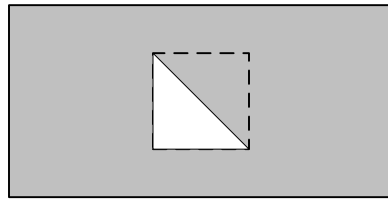


Figure 5-36: Triangle restrictor plate.

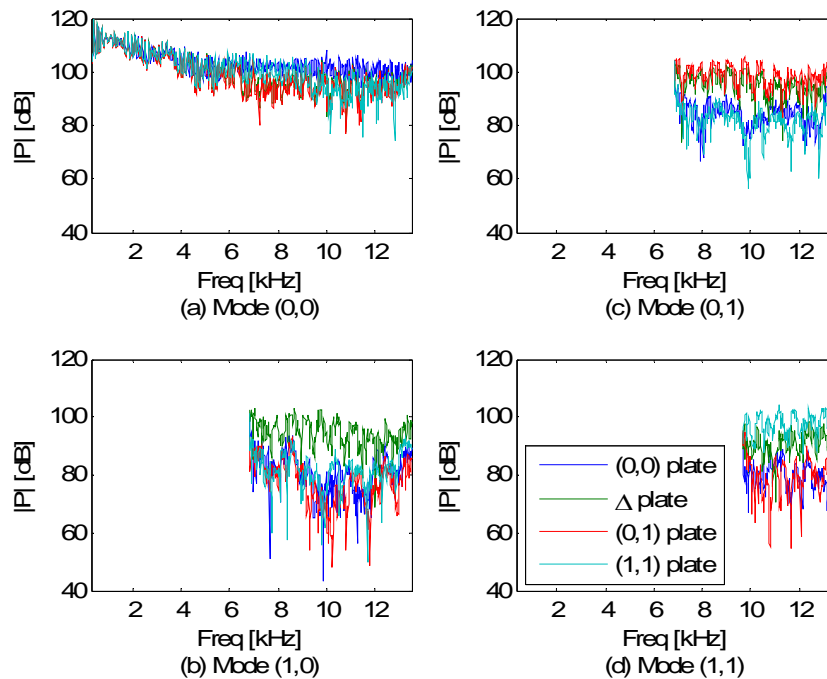


Figure 5-37: Incident pressure field for the MDM for the rigid termination.

unreliable. To confirm this conclusion, the measurement should be repeated with a different spacing between the microphone groups.

The magnitude and phase of the reflection coefficients are shown in Figure 5-40 along with results from both TMM measurements. The estimate of the plane wave

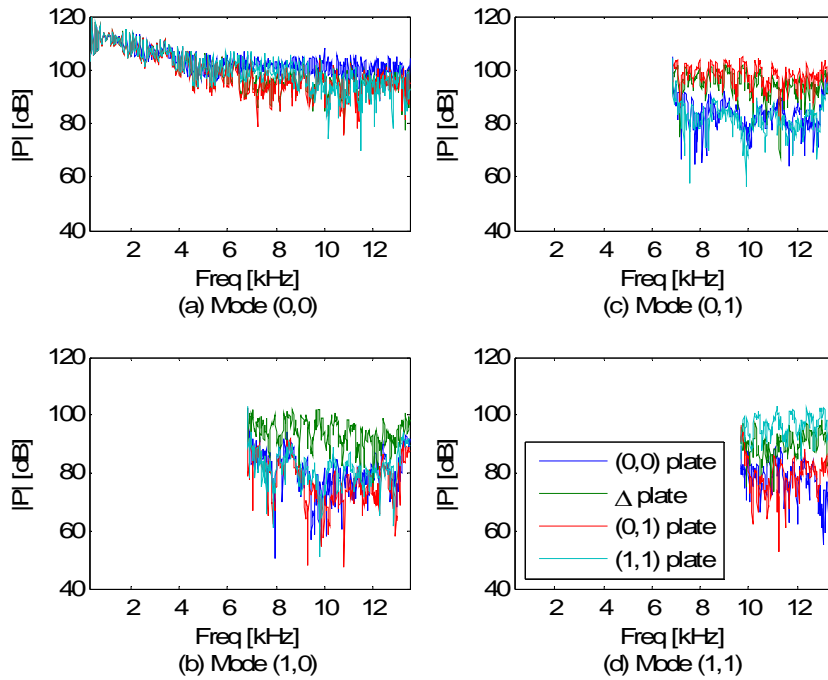


Figure 5-38: Reflected pressure field for the MDM for the rigid termination.

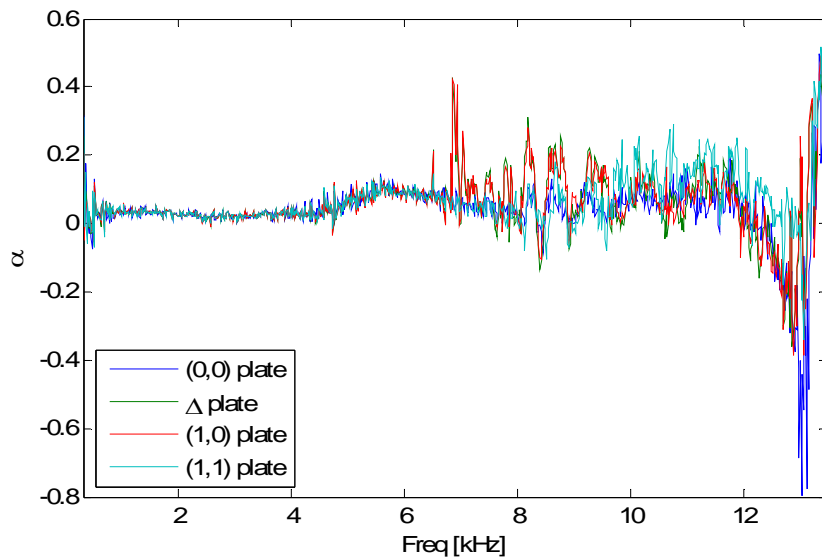


Figure 5-39: Power absorption coefficient for the rigid termination for the MDM.

reflection coefficient provided by the MDM agrees with the TMM in the large waveguide to within its 95% confidence interval estimates, which are not shown in the figures for clarity. The figure also shows that the estimate of the plane wave reflection coefficient by the MDM is affected by the same singularity that affects the high frequency TMM at 13.5 kHz. The reduction in the magnitude of the reflection coefficient estimated by the high frequency TMM is easily seen to be greater than in either the standard TMM or the MDM in Figure 5-40. This suggests issues with either the small waveguide or the specimen. Figure 5-41 shows the SWR for the plane wave mode. The approximate SWR is 40 *dB* and the drop in the SWR around 5 kHz is reduced. Figure 5-42 through Figure 5-45 show the mode scattering coefficients estimated by the MDM. The magnitude of the mode scattering coefficients is less than 0.2 for all frequencies, except for the frequencies near the (1,1) mode cut-on or for coefficients going into the plane wave mode near 13.5 kHz. Both of these exceptions are unreliable due to either the cut-on phenomenon or the microphone spacing issue. The figures also show that there is no dominant mode of scatter, unlike the CT65 or CT73 specimens.

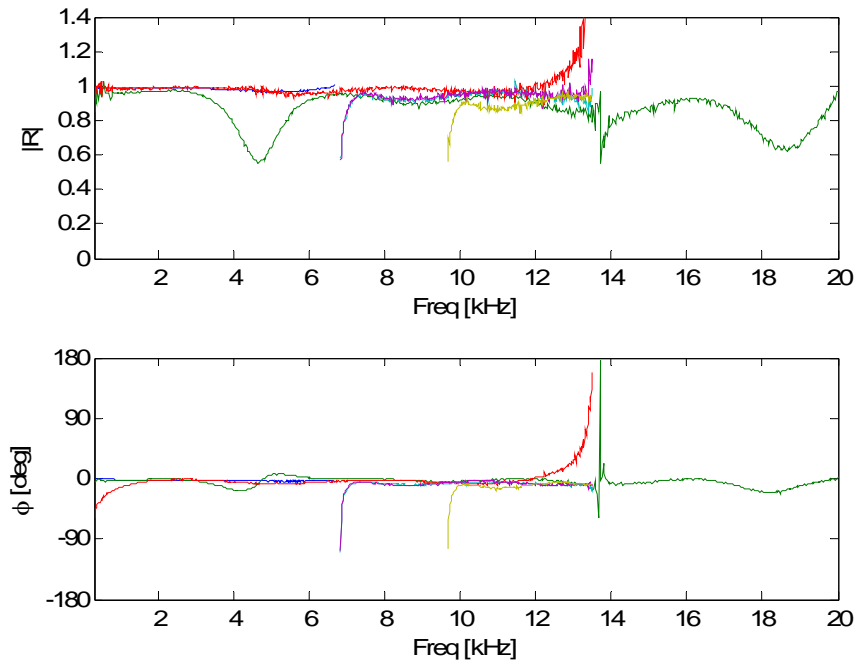


Figure 5-40: Comparison of the reflection coefficient estimates for the rigid termination via all three methods. — TMM, — high frequency TMM, — MDM (0,0) mode, — MDM (1,0) mode, — MDM (0,1) mode, and — MDM (1,1) mode.

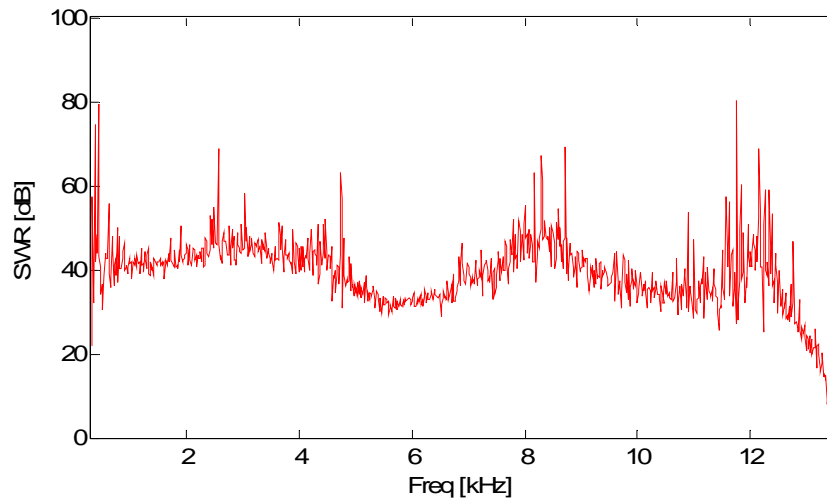


Figure 5-41: SWR for the rigid termination calculated from the MDM.

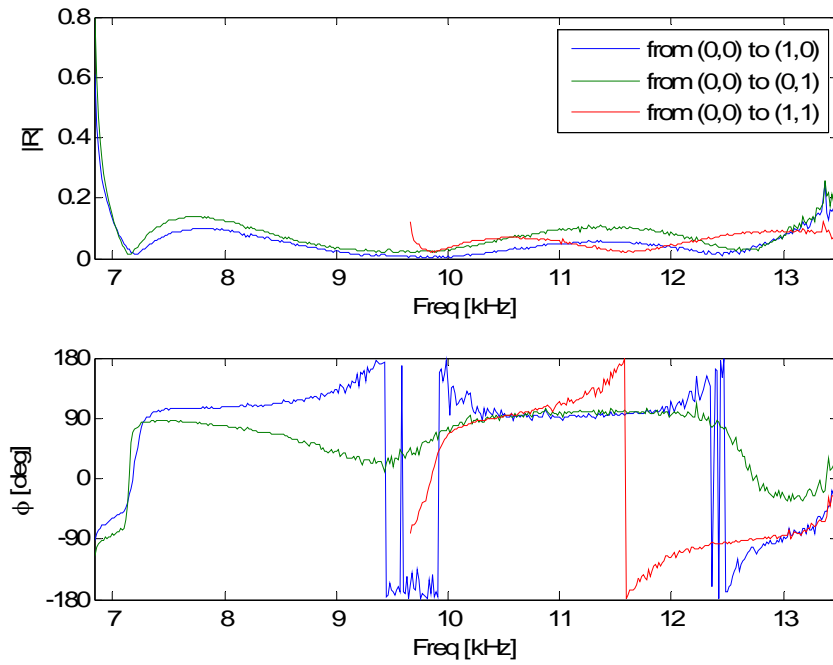


Figure 5-42: Mode scattering coefficients for rigid termination from the (0,0) mode to the other propagating modes.

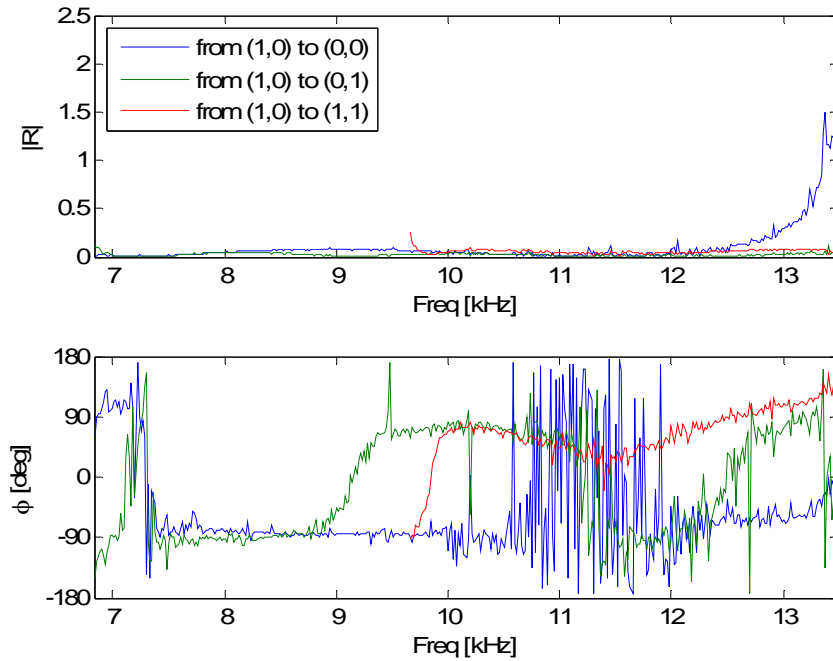


Figure 5-43: Mode scattering coefficients for rigid termination from the (1,0) mode to the other propagating modes.

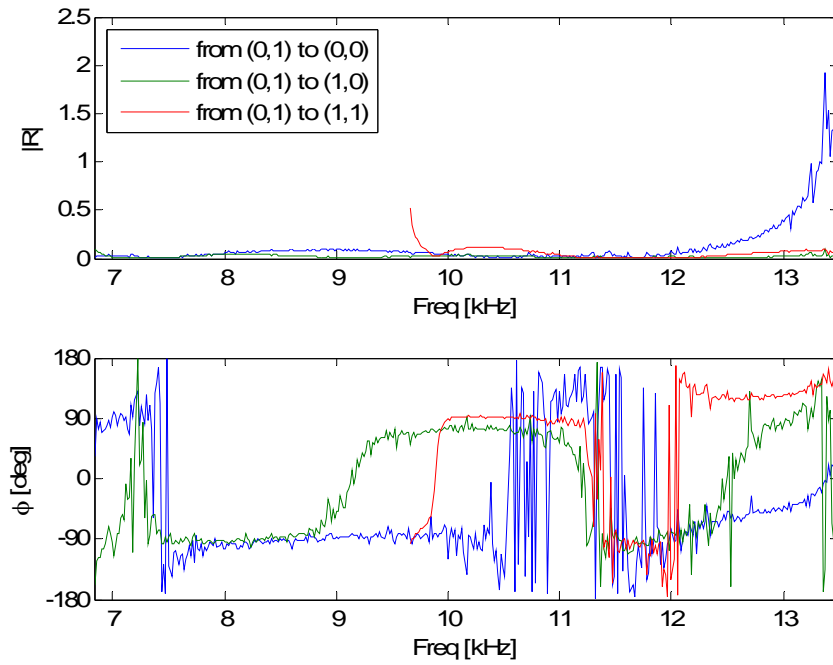


Figure 5-44: Mode scattering coefficients for rigid termination from the (0,1) mode to the other propagating modes.

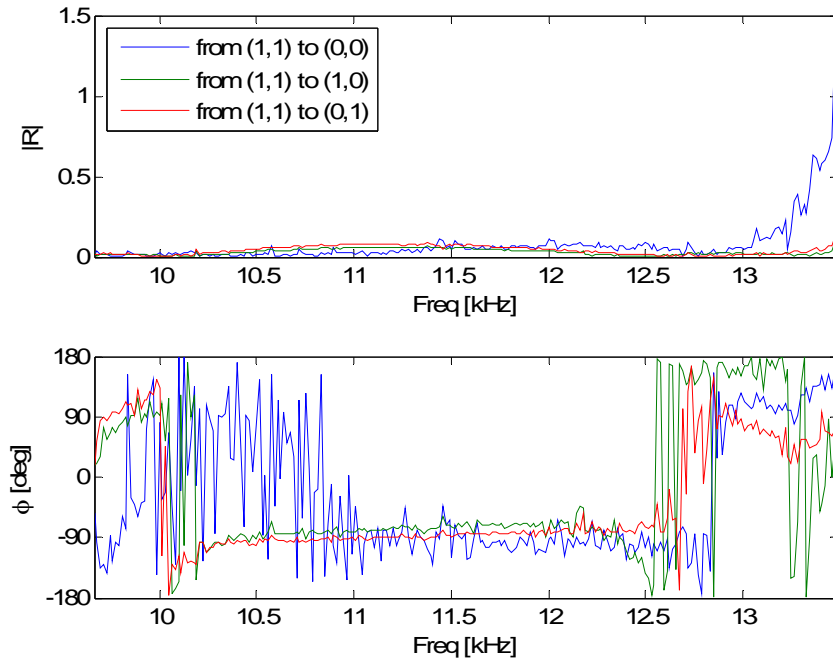


Figure 5-45: Mode scattering coefficients for rigid termination from the (1,1) mode to the other propagating modes.

5.4 SDOF Liner

The next specimen tested is a single degree-of-freedom liner donated from Pratt and Whitney Aircraft. The specimen is constructed of perforate face sheet adhered to a metal honeycomb substructure with an atypical pattern, all backed by a rigid plate. The specimen material is shown in Figure 5-46 with the perforate sheet removed. The perforate face sheet is 0.5 mm thick with 1.3 mm-diameter holes that cover approximately 7.3% of the surface. The circular holes are set in a 60° staggered pattern with a distance of 4.6 mm between the centers of two holes. The honeycomb cells have an area of approximately 108 mm², with a height of 19 mm. The maximum cross-sectional dimension of the honeycomb is approximately 20 mm. This dimension is larger than the length of a side of the small waveguide, therefore this material cannot be tested up to 20 kHz using the high frequency TMM. This demonstrates the need to increase the frequency range of acoustic impedance testing while maintaining a usable specimen size, and thus the results presented in this section are for only the standard TMM and the MDM.

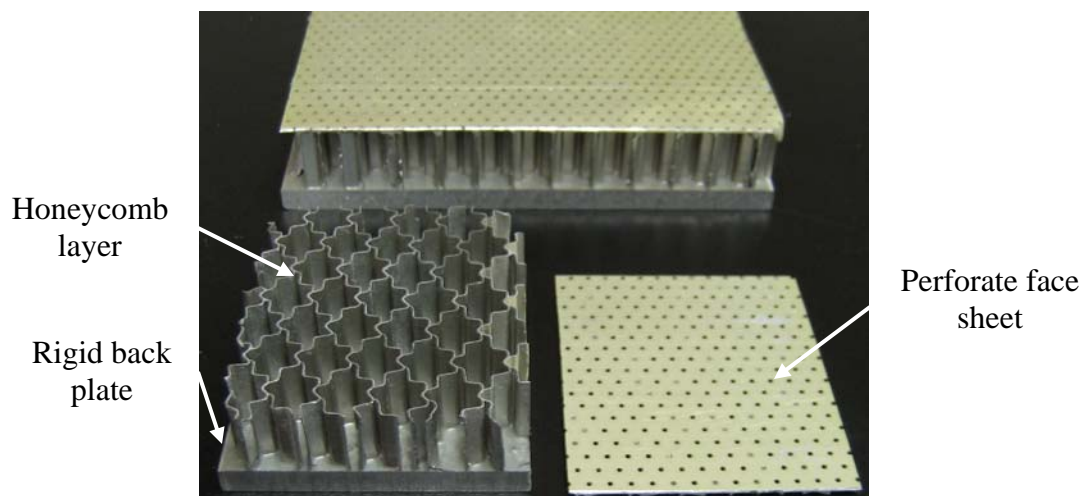


Figure 5-46: SDOF liner showing the irregular honeycomb and perforated face sheet.

5.4.1 TMM Results

The results from the standard TMM are presented in Figure 5-47 for the reflection coefficient and Figure 5-48 for the normalized specific acoustic impedance, both with uncertainty estimates. The graphs for the coherence and the FRF are given in Appendix F. The coherence between the two microphones for the original and switched positions shows decreases at three small frequency ranges. The frequency ranges are 1.1-1.5, 3.6-3.9, and 5.2-5.4 kHz, but the coherence remains above 0.82 for the entire bandwidth of the measurement. The uncertainty estimates of the magnitude of the reflection coefficient show an overall increase with frequency. The results for the estimates of the reflection coefficient, the normalized specific acoustic impedance, and confidence intervals are jagged. The magnitude of the reflection coefficient also shows a gradual decrease in the range of 0.3 to 2.2 kHz to a minimum value of approximately 0.4. Afterwards, the magnitude of the reflection coefficient gradually increases to approach unity. At the minimum value in the magnitude, the phase of the reflection coefficient goes through a 360 degree phase wrap. Also, at approximately 2.3 kHz the reactance passes, through zero indicating a resonance.

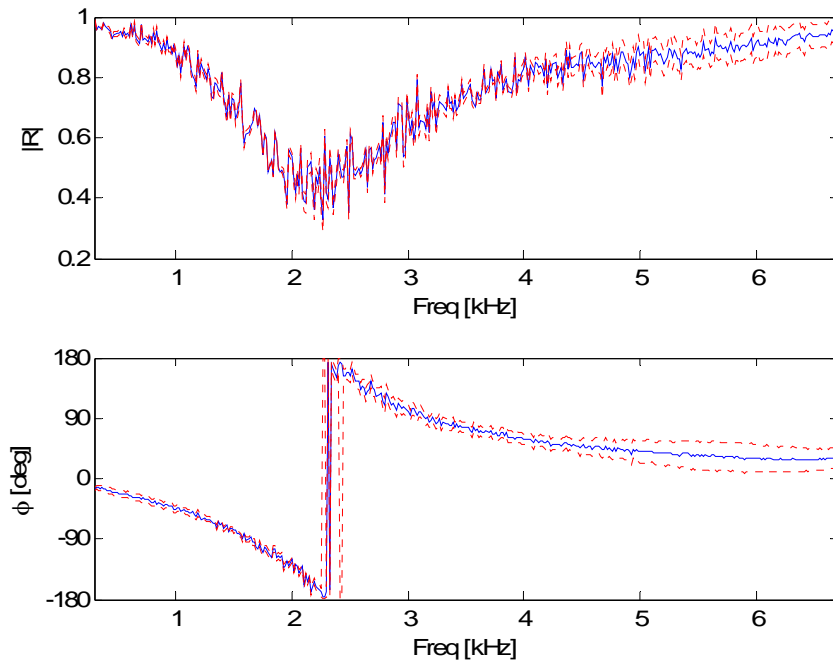


Figure 5-47: Reflection coefficient for the SDOF specimen for the TMM. — Estimated value, - - - Uncertainty estimates.

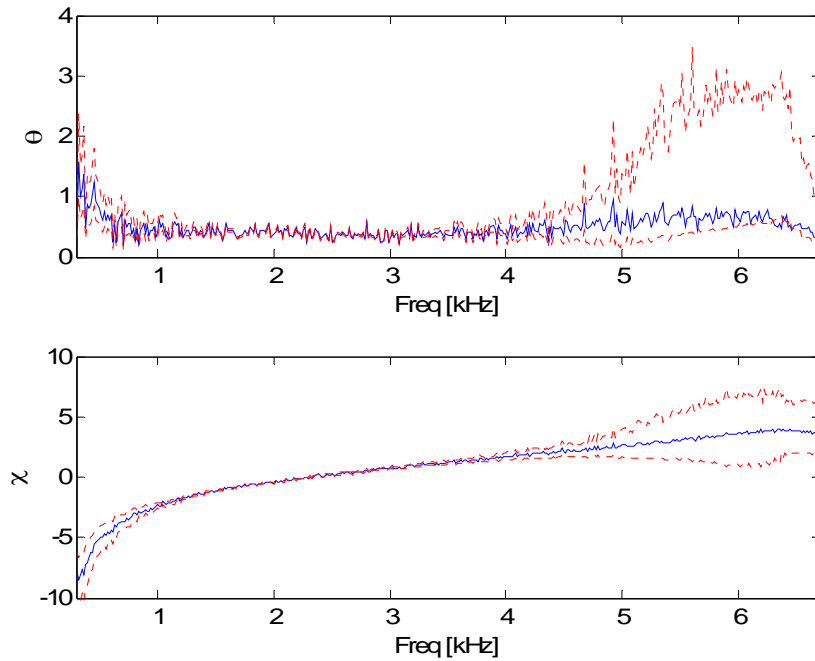


Figure 5-48: Normalized specific acoustic impedance estimates for the SDOF specimen via TMM. — Estimated value, - - - Uncertainty estimates.

5.4.2 MDM Results and Comparison

The standard TMM and the MDM experimental results for the SDOF specimen are compared in this section, but first the MDM results for the incident and reflected pressure fields and the power absorption coefficient are presented. The cut-on frequencies for the higher-order modes are 6.83 kHz for the (1,0) and (0,1) modes, and 9.66 kHz for the (1,1) mode, based on the measured temperature during the MDM measurements. Figure 5-49 shows the incident pressure field measured near the specimen for each of the restrictor plates, and reveals that one of the sources generates a pressure level approximately 5-10 dB higher than the other three sources for the higher-order modes. The exception is for the plane wave mode, where the restrictor plate produces pressure levels only marginally higher than the others. The data for the reflected pressure fields for each of the restrictor plates are presented in Figure 5-50, and this figure shows less evidence of mode scattering than the previous specimens, since there is a significant difference in pressure amplitude of each for the sources, as shown in the incident pressure field.

The absorption coefficient is shown in Figure 5-51 for all four restrictor plates. The data show that the total power absorbed is almost independent on the modal content of the acoustic field for this specimen, since the absorption coefficient does not vary much between the sources after the cut-on frequency for the first higher-order mode. The data also confirms the experimental setup and measurement, since the computed value for the absorption coefficient remains bounded between zero and unity, except at the known singularity at 13.5 kHz, where the data are unreliable.

The magnitude and argument of the reflection coefficients are shown in Figure 5-52 along with results from both TMM measurements. Unlike the other specimens, the estimate of the plane wave reflection coefficient provided by the MDM does not agree

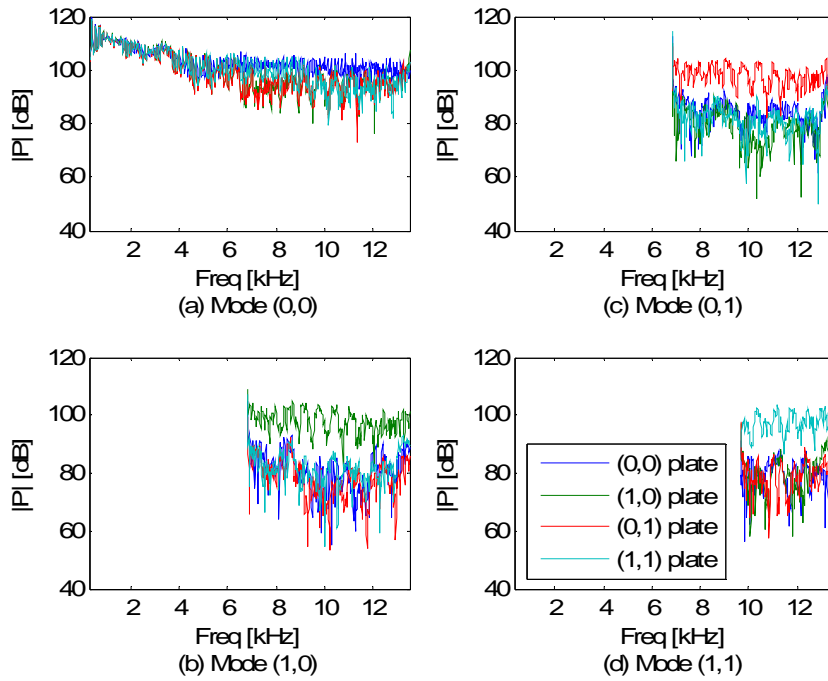


Figure 5-49: Incident pressure field for the MDM for the SDOF specimen.

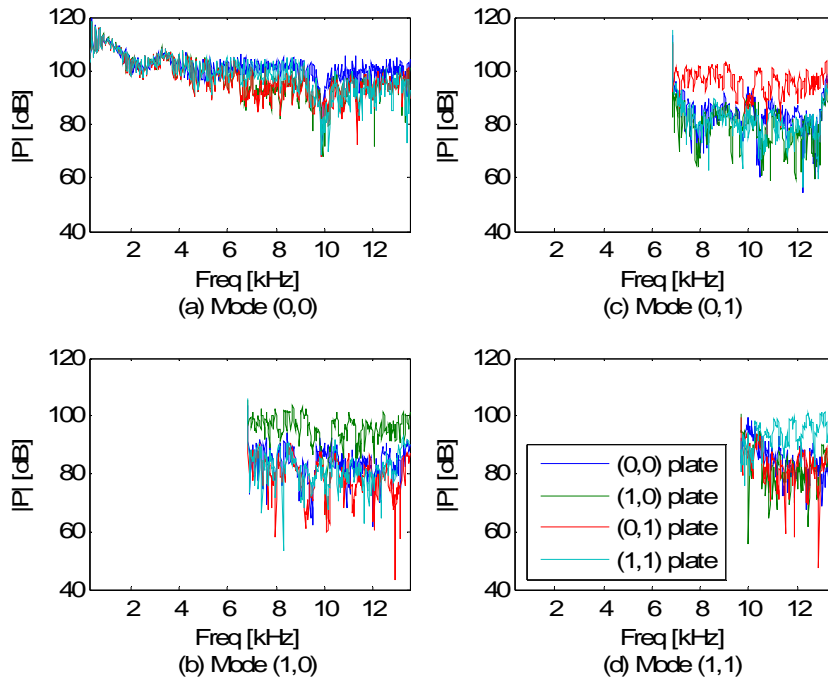


Figure 5-50: Reflected pressure field for the MDM for the SDOF specimen.

with the TMM to within its 95% confidence interval estimates, even though there appears to be a good agreement in the figures. The estimate via the MDM is just outside the edge of the confidence interval for the TMM the majority of the frequency range. The data only agree to within confidence intervals of the standard TMM results after approximately 4 kHz. The figure also shows that the estimate of the plane wave reflection coefficient by the MDM is affected by the same singularity that affects the high frequency TMM at 13.5 kHz. Figure 5-53 through Figure 5-56 show the mode scattering coefficients estimated by the MDM. The magnitude of the mode scattering coefficients is less than 0.2 for all frequencies, except around 10 kHz for the plane wave mode scattering into the (1,1) mode. Unreliable results are also present around 13.5 kHz, as discussed before.

The results for the acoustic impedance ratio are shown in Figure 5-57, and Figure 5-58 shows the normalized specific acoustic impedance. The test specimen is assumed to be a locally reactive material and thus the transmission angle is assumed to be normal to the surface. The MDM results show an anti-resonance at approximately 9 kHz that is missed by the standard TMM because of the limited frequency range. This demonstrates the benefit of the MDM over the standard TMM. As with the reflection coefficient results, the results of the acoustic impedance ratio and normalized specific acoustic impedance do not agree with each other for the two methods until after 4 kHz. This suggests that test conditions, such as the mounting of the specimen, may have varied in between tests. As for verifying the locally reactive assumption, the agreement between the results for the normalized specific acoustic impedance between the different modes is reasonable. The greatest difference in values is at the peak of the anti-resonance.

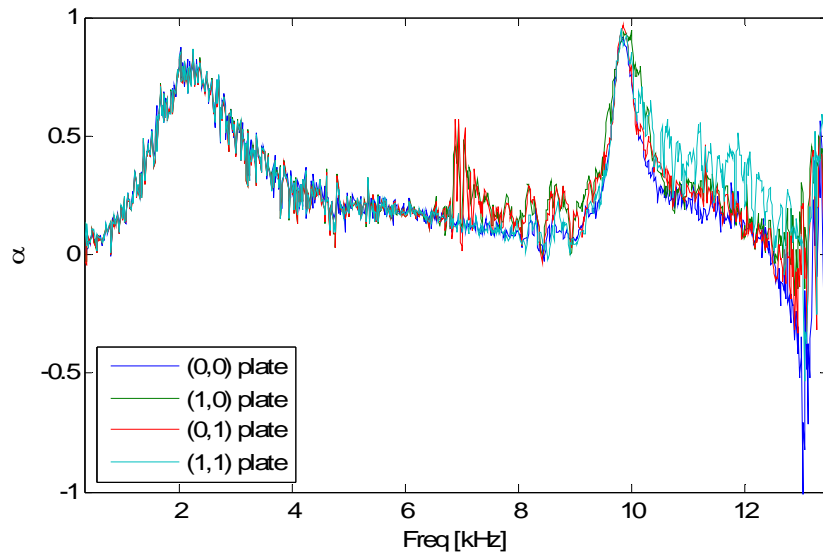


Figure 5-51: Power absorption coefficient for the SDOF specimen for the MDM.

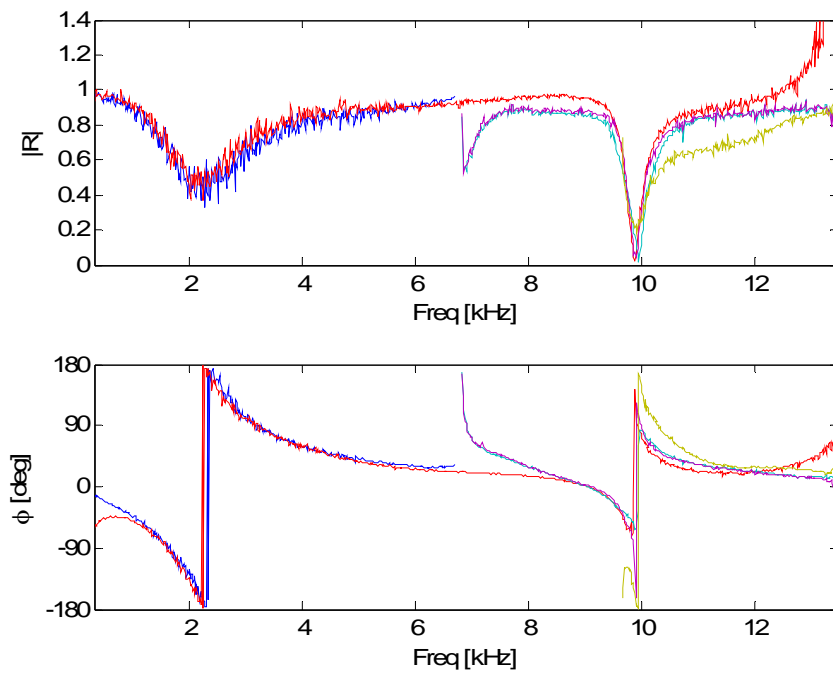


Figure 5-52: Comparison of the reflection coefficient estimates for the SDOF specimen via the TMM and MDM. — TMM, — MDM (0,0) mode, — MDM (1,0) mode, — MDM (0,1) mode, and — MDM (1,1) mode.

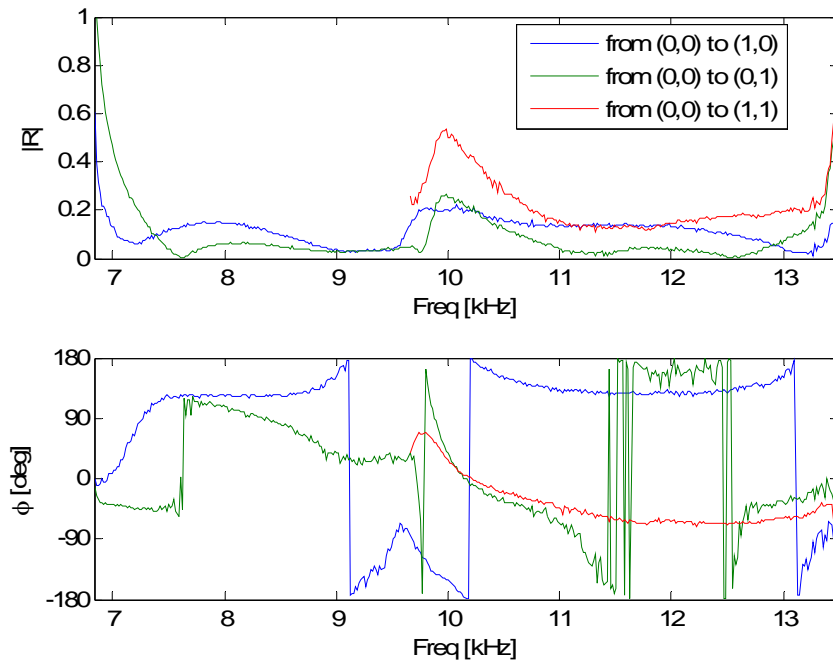


Figure 5-53: Mode scattering coefficients for SDOF specimen from the (0,0) mode to the other propagating modes.

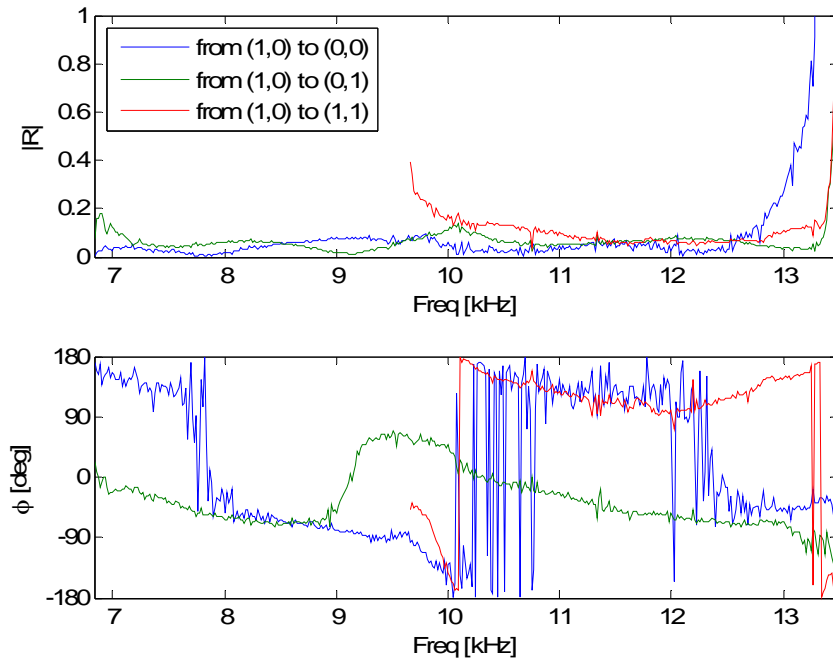


Figure 5-54: Mode scattering coefficients for SDOF specimen from the (1,0) mode to the other propagating modes.

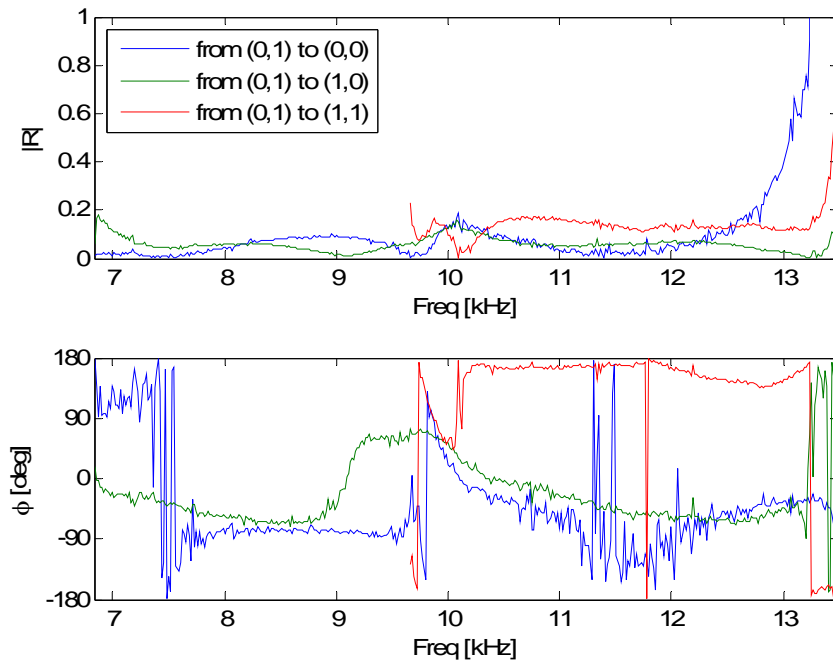


Figure 5-55: Mode scattering coefficients for SDOF specimen from the (0,1) mode to the other propagating modes.

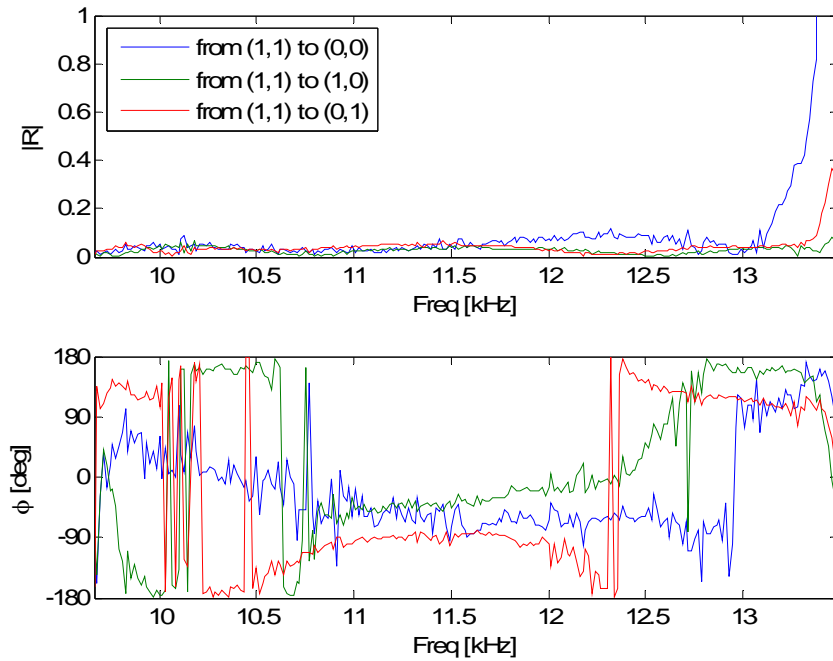


Figure 5-56: Mode scattering coefficients for SDOF specimen from the (1,1) mode to the other propagating modes.

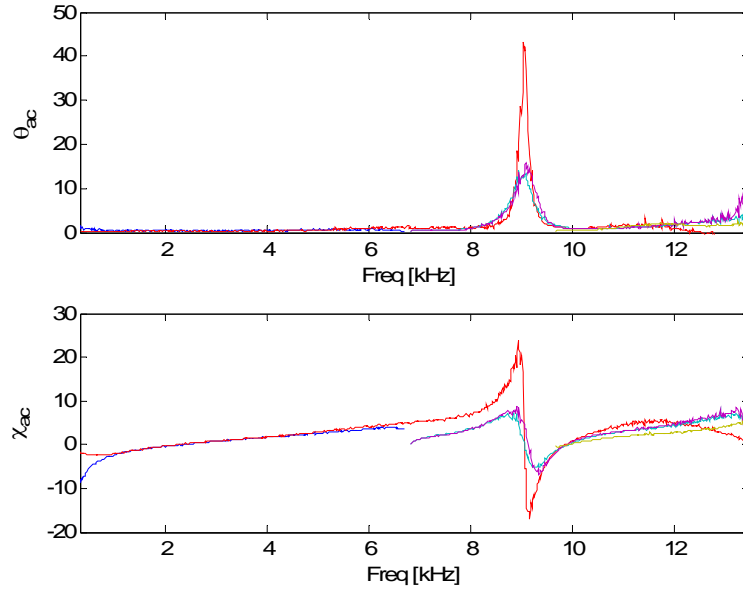


Figure 5-57: Comparison of the acoustic impedance ratio estimates for the SDOF specimen via the TMM and MDM. — TMM, — MDM (0,0) mode, — MDM (1,0) mode, — MDM (0,1) mode, and — MDM (1,1) mode.

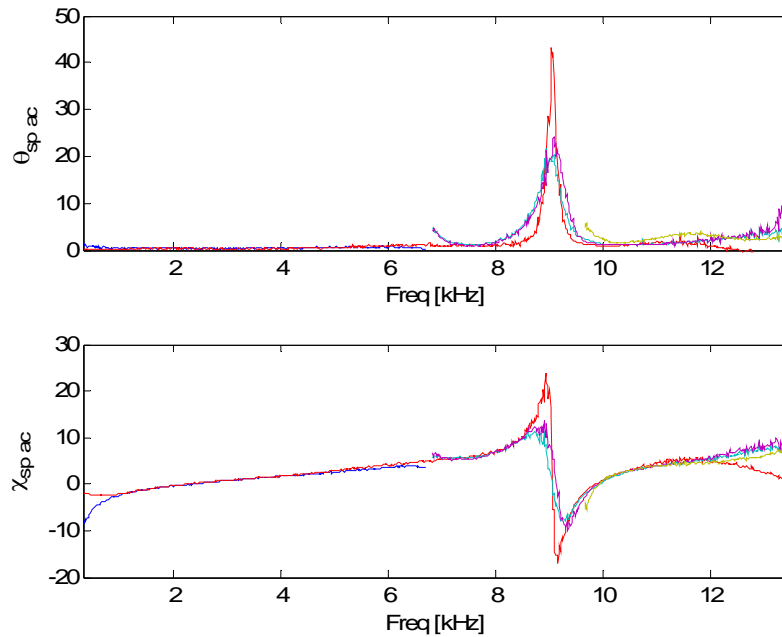


Figure 5-58: Comparison of the normalized specific acoustic impedance estimates for the SDOF specimen via the TMM and MDM. — TMM, — MDM (0,0) mode, — MDM (1,0) mode, — MDM (0,1) mode, and — MDM (1,1) mode.

5.5 Mode Scattering Specimen

The specimen measured is a specimen designed to promote mode scattering into the (1,1) mode. The specimen is constructed of 38.1 mm thick aluminum (type 6061-T6) with 25.4 mm-deep square holes drilled out in two of the four quadrants, similar to the (1,1) restrictor plate. The two holes are then filled with Nomex, an acoustic absorption material, to present the propagating waves with a contrast of acoustic impedance. The specimen is shown in Figure 5-59. Since the purpose of this specimen is to scatter modal energy, only the MDM is used to measure the acoustic properties.



Figure 5-59: Photograph of the mode scattering specimen.

5.5.1 MDM Results

The MDM results for the incident and reflected pressure fields and the power absorption coefficient are presented. The cut-on frequencies for the higher-order modes are 6.83 kHz for the (1,0) and (0,1) modes, and 9.66 kHz for the (1,1) mode, based on the measured temperature during the MDM measurements. Figure 5-60 shows the incident pressure field measured near the specimen for each of the restrictor plates, and reveals that one of the sources generates a pressure level approximately 5-10 dB higher than the other three sources for the higher-order modes. The exception is the plane wave mode, where the restrictor plate produces pressure levels only marginally higher than the others.

The data for the reflected pressure field for each of the restrictor plates are presented in Figure 5-61, and this figure shows evidence of mode scattering, since there is no longer the same difference between the pressure amplitude of each of the sources as shown in the incident pressure field, but there is a noticeable difference between the (1,0) and (0,1) restrictor plates and the other two restrictor plates for the (1,0) and (0,1) modes. Also, the amplitude of the (1,1) mode for all the restrictor plates has increased compared to the incident pressure amplitude, most noticeably for the (0,0) restrictor plate. This offers evidence that the specimen is scattering predominantly into the desired (1,1) mode.

The absorption coefficient is shown in Figure 5-62 for all four restrictor plates. The data show that the total power absorbed is dependent on the modal content of the acoustic field, especially after the (1,1) mode cuts on. The absorption coefficient for the (0,0) restrictor plate falls dramatically after 9.5 kHz and remains lower than the other values. The energy from the (0,0) restrictor plate is not efficiently being absorbed and this helps to justify physically the increase in the reflection pressure amplitudes seen in Figure 5-61.

The magnitude and argument of the reflection coefficients are shown in Figure 5-63. The results show that the highest magnitude for the reflection coefficient is for the plane wave mode, but these results only show the same mode reflections, which this specimen is not designed to maximize. The results of the phase of the reflection coefficients show that the wave is mostly reflected back in-phase, much like a sound-hard termination. The figure also shows that the estimate of the plane wave reflection coefficient by the MDM is affected by the same singularity that affects the high

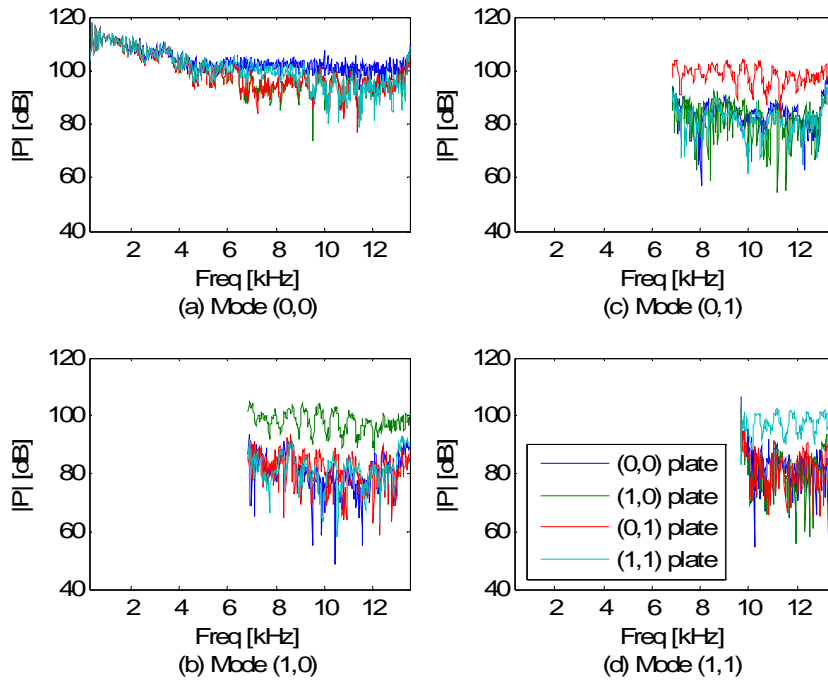


Figure 5-60: Incident pressure field for the MDM for the mode scattering specimen.

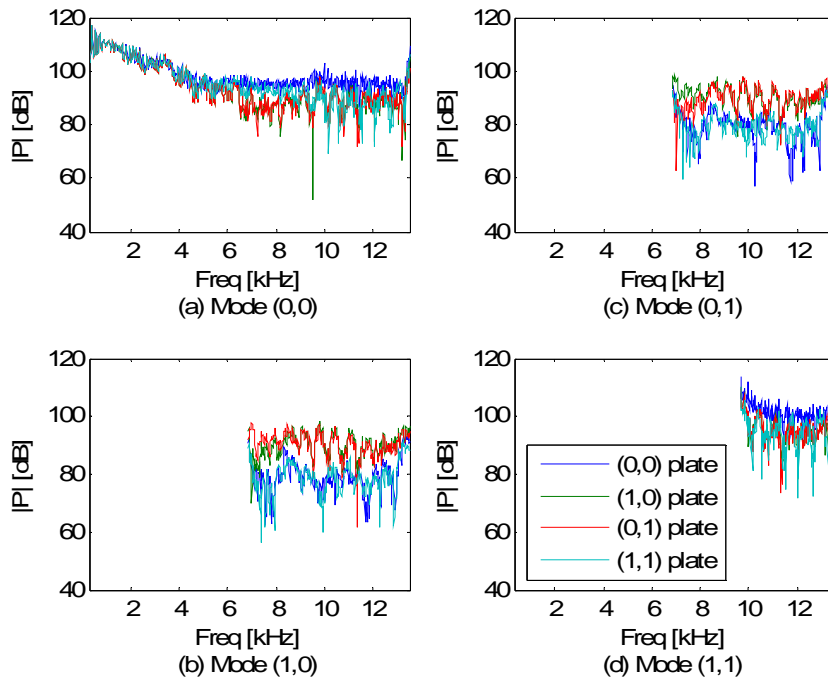


Figure 5-61: Reflected pressure field for the MDM for the mode scattering specimen.

frequency TMM at 13.5 kHz. Figure 5-64 through Figure 5-67 show the mode scattering coefficients estimated by the MDM. The largest magnitude for the mode scattering coefficients is for the plane wave mode scattering into the (1,1) mode, with a value of unity or greater. Physically, this is showing that the specimen is promoting the conversion of energy from the (0,0) mode into the (1,1) mode, as the design of the specimen is intended to do. There is also significant mode scattering between the (1,0) and (0,1) modes, with a value of 0.4 and almost no phase change. The results still show the unreliable estimates due to either the cut-on phenomenon or the microphone spacing issue, as explained before.

The results for the acoustic impedance ratio are shown in Figure 5-68, and Figure 5-69 shows the normalized specific acoustic impedance. The results for the normalized acoustic impedance show resonance at 8.6 and 12.4 kHz and anti-resonance at 9.6 and 13.4 kHz. The last values for the resonance and anti-resonance are unreliable because of the microphone spacing issue at 13.5 kHz. Actually, the resonances and anti-resonances may not exist at all, since the MDM is derived for a constant acoustic impedance

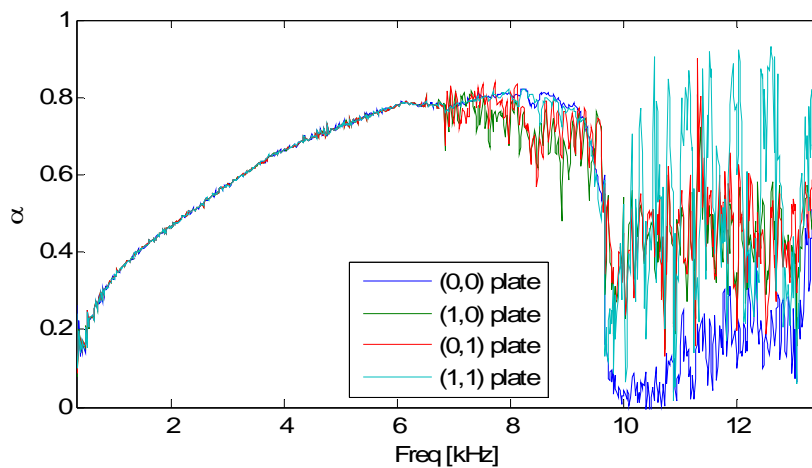


Figure 5-62: Power absorption coefficient for the mode scattering specimen for the MDM.

termination mounted to the waveguide. The displayed values in Figure 5-68 and in Figure 5-69 represent an averaged value of the acoustic impedances. The results for the normalized specific acoustic impedance show that the locally reactive assumption is not valid for this specimen. There are large differences between the estimates for the various modes.

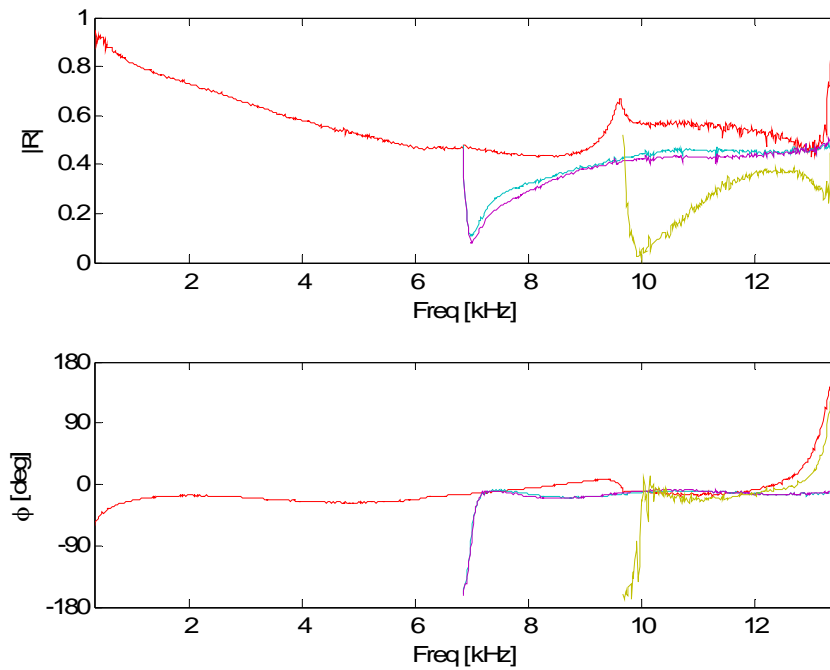


Figure 5-63: Comparison of the reflection coefficient estimates for the mode scattering specimen via the MDM. — MDM (0,0) mode, — MDM (1,0) mode, — MDM (0,1) mode, and — MDM (1,1) mode.

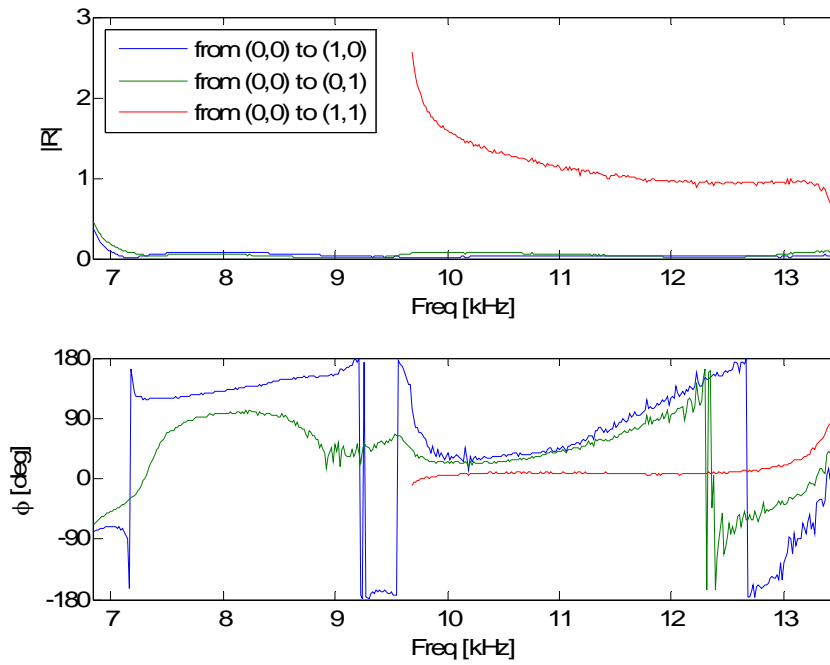


Figure 5-64: Mode scattering coefficients for the mode scattering specimen from the (0,0) mode to the other propagating modes.

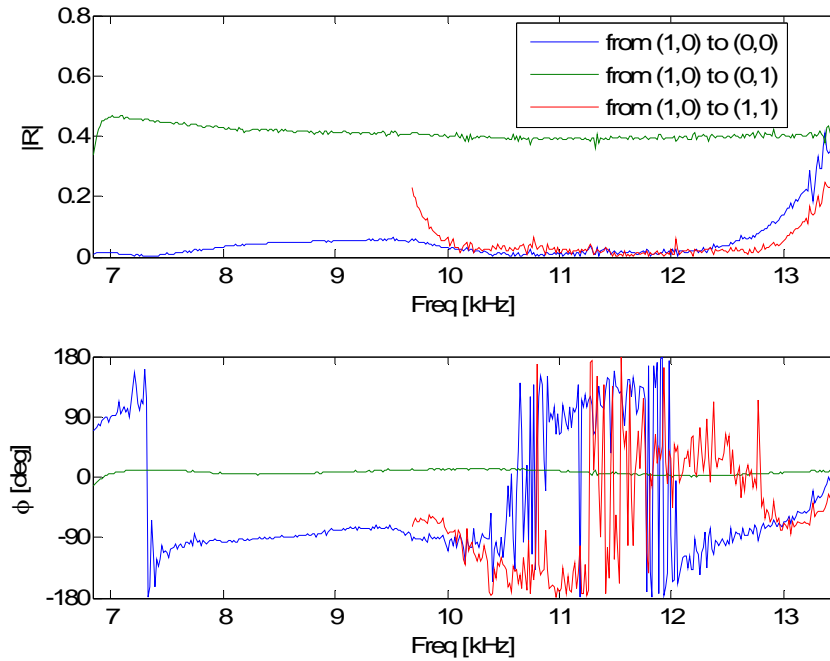


Figure 5-65: Mode scattering coefficients for the mode scattering specimen from the (1,0) mode to the other propagating modes.

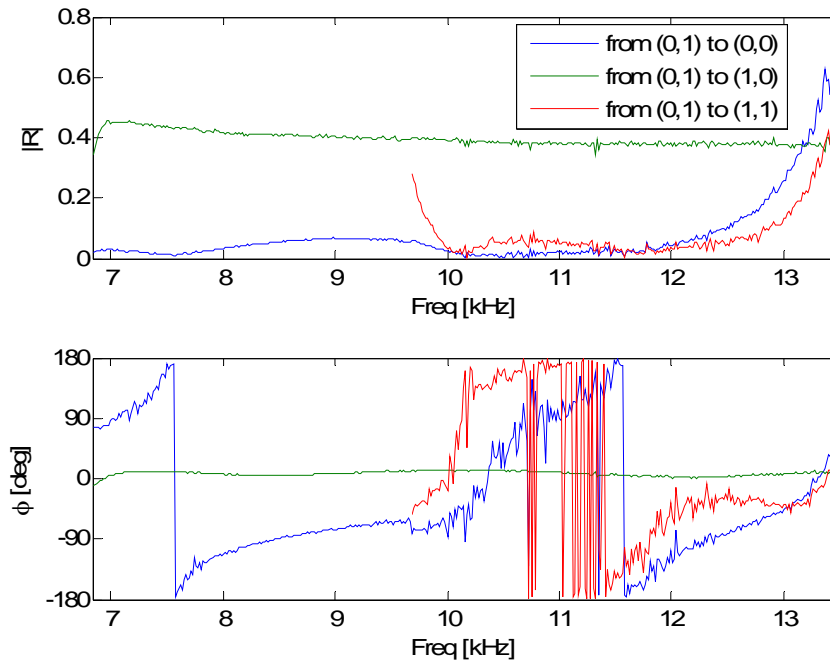


Figure 5-66: Mode scattering coefficients for the mode scattering specimen from the (0,1) mode to the other propagating modes.

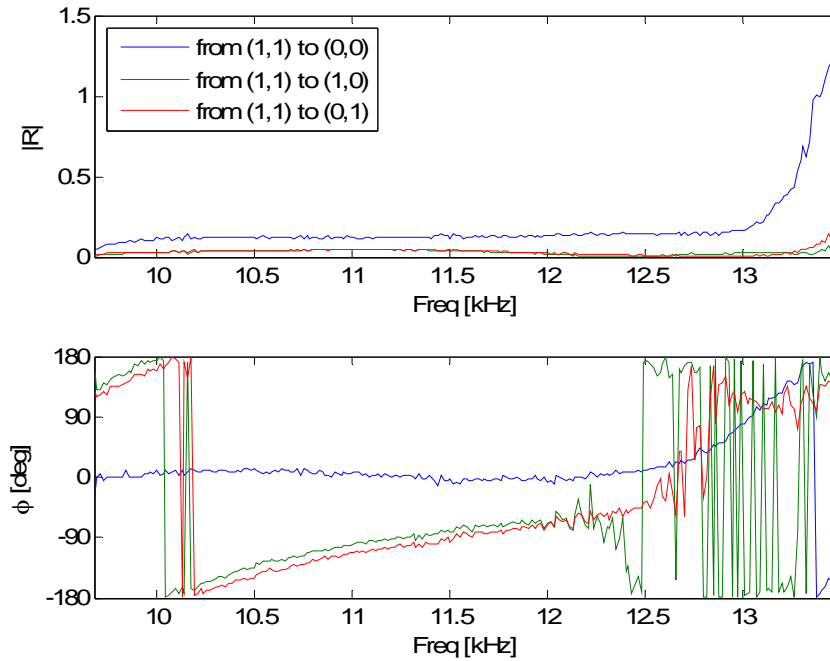


Figure 5-67: Mode scattering coefficients for the mode scattering specimen from the (1,1) mode to the other propagating modes.

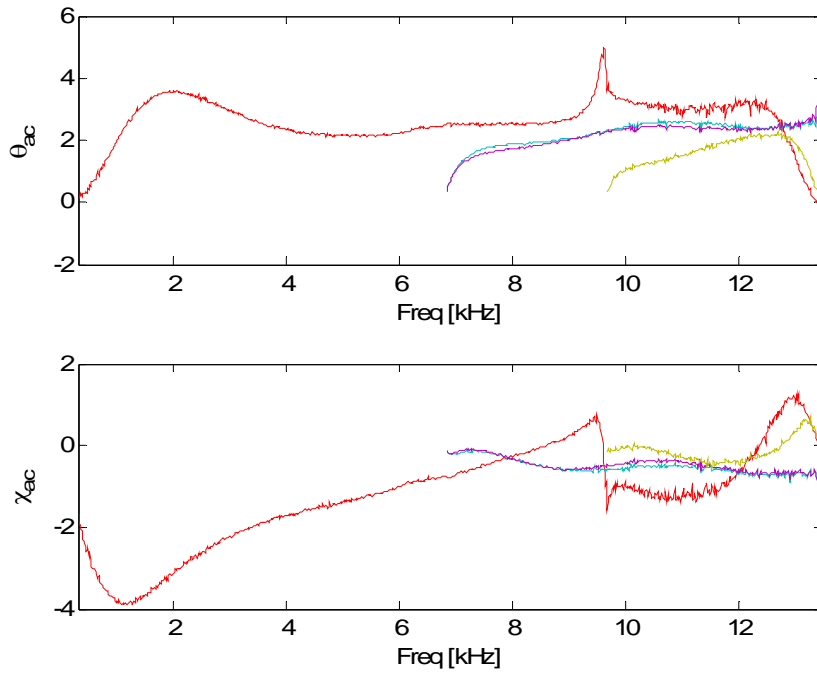


Figure 5-68: Comparison of the acoustic impedance ratio estimates for the mode scattering specimen via the MDM. — MDM (0,0) mode, — MDM (1,0) mode, — MDM (0,1) mode, and — MDM (1,1) mode.

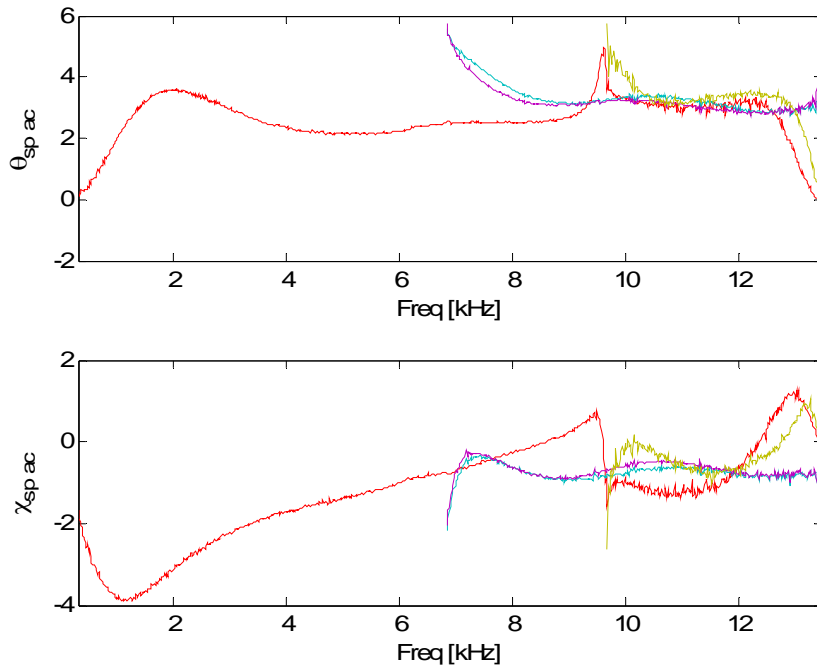


Figure 5-69: Comparison of the normalized specific acoustic impedance estimates for the mode scattering specimen via the MDM. — MDM (0,0) mode, — MDM (1,0) mode, — MDM (0,1) mode, and — MDM (1,1) mode.

CHAPTER 6 CONCLUSIONS AND FUTURE WORK

This chapter summarizes the work presented in this dissertation. The technologies developed have been successful in estimating the accuracy of existing acoustic impedance measurement techniques and in extending the bandwidth of normal incident acoustic impedance testing. Conclusions and potential paths for future work are discussed for the two major impact areas: the TMM uncertainty analysis and the MDM.

6.1 TMM Uncertainty Analysis

This dissertation demonstrated the multivariate uncertainty technique on the TMM for acoustic impedance testing compared to Monte Carlo methods. When all of the component uncertainties are very small ($= 1\%$) or the specimen is sound-hard, the multivariate method matches the results from Monte Carlo method. When the component uncertainties assume values typical of current experimental configurations, they are large enough to violate the linear assumption. Hence, the perturbations caused on the output are nonlinear and also distort the output probability distribution from Gaussian behavior. The distortion of the output probability distribution is thus a function of the acoustic impedance of the specimen itself. The actual probability density function is estimated numerically from Monte Carlo simulations and is integrated to accurately estimate the uncertainty with realistic nonlinear perturbations. This tends to increase the complexity of the uncertainty analysis program and requires more computation time than the multivariate method. This method was demonstrated and applied to experimental data for four material specimens: CT65, CT73, a rigid termination, and a SDOF liner.

The Monte Carlo results demonstrated the potential for asymmetric uncertainty estimates and the general Monte Carlo is recommended as the method for accurate uncertainty estimates.

The main contribution of this research is thus a verified systematic framework to estimate frequency-dependent uncertainties in the complex reflection and normalized acoustic impedance using a multivariate approach and a Monte Carlo approach. Presumably, this tool will be useful to assess the suitability of candidate acoustic liner materials. Future improvements to the uncertainty analysis can include changing the uncertainty estimation program to compute the uncertainty of the unwrapped phase, increasing the number of Monte Carlo iterations, and increasing the number of discrete bins used to approximate the probability density function. Increasing the number of iterations will increase the demand on computer resources and will exceed those available on a typical desktop computer. Also, multiple microphone spacings should be used to avoid the troublesome singularity that occurs when $ks = n\pi$, when the spacing is equal to a half wavelength. This singularity was demonstrated to have a large impact on the results in the data from the high frequency TMM. To improve the accuracy of the computed acoustic impedance, the uncertainty in the locations of the microphones and the uncertainty in the measure of the temperature should be improved, along with a rigorous investigation of the periodic structures in the uncertainty estimates for the reflection coefficients for specimens CT65 and CT73. Understanding the conditions at the minimums in the uncertainty estimates could lead to reducing the sensitivity of the estimated reflection coefficient and acoustic impedance values to the uncertainty in the input quantities. The accuracy of the microphone locations can be improved by using a

method that measures the locations of the microphones installed in the waveguide and accounts for the acoustic centers (Katz 2000). For the high frequency TMM, spatial averaging of the microphone measurements may present an error source that can be reduced with probe tips attached to the microphones (Franzoni and Elliott 1998) or by using microphones with a smaller diameter, such as MEMS-based microphones (Arnold et al. 2003). The uncertainty estimates from the TMM in the small waveguide showed large confidence intervals in the data starting at approximately 12 kHz. The results also demonstrated the difficulties of creating a termination that could accurately represent a sound-hard boundary. Improvements in the reflection coefficient might be attainable through the development of an improved mounting system for the specimen and the microphones. Other improvement may include the use of probe tips on the microphones to reduce the effects of spatial averaging, especially for the high frequency TMM.

The comparison between the data for the small waveguide and the large waveguide demonstrated that the specimen size can impacted the estimated acoustic impedance values. For the same material, the two measurements did not agree with each other to within the uncertainty estimates possibly due to local variations in the material. In order to definitively define the local variation in the materials, a statistical number (>10) of different specimens of a single material type should be tested in both waveguides. Then the statistical analysis of the estimated acoustic impedance values for a given waveguide can be used to characterize the local variations in the material and the averaged values can be compared between the two waveguides.

6.2 Modal Decomposition Method

The MDM offers the ability to extend the bandwidth of acoustic impedance testing by accommodating the propagation of higher-order modes and maintaining a larger

specimen size to avoid sample size effects. This also gives the ability to obtain acoustic impedance data at oblique angles of incidence, with the primary drawback being increased complexity as compared to the TMM. A direct MDM procedure was developed for a square duct using the first four modes. This dissertation restricted the maximum number of propagating modes to four for a proof-of-concept demonstration. The routines presented can easily be expanded to handle more propagating modes through the addition of measurement microphones. As the bandwidth of the MDM is increased, spatial averaging of the microphone measurements may present an error source that can be reduced with probe tips attached to the microphones (Franzoni and Elliott 1998) or by using microphones with a smaller diameter, such as MEMS-based microphones (Arnold, Nishida, Cattafesta and Sheplak 2003). Also, diffraction effects of the sound scattering off the protective grids of the microphones can introduce error (Underbrink 2002). To achieve the 20 kHz bandwidth goal for the 25.4 mm-square waveguide, modes up to and including the (2,2) mode must be accounted for. This requires 18 microphone measurements in order to resolve the nine propagating modes, and will require nine independent source conditions. The additional microphones could be placed at new axial locations around the perimeter of the waveguide. The additional axial locations will also help in reducing the effects of the singularity when the existing spacing equals a half wavelength. The additional source conditions could be created with additional restrictor plates. The routines can also be applied to rectangular and cylindrical ducts through substitution of the correct transverse factor, but a square duct was chosen because geometry allows for the largest cross-section for a given cut-on

frequency for the first higher-order mode and allows for the microphones to be easily flush-mounted to the duct walls.

The results presented show that the MDM can accurately resolve the sound field inside the waveguide and decompose the modal coefficients, except near the cut-on frequencies, and provide estimates for the complete reflection coefficient matrix. The MDM results were consistent with the TMM in the large waveguide results to within the 95% confidence interval estimates for the TMM results, except for the SDOF specimen. To fully characterize the MDM, uncertainty estimates are needed along with results of repeated testing on existing specimens. The comparison should also be conducted with other testing facilities, such as the NASA Langley Research Center. The inclusion of the uncertainty estimates would allow for statements to be made about the equality of the estimates of the specific acoustic impedance for the different modes, and thus would allow for statements about the validity of the locally reactive assumption. Another goal of future work should focus on extending the frequency range of the MDM up to approximately 20 kHz, as is desired for aeroacoustic testing.

APPENDIX A VISCOTHERMAL LOSSES

The propagation of sound in a real fluid involves a loss in amplitude due to viscosity and heat transfer within the fluid and surroundings. In many cases, the absorption of sound in the bulk fluid can be neglected, especially for a bounded domain where the bulk losses are small compared to the boundary layer losses (Kirchhoff 1869; Weston 1953; Tijdeman 1975; Blackstock 2000). An example of such a case is the propagation of an acoustic wave within a pipe or duct that has a characteristic length of its cross-section larger than the boundary layer thickness but an area not so large that the mainstream bulk losses are important. Quantitatively, this restriction can be written as (Blackstock 2000)

$$\delta \ll \frac{L}{2} \ll \frac{c_0^2}{\omega^2 \delta}, \quad (\text{A.1})$$

where δ is the viscous boundary layer thickness and L is the hydraulic diameter. The two rectangular waveguides described in this dissertation satisfy this condition for the bandwidth of plane waves. Under this restriction, the acoustic flow can be separated and treated as two distinct regions. Thus the attenuation of the amplitude of the sound can be found by solving fluid dynamic equations in the boundary layer and using the velocity and temperature profiles to estimate a wall shear stress and a heat flux. The wall shear stress and heat flux are then used as sinks for momentum and energy in the derivation of the fluid dynamic equations for the mainstream. Also, since the boundary layers are small compared to the hydraulic diameter and only occupy a small percentage of the

cross-sectional area, the duct boundary can be unwrapped and the problem treated as a two dimensional problem with an axial and a transverse coordinate.

First, the geometry and boundary conditions are presented to define the problem to be solved. Then the Navier-Stokes equations are presented and nondimensionalized to determine the important parameters governing the solution. The velocity and temperature profiles are then found for the boundary layer and the wall shear stress and heat flux are computed. The wall shear stress and heat flux are used to derive the fluid dynamic equations for the mainstream, which are then used to estimate the axial attenuation of the amplitude of the sound wave propagating down the duct.

A.1 Nondimensionalization and Linearization of the Navier-Stokes Equations

The problem to solve is a purely oscillating flow of a thermally and calorically perfect gas over a flat plate, as shown in Figure A-1. The problem is assumed to be two-dimensional, with constant thermodynamic transport properties, and governed by the Navier-Stokes equations, neglecting bulk viscosity and molecular relaxation. The conservation equations are

$$\frac{\partial \rho}{\partial t} + \frac{\partial(\rho u)}{\partial x} + \frac{\partial(\rho v)}{\partial y} = 0, \quad (\text{A.2})$$

$$\rho \frac{\partial u}{\partial t} + \rho u \frac{\partial u}{\partial x} + \rho v \frac{\partial u}{\partial y} = -\frac{\partial p}{\partial x} + \mu \left(\frac{\partial^2 u}{\partial x^2} + \frac{\partial^2 u}{\partial y^2} \right) + \frac{\mu}{3} \frac{\partial}{\partial x} \left(\frac{\partial u}{\partial x} + \frac{\partial v}{\partial y} \right), \quad (\text{A.3})$$

$$\rho \frac{\partial v}{\partial t} + \rho u \frac{\partial v}{\partial x} + \rho v \frac{\partial v}{\partial y} = -\frac{\partial p}{\partial y} + \mu \left(\frac{\partial^2 v}{\partial x^2} + \frac{\partial^2 v}{\partial y^2} \right) + \frac{\mu}{3} \frac{\partial}{\partial y} \left(\frac{\partial u}{\partial x} + \frac{\partial v}{\partial y} \right), \quad (\text{A.4})$$

$$\rho c_p \left(\frac{\partial T}{\partial t} + u \frac{\partial T}{\partial x} + v \frac{\partial T}{\partial y} \right) = \kappa \left(\frac{\partial^2 T}{\partial x^2} + \frac{\partial^2 T}{\partial y^2} \right) + \frac{\partial p}{\partial t} + u \frac{\partial p}{\partial x} + v \frac{\partial p}{\partial y} + \Phi, \quad (\text{A.5})$$

and

$$p = \rho R_{gas} T, \quad (A.6)$$

where ρ is the density, u, v are the flow velocities in the x, y -directions respectively, p is the pressure, T is the temperature, μ is the dynamic viscosity, Φ is the nonlinear viscous dissipation function, c_p is the specific heat at constant pressure, and R_{gas} is the idea gas constant for the fluid, in most cases air. Other thermodynamic relations that will come in handy are

$$c_0^2 = \gamma R_{gas} T = \gamma \frac{P_0}{\rho_0}, \quad (A.7)$$

and

$$R_{gas} = c_v (\gamma - 1), \quad (A.8)$$

where $\gamma = c_p / c_v$ is the ratio of specific heats, c_v is the specific heat at constant volume and the $()_0$ subscript references the mean isentropic condition.

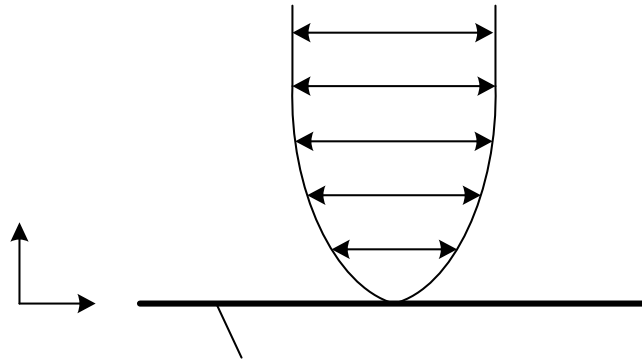


Figure A-1: Oscillating flow over a flat plate.

Now the appropriate scales must be chosen to nondimensionalize the dependent and independent variables of the governing equations. Also, at this stage the dependent variables will be decomposed into a mean and a perturbation. The appropriate time scale for this problem is $1/\omega$, where ω is the angular frequency, since the flow is oscillatory.

The oscillatory nature of the flow provides an the length scale for the x -direction as c_0/ω . The length scale for the y -direction should be representative of the cross-section and given by the hydraulic diameter, $L = 4A/l_{perimeter}$, and allow the nondimensionalization to apply to an arbitrary cross-section. The dependent variables are nondimensionalized by their mean isentropic state and are assumed to be decomposed into a mean and a perturbation. The flow velocity components are only composed of a perturbation and therefore are nondimensionalized by the isentropic speed of sound. Thus, the new nondimensional variables are

$$t = \frac{t^*}{\omega}, \quad (\text{A.9})$$

$$x = \frac{c_0}{\omega} x^*, \quad (\text{A.10})$$

$$y = Ly^*, \quad (\text{A.11})$$

$$p = p_0(1 + p^*), \quad (\text{A.12})$$

$$\rho = \rho_0(1 + \rho^*), \quad (\text{A.13})$$

$$T = T_0(1 + T^*) \quad (\text{A.14})$$

$$u = c_0 u^*, \quad (\text{A.15})$$

and

$$v = c_0 v^*. \quad (\text{A.16})$$

When Equations (A.9)-(A.16) are substituted into the governing equations, Equations (A.2)-(A.6), the perturbations of the dependent variables are to be assumed small such that the resulting equations can be linearized.

A.1.1 Continuity

Beginning with the continuity equation, Equation (A.2) is transformed as follows:

$$\frac{\partial(\rho_0(1+\rho^*))}{\partial\left(\frac{t^*}{\omega}\right)} + \frac{\partial(\rho_0(1+\rho^*)c_0u^*)}{\partial\left(\frac{c_0}{\omega}x^*\right)} + \frac{\partial(\rho_0(1+\rho^*)c_0v^*)}{\partial(Ly^*)} = 0,$$

$$\rho_0\omega\frac{\partial(\rho^*)}{\partial t^*} + \frac{\omega}{c_0}\rho_0c_0\frac{\partial(u^* + \rho^*u^*)}{\partial x^*} + \frac{\rho_0c_0}{L}\frac{\partial(v^* + \rho^*v^*)}{\partial y^*} = 0.$$

Now, neglecting the higher-order terms and dividing by $\rho_0\omega$,

$$\frac{\partial\rho^*}{\partial t^*} + \frac{\partial u^*}{\partial x^*} + \frac{c_0}{\omega L}\frac{\partial v^*}{\partial y^*} = 0.$$

Substituting the definition of the wavenumber, $k = \omega/c_0$, the nondimensionalized continuity equation becomes

$$\frac{\partial\rho^*}{\partial t^*} + \frac{\partial u^*}{\partial x^*} + \frac{1}{kL}\frac{\partial v^*}{\partial y^*} = 0. \quad (\text{A.17})$$

A.1.2 x -direction Momentum Equation

The x -direction momentum equation, Equation (A.3), is nondimensionalized as follows:

$$\begin{aligned} & \rho_0(1+\rho^*)\frac{\partial(c_0u^*)}{\partial\left(\frac{t^*}{\omega}\right)} + \rho_0(1+\rho^*)c_0u^*\frac{\partial(c_0u^*)}{\partial\left(\frac{c_0}{\omega}x^*\right)} + \rho_0(1+\rho^*)c_0v^*\frac{\partial(c_0u^*)}{\partial(Ly^*)} \\ &= -\frac{\partial(p_0(1+p^*))}{\partial\left(\frac{c_0}{\omega}x^*\right)} + \mu\left[\frac{\partial^2(c_0u^*)}{\partial\left(\frac{c_0}{\omega}x^*\right)^2} + \frac{\partial^2(c_0u^*)}{\partial(Ly^*)^2}\right] + \frac{\mu}{3}\frac{\partial}{\partial\left(\frac{c_0}{\omega}x^*\right)}\left[\frac{\partial(c_0u^*)}{\partial\left(\frac{c_0}{\omega}x^*\right)} + \frac{\partial(c_0v^*)}{\partial(Ly^*)}\right]. \end{aligned}$$

Simplifying and neglecting the higher-order terms,

$$\rho_0 c_0 \omega \frac{\partial u^*}{\partial t^*} = -\frac{\omega}{c_0} p_0 \frac{\partial p^*}{\partial x^*} + \mu \left(c_0 \left(\frac{\omega}{c_0} \right)^2 \frac{\partial^2 u^*}{\partial x^{*2}} + \frac{c_0}{L^2} \frac{\partial^2 u^*}{\partial y^{*2}} \right) + \frac{\mu \omega}{3 c_0} \frac{\partial}{\partial x^*} \left(c_0 \frac{\omega}{c_0} \frac{\partial u^*}{\partial x^*} + \frac{c_0}{L} \frac{\partial v^*}{\partial y^*} \right).$$

Simplifying and recalling the definition of the wavenumber,

$$\rho_0 c_0 \omega \frac{\partial u^*}{\partial t^*} = -\frac{\omega}{c_0} p_0 \frac{\partial p^*}{\partial x^*} + \mu \frac{c_0}{L^2} \left((kL)^2 \frac{\partial^2 u^*}{\partial x^{*2}} + \frac{\partial^2 u^*}{\partial y^{*2}} \right) + \frac{\mu \omega}{3 L} \frac{\partial}{\partial x^*} \left(kL \frac{\partial u^*}{\partial x^*} + \frac{\partial v^*}{\partial y^*} \right).$$

Now divide the equation by $\rho_0 c_0 \omega$ to get

$$\frac{\partial u^*}{\partial t^*} = -\frac{p_0}{\rho_0 c_0^2} \frac{\partial p^*}{\partial x^*} + \frac{\nu}{\omega L^2} \left((kL)^2 \frac{\partial^2 u^*}{\partial x^{*2}} + \frac{\partial^2 u^*}{\partial y^{*2}} \right) + \frac{1}{3} \frac{\nu}{c_0 \omega} \frac{\omega}{L} \frac{\partial}{\partial x^*} \left(kL \frac{\partial u^*}{\partial x^*} + \frac{\partial v^*}{\partial y^*} \right),$$

$$\frac{\partial u^*}{\partial t^*} = -\frac{p_0}{\rho_0 c_0^2} \frac{\partial p^*}{\partial x^*} + \frac{\nu}{\omega L^2} \left((kL)^2 \frac{\partial^2 u^*}{\partial x^{*2}} + \frac{\partial^2 u^*}{\partial y^{*2}} \right) + \frac{1}{3} \left(\frac{\nu}{\omega L^2} \right) \left(\frac{\omega}{c_0} L \right) \frac{\partial}{\partial x^*} \left(kL \frac{\partial u^*}{\partial x^*} + \frac{\partial v^*}{\partial y^*} \right),$$

where ν is the kinematic viscosity. The Stokes number, $S = \sqrt{\omega L^2 / \nu}$, can be recognized

and the expression simplified farther with the help of Equation (A.7) when solved for p_0

to achieve

$$\frac{\partial u^*}{\partial t^*} = -\frac{\rho_0 c_0^2}{\gamma} \frac{\partial p^*}{\partial x^*} + \frac{1}{S^2} \left((kL)^2 \frac{\partial^2 u^*}{\partial x^{*2}} + \frac{\partial^2 u^*}{\partial y^{*2}} \right) + \frac{1}{3} \frac{1}{S^2} kL \frac{\partial}{\partial x^*} \left(kL \frac{\partial u^*}{\partial x^*} + \frac{\partial v^*}{\partial y^*} \right),$$

or finally,

$$\frac{\partial u^*}{\partial t^*} = -\frac{1}{\gamma} \frac{\partial p^*}{\partial x^*} + \frac{1}{S^2} \left((kL)^2 \frac{\partial^2 u^*}{\partial x^{*2}} + \frac{\partial^2 u^*}{\partial y^{*2}} \right) + \frac{1}{3} \frac{1}{S^2} (kL)^2 \frac{\partial}{\partial x^*} \left(\frac{\partial u^*}{\partial x^*} + \frac{1}{kL} \frac{\partial v^*}{\partial y^*} \right). \quad (\text{A.18})$$

A.1.3 y-direction Momentum Equation

The y-direction momentum equation, Equation (A.4), is nondimensionalized as

follows:

$$\begin{aligned} & \rho_0(1+\rho^*) \frac{\partial(c_0 v^*)}{\partial\left(\frac{t^*}{\omega}\right)} + \rho_0(1+\rho^*)c_0 u^* \frac{\partial(c_0 v^*)}{\partial\left(\frac{c_0}{\omega} x^*\right)} + \rho_0(1+\rho^*)c_0 v^* \frac{\partial(c_0 v^*)}{\partial(Ly^*)} \\ &= -\frac{\partial(p_0(1+p^*))}{\partial(Ly^*)} + \mu \left(\frac{\partial^2(c_0 v^*)}{\partial\left(\frac{c_0}{\omega} x^*\right)^2} + \frac{\partial^2(c_0 v^*)}{\partial(Ly^*)^2} \right) + \frac{\mu}{3} \frac{\partial}{\partial(Ly^*)} \left(\frac{\partial(c_0 u^*)}{\partial\left(\frac{c_0}{\omega} x^*\right)} + \frac{\partial(c_0 v^*)}{\partial(Ly^*)} \right). \end{aligned}$$

Simplifying and neglecting higher-order terms,

$$\rho_0 c_0 \omega \frac{\partial v^*}{\partial t^*} = -\frac{p_0}{L} \frac{\partial p^*}{\partial y^*} + \mu \left(c_0 \left(\frac{\omega}{c_0} \right)^2 \frac{\partial^2 v^*}{\partial x^{*2}} + \frac{c_0}{L^2} \frac{\partial^2 v^*}{\partial y^{*2}} \right) + \frac{\mu}{3L} \frac{\partial}{\partial y^*} \left(c_0 \frac{\omega}{c_0} \frac{\partial u^*}{\partial x^*} + \frac{c_0}{L} \frac{\partial v^*}{\partial y^*} \right).$$

Simplifying and recalling the definition of the wavenumber

$$\begin{aligned} \rho_0 c_0 \omega \frac{\partial v^*}{\partial t^*} &= -\frac{p_0}{L} \frac{\partial p^*}{\partial y^*} + \mu \frac{c_0}{L^2} \left(\left(\frac{\omega}{c_0} L \right)^2 \frac{\partial^2 v^*}{\partial x^{*2}} + \frac{\partial^2 v^*}{\partial y^{*2}} \right) + \frac{\mu c_0}{3L} \frac{\partial}{\partial y^*} \left(\frac{\omega}{c_0} L \frac{\partial u^*}{\partial x^*} + \frac{\partial v^*}{\partial y^*} \right), \\ \rho_0 c_0 \omega \frac{\partial v^*}{\partial t^*} &= -\frac{p_0}{L} \frac{\partial p^*}{\partial y^*} + \mu \frac{c_0}{L^2} \left((kL)^2 \frac{\partial^2 v^*}{\partial x^{*2}} + \frac{\partial^2 v^*}{\partial y^{*2}} \right) + \frac{\mu c_0}{3L^2} \frac{\partial}{\partial y^*} \left(kL \frac{\partial u^*}{\partial x^*} + \frac{\partial v^*}{\partial y^*} \right). \end{aligned}$$

Now, dividing the equation by $\rho_0 c_0 \omega$ and recalling the definition of the Stokes number,

$$\begin{aligned} \frac{\partial v^*}{\partial t^*} &= -\frac{p_0}{\rho_0 c_0 \omega L} \frac{\partial p^*}{\partial y^*} + \mu \frac{c_0}{\rho_0 c_0 \omega L^2} \left((kL)^2 \frac{\partial^2 v^*}{\partial x^{*2}} + \frac{\partial^2 v^*}{\partial y^{*2}} \right) + \frac{\mu c_0}{3\rho_0 c_0 \omega L^2} \frac{\partial}{\partial y^*} \left(kL \frac{\partial u^*}{\partial x^*} + \frac{\partial v^*}{\partial y^*} \right), \\ \frac{\partial v^*}{\partial t^*} &= -\frac{p_0}{\rho_0 c_0 \omega L} \frac{\partial p^*}{\partial y^*} + \frac{\nu}{\omega L^2} \left((kL)^2 \frac{\partial^2 v^*}{\partial x^{*2}} + \frac{\partial^2 v^*}{\partial y^{*2}} \right) + \frac{1}{3} \frac{\nu}{\omega L^2} \frac{\partial}{\partial y^*} \left(kL \frac{\partial u^*}{\partial x^*} + \frac{\partial v^*}{\partial y^*} \right), \\ \frac{\partial v^*}{\partial t^*} &= -\frac{p_0}{\rho_0 c_0 \omega L} \frac{\partial p^*}{\partial y^*} + \frac{1}{S^2} \left((kL)^2 \frac{\partial^2 v^*}{\partial x^{*2}} + \frac{\partial^2 v^*}{\partial y^{*2}} \right) + \frac{1}{3} \frac{1}{S^2} \frac{\partial}{\partial y^*} \left(kL \frac{\partial u^*}{\partial x^*} + \frac{\partial v^*}{\partial y^*} \right). \end{aligned}$$

The expression simplified further with the help of Equation (A.7) when solved for p_0 to achieve

$$\frac{\partial v^*}{\partial t^*} = -\frac{\rho_0 c_0^2}{\gamma} \frac{\partial p^*}{\partial y^*} + \frac{1}{S^2} \left((kL)^2 \frac{\partial^2 v^*}{\partial x^{*2}} + \frac{\partial^2 v^*}{\partial y^{*2}} \right) + \frac{1}{3} \frac{1}{S^2} \frac{\partial}{\partial y^*} \left(kL \frac{\partial u^*}{\partial x^*} + \frac{\partial v^*}{\partial y^*} \right),$$

$$\frac{\partial v^*}{\partial t^*} = -\frac{1}{\gamma} \frac{c_0}{\omega L} \frac{\partial p^*}{\partial y^*} + \frac{1}{S^2} \left((kL)^2 \frac{\partial^2 v^*}{\partial x^{*2}} + \frac{\partial^2 v^*}{\partial y^{*2}} \right) + \frac{1}{3} \frac{1}{S^2} \frac{\partial}{\partial y^*} \left(kL \frac{\partial u^*}{\partial x^*} + \frac{\partial v^*}{\partial y^*} \right),$$

or finally

$$\frac{\partial v^*}{\partial t^*} = -\frac{1}{\gamma} \frac{1}{kL} \frac{\partial p^*}{\partial y^*} + \frac{1}{S^2} \left((kL)^2 \frac{\partial^2 v^*}{\partial x^{*2}} + \frac{\partial^2 v^*}{\partial y^{*2}} \right) + \frac{1}{3} \frac{kL}{S^2} \frac{\partial}{\partial y^*} \left(\frac{\partial u^*}{\partial x^*} + \frac{1}{kL} \frac{\partial v^*}{\partial y^*} \right). \quad (\text{A.19})$$

A.1.4 Thermal Energy Equation

The nondimensionalization of the thermal energy equation, Equation (A.5), starts by neglecting the viscous dissipation term. Since the viscous dissipation term is nonlinear, the resulting term after the substitution of Equations (A.12)-(A.16) will be a higher-order term and is therefore neglected as part of the linearization. The remaining steps for the thermal energy equation are as follows:

$$\rho_0 (1 + \rho^*) c_p \left(\frac{\partial (T_0 (1 + T^*))}{\partial \left(\frac{t^*}{\omega} \right)} + c_0 u^* \frac{\partial (T_0 (1 + T^*))}{\partial \left(\frac{c_0}{\omega} x^* \right)} + c_0 v^* \frac{\partial (T_0 (1 + T^*))}{\partial (Ly^*)} \right)$$

$$= \kappa \left(\frac{\partial^2 (T_0 (1 + T^*))}{\partial \left(\frac{c_0}{\omega} x^* \right)^2} + \frac{\partial^2 (T_0 (1 + T^*))}{\partial (Ly^*)^2} \right) + \frac{\partial (p_0 (1 + p^*))}{\partial \left(\frac{t^*}{\omega} \right)} + u \frac{\partial (p_0 (1 + p^*))}{\partial \left(\frac{c_0}{\omega} x^* \right)}$$

$$+ v \frac{\partial (p_0 (1 + p^*))}{\partial (Ly^*)}.$$

Neglecting the higher-order terms and simplifying,

$$\rho_0 T_0 \omega c_p \frac{\partial T^*}{\partial t^*} = \kappa T_0 \left(\left(\frac{\omega}{c_0} \right)^2 \frac{\partial^2 T^*}{\partial x^{*2}} + \frac{1}{L^2} \frac{\partial^2 T^*}{\partial y^{*2}} \right) + \omega p_0 \frac{\partial p^*}{\partial t^*}.$$

Now dividing the expression by $\rho_0 T_0 \omega c_p$,

$$\frac{\partial T^*}{\partial t^*} = \frac{\kappa}{\rho_0 \omega c_p} \left(\left(\frac{\omega}{c_0} \right)^2 \frac{\partial^2 T^*}{\partial x^{*2}} + \frac{1}{L^2} \frac{\partial^2 T^*}{\partial y^{*2}} \right) + \frac{p_0}{\rho_0 T_0 c_p} \frac{\partial p^*}{\partial t^*}.$$

Simplifying,

$$\frac{\partial T^*}{\partial t^*} = \frac{\kappa}{\mu c_p \rho_0 \omega} \frac{\mu}{L^2} \left(\left(\frac{\omega}{c_0} L \right)^2 \frac{\partial^2 T^*}{\partial x^{*2}} + \frac{\partial^2 T^*}{\partial y^{*2}} \right) + \frac{1}{c_p} \frac{p_0}{\rho_0 T_0} \frac{\partial p^*}{\partial t^*},$$

$$\frac{\partial T^*}{\partial t^*} = \frac{\kappa}{\mu c_p} \frac{\nu}{\omega L^2} \left((kL)^2 \frac{\partial^2 T^*}{\partial x^{*2}} + \frac{\partial^2 T^*}{\partial y^{*2}} \right) + \frac{1}{c_p} \frac{p_0}{\rho_0 T_0} \frac{\partial p^*}{\partial t^*}.$$

Now, simplify by recalling the definition of the Prandtl number, $\text{Pr} = \mu c_p / \kappa$, and the

Stokes number and substituting in the equation of state, Equation (A.6), to get

$$\frac{\partial T^*}{\partial t^*} = \frac{1}{\text{Pr} S^2} \left((kL)^2 \frac{\partial^2 T^*}{\partial x^{*2}} + \frac{\partial^2 T^*}{\partial y^{*2}} \right) + \frac{R_{gas}}{c_p} \frac{\partial p^*}{\partial t^*}.$$

Using the thermodynamics relation given in Equation (A.8), the expression can be simplified to

$$\frac{\partial T^*}{\partial t^*} = \frac{1}{\text{Pr} S^2} \left((kL)^2 \frac{\partial^2 T^*}{\partial x^{*2}} + \frac{\partial^2 T^*}{\partial y^{*2}} \right) + \frac{c_v (\gamma - 1)}{c_p} \frac{\partial p^*}{\partial t^*},$$

or finally

$$\frac{\partial T^*}{\partial t^*} = \frac{1}{\text{Pr} S^2} \left((kL)^2 \frac{\partial^2 T^*}{\partial x^{*2}} + \frac{\partial^2 T^*}{\partial y^{*2}} \right) + \frac{\gamma - 1}{\gamma} \frac{\partial p^*}{\partial t^*}. \quad (\text{A.20})$$

A.1.5 Equation of State for an Ideal Gas

The equation of state, Equation (A.6), is nondimensionalized as follows:

$$p_0 (1 + p^*) = \rho_0 (1 + \rho^*) R_{gas} T_0 (1 + T^*).$$

Divide the expression by the equation of state for the isentropic state, $p_0 = \rho_0 R_{gas} T_0$, to

get

$$\frac{p_0(1+p^*)}{p_0} = \frac{\rho_0(1+\rho^*)R_{gas}T_0(1+T^*)}{\rho_0R_{gas}T_0},$$

$$1+p^* = (1+\rho^*)(1+T^*),$$

$$1+p^* = 1+\rho^*+T^*+\rho^*T^*.$$

Finally, neglecting the higher-order terms,

$$p^* = \rho^* + T^*. \quad (\text{A.21})$$

A.1.6 Summary of the Nondimensional, Linearized Equations

The nondimensional, linear equations are summarized below for oscillatory flow over a flat plate assuming a time-harmonic solution. They are

$$\frac{\partial \rho^*}{\partial t^*} + \frac{\partial u^*}{\partial x^*} + \frac{1}{kL} \frac{\partial v^*}{\partial y^*} = 0, \quad (\text{A.22})$$

$$\frac{\partial u^*}{\partial t^*} = -\frac{1}{\gamma} \frac{\partial p^*}{\partial x^*} + \frac{1}{S^2} \left((kL)^2 \frac{\partial^2 u^*}{\partial x^{*2}} + \frac{\partial^2 u^*}{\partial y^{*2}} \right) + \frac{1}{3} \frac{(kL)^2}{S^2} \frac{\partial}{\partial x^*} \left(\frac{\partial u^*}{\partial x^*} + \frac{1}{kL} \frac{\partial v^*}{\partial y^*} \right), \quad (\text{A.23})$$

$$\frac{\partial v^*}{\partial t^*} = -\frac{1}{\gamma} \frac{1}{kL} \frac{\partial p^*}{\partial y^*} + \frac{1}{S^2} \left((kL)^2 \frac{\partial^2 v^*}{\partial x^{*2}} + \frac{\partial^2 v^*}{\partial y^{*2}} \right) + \frac{1}{3} \frac{kL}{S^2} \frac{\partial}{\partial y^*} \left(\frac{\partial u^*}{\partial x^*} + \frac{1}{kL} \frac{\partial v^*}{\partial y^*} \right), \quad (\text{A.24})$$

$$\frac{\partial T^*}{\partial t^*} = \frac{1}{\text{Pr} S^2} \left((kL)^2 \frac{\partial^2 T^*}{\partial x^{*2}} + \frac{\partial^2 T^*}{\partial y^{*2}} \right) + \frac{\gamma-1}{\gamma} \frac{\partial p^*}{\partial t^*}, \quad (\text{A.25})$$

and

$$p^* = \rho^* + T^*. \quad (\text{A.26})$$

A.2 Boundary Layer Solution

The flow in the boundary layer is driven by an oscillating pressure gradient in the mainstream, but the thickness of the boundary layer is assumed to be much smaller than the dimensions of the cross-section. This assumption allows the problem to be reduced to a simple model of oscillating flow over a flat plate, but assuming that the boundary layer thickness is much smaller than the wavelength allows for the assumption of incompressible flow in the boundary layer. With this assumption the driving pressure wave appears to propagate through the boundary layer instantaneously. This simplifies the continuity equation, Equation (A.22), to

$$\frac{\partial u^*}{\partial x^*} + \frac{1}{kL} \frac{\partial v^*}{\partial y^*} = 0. \quad (\text{A.27})$$

The solution in the boundary layer is simplified further by the use of the boundary layer assumption, which states that the changes in the transverse direction are more important than changes along the axial direction. Mathematically, this is represented by

$$\frac{\partial^n}{\partial y^n} \gg \frac{\partial^n}{\partial x^n}, \quad (\text{A.28})$$

and thus the axial derivative can be neglected. Also, the transverse velocity component is assumed much smaller than the axial velocity component, and is thus neglected.

The above assumptions allow the governing equations to be simplified. Equations (A.23)-(A.25) become

$$\frac{\partial u^*}{\partial t^*} = -\frac{1}{\gamma} \frac{\partial p^*}{\partial x^*} + \frac{1}{S^2} \frac{\partial^2 u^*}{\partial y^{*2}}, \quad (\text{A.29})$$

$$0 = -\frac{1}{\gamma} \frac{1}{kL} \frac{\partial p^*}{\partial y^*}, \quad (\text{A.30})$$

and

$$\frac{\partial T^*}{\partial t^*} = \frac{1}{\text{Pr} S^2} \frac{\partial^2 T^*}{\partial y^{*2}} + \frac{\gamma - 1}{\gamma} \frac{\partial p^*}{\partial t^*}. \quad (\text{A.31})$$

Equation (A.30) shows that the pressure field does not vary within the boundary layer and is only a function of the axial coordinate. This is consistent with the assumptions made above, and thus the axial pressure gradient is determined by the mainstream pressure gradient, denoted by p_∞^* , and now is a known parameter with respect to the boundary layer solution. Therefore the problem is reduced to solving

$$\frac{\partial u^*}{\partial t^*} = -\frac{1}{\gamma} \frac{\partial p_\infty^*}{\partial x^*} + \frac{1}{S^2} \frac{\partial^2 u^*}{\partial y^{*2}}, \quad (\text{A.32})$$

and

$$\frac{\partial T^*}{\partial t^*} = \frac{1}{\text{Pr} S^2} \frac{\partial^2 T^*}{\partial y^{*2}} + \frac{\gamma - 1}{\gamma} \frac{\partial p_\infty^*}{\partial t^*}, \quad (\text{A.33})$$

for u^* and T^* with the boundary conditions

$$u^*(y^* = 0) = T^*(y^* = 0) = 0, \quad (\text{A.34})$$

and

$$u^*(y^* \rightarrow \infty) = T^*(y^* \rightarrow \infty) = \text{finite}. \quad (\text{A.35})$$

A time-harmonic solution is assumed and is represented by

$$\begin{aligned} p_\infty^* &= \underline{p}_\infty e^{jt^*}, \\ T^* &= \underline{T} e^{jt^*}, \end{aligned}$$

and

$$u^* = \underline{u} e^{jt^*}.$$

The boundary layer problem to solve becomes

$$j\underline{u} = -\frac{1}{\gamma} \frac{dp_\infty}{dx^*} + \frac{1}{S^2} \frac{\partial^2 \underline{u}}{\partial y^{*2}}, \quad (\text{A.36})$$

$$j\underline{T} = \frac{1}{\text{Pr} S^2} \frac{\partial^2 \underline{T}}{\partial y^{*2}} + j \frac{\gamma-1}{\gamma} \underline{p}_\infty, \quad (\text{A.37})$$

with

$$\underline{u}(y^* = 0) = \underline{T}(y^* = 0) = 0, \quad (\text{A.38})$$

and

$$\underline{u}(y^* \rightarrow \infty) = \underline{T}(y^* \rightarrow \infty) = \text{finite}. \quad (\text{A.39})$$

The solutions for the velocity and temperature profiles are easily found from Equations (A.36) and (A.37) with the boundary conditions defined in Equations (A.38) and (A.39). The velocity profile is

$$\underline{u}(y^*) = j \frac{1}{\gamma} \frac{dp_\infty}{dx^*} \left(1 - e^{-\frac{1+j}{\sqrt{2}} S y^*} \right). \quad (\text{A.40})$$

The boundary layer thickness is found by solving for the y^* location where the velocity is equal to 99% of the mainstream velocity, $0.99u^*(y^* \rightarrow \infty)$. The boundary layer thickness is given as

$$\delta^* = -\sqrt{2} \ln(0.01) \frac{1}{S}, \quad (\text{A.41})$$

or in dimensional terms

$$\delta \approx 6.5 \sqrt{\frac{\nu}{\omega}}. \quad (\text{A.42})$$

Equation (A.42) shows that the boundary layer thickness is inversely proportional to the frequency and that the thickest boundary layers will be at low frequencies. At 100 Hz, the boundary layer thickness for air is 0.45 mm. This is much smaller than the hydraulic

diameter for the two waveguides described in this dissertation (8.5 mm and 25.4 mm) and verifies the small boundary layer assumption.

The temperature profile is

$$\underline{T}(y^*) = \frac{\gamma-1}{\gamma} \underline{p}_\infty \left(1 - e^{-\frac{1+j}{\sqrt{2}} \sqrt{\text{Pr}} S y^*} \right). \quad (\text{A.43})$$

The thermal boundary layer thickness is found by solving for the y^* location where the temperature is equal to 99% of the mainstream temperature, $0.99T^*(y^* \rightarrow \infty)$. The thermal boundary thickness is

$$\delta_{th}^* = -\sqrt{2} \ln(0.01) \frac{1}{\sqrt{\text{Pr}} S}, \quad (\text{A.44})$$

or in dimensional terms

$$\delta_{th} \approx 6.5 \sqrt{\frac{\nu}{\omega \text{Pr}}} = \frac{\delta}{\sqrt{\text{Pr}}}. \quad (\text{A.45})$$

Equation (A.45) shows that the thermal boundary layer thickness is related to the viscous boundary thickness by a factor of $\sqrt{\text{Pr}}$ and also has the same dependence on frequency. At 100 Hz, the thermal boundary layer thickness for air is 0.54 mm and again this is small as compared to the hydraulic diameter for the two waveguides.

In summary, the full velocity and temperature profiles are

$$u^*(y^*) = j \frac{1}{\gamma} \frac{dp_\infty}{dx^*} \left(1 - e^{-\frac{1+j}{\sqrt{2}} S y^*} \right) e^{jt^*}, \quad (\text{A.46})$$

and

$$T^*(y^*) = \frac{\gamma-1}{\gamma} \underline{p}_\infty \left(1 - e^{-\frac{1+j}{\sqrt{2}} \sqrt{\text{Pr}} S y^*} \right) e^{jt^*}. \quad (\text{A.47})$$

A.2.1 Wall Shear Stress

Now that the velocity profile is known, the wall shear stress can be found. In dimensional terms, the wall shear stress is given as

$$\tau_w = \mu \left. \frac{\partial u}{\partial y} \right|_{y=0}, \quad (\text{A.48})$$

which can be nondimensionalized by substituting in the definitions given in Equations (A.11) and (A.15). This results in

$$\tau_w = \frac{\mu c_0}{L} \left. \frac{\partial u^*}{\partial y^*} \right|_{y^*=0}.$$

By defining the nondimensional shear stress as

$$\tau_w^* = \frac{\tau_w}{\frac{\mu c_0}{L}}, \quad (\text{A.49})$$

Equation (A.48) becomes

$$\tau_w^* = \left. \frac{\partial u^*}{\partial y^*} \right|_{y^*=0}. \quad (\text{A.50})$$

By evaluating the derivative with the aid of the velocity profile in Equation (A.46), the wall shear stress is

$$\tau_w^* = \frac{(-1+j)S}{\sqrt{2}} \frac{dp_\infty}{\gamma dx^*} e^{jt^*} = \frac{(-1+j)S}{\sqrt{2}} \frac{\partial p_\infty^*}{\gamma \partial x^*}. \quad (\text{A.51})$$

This represents the shear force applied to the wall due to the fluid motion. This will be used in the derivation of the governing equations for the mainstream flow to account for the viscous losses.

A.2.2 Wall Heat Flux

The heat flux at the wall is found from the temperature profile and Fourier's heat conduction law. The wall heat flux is given as

$$q_w = -\kappa \left. \frac{\partial T}{\partial y} \right|_{y=0}, \quad (\text{A.52})$$

or substituting in the definitions of the nondimensional temperature and y -coordinate,

$$q_w = -\frac{\kappa T_0}{L} \left. \frac{\partial T^*}{\partial y^*} \right|_{y^*=0}.$$

Defining the nondimensional wall heat flux as

$$q_w^* = \frac{q_w}{\frac{\kappa T_0}{L}}, \quad (\text{A.53})$$

the nondimensional Fourier's heat conduction law becomes

$$q_w^* = -\left. \frac{\partial T^*}{\partial y^*} \right|_{y^*=0}. \quad (\text{A.54})$$

By evaluating the derivative with the aid of temperature profile in Equation (A.47), the wall heat flux is

$$q_w^* = -\frac{1+j}{\sqrt{2}} S \sqrt{\text{Pr}} \frac{\gamma-1}{\gamma} \underline{p}_\infty e^{j t^*} = -\frac{1+j}{\sqrt{2}} S \sqrt{\text{Pr}} \frac{\gamma-1}{\gamma} p_\infty^*, \quad (\text{A.55})$$

which represents the heat flux through the wall in the transverse direction. This will be used in the derivation of the governing equations for the mainstream flow to account for heat conduction.

A.3 Mainstream Flow

The mainstream flow is modeled with the same assumptions previously stated in this appendix, with the exception of incompressibility and the addition of inviscid flow

with the losses due to the boundary layer handled with an applied external shear stress and heat flux at the boundaries. The propagating waves are assumed to be plane waves, thus requiring that $v = 0$ throughout the entire flow field. The governing equations will be modified to include the new loss term for the axial momentum equation and the thermal energy equations. A control volume analysis is easily used to construct the new governing equations, and since the boundary layer thicknesses are small compared to the hydraulic diameter, the cross-section of the mainstream flow is assumed to be the same as the cross-section of the waveguide. In the mainstream, the continuity equation is given as

$$\frac{\partial \rho}{\partial t} + \frac{\partial(\rho u)}{\partial x} = 0, \quad (\text{A.56})$$

or if linearized and nondimensionalized as

$$\frac{\partial \rho^*}{\partial t^*} + \frac{\partial u^*}{\partial x^*} = 0. \quad (\text{A.57})$$

A.3.1 Axial Momentum

The two-dimensional control volume is seen in Figure A-2, showing the external forces and the velocities that cross the boundaries. Applying an Eulerian view of Newton's Second Law to the control volume to obtain

$$\frac{\partial(\rho u A dx)}{\partial t} = \rho u^2 A|_x - \rho u^2 A|_{x+dx} + p A|_x - p A|_{x+dx} - \tau_w l_{perimeter} dx.$$

Note that p now denotes the mainstream pressure and that the infinity subscript has been dropped for convenience. The expression can be simplified as follows:

$$\begin{aligned} A dx \frac{\partial(\rho u)}{\partial t} + A \rho u^2|_{x+dx} - A \rho u^2|_x + A p|_{x+dx} - A p|_x &= -\tau_w l_{perimeter} dx, \\ \frac{\partial(\rho u)}{\partial t} + \frac{\rho u^2|_{x+dx} - \rho u^2|_x}{dx} + \frac{p|_{x+dx} - p|_x}{dx} &= -4 \frac{l_{perimeter}}{4A} \tau_w. \end{aligned}$$

$$\frac{\partial u^*}{\partial t^*} + \frac{1}{\gamma} \frac{\partial p^*}{\partial x^*} = -\frac{4}{S^2} \tau_w^* \quad (\text{A.58})$$

Now substitute in Equation (A.51) for the wall shear stress to obtain

$$\frac{\partial u^*}{\partial t^*} + \frac{1}{\gamma} \frac{\partial p^*}{\partial x^*} = \frac{2\sqrt{2}}{\gamma S} (1-j) \frac{\partial p^*}{\partial x^*} \quad (\text{A.59})$$

Equation (A.59) is the axial momentum equation for the mainstream flow which includes a correction term for the viscous losses due to the presence of the boundary layer. The equation shows that force provided by the driving pressure gradient is split between the time rate of change of momentum and the losses at the boundary layer.

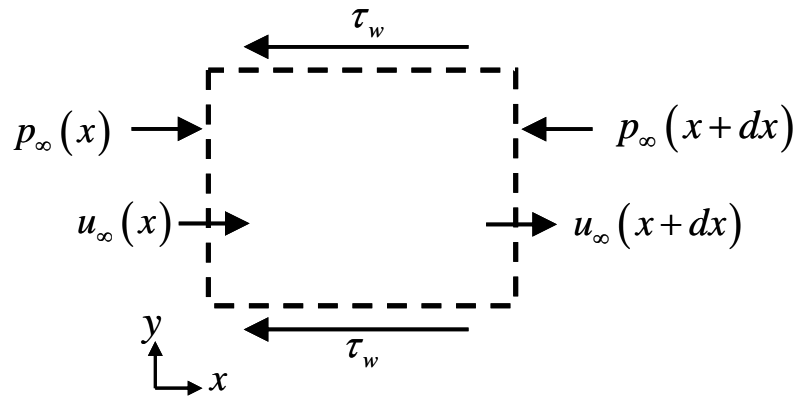


Figure A-2: Control volume showing the external forces and flows crossing the boundaries.

A.3.2 Energy Equation

The two-dimensional control volume is seen in Figure A-3, showing the external heat fluxes, pressure work boundaries, and the velocities that cross the boundaries.

Applying an Eulerian view of conversion of energy to the control volume to obtain

$$\frac{\partial}{\partial t} (\rho e A dx) = \rho u e A|_x - \rho u e A|_{x+dx} + p u A|_x - p u A|_{x+dx} + q_w l_{perimeter} dx,$$

where e is the internal energy. The expression can be simplified as follows:

$$A dx \frac{\partial}{\partial t} (\rho e) + A \rho u e|_{x+dx} - A \rho u e|_x + A p u|_{x+dx} - A p u|_x = q_w l_{perimeter} dx,$$

$$\frac{\partial}{\partial t}(\rho e) + \frac{\rho e|_{x+dx} - \rho e|_x}{dx} + \frac{pu|_{x+dx} - pu|_x}{dx} = q_w \frac{l_{\text{perimeter}}}{A}.$$

Taking the limit as $dx \rightarrow 0$ to convert the second and third terms to derivatives to obtain

$$\frac{\partial(\rho e)}{\partial t} + \frac{\partial(\rho e)}{\partial x} + \frac{\partial(pu)}{\partial x} = 4q_w \frac{l_{\text{perimeter}}}{4A},$$

$$\frac{\partial(\rho e)}{\partial t} + \frac{\partial(\rho e)}{\partial x} + \frac{\partial(pu)}{\partial x} = \frac{4}{L}q_w.$$

Expanding the derivatives and using continuity as follows:

$$\rho \frac{\partial e}{\partial t} + e \frac{\partial \rho}{\partial t} + \rho u \frac{\partial e}{\partial x} + e \frac{\partial(\rho u)}{\partial x} + \frac{\partial(pu)}{\partial x} = \frac{4}{L}q_w,$$

$$\rho \frac{\partial e}{\partial t} + \rho u \frac{\partial e}{\partial x} + e \left(\frac{\partial \rho}{\partial t} + \frac{\partial(\rho u)}{\partial x} \right) + \frac{\partial(pu)}{\partial x} = \frac{4}{L}q_w,$$

$\underbrace{\hspace{10em}}_{=0 \text{ from continuity}}$

$$\rho \frac{\partial e}{\partial t} + \rho u \frac{\partial e}{\partial x} + \frac{\partial(pu)}{\partial x} = \frac{4}{L}q_w.$$

For this situation, the internal energy is given by $e = \varepsilon + u^2/2$, and is to simplify the expression for energy as follows:

$$\rho \frac{\partial(\varepsilon + u^2/2)}{\partial t} + \rho u \frac{\partial(\varepsilon + u^2/2)}{\partial x} + \frac{\partial(pu)}{\partial x} = \frac{4}{L}q_w,$$

$$\rho \frac{\partial \varepsilon}{\partial t} + \rho \frac{\partial(u^2/2)}{\partial t} + \rho u \frac{\partial \varepsilon}{\partial x} + \rho u \frac{\partial(u^2/2)}{\partial x} + u \frac{\partial p}{\partial x} + p \frac{\partial u}{\partial x} = \frac{4}{L}q_w,$$

$$\rho \frac{\partial \varepsilon}{\partial t} + \rho u \frac{\partial u}{\partial t} + \rho u \frac{\partial \varepsilon}{\partial x} + \rho u u \frac{\partial u}{\partial x} + u \frac{\partial p}{\partial x} + p \frac{\partial u}{\partial x} = \frac{4}{L}q_w,$$

$$\rho \frac{\partial \varepsilon}{\partial t} + \rho u \frac{\partial \varepsilon}{\partial x} + u \left(\rho \frac{\partial u}{\partial t} + \rho u \frac{\partial u}{\partial x} + \frac{\partial p}{\partial x} \right) + p \frac{\partial u}{\partial x} = \frac{4}{L}q_w.$$

Recall that for inviscid flow, the momentum equation in the x -direction is given by

$$\rho \frac{\partial u}{\partial t} + \rho u \frac{\partial u}{\partial x} + \frac{\partial p}{\partial x} = 0,$$

which is used to simplify the energy equation to

$$\rho \frac{\partial \varepsilon}{\partial t} + \rho u \frac{\partial \varepsilon}{\partial x} + p \frac{\partial u}{\partial x} = \frac{4}{L} q_w,$$

or switching to the material derivative denoted by D/Dt ,

$$\rho \frac{D\varepsilon}{Dt} + p \frac{\partial u}{\partial x} = \frac{4}{L} q_w.$$

Recall continuity in material derivative form as

$$\frac{1}{\rho} \frac{D\rho}{Dt} = -\frac{\partial u}{\partial x},$$

and substitute into the expression for the energy equation to obtain

$$\rho \frac{D\varepsilon}{Dt} - \frac{p}{\rho} \frac{D\rho}{Dt} = \frac{4}{L} q_w.$$

Now note that material derivative of the pressure can be expressed as

$$\frac{Dp}{Dt} = \frac{D\left(\rho \frac{p}{\rho}\right)}{Dt} = \rho \frac{D\left(\frac{p}{\rho}\right)}{Dt} + \frac{p}{\rho} \frac{D\rho}{Dt},$$

or more conveniently as

$$\frac{p}{\rho} \frac{D\rho}{Dt} = \frac{Dp}{Dt} - \rho \frac{D\left(\frac{p}{\rho}\right)}{Dt}.$$

Substituting this expression into the energy equation gives

$$\rho \frac{D\varepsilon}{Dt} - \frac{Dp}{Dt} + \rho \frac{D\left(\frac{p}{\rho}\right)}{Dt} = \frac{4}{L} q_w,$$

$$\rho \left(\frac{D\varepsilon}{Dt} + \frac{D\left(\frac{p}{\rho}\right)}{Dt} \right) - \frac{Dp}{Dt} = \frac{4}{L} q_w,$$

$$\rho \frac{D\left(\varepsilon + \frac{p}{\rho}\right)}{Dt} - \frac{Dp}{Dt} = \frac{4}{L} q_w.$$

This expression can be simplified farther by noting the definition of enthalpy as

$$h = \varepsilon + \frac{p}{\rho}, \quad (\text{A.60})$$

thus reducing the energy equation to

$$\rho \frac{Dh}{Dt} - \frac{Dp}{Dt} = \frac{4}{L} q_w.$$

For a thermally and calorically perfect gas, enthalpy is given as

$$h = c_p T, \quad (\text{A.61})$$

thus allowing the energy equation to be written in terms of temperature as

$$\rho c_p \frac{DT}{Dt} - \frac{Dp}{Dt} = \frac{4}{L} q_w,$$

$$\rho c_p \frac{\partial T}{\partial t} + \rho c_p u \frac{\partial T}{\partial x} - \frac{\partial p}{\partial t} - u \frac{\partial p}{\partial x} = \frac{4}{L} q_w.$$

Now the energy equation is nondimensionalized and linearized as follows:

$$\begin{aligned} & \rho_0 (1 + \rho^*) c_p \frac{\partial (T_0 (1 + T^*))}{\partial \left(\frac{t}{\omega}\right)} + \rho_0 (1 + \rho^*) c_p c_0 u^* \frac{\partial (T_0 (1 + T^*))}{\partial \left(\frac{c_0}{\omega} x^*\right)} \\ & - \frac{\partial (p_0 (1 + p^*))}{\partial \left(\frac{t}{\omega}\right)} - c_0 u^* \frac{\partial (p_0 (1 + p^*))}{\partial \left(\frac{c_0}{\omega} x^*\right)} = \frac{4}{L} \frac{\kappa T_0}{L} q_w^*, \end{aligned}$$

$$\rho_0 T_0 c_p \omega \frac{\partial T^*}{\partial t^*} - p_0 \omega \frac{\partial p^*}{\partial t^*} = 4 \frac{\kappa T_0}{L^2} q_w^*.$$

Now divide the expression by $\rho_0 T_0 c_p \omega$ to obtain

$$\frac{\partial T^*}{\partial t^*} - \frac{p_0 \omega}{\rho_0 T_0 c_p \omega} \frac{\partial p^*}{\partial t^*} = 4 \frac{1}{\rho_0 T_0 c_p \omega} \frac{\kappa T_0}{L^2} q_w^*,$$

$$\frac{\partial T^*}{\partial t^*} - \frac{p_0}{\rho_0 T_0} \frac{1}{c_p} \frac{\partial p^*}{\partial t^*} = 4 \frac{\kappa}{\mu c_p} \frac{\mu}{\rho_0 \omega L^2} q_w^*.$$

Using the equation of state for a perfect gas, the thermodynamic relation given in Equation (A.8), and the definition of the ratio of specific heats, the Stokes number and the Prandtl number, the energy equation is simplified as follows:

$$\frac{\partial T^*}{\partial t^*} - \frac{R}{c_p} \frac{\partial p^*}{\partial t^*} = 4 \frac{1}{\text{Pr}} \frac{\nu}{\omega L^2} q_w^*,$$

$$\frac{\partial T^*}{\partial t^*} - \frac{c_v (\gamma - 1)}{c_p} \frac{\partial p^*}{\partial t^*} = 4 \frac{1}{\text{Pr} S^2} q_w^*,$$

and finally

$$\frac{\partial T^*}{\partial t^*} - \frac{(\gamma - 1)}{\gamma} \frac{\partial p^*}{\partial t^*} = 4 \frac{1}{\text{Pr} S^2} q_w^*. \quad (\text{A.62})$$

Substituting in Equation (A.55) to put the energy equation in terms of only the field variables results in

$$\frac{\partial T^*}{\partial t^*} - \frac{(\gamma - 1)}{\gamma} \frac{\partial p^*}{\partial t^*} = -4 \frac{1}{\text{Pr} S^2} \frac{1+j}{\sqrt{2}} \sqrt{\text{Pr} S} \frac{\gamma-1}{\gamma} p^*,$$

or

$$\frac{\partial T^*}{\partial t^*} - \frac{(\gamma - 1)}{\gamma} \frac{\partial p^*}{\partial t^*} = -2\sqrt{2} \frac{1+j}{\sqrt{\text{Pr} S}} \frac{\gamma-1}{\gamma} p^*. \quad (\text{A.63})$$

Equation (A.63) is the thermal energy equation for the mainstream flow including losses due to heat conduction at the wall.

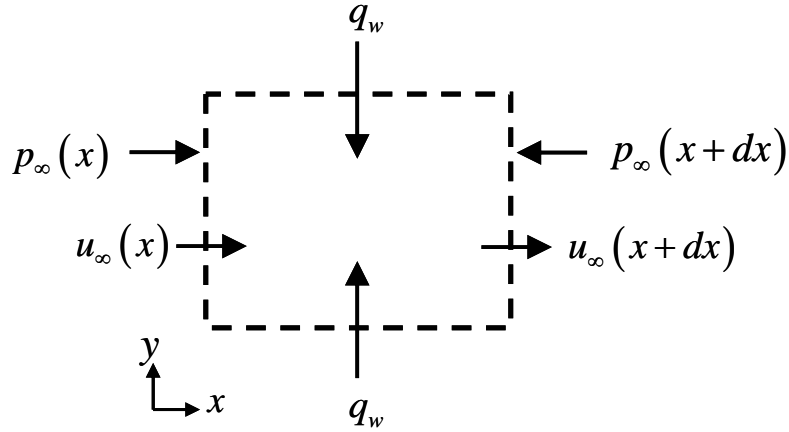


Figure A-3: Control volume showing the external heat fluxes and flows crossing the boundaries.

A.3.3 Summary of the Mainstream Flow Equations

The system of equations governing the mainstream flow is given here for reference.

The equations are

$$\frac{\partial \rho^*}{\partial t^*} + \frac{\partial u^*}{\partial x^*} = 0, \quad (\text{A.64})$$

$$\frac{\partial u^*}{\partial t^*} = \frac{1}{\gamma} \left(\frac{2\sqrt{2}}{S} (1-j) - 1 \right) \frac{\partial p^*}{\partial x^*}, \quad (\text{A.65})$$

$$\frac{\partial T^*}{\partial t^*} = \frac{\gamma-1}{\gamma} \frac{\partial p^*}{\partial t^*} - \frac{2\sqrt{2}}{\gamma S} \frac{(\gamma-1)}{\sqrt{\text{Pr}}} (1+j) p^*, \quad (\text{A.66})$$

and

$$p^* = \rho^* + T^*. \quad (\text{A.67})$$

These are the equations that need to be solved to determine the decay in the amplitude and the shift in phase speed due to thermoviscous losses for a sound wave that propagates down a duct.

A.3.4 Mainstream Flow Wave Equation

The equations summarized in Section A.3.3 are combined to form a single wave equation for the mainstream flow in terms of the acoustic pressure. To start, the equation of state, Equation (A.67), is used to eliminate ρ^* from continuity, Equation (A.64). The new form of the continuity equation is

$$\frac{\partial p^*}{\partial t^*} - \frac{\partial T^*}{\partial t^*} + \frac{\partial u^*}{\partial x^*} = 0,$$

which is rearranged to become

$$\frac{\partial T^*}{\partial t^*} = \frac{\partial p^*}{\partial t^*} + \frac{\partial u^*}{\partial x^*}.$$

Now this expression is used to replace T^* in the energy equation, Equation (A.66). The result is

$$\frac{\partial p^*}{\partial t^*} + \frac{\partial u^*}{\partial x^*} = \frac{\gamma - 1}{\gamma} \frac{\partial p^*}{\partial t^*} - \frac{2\sqrt{2}(\gamma - 1)}{\gamma S \sqrt{\text{Pr}}} (1 + j) p^*,$$

or

$$\frac{\partial u^*}{\partial x^*} = -\frac{\partial p^*}{\partial t^*} + \frac{\partial p^*}{\partial t^*} - \frac{1}{\gamma} \frac{\partial p^*}{\partial t^*} - \frac{2\sqrt{2}(\gamma - 1)}{\gamma S \sqrt{\text{Pr}}} (1 + j) p^*,$$

$$\frac{\partial u^*}{\partial x^*} = -\frac{1}{\gamma} \frac{\partial p^*}{\partial t^*} - \frac{2\sqrt{2}(\gamma - 1)}{\gamma S \sqrt{\text{Pr}}} (1 + j) p^*. \quad (\text{A.68})$$

Now the system of four equations with four unknowns has been reduced to a system of two equations, Equations (A.65) and (A.68), with only two unknowns. To combine these two equations into a single wave equation, differentiate Equation (A.65) with respect to x^* and derivate Equation (A.68) with respect to t^* . This yields

$$\frac{\partial^2 u^*}{\partial x^* \partial t^*} = \frac{1}{\gamma} \left(\frac{2\sqrt{2}}{S} (1-j) - 1 \right) \frac{\partial^2 p^*}{\partial x^{*2}},$$

and

$$\frac{\partial^2 u^*}{\partial x^* \partial t^*} = -\frac{1}{\gamma} \frac{\partial^2 p^*}{\partial t^{*2}} - \frac{2\sqrt{2}}{\gamma S} \frac{(\gamma-1)}{\sqrt{\text{Pr}}} (1+j) \frac{\partial p^*}{\partial t^*}.$$

Now subtract the two equations to get

$$0 = \frac{1}{\gamma} \left(\frac{2\sqrt{2}}{S} (1-j) - 1 \right) \frac{\partial^2 p^*}{\partial x^{*2}} + \frac{1}{\gamma} \frac{\partial^2 p^*}{\partial t^{*2}} + \frac{2\sqrt{2}}{\gamma S} \frac{(\gamma-1)}{\sqrt{\text{Pr}}} (1+j) \frac{\partial p^*}{\partial t^*},$$

and simplify as

$$\left(\frac{2\sqrt{2}}{S} (1-j) - 1 \right) \frac{\partial^2 p^*}{\partial x^{*2}} + \frac{\partial^2 p^*}{\partial t^{*2}} = -\frac{2\sqrt{2}}{S} \frac{(\gamma-1)}{\sqrt{\text{Pr}}} (1+j) \frac{\partial p^*}{\partial t^*}. \quad (\text{A.69})$$

Equation (A.69) is the lossy, nondimensional wave equation for the mainstream flow that accounts for the losses due to the boundary layer but neglects losses in the bulk fluid.

A.3.5 Dissipation and Dispersion Relations

To find the dissipation and dispersion relations, the pressure is assumed to have the form

$$p^* = \underline{P}_s e^{-j\Gamma x^*} e^{jt^*}, \quad (\text{A.70})$$

where Γ is the nondimensional propagation constant and \underline{P}_s is a constant that determines the amplitude of the sound wave. Next, substitute Equation (A.70) into the wave equation, Equation (A.69), and solve for the propagation constant as follows;

$$\left(\frac{2\sqrt{2}}{S} (1-j) - 1 \right) (-j\Gamma)^2 p^* + j^2 p^* = -\frac{2\sqrt{2}}{S} \frac{(\gamma-1)}{\sqrt{\text{Pr}}} (1+j) j p^*,$$

$$\left(1 - \frac{2\sqrt{2}}{S} (1-j) \right) \Gamma^2 = 1 + \frac{2\sqrt{2}}{S} \frac{(\gamma-1)}{\sqrt{\text{Pr}}} (1-j),$$

so finally, when choosing the positive square root, the propagation constant is

$$\Gamma = \frac{\sqrt{1 + \frac{2\sqrt{2}(\gamma-1)}{S\sqrt{\text{Pr}}}(1-j)}}{\sqrt{1 - \frac{2\sqrt{2}}{S}(1-j)}}. \quad (\text{A.71})$$

The nondimensional propagation constant can be simplified further by expanding the two square roots into series. The series expansions require that the second term in each of the square roots have a magnitude of less than one for the series to converge.

This can be expressed mathematically as

$$\left| \frac{2\sqrt{2}(\gamma-1)}{S\sqrt{\text{Pr}}}(1-j) \right| < 1,$$

and

$$\left| \frac{2\sqrt{2}}{S}(1-j) \right| < 1.$$

In order for these requirements to be satisfied, $1/S$ will have to be a small parameter.

The two expressions can be simplified using the definition of the Stokes number, and this results in

$$f > \frac{8}{\pi} \frac{\nu}{L^2} \frac{(\gamma-1)^2}{\text{Pr}} \quad (\text{A.72})$$

and

$$f > \frac{8}{\pi} \frac{\nu}{L^2}, \quad (\text{A.73})$$

respectively. Table A-1 gives the minimum frequencies to satisfy the two requirements for the series expansion for the two waveguides presented in this dissertation for air at

20°C . The results in the table show that the minimum frequencies are easily exceeded in any practical experiment for this dissertation and therefore the series expansion is valid.

Table A-1: Minimum frequency required for series expansion for the two waveguides for air at 20°C.

Requirement	$L = 8.5 \text{ mm}$	$L = 25.4 \text{ mm}$
(A.72)	0.12 Hz	0.014 Hz
(A.73)	0.6 Hz	0.06 Hz

The expression for the propagation constant, Equation (A.71), is expanded using the series expansions for the two square roots. This results in

$$\Gamma = \left(1 + \frac{1}{2} \frac{2\sqrt{2}}{S} \frac{(\gamma-1)}{\sqrt{\text{Pr}}} (1-j) - \frac{1}{8} \left(\frac{2\sqrt{2}}{S} \frac{(\gamma-1)}{\sqrt{\text{Pr}}} (1-j) \right)^2 + \text{K} \right) \times \left(1 + \frac{1}{2} \frac{2\sqrt{2}}{S} (1-j) + \frac{3}{8} \left(\frac{2\sqrt{2}}{S} (1-j) \right)^2 + \text{K} \right).$$

This is simplified as follows:

$$\Gamma = 1 + \frac{1}{2} \frac{2\sqrt{2}}{S} (1-j) + \frac{1}{2} \frac{2\sqrt{2}}{S} \frac{(\gamma-1)}{\sqrt{\text{Pr}}} (1-j) + \frac{1}{2} \frac{2\sqrt{2}}{S} (1-j) \frac{1}{2} \frac{2\sqrt{2}}{S} \frac{(\gamma-1)}{\sqrt{\text{Pr}}} (1-j) + \text{K}.$$

Since $1/S$ is a small parameter, terms of order $(1/S)^2$ or higher are neglected. This simplifies the propagation constant to

$$\Gamma = 1 + \frac{1}{2} \frac{2\sqrt{2}}{S} (1-j) + \frac{1}{2} \frac{2\sqrt{2}}{S} \frac{(\gamma-1)}{\sqrt{\text{Pr}}} (1-j),$$

or to

$$\Gamma = 1 + (1-j) \frac{\sqrt{2}}{S} \left(1 + \frac{(\gamma-1)}{\sqrt{\text{Pr}}} \right). \quad (\text{A.74})$$

To extract the dissipation and dispersion relations, the pressure solution must be considered and dimensionalized. Starting with Equation (A.70) and substituting in the dimensional variables and expanding yields

$$p = p_0 \underline{P}_s e^{-j\Gamma_R \frac{\omega}{c_0} x + \Gamma_I \frac{\omega}{c_0} x} e^{j\omega t},$$

or

$$p = p_0 \underline{P}_s e^{\Gamma_I \frac{\omega}{c_0} x} e^{-j\Gamma_R \frac{\omega}{c_0} x} e^{j\omega t},$$

where $\Gamma_R = \text{Re}(\Gamma)$ and $\Gamma_I = \text{Im}(\Gamma)$. This equation must be equal to

$$p = (\text{const}) e^{-\beta x} e^{-j\frac{\omega}{c} x} e^{j\omega t},$$

Thus, by inspection, the equations for the dissipation constant, β , and phase speed, c , are determined to be

$$\beta = -\frac{\omega}{c_0} \Gamma_I,$$

and

$$c = c_0 \frac{1}{\Gamma_R}.$$

Substituting in the imaginary part of Γ into the expression for β , the dissipation constant is

$$\beta = \frac{\sqrt{2}}{S} \left(1 + \frac{\gamma - 1}{\sqrt{\text{Pr}}} \right) \left(\frac{\omega}{c_0} \right), \quad (\text{A.75})$$

or

$$\beta = \frac{\sqrt{2}}{L} \sqrt{\frac{\nu}{\omega}} \left(1 + \frac{\gamma - 1}{\sqrt{\text{Pr}}} \right) \left(\frac{\omega}{c_0} \right). \quad (\text{A.76})$$

This is the equation for the dissipation constant presented in Section 2.2.2. Substituting in the real part of Γ into the expression for c , the phase speed is given as

$$c = c_0 \frac{1}{1 + \frac{\sqrt{2}}{S} \left(1 + \frac{\gamma - 1}{\sqrt{\text{Pr}}} \right)}.$$

Assuming that the second term in the denominator is small, the expression is expanded into a series as

$$c = c_0 \left(1 - \frac{\sqrt{2}}{S} \left(1 + \frac{\gamma - 1}{\sqrt{\text{Pr}}} \right) + K \right).$$

Only the first two terms in the series are retained, thus

$$c = c_0 \left(1 - \frac{\sqrt{2}}{S} \left(1 + \frac{\gamma - 1}{\sqrt{\text{Pr}}} \right) \right), \quad (\text{A.77})$$

or

$$c = c_0 \left(1 - \frac{\sqrt{2}}{L} \sqrt{\frac{\nu}{\omega}} \left(1 + \frac{\gamma - 1}{\sqrt{\text{Pr}}} \right) \right). \quad (\text{A.78})$$

Again, this is the dispersion relation given for the phase in Section 2.2.2.

APPENDIX B RANDOM UNCERTAINTY ESTIMATES FOR THE FREQUENCY RESPONSE FUNCTION

Uncertainty estimation is an important part of any measurement, but it is often neglected for complex-valued or multivariate data (e.g., vectors). This appendix presents a methodology for estimating the uncertainty in multivariate experimental data and applies it to the measurement of the frequency response function obtained using a periodic random input signal. This multivariate uncertainty method is an extension of classical uncertainty methods used for scalar variables and tracks the correlation between all variates along with the sample variance instead of just tracking the standard uncertainty. The method is used in this dissertation to propagate the sample covariance matrix from spectral density estimates to the uncertainty in the frequency response function estimate for two different system models. The first model considers the case when only the output signal is corrupted by noise, while the second model examines when both the input and output signals are corrupted by uncorrelated noise sources. The results for the single-noise model are verified by comparing them to published expressions in the literature, while the results for the two-noise model are verified using a direct computation of the statistics. Finally, the method is applied to experimental data from two microphone measurements within an acoustic waveguide. The random uncertainty estimates in the frequency response function from the multivariate method agree well with the results from a direct computation of the statistics.

B.1 Introduction

Linear, time-invariant systems occur in many engineering applications and are completely characterized by a frequency response function (FRF). Examples of applications include digital and analog filters and acoustic impedance measurements. Measurements of the FRF are commonly performed to test unknown systems and verify analytical models, but knowledge of the uncertainty in the estimated FRF is also desirable if not essential. The advent of inexpensive and powerful microprocessors has made the computation of the FRF using the Fast Fourier Transform (FFT) routine. Early efforts used a Gaussian random noise input, which prompted research on the associated measurement uncertainty in the FRF (Bendat and Piersol 2000), spectral leakage (Schmidt 1985; Bendat and Piersol 2000), the development of specialized window functions (Gade and Herlufsen 1987), and the use of periodic input signals to eliminate leakage (Pintelon and Schoukens 2001a; Pintelon and Schoukens 2001b; Pintelon, Rolain and Moer 2002; Schoukens et al. 2003). Where possible, the use of a periodic random (or pseudo-random) noise input is acknowledged as the preferred approach to eliminate bias errors in the FRF associated with spectral leakage, but the random errors associated with such an input differ from the corresponding white noise input case. Indeed, modern spectrum analyzers now incorporate these features but do not provide an estimate of the measurement uncertainty. The contribution of this appendix is to demonstrate a multivariate statistical methodology for estimating the random uncertainty in the frequency response function using a periodic random noise input. Two different system models are considered, one with noise only on the output signal and the other with uncorrelated noise on both the input and output signals.

The outline of the appendix is as follows. Section B.2 contains a brief review of classical uncertainty analysis, which sets the stage for a discussion of multivariate methods. The section also includes a simple demonstration of the multivariate method by converting the uncertainty in real and imaginary parts of a complex variable to magnitude and phase. Section B.3 discusses and provides expressions for the random uncertainty in the FRF estimate using a periodic random input for the two system models mentioned above to discern the effects of input and output noise. The results for the single-noise model are verified by comparing them to published expressions in the literature (Bendat and Piersol 2000), while the results for the two-noise model are verified using a direct computation of the statistics. The multivariate uncertainty method is then applied to data from an acoustic application that requires the measurement of the FRF between two microphones.

B.2 Uncertainty Analysis

Experimental data analysis consists of two parts: estimating the measured quantity and the corresponding uncertainty. The estimate of the measured quantity, called the *measurand*, is an estimate of the true value of the quantity. The uncertainty quantifies the estimated accuracy in terms of a confidence interval (Kline and McClintock 1953).

Many articles and books have been published outlining methods to estimate uncertainty in experimental data. One of the first publications, by Kline and McClintock in 1953 (Kline and McClintock 1953), was revisited in 1983 by the ASME Symposium on Uncertainty Analysis and published in the Transactions of the ASME in 1985 (Kline 1985). Currently, the many texts available on the subject include the *Guide to the Expression of Uncertainty in Measurements* published by ISO (1995) (referred to as the ISO Guide), the *NIST Technical Note 1297* by Taylor and Kuyatt (Taylor and Kuyatt

1994), and *Experimentation and Uncertainty Analysis for Engineers* by Coleman and Steele (Coleman and Steele 1999). All these publications prescribe essentially the same procedure, which is summarized in the next section, except they vary slightly in the philosophy of uncertainty source classification. This dissertation will classify uncertainty sources as random and bias (Kline and McClintock 1953; Kline 1985; Coleman and Steele 1999) as opposed to Type A and Type B (Taylor and Kuyatt 1994; 1995).

The approaches to uncertainty analysis described in (Kline and McClintock 1953; Kline 1985; Taylor and Kuyatt 1994; 1995; Coleman and Steele 1999) are limited to scalar or real-valued data. These methods do not apply to data that are multi-dimensional or *multivariate*. Multivariate data have multiple, possibly correlated, components. Examples of multivariate data include measurements of vector quantities and complex-valued data such as the FRF. Relevant examples using multivariate uncertainty analysis that parallel classical work are presented in references (Ridler and Salter 2002; Willink and Hall 2002; Hall 2003; Hall 2004).

B.2.1 Classical Uncertainty Analysis

The classical uncertainty method described in (Kline and McClintock 1953; Kline 1985; Taylor and Kuyatt 1994; 1995; Coleman and Steele 1999) estimates the uncertainty associated with a data reduction equation using a first-order Taylor series expansion. Thus, the uncertainties of the input variables must be small enough such that they do not violate the local linear approximation. The uncertainty propagation equation for the standard uncertainty or sample standard deviation, u_r , is

$$u_r = \sqrt{\sum_{i=1}^n (\theta_i u_{x_i})^2 + 2 \sum_{i=1}^{n-1} \sum_{j=i+1}^n \theta_i \theta_j u_{x_i x_j}}, \quad (\text{B.1})$$

where u_{x_i} is the standard uncertainty or sample standard deviation of the i^{th} input variable, $u_{x_i x_j}$ is the sample covariance between the i^{th} and j^{th} input variables, and

$\theta_i = \frac{\partial r}{\partial x_i}$ is the sensitivity coefficient. The confidence interval is estimated by

multiplying u_r by a coverage factor, k , that is a function of the distribution of the variable and the confidence level desired. Methods for computing the coverage factor based on the t -distribution are given in (Taylor and Kuyatt 1994; 1995; Coleman and Steele 1999). Moffat provides an extension to the above classical method by eliminating the requirement of computing the derivatives analytically via numerical approximations (Moffat 1985). Another subtlety in the classical method is that the underlying statistical distributions of the input variables are not propagated in the analysis. Therefore, one must assume a form of the distribution in order to complete the uncertainty analysis and estimate the confidence interval. Monte Carlo methods offer an alternative to assuming a distribution but are computationally expensive (Coleman and Steele 1999). In spite of these issues, classical uncertainty analysis provides a way to estimate a confidence interval for experimental data and can be used before any measurements are taken for experimental design purposes.

B.2.2 Multivariate Uncertainty Analysis

Multivariate uncertainty analysis extends classical methods to multivariate problems via systematic use of the correlation between variates both in the input and output variables. The multivariate method provides greater insight into uncertainty than the approach outlined in (Pintelon and Schoukens 2001a; Pintelon and Schoukens 2001b), where complex statistics are used. The complex statistics approach represents

the sample standard deviation of a complex number with a single real-valued number and does not treat the real and imaginary parts as separate variates. Thus, confidence regions cannot be estimated from complex statistics. Finally, the complex statistics approach does not offer a methodology to propagate the uncertainty through a data reduction routine like the multivariate method does. For these reasons, this paper focuses on the use of the multivariate method instead of the complex statistics approach.

B.2.2.1 Fundamentals

Before outlining the procedure for multivariate uncertainty analysis, some general information is needed. First, a multivariate problem with p variates will have p^2 uncertainty components, but not all the components are independent due to the symmetry of the covariance matrix (Johnson and Wichern 2002). Thus, the covariance matrix will have only $p(p+1)/2$ independent elements. The task of the multivariate uncertainty analysis is to propagate the covariance matrix through the data reduction equation. The result is another covariance matrix that represents the variation in the calculated output variables.

Complex-valued data can be thought of as *bivariate* because each variable has *two* parts. The two parts of any complex variable can be represented in either real and imaginary parts or magnitude and phase polar form. All complex computations are performed with the real and imaginary parts and converted into magnitude and phase if desired. The real and imaginary axes extend to infinity in both directions as compared to the magnitude and phase axes, in which the magnitude is constrained to be a positive real number, and the phase lies between -180° and $+180^\circ$. This forces the use of modular arithmetic that can influence the prediction of the uncertainty (Ridler and Salter 2002).

In addition to complex-valued variables, another difference compared to the classical method is that a confidence interval is now extended to multidimensional space. For bivariate data, the confidence interval is extended to a confidence area. The shape of the confidence area is a function of the uncertainty in each of the variates and the correlation between them. For a multivariate normally distributed variable, the confidence region is defined by the probability statement (Johnson and Wichern 2002)

$$\text{Prob} \left((\mathbf{x} - \bar{\mathbf{x}}) \mathbf{s}^{-1} (\mathbf{x} - \bar{\mathbf{x}}) \leq \frac{\nu_{eff} p}{\nu_{eff} + 1 - p} F_{p, \nu_{eff} + 1 - p, \alpha} \right) = 1 - \alpha, \quad (\text{B.2})$$

where \mathbf{x} is a vector representing the multivariate variable, $\bar{\mathbf{x}}$ is the sample mean vector, \mathbf{s} is the sample covariance matrix, $F_{p, \nu_{eff} + 1 - p, \alpha}$ is the statistic of the F distribution with p , $\nu_{eff} + 1 - p$ degrees of freedom and a probability $1 - \alpha$, $\alpha \leq 1$ is the level of significance, p is the number of variates, and ν_{eff} is the effective number of degrees of freedom in the measurements. For a single random variable, the effective number of degrees of freedom is the number of measurements less one. Otherwise, Willink and Hall discuss in detail how to estimate the effective number of degrees of freedom (Willink and Hall 2002). The method estimates the effective degrees of freedom by matching the generalized variances for all the input variates and reduces to the Welch-Satterthwaite method for a univariate problem. The Welch-Satterthwaite is the method recommended to estimate the effective number of degrees of freedom in (Taylor and Kuyatt 1994; 1995).

Application of Equation (B.2) for a complex variable shows that the confidence region is an ellipse. If x_r and x_i are the real and imaginary parts of a complex variable, respectively, then the confidence region is given by

$$\left(\frac{x_R - \bar{x}_R}{u_{x_R}} \right)^2 - 2\rho \frac{x_R - \bar{x}_R}{u_{x_R}} \frac{x_I - \bar{x}_I}{u_{x_I}} + \left(\frac{x_I - \bar{x}_I}{u_{x_I}} \right)^2 \leq (1 - \rho^2) \frac{v_{eff} P}{v_{eff} + 1 - p} F_{p, v_{eff} + 1 - p, \alpha}, \quad (\text{B.3})$$

where u_{x_R} and u_{x_I} are the sample standard deviations of x_R and x_I , respectively, and ρ is the correlation coefficient, defined as

$$\rho = \frac{E[(x_R - \bar{x}_R)(x_I - \bar{x}_I)]}{u_{x_R} u_{x_I}}, \quad (\text{B.4})$$

where $E[\]$ is the expectation operator. From Equation (B.3), the simultaneous uncertainty bounds on the real and imaginary parts are given by the projections of the ellipse onto the respective axis and the correlation determines the orientation of the ellipse. For the case of no correlation, $\rho = 0$, the axes of the ellipse are aligned with the real and imaginary axes. For the case of perfect correlation, $\rho \rightarrow \pm 1$, the ellipse collapses to a line. This is intuitive because, if the two variates are perfectly correlated, then only knowledge of one of them is required to determine the other variable.

If the entire confidence region is not desired, the simultaneous confidence interval estimates of the uncertainty for each variate can be computed from

$$U_n = k_{cf} u_n, \quad (\text{B.5})$$

where u_n is the estimate of the sample standard deviation for the n^{th} variate, and k_{cf} is the coverage factor given by

$$k_{cf} = \sqrt{\frac{v_{eff} P}{v_{eff} + 1 - p} F_{p, v_{eff} + 1 - p, \alpha}}. \quad (\text{B.6})$$

The F -distribution is necessary to accommodate the correlated multiple dimensions since the population distribution is assumed to be a multivariate normal distribution (Johnson

and Wichern 2002; Ridler and Salter 2002). For the remainder of this paper, the coverage factor will be computed using two variates for complex data and the number of spectral records minus one. Thus the uncertainty reported for one of the variates would be $x_n \pm U_n$, and a corresponding expression can be written for each variate.

B.2.2.2 Multivariate uncertainty propagation

The task of the multivariate method for uncertainty analysis is to propagate the uncertainty estimates through a data reduction equation. The difference versus the classical method is that the multivariate method simultaneously computes the uncertainty estimates for each variate along with the correlation between them, while the univariate approach only estimates the uncertainty for a single variable. Consider a generalized data reduction equation of the form

$$\mathbf{r} = r(\mathbf{x}), \quad (\text{B.7})$$

where \mathbf{r} is the real-valued vector of output variates, and \mathbf{x} is the real-valued vector containing all input variates. Note that any data reduction equation that has multiple input variables can be recast in the form of a single input variable with multiple variates. The first step is to create a separate expression for each output variate r_1, \dots, r_p and then form the Jacobian matrix

$$\mathbf{J} = \begin{bmatrix} \frac{\partial r_1}{\partial x_1} & \frac{\partial r_1}{\partial x_2} & \mathbf{L} & \frac{\partial r_1}{\partial x_p} \\ \frac{\partial r_2}{\partial x_1} & \frac{\partial r_2}{\partial x_2} & \mathbf{L} & \frac{\partial r_2}{\partial x_p} \\ \mathbf{M} & \mathbf{M} & \mathbf{O} & \mathbf{M} \\ \frac{\partial r_p}{\partial x_1} & \frac{\partial r_p}{\partial x_2} & \mathbf{L} & \frac{\partial r_p}{\partial x_p} \end{bmatrix}, \quad (\text{B.8})$$

where the subscript denotes the variate. The uncertainty propagation equation now takes the form (Ridler and Salter 2002; Willink and Hall 2002; Hall 2003; Hall 2004)

$$\mathbf{s}_r = \mathbf{J} \mathbf{s}_x \mathbf{J}^T, \quad (\text{B.9})$$

where \mathbf{s}_r is the sample covariance matrix for the output variable, and \mathbf{s}_x is the sample covariance matrix for the input variable. If Equation (B.9) is used for a univariate output, the result identically matches the expression given in Equation (B.1) for the classical uncertainty analysis method. The limitations and remedies of the multivariate uncertainty analysis are the same as those for the classical uncertainty analysis discussed above, and include linearization and numerical approximations.

B.2.2.3 Application: Converting uncertainty from real and imaginary parts to magnitude and phase

The multivariate uncertainty method is now demonstrated for converting complex-valued data from real and imaginary parts to magnitude and phase. For this example, the true mean value is $x_{true} = 4 + j3 = 5e^{j0.644}$, and the population covariance matrix is

$$\text{cov}(x_{true,R}, x_{true,I}) = \begin{bmatrix} 0.01 & 0.0021 \\ 0.0021 & 0.0049 \end{bmatrix}. \quad (\text{B.10})$$

The population distribution is a bivariate normal distribution. The sample covariance matrix is estimated from ten random data samples, and the uncertainty is propagated to the magnitude and phase using Equation (B.9). Also, each of the ten data points are converted to a polar representation, and the output sample covariance matrix of the magnitude and phase are calculated directly. The estimates of the output sample covariance matrix are then compared to illustrate the effectiveness of both methods. To conclude the example, the coverage factor is computed and the confidence region is plotted using Equation (B.3), along with a scatter plot of the data.

The sample means of the real and imaginary parts of the data are 4.01 and 3.04, respectively. The raw data are plotted in Figure B-1 along with the sample mean value, the population mean value and the estimate of the 95% confidence region around the sample mean value. The computed coverage factor from Equation (B.6) is 3.08. Notice that the major and minor ellipse axes are not parallel to the respective coordinate axes due to the correlation between the two variates. The figure shows that the estimated confidence region contains the true value of the population mean.

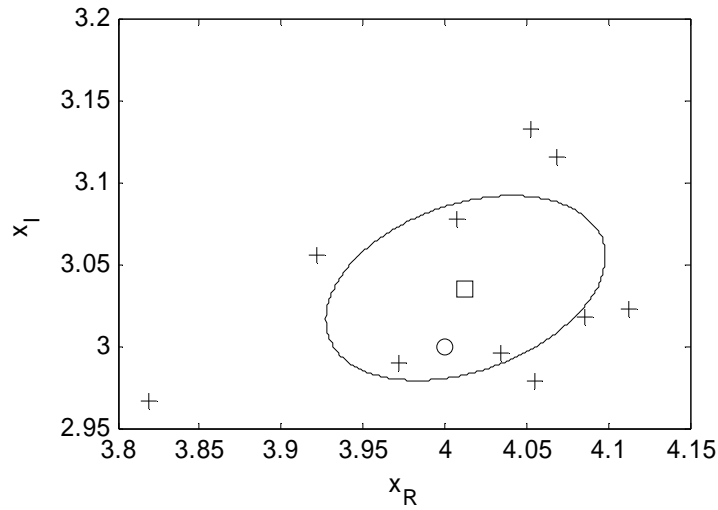


Figure B-1: A plot of the raw data and estimates for a randomly generated complex variable. + data points, □ estimated mean value, ○ true value, — 95% confidence region.

Now that the sample covariance matrix and the uncertainty region are computed and verified for the real and imaginary parts, the uncertainty can be propagated to the magnitude and phase. The Jacobian matrix becomes

$$\mathbf{J} = \begin{bmatrix} \frac{\partial |x|}{\partial x_R} & \frac{\partial |x|}{\partial x_I} \\ \frac{\partial (\angle x)}{\partial x_R} & \frac{\partial (\angle x)}{\partial x_I} \end{bmatrix} = \begin{bmatrix} \frac{x_R}{\sqrt{x_R^2 + x_I^2}} & \frac{x_I}{\sqrt{x_R^2 + x_I^2}} \\ -\frac{x_I}{x_R^2 + x_I^2} & \frac{x_R}{x_R^2 + x_I^2} \end{bmatrix}. \quad (\text{B.11})$$

The Jacobian matrix is evaluated at the sample mean values and Equation (B.9) is used to propagate the standard uncertainty. The propagated sample covariance matrix computed is

$$\mathbf{s}_{polar,propagated} = \begin{bmatrix} 0.783 & -0.0322 \\ -0.0322 & 0.0130 \end{bmatrix} \times 10^{-3}, \quad (\text{B.12})$$

and the sample covariance matrix computed directly from the 10 sample data points in polar form is

$$\mathbf{s}_{polar,direct} = \begin{bmatrix} 0.782 & -0.0335 \\ -0.0335 & 0.0130 \end{bmatrix} \times 10^{-3}. \quad (\text{B.13})$$

The element (1,1) in Equations (B.12) and (B.13) represents the variance in the magnitude, and element (2,2) represents the variance in the phase. The off-diagonal elements give the covariance between the magnitude and phase. The difference between any two corresponding elements in the two estimates for the sample covariance matrix is less than 5%. The data, the mean values, and the uncertainty estimates are shown in Figure B-2, where again the true value is contained within the confidence region. The computed coverage factor from Equation (B.6) applied to the estimates of the standard uncertainty to compute the 95% confidence estimates is 3.08. The estimated values for the magnitude and phase with uncertainties are $|\bar{x}| = 5.03 \pm 0.09$ and $\angle \bar{x} = 0.648 \pm 0.011$ [rad]. This simple example demonstrates the usefulness of the multivariate uncertainty analysis and provides some insight concerning the terms and concepts described above.

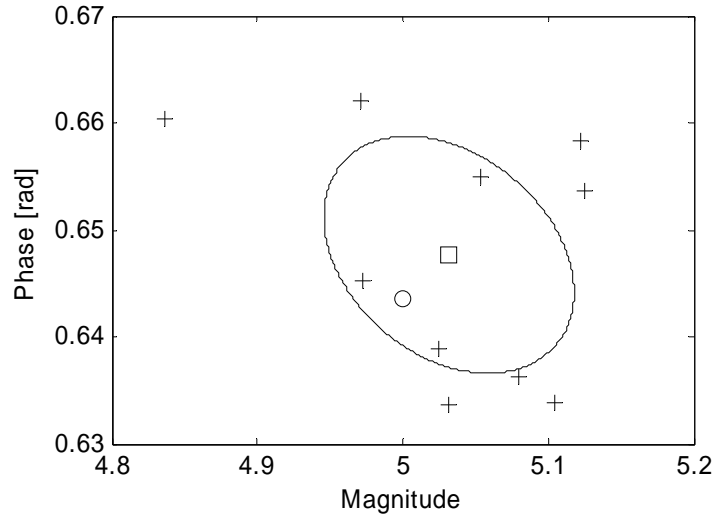


Figure B-2: A plot of the raw data and estimates in polar form for a randomly generated complex variable. + data points, \square estimated mean value, \circ true value, — 95% confidence region.

B.3 Frequency Response Function Estimates

The FRF is ubiquitous in engineering systems, yet the measurement and estimation of its uncertainty is nontrivial. There are many factors to consider when measuring and estimating a nonparametric FRF, such as analog-to-digital sampling settings, FFT settings, the assumption of a system model describing the way noise enters the signals, etc. Previous researchers have studied techniques for reducing the error in the FRF but few have studied the uncertainty in the final estimate. Bendat and Piersol (Bendat and Piersol 2000), Schmidt (Schmidt 1985) and Pintelon et al. (Pintelon, Rolain and Moer 2002) have derived expressions for the uncertainty in the FRF for some special cases. This paper, however, provides a systematic framework to extend their analysis to other cases involving periodic deterministic inputs and to propagate the resulting uncertainty to derived quantities. This section analyzes the random uncertainty for two system models and the data reduction equations for estimating the FRF using the multivariate uncertainty analysis framework. The first model is a single-input/single-output (SISO) system with

Gaussian noise added only to the output signal, which is relevant for system identification applications involving a noise-free input signal and a (perhaps) noisy output sensor signal. The expressions derived by the multivariate method are compared to the results given in Bendat and Piersol (Bendat and Piersol 2000). The second model is another SISO system, but uncorrelated Gaussian noise signals are added to both the input and output signals. The results of this case are compared to numerical simulations designed to verify the derived uncertainty expressions.

The systems studied in this dissertation are assumed to be excited by a periodic random input signal. This type of signal, which is standard in most modern spectrum analyzers, is tailored to the parameters chosen for the spectral analysis and designed to prevent spectral leakage. An example of this type is called pseudo-random noise (Randall 1987). This signal is actually deterministic and consists of a finite summation of discrete sine waves at exact bin frequencies for the spectral analysis, but each component has a random, uniformly distributed phase angle. The probability density function for the pseudo-random signal approaches a Gaussian distribution as the number of components is increased. In practice, the distribution can be approximated as Gaussian if 400 or more discrete sine waves are used. The periodicity of the input signal prevents any bias error in the estimated spectrum due to spectral leakage when a uniform or boxcar window is used; thus the remainder of this appendix assumes that there is no bias uncertainty due to leakage in the spectral estimates.

B.3.1 Output Noise Only System Model

The first system model is illustrated in Figure B-3, where x is the pseudo-random input signal, v is the noise free output of the system, n is a zero-mean, Gaussian noise

signal, y is the measured output, $H(f)$ is the FRF of the linear system, and f is the frequency. For this case, the noise signal models all measurement noise and also includes unmodeled system inputs. This model is appropriate for linear systems where noise in the input signal is negligible, such as when an input signal is the output from a function generator.

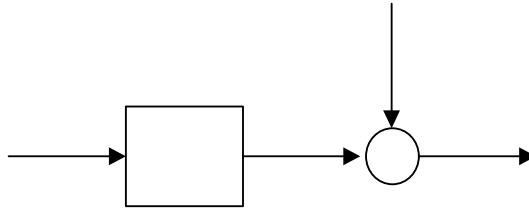


Figure B-3: System model with output noise only.

The time-domain output signal is the sum of the noise-free output and the noise

$$y(t) = v(t) + n(t) = h(t) * x(t) + n(t), \quad (\text{B.14})$$

where t is time, $h(t)$ is the impulse response function, and “*” denotes the convolution.

The Fourier transform representation is

$$Y(f) = V(f) + N(f) = H(f)X(f) + N(f). \quad (\text{B.15})$$

Equation (B.15) and the Fourier transform of the input signal X are substituted into the definitions of the auto- and cross-spectrum density functions (Bendat and Piersol 2000).

Then the spectra functions are substituted into convenient forms defining the population variance and covariance, which are

$$\text{var}[\hat{A}^0] = E[\hat{A}^0 \hat{A}^0] - \bar{A}^2, \quad (\text{B.16})$$

and

$$\text{cov}[\hat{A}^0, \hat{B}^0] = E[\hat{A}^0 \hat{B}^0] - \bar{A}\bar{B}. \quad (\text{B.17})$$

Here, \hat{A}^c and \hat{B}^c are random complex variables and \bar{A} and \bar{B} are the corresponding mean values. The resulting expressions are expanded, and the expectation operator is applied to each term, noting that the noise $N(f)$ is the only random variable and is uncorrelated with x and v . Then the equations

$$E[N_R N_I] = 0 \quad (\text{B.18})$$

and

$$E[N_R^2] = E[N_I^2] = \left(\frac{T}{4}\right) \hat{G}_{nn}, \quad (\text{B.19})$$

from Section 9.1 of Bendat and Piersol, are used to simplify the expectation operations of the Gaussian noise signal (Bendat and Piersol 2000), where \hat{G}_{nn} is the autopower spectral density of the noise signal, and T is the record length. The sample variance and sample covariance of the mean are obtained by simply dividing the variance and covariance by the number of sample records, n_{rec} . The resulting sample covariance matrix between the spectral components is

$$\mathbf{s}(\hat{G}_{xx}, \hat{G}_{yy}, \hat{C}_{xy}, \hat{Q}_{xy}) = \begin{bmatrix} 0 & 0 & 0 & 0 \\ 0 & \frac{(1 - \hat{\gamma}_{xy}^2)^2 \hat{G}_{yy}^2}{n_{rec}} & \frac{(1 - \hat{\gamma}_{xy}^2) \hat{G}_{yy} \hat{C}_{xy}}{n_{rec}} & \frac{(1 - \hat{\gamma}_{xy}^2) \hat{G}_{yy} \hat{Q}_{xy}}{n_{rec}} \\ 0 & \frac{(1 - \hat{\gamma}_{xy}^2) \hat{G}_{yy} \hat{C}_{xy}}{n_{rec}} & \frac{(1 - \hat{\gamma}_{xy}^2) \hat{G}_{xx} \hat{G}_{yy}}{2n_{rec}} & 0 \\ 0 & \frac{(1 - \hat{\gamma}_{xy}^2) \hat{G}_{yy} \hat{Q}_{xy}}{n_{rec}} & 0 & \frac{(1 - \hat{\gamma}_{xy}^2) \hat{G}_{xx} \hat{G}_{yy}}{2n_{rec}} \end{bmatrix}, \quad (\text{B.20})$$

where $\hat{\gamma}_{xy}^2 = |\hat{G}_{xy}|^2 / (\hat{G}_{xx} \hat{G}_{yy})$ is the estimate of the ordinary coherence function, \hat{G}_{xx} and \hat{G}_{yy} are the estimates of the power spectral densities of the input and output signals,

respectively, and \hat{C}_{xy} and \hat{Q}_{xy} are the estimates of the co- and quad-spectral densities. The cross-spectral density, \hat{G}_{xy} , is given by $\hat{G}_{xy} = \hat{C}_{xy} + j\hat{Q}_{xy}$. A convenient feature of this model is that the sample covariance matrix can be estimated from just the measurement of the input signal and the output signal. Since the input signal is noise-free, there is no variation in its power spectral density and it is uncorrelated with any other spectral quantity. This is reflected by the row and column of zeros in Equation (B.20). The other two zeros in the sample covariance matrix show that the co- and quad-spectral densities are also uncorrelated to each other. The remaining nonzero elements quantify the variance, if on the diagonal, and the covariance, if off the diagonal.

The uncertainty in the FRF is found by using a multivariate method to propagate the uncertainty from the spectral estimates given in Equation (B.20) to the FRF estimator. The unbiased estimator of the FRF for this system model is (Vold et al. 1984; Bendat and Piersol 2000)

$$\hat{H}_1 = \frac{\hat{G}_{xy}}{\hat{G}_{xx}}, \quad (\text{B.21})$$

or, using real and imaginary forms that are more convenient for the multivariate method,

$$\begin{bmatrix} \hat{H}_{1,R} \\ \hat{H}_{1,I} \end{bmatrix} = \begin{bmatrix} \hat{C}_{xy} \\ \hat{G}_{xx} \\ \hat{Q}_{xy} \\ \hat{G}_{xx} \end{bmatrix}. \quad (\text{B.22})$$

With the data reduction equation defined, the Jacobian matrix becomes

$$\mathbf{J}_{H_1} = \begin{bmatrix} \frac{\partial H_{1R}}{\partial G_{xx}} & \frac{\partial H_{1R}}{\partial G_{yy}} & \frac{\partial H_{1R}}{\partial C_{xy}} & \frac{\partial H_{1R}}{\partial Q_{xy}} \\ \frac{\partial H_{1I}}{\partial G_{xx}} & \frac{\partial H_{1I}}{\partial G_{yy}} & \frac{\partial H_{1I}}{\partial C_{xy}} & \frac{\partial H_{1I}}{\partial Q_{xy}} \end{bmatrix} = \begin{bmatrix} -\frac{\hat{C}_{xy}}{\hat{G}_{xx}^2} & 0 & \frac{1}{\hat{G}_{xx}} & 0 \\ -\frac{\hat{Q}_{xy}}{\hat{G}_{xx}^2} & 0 & 0 & \frac{1}{\hat{G}_{xx}} \end{bmatrix}. \quad (\text{B.23})$$

Thus, the sample covariance matrix for the estimate of the FRF is given by Equation (B.9) as

$$\mathbf{s}(\hat{H}_{1,R}, \hat{H}_{1,I}) = \begin{bmatrix} \frac{(1-\hat{\gamma}_{xy}^2)}{2n_{rec}} \frac{\hat{G}_{yy}}{\hat{G}_{xx}} & 0 \\ 0 & \frac{(1-\hat{\gamma}_{xy}^2)}{2n_{rec}} \frac{\hat{G}_{yy}}{\hat{G}_{xx}} \end{bmatrix}. \quad (\text{B.24})$$

Equation (B.24) gives the standard uncertainty that is used to propagate the uncertainty in the FRF through any subsequent data reduction equation. Using Equations (B.9) and (B.11) and simplifying gives the polar form of the uncertainty as

$$\mathbf{s}(|\hat{H}_1|, \angle \hat{H}_1) = \begin{bmatrix} \frac{(1-\gamma_{xy}^2)}{2n_{rec} \gamma_{xy}^2} |\hat{H}_1|^2 & 0 \\ 0 & \frac{(1-\gamma_{xy}^2)}{2n_{rec} \gamma_{xy}^2} \end{bmatrix}. \quad (\text{B.25})$$

The square roots of the diagonal terms in Equation (B.25) exactly match those given in Table 9.6 in Bendat and Piersol (Bendat and Piersol 2000), thus validating the multivariate technique used to derive those expressions. This approach is extended in the next section to a more complex system model where expressions for the uncertainty are not available in the literature.

Equation (B.25) shows that the uncertainty in the FRF is related to the number of spectral averages, the ordinary coherence function, and the magnitude of the FRF itself. Increasing the value of the ordinary coherence function will lower the standard

uncertainty in the FRF. This can be accomplished by designing the measurement to minimize unmodeled dynamics, to reduce any nonlinearities and to reduce noise sources. Increasing the number of averages will also decrease the sample covariance matrix but only reduces the standard uncertainties as $\propto 1/\sqrt{n_{rec}}$.

B.3.2 Uncorrelated Input/Output Noise System Model

The second model, with uncorrelated noise added to the input and output signals, is shown in Figure B-4. An example of such a system is the measurement of the mechanical impedance or admittance of a structure. Here, where u is the pseudo-random input signal, v is the noise free output of the system, m and n are uncorrelated, zero-mean, Gaussian noise signals, x is the measured input signal, y is the measured output signal, and $H(f)$ is the FRF of the system. Again, the noise signals account for measurement noise and unmodeled dynamics. This model is appropriate for systems in which an input signal is supplied to an actuator that excites the system, and the outputs of the actuator (instead of the function generator) and the system are both measured.

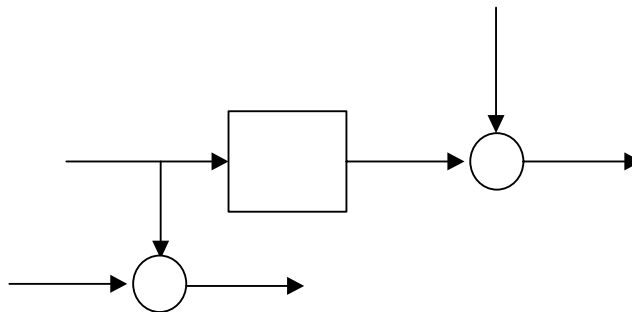


Figure B-4: System model with uncorrelated input/output noise.

The time-domain input signal is

$$x(t) = u(t) + m(t), \quad (\text{B.26})$$

and the Fourier transform representation is

$$X(f) = U(f) + M(f). \quad (\text{B.27})$$

The corresponding output signals are

$$y(t) = v(t) + n(t) = h(t) * u(t) + n(t) \quad (\text{B.28})$$

and

$$Y(f) = V(f) + N(f) = H(f)U(f) + N(f). \quad (\text{B.29})$$

The expressions for the random uncertainty and the variance are derived in a similar manner as before. One important note for this case is the assumption of uncorrelated noise sources. Since m and n are assumed to be uncorrelated, the cross-spectral density function between them is identically zero. This fact is used to simplify the variance and covariance expressions along with the expressions for the expectations of two zero-mean, Gaussian signals given in Equations (B.18) and (B.19), with corresponding version for m , and with

$$E[M_R N_R] = E[M_I N_I] = \left(\frac{T}{4}\right) \hat{C}_{mn} = 0 \quad (\text{B.30})$$

and

$$E[M_R N_I] = -E[M_I N_R] = \left(\frac{T}{4}\right) \hat{Q}_{mn} = 0, \quad (\text{B.31})$$

all provided in Section 9.1 of (Bendat and Piersol 2000), where \hat{C}_{mn} and \hat{Q}_{mn} are the co- and quad-spectral density of the two noise signals. The simplified result for the estimate of the sample covariance matrix is

$$\mathbf{s}(\hat{G}_{xx}, \hat{G}_{yy}, \hat{C}_{xy}, \hat{Q}_{xy}) = \begin{bmatrix} \frac{\hat{G}_{mm}(2\hat{G}_{xx} - \hat{G}_{mm})}{n} & 0 & \frac{\hat{G}_{mm}\hat{C}_{xy}}{n} & \frac{\hat{G}_{mm}\hat{Q}_{xy}}{n} \\ 0 & \frac{\hat{G}_{nn}(2\hat{G}_{yy} - \hat{G}_{nn})}{n} & \frac{\hat{G}_{nn}\hat{C}_{xy}}{n} & \frac{\hat{G}_{nn}\hat{Q}_{xy}}{n} \\ \frac{\hat{G}_{mm}\hat{C}_{xy}}{n} & \frac{\hat{G}_{nn}\hat{C}_{xy}}{n} & \frac{\psi}{2n} & 0 \\ \frac{\hat{G}_{mm}\hat{Q}_{xy}}{n} & \frac{\hat{G}_{nn}\hat{Q}_{xy}}{n} & 0 & \frac{\psi}{2n} \end{bmatrix}, \quad (\text{B.32})$$

where $\psi = \hat{G}_{nn}\hat{G}_{xx} + \hat{G}_{mm}\hat{G}_{yy} - \hat{G}_{mm}\hat{G}_{nn}$, \hat{G}_{mm} is an estimate of the power spectral density of the input noise signal, and \hat{G}_{nn} is an estimate of the power spectral density of the output noise signal. The zero elements (1,2) and (2,1) in Equation (B.32) show that the estimates of the power spectral density for the input signal and output signal are uncorrelated. Similarly, the zero elements (3,4) and (4,3) in Equation (B.32) show that the co- and quad-spectral densities are again uncorrelated. Note that this system is *not* completely characterized by measurements of just the input and output signals, because estimates of \hat{G}_{mm} and \hat{G}_{nn} are also required. In practice, these can be estimated by either measuring the input and output signals when the source is turned off, thus setting $u = 0$, or using application-specific noise models. With no input signal, the measured quantities arise solely due to the noise. Inherent to this approach is the assumption that the addition of the input signal does not change the estimates of the noise power spectra.

To propagate the uncertainty to the FRF, a form of the FRF must be chosen. If the definitions of the spectral estimate are substituted into Equation (B.21), the result is

$$\hat{H}_1 = H \frac{1}{1 + \frac{\hat{G}_{mm}}{\hat{G}_{uu}}}, \quad (\text{B.33})$$

where H is the true FRF. The result is clearly biased by the noise-to-signal ratio of the input (Vold, Crowley and Rocklin 1984; Bendat and Piersol 2000). Another common estimate of the FRF is

$$\hat{H}_2 = \frac{\hat{G}_{yy}}{\hat{G}_{yx}}, \quad (\text{B.34})$$

and for this case \hat{H}_2 becomes

$$\hat{H}_2 = H \left(1 + \frac{\hat{G}_{mn}}{\hat{G}_{vv}} \right), \quad (\text{B.35})$$

which is biased by the noise-to-signal ratio of the output (Vold, Crowley and Rocklin 1984; Bendat and Piersol 2000).

A third estimate for the FRF uses a geometric average (Vold, Crowley and Rocklin 1984)

$$\hat{H}_3 = \sqrt{\hat{H}_1 \hat{H}_2}. \quad (\text{B.36})$$

Substituting in the definitions for \hat{H}_1 , \hat{H}_2 , and the spectral densities, Equation (B.36)

becomes

$$\hat{H}_3 = H \sqrt{\frac{1 + \frac{\hat{G}_{mn}}{\hat{G}_{vv}}}{1 + \frac{\hat{G}_{mm}}{\hat{G}_{uu}}}}. \quad (\text{B.37})$$

Equation (B.37) shows that \hat{H}_3 is also biased, but if the input and output noise-to-signal ratios are either both small or non-negligible but the same order of magnitude, these biases tend to cancel each other, providing a better estimate of the FRF in the case with two uncorrelated noise sources (Herlufsen 1984).

One other choice for an estimate of the FRF is described in (Pintelon and Schoukens 2001b; Pintelon and Schoukens 2001a)

$$\hat{H}_{fft} = \frac{\hat{Y}}{\hat{X}}, \quad (\text{B.38})$$

which is the ratio of the Fourier transform coefficients. Substituting in the definitions of \hat{X} and \hat{Y} as given in Equations (B.15) and (B.27), Equation (B.38) becomes

$$\hat{H}_{fft} = H \left(\frac{1 + \frac{\hat{N}}{\hat{V}}}{1 + \frac{\hat{M}}{\hat{U}}} \right). \quad (\text{B.39})$$

Equation (B.39) shows that there are two disadvantages to this estimate as compared to \hat{H}_3 . First, the bias term in \hat{H}_{fft} is complex, and thus both the magnitude and phase of the estimate are biased. The bias term of \hat{H}_3 is real-valued and therefore only affects the magnitude, leaving the phase unbiased. Second, the bias on \hat{H}_3 will be smaller because of the square root function. For these reasons, \hat{H}_3 is used in this dissertation.

The resulting form of \hat{H}_3 for the multivariate uncertainty analysis is

$$\begin{bmatrix} \hat{H}_{3,R} \\ \hat{H}_{3,I} \end{bmatrix} = \begin{bmatrix} \sqrt{\frac{\hat{G}_{yy}}{\hat{G}_{xx}(\hat{C}_{xy}^2 + \hat{Q}_{xy}^2)}} \hat{C}_{xy} \\ \sqrt{\frac{\hat{G}_{yy}}{\hat{G}_{xx}(\hat{C}_{xy}^2 + \hat{Q}_{xy}^2)}} \hat{Q}_{xy} \end{bmatrix}. \quad (\text{B.40})$$

The Jacobian matrix for \hat{H}_3 is

$$\mathbf{J}_{H_3} = \begin{bmatrix} -\sqrt{\frac{\hat{G}_{yy}}{\hat{G}_{xx}}} \frac{\hat{C}_{xy}}{2\hat{G}_{xx}|\hat{G}_{xy}|} & \frac{\hat{C}_{xy}}{2\sqrt{\hat{G}_{xx}\hat{G}_{yy}|\hat{G}_{xy}|^2}} & \sqrt{\frac{\hat{G}_{yy}}{\hat{G}_{xx}}} \frac{\hat{Q}_{xy}^2}{|\hat{G}_{xy}|^3} & -\sqrt{\frac{\hat{G}_{yy}}{\hat{G}_{xx}}} \frac{\hat{C}_{xy}\hat{Q}_{xy}}{|\hat{G}_{xy}|^3} \\ -\sqrt{\frac{\hat{G}_{yy}}{\hat{G}_{xx}}} \frac{\hat{Q}_{xy}}{2\hat{G}_{xx}|\hat{G}_{xy}|} & \frac{\hat{Q}_{xy}}{2\sqrt{\hat{G}_{xx}\hat{G}_{yy}|\hat{G}_{xy}|^2}} & -\sqrt{\frac{\hat{G}_{yy}}{\hat{G}_{xx}}} \frac{\hat{C}_{xy}\hat{Q}_{xy}}{|\hat{G}_{xy}|^3} & \sqrt{\frac{\hat{G}_{yy}}{\hat{G}_{xx}}} \frac{\hat{C}_{xy}^2}{|\hat{G}_{xy}|^3} \end{bmatrix}, \quad (\text{B.41})$$

where $|\hat{G}_{xy}| = \sqrt{\hat{C}_{xy}^2 + \hat{Q}_{xy}^2}$. Equation (B.41) reveals that the uncertainty in \hat{H}_3 scales with

$\sqrt{\frac{\hat{G}_{yy}}{\hat{G}_{xx}}}$. Thus, the uncertainty increases at resonance, where the output is large for a small

input. While the opposite may appear to be true at anti-resonance, in this case the output signal is low, and this measurement condition is also often dominated by noise.

The Jacobian matrix in Equation (B.41) and the sample covariance matrix in Equation (B.32) are cumbersome and do not lend themselves to directly propagating the uncertainties analytically. A suitable option is to evaluate each term numerically and then use matrix multiplication as required by Equation (B.9). The 95% simultaneous confidence intervals for each variate are then estimated by taking the square root of the diagonal element and multiplying by the coverage factor computed from Equation (B.6), with two variates and the correct effective degrees of freedom.

A numerical simulation is performed to verify the expressions derived in this section. A normalized two degree of freedom system model is chosen for the numerical simulations to represent a system with a known FRF. The model of the FRF is

$$H = \frac{1 - \left(\frac{f}{f_1}\right)^2 + j2\zeta_1 \frac{f}{f_1}}{\left(1 - \left(\frac{f}{f_2}\right)^2 + j2\zeta_2 \frac{f}{f_2}\right) \left(1 - \left(\frac{f}{f_3}\right)^2 + j2\zeta_3 \frac{f}{f_3}\right)}, \quad (\text{B.42})$$

where f is the frequency, f_1 is the anti-resonance frequency, f_2 and f_3 are the resonance frequencies, ζ_1 is the anti-resonance damping ratio, and ζ_2 and ζ_3 are the damping ratios associated with the two resonance frequencies. The values of the parameters chosen for the simulations are $f_1 = 20$ Hz, $f_2 = 10$ Hz, $f_3 = 30$ Hz, $\zeta_1 = 0.05$, $\zeta_2 = 0.2$, and $\zeta_3 = 0.05$, as a matter of convenience. The spectral analysis is performed with 1,000 sample records of data with 1,024 samples each, and the Nyquist frequency is set to 128 Hz. The pseudo-random noise signal is constructed as the summation of 512 sine wave components at the bin frequencies with the dc component set to zero; thus the uncertainty of the dc component is ignored. Each sine wave component has unit amplitude and the power in the input noise signal is 2.56×10^{-2} units squared and the power in the output noise signals is 2.5×10^{-3} units squared. The overall signal-to-noise ratio is thus 40 dB for the input signal, x , and is 45 dB for the output signal, y . A uniform window with no overlap is used for the spectral analysis.

The procedure of the simulation is as follows. First, one block of the noise-free pseudo-random noise signal is generated and passed through the system FRF in the frequency domain to determine the noise-free output. After applying an inverse Fourier transform to both signals, independent, zero-mean, Gaussian noise signals are added to both noise-free signals in the time domain. The spectral quantities are then computed and \hat{H}_3 is estimated using Equation (B.40). This procedure is repeated for each of the 1,000 sample records. Finally, the uncertainties are computed using the results of this section via the multivariate method, as well as directly from the statistics of the 1,000 sample records.

The results of the FRF from the simulation are shown in Figure B-5. The results for this simulation are limited to the frequency range of 0 to 60 Hz to avoid the bias error described in Equation (B.37). Since the modeled system attenuates the output signal at higher frequencies, the signal-to-noise ratio of the output signal will decrease, as the power in the noise signal is assumed to be constant across all frequencies. By limiting the results to 60 Hz, the bias error in the estimated FRF is less than 0.15%. The uncertainty estimates are not shown in Figure B-5 for clarity but are plotted in Figure B-6 using both the multivariate method and the calculated statistics. The distribution of the 1,000 raw averages is a bivariate normal distribution; thus the confidence region is assumed to be symmetric and is computed by estimating the sample covariance matrix and applying the coverage factor to the square of the diagonal elements. The value of the 95% coverage factor is 2.45, as is computed from Equation (B.6). The two methods to estimate the uncertainty are essentially indistinguishable in Figure B-6. The largest difference between the two uncertainty methods is 5% for the magnitude and 1.1×10^{-2} degrees for the phase, and the average difference is 1.5% for the magnitude and 1.3×10^{-3} degrees for the phase. The true value of the FRF falls outside the uncertainty range at only 5 frequency bins for the magnitude and only 7 frequency bins for the phase. Under the assumption that for a linear system, each frequency bin is independent, the estimated value of the FRF is consistent with a 95% confidence interval.

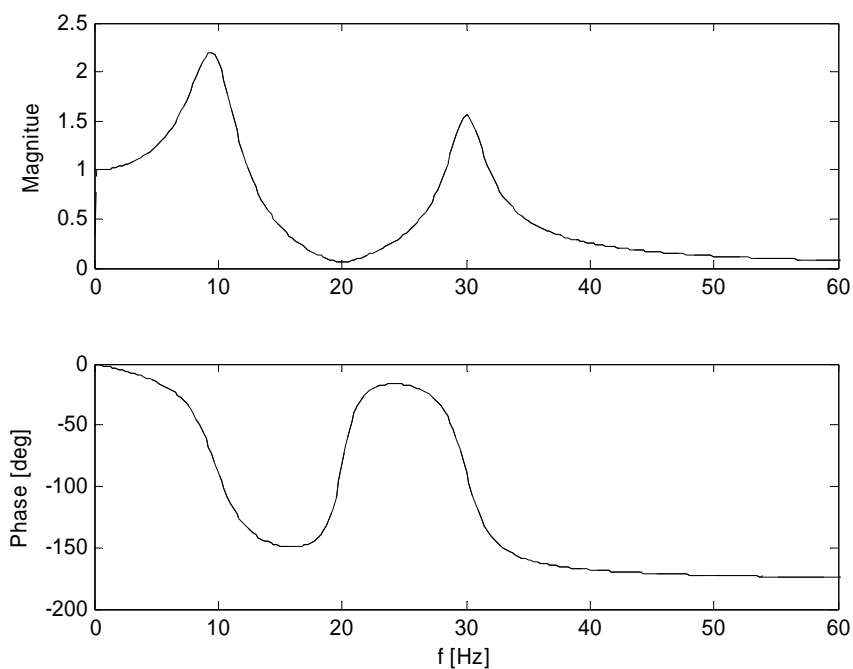


Figure B-5: Bode plot of the true FRF and the experimental estimate. — True FRF, — — FRF Estimate. The true and estimated FRF are indistinguishable.

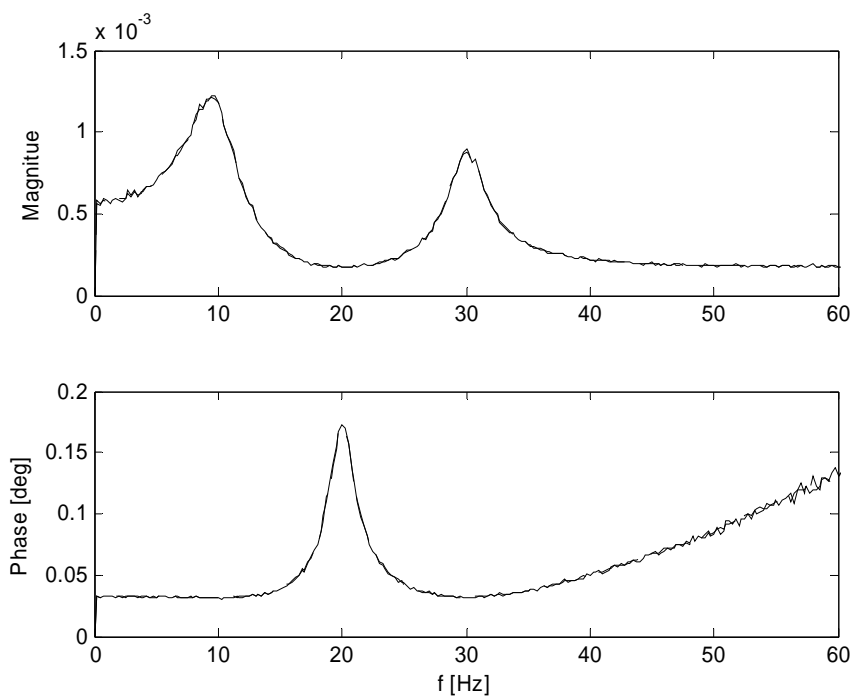


Figure B-6: Magnitude and phase plot of the uncertainty estimates. — Direct Computation, — — Multivariate Method. The two methods to estimate the uncertainty are essentially indistinguishable.

The plot of the uncertainty estimates shows that the maximum uncertainty in the magnitude is at the resonance frequencies, and the minimum is at anti-resonance frequency. Conversely, the maximum uncertainty in the phase of the FRF is at the anti-resonance. At both resonance and anti-resonance, one of the transducers will have problematic signal-to-noise ratios. Figure B-6 also shows that the uncertainty in the phase angle continues to increase as the frequency is increased. This reveals that at high frequencies the uncertainty in the phase angle may be dominant and may determine the accuracy and number of spectral averages needed to obtain the desired uncertainty in the FRF estimate.

B.4 Application: Measurement of the FRF Between Two Microphones in a Waveguide

The multivariate uncertainty method is now demonstrated on actual experimental data in an important acoustic application. The Two-Microphone Method (TMM) is the standard technique for measuring the specific acoustic impedance of a material specimen (ASTM-E1050-98 1998; ISO-10534-2:1998 1998). This method uses a waveguide with a compression driver mounted at one end, while the specimen is mounted at the other end. Two microphones are flush-mounted to the side of the waveguide at two different axial locations. The compression driver is typically excited with a broadband signal, such as a pseudo-random noise signal, to produce plane traveling waves within the waveguide over a limited frequency range. The incident waves reflect off the specimen mounted at the end and create a standing wave pattern. The FRF is measured between the two microphones and a data reduction equation is then used to compute the acoustic properties of the specimen from the FRF and a few other measurements, such as the temperature and the locations of the microphones. To estimate the uncertainty in the

computed acoustic properties, such as the complex-valued reflection coefficient, the uncertainty in the FRF must first be known. This section will estimate the random uncertainty using the multivariate method and via direct computation of the statistics.

The two measured acoustic signals are assumed to be corrupted by uncorrelated Gaussian noise. One of the microphones is assigned to be the input signal, and the other is assigned to be the output signal. Therefore, both the input and output signals contain noise, and the appropriate system model is shown in Figure B-4.

The measurement of the FRF is subject to random and bias errors, the latter of which is primarily due to calibration errors in the two measurement channels when a periodic excitation signal is used. To remove this bias, measurements are taken in original and switched positions (ASTM-E1050-98 1998; ISO-10534-2:1998 1998). The original FRF estimate, \hat{H}^o , and the switched FRF estimate, \hat{H}^s , are geometrically averaged to remove the calibration bias, resulting in

$$\hat{H} = \sqrt{\frac{\hat{H}^o}{\hat{H}^s}}. \quad (\text{B.43})$$

An appropriate form of the real and imaginary part of \hat{H} for the multivariate method is

$$\hat{H} = \begin{bmatrix} \frac{(\hat{H}_R^{o^2} + \hat{H}_I^{o^2})^{1/4}}{(\hat{H}_R^{s^2} + \hat{H}_I^{s^2})^{1/4}} \cos(\theta) \\ \frac{(\hat{H}_R^{o^2} + \hat{H}_I^{o^2})^{1/4}}{(\hat{H}_R^{s^2} + \hat{H}_I^{s^2})^{1/4}} \sin(\theta) \end{bmatrix}, \quad (\text{B.44})$$

where

$$\theta = \frac{\tan^{-1}\left(\frac{\hat{H}_I^O}{\hat{H}_R^O}\right) - \tan^{-1}\left(\frac{\hat{H}_I^S}{\hat{H}_R^S}\right)}{2}. \quad (\text{B.45})$$

The uncertainty in \hat{H} can be estimated by calculating the uncertainty in the original and switched estimates and then propagating the result to \hat{H} using the multivariate method. The input sample covariance matrix is formed by applying Equations (B.32) and (B.41) to each of the FRF in the original, $\mathbf{s}_{\hat{H}^O}$, and switched positions, $\mathbf{s}_{\hat{H}^S}$, to form their respective sample covariance matrices as outlined in Section B.3.2. The two sample covariance matrices are formed into a single input covariance matrix as

$$\mathbf{s}_{\hat{H}} = \begin{bmatrix} \mathbf{s}_{\hat{H}^O} & \mathbf{0} \\ \mathbf{0} & \mathbf{s}_{\hat{H}^S} \end{bmatrix}, \quad (\text{B.46})$$

where $\mathbf{0}$ is the zero matrix. The Jacobian for Equation (B.44) is

$$J_{\hat{H}} = \begin{bmatrix} \frac{A_{1,1}}{2|\hat{H}^O|^{3/2}|\hat{H}^S|^{1/2}} & \frac{A_{1,2}}{2|\hat{H}^O|^{3/2}|\hat{H}^S|^{1/2}} & \frac{|\hat{H}^O|^{1/2}}{2|\hat{H}^S|^{5/2}} A_{1,3} & \frac{|\hat{H}^O|^{1/2}}{2|\hat{H}^S|^{5/2}} A_{1,4} \\ \frac{A_{2,1}}{2|\hat{H}^O|^{3/2}|\hat{H}^S|^{1/2}} & \frac{A_{2,2}}{2|\hat{H}^O|^{3/2}|\hat{H}^S|^{1/2}} & \frac{|\hat{H}^O|^{1/2}}{2|\hat{H}^S|^{5/2}} A_{2,3} & \frac{|\hat{H}^O|^{1/2}}{2|\hat{H}^S|^{5/2}} A_{2,4} \end{bmatrix}, \quad (\text{B.47})$$

where $|\hat{H}^O| = \sqrt{\hat{H}_R^{O^2} + \hat{H}_I^{O^2}}$, $|\hat{H}^S| = \sqrt{\hat{H}_R^{S^2} + \hat{H}_I^{S^2}}$, and

$$\begin{aligned} A_{1,1} &= \hat{H}_R^O \cos(\theta) + \hat{H}_I^O \sin(\theta), & A_{2,1} &= -\hat{H}_I^O \cos(\theta) + \hat{H}_R^O \sin(\theta), \\ A_{1,2} &= \hat{H}_I^O \cos(\theta) - \hat{H}_R^O \sin(\theta), & A_{2,2} &= \hat{H}_R^O \cos(\theta) + \hat{H}_I^O \sin(\theta), \\ A_{1,3} &= -\hat{H}_R^S \cos(\theta) - \hat{H}_I^S \sin(\theta), & A_{2,3} &= \hat{H}_I^S \cos(\theta) - \hat{H}_R^S \sin(\theta), \\ A_{1,4} &= -\hat{H}_I^S \cos(\theta) + \hat{H}_R^S \sin(\theta), & A_{2,4} &= -\hat{H}_R^S \cos(\theta) - \hat{H}_I^S \sin(\theta). \end{aligned} \quad (\text{B.48})$$

The waveguide used in this experiment has a cross-section of 25.4 mm by 25.4 mm and a usable frequency range of 0.5 to 6.7 kHz. The acoustic pressure signals are

measured using two Brüel and Kjær Type 4138 microphones and a Brüel and Kjær Pulse Analyzer data acquisition system. The two microphone signals are sampled at a rate of 16,384 Hz with a record length of 0.125 s for a total of 100 spectral averages. A periodic pseudo-random excitation signal is generated by the Pulse system and amplified with a Techron Model 7540 power amplifier before application to the BMS 4590P compression driver. The microphones are calibrated with a Brüel and Kjær Type 4228 Pistonphone. The microphone that is initially mounted furthest from the specimen is considered the reference signal and is denoted the input signal, x . The excitation signal is then applied, and the amplifier gain is adjusted such that the sound pressure level at the reference microphone is approximately 120 dB (reference 20 μPa) for all frequency bins. Then the full-scale voltage on the two measurement channels of the Pulse system is adjusted to maximize the dynamic range of the data system. The excitation signal is turned off and the microphone signals are measured to estimate the noise spectra. The excitation signal is turned on and the two microphone signals are recorded with the microphones in their original positions and switched positions.

The time-series data are used to compute the power spectra and the cross-spectra between the two microphones for the original position and switched positions. The spectra are used to compute \hat{H}_3 using Equation (B.40) and the sample covariance matrices using Equation (B.41). The computed FRF is shown in Figure B-7. The uncertainty in the spectral estimates is propagated to the magnitude and phase of the averaged FRF via the multivariate method using Equation (B.9) with Equations (B.46) and (B.47). The value of the 95% coverage factor for the averaged FRF is 2.50, as computed from Equation (B.6) using $n_{rec} - 1$. The computation of the effective degrees

of freedom, as described by (Willink and Hall 2002), would limit the effective degrees of freedom of the averaged FRF between the least amount of degrees of freedom for an input variable (99) and the sum of all the degrees of freedom for all input variables (198). Within this range, the 95% coverage factor will only change by a maximum of 1%, and thus this change is neglected for this demonstration. The confidence intervals are computed from Equation (B.5). Then the 100 sample estimates of the FRF are used to compute the sample covariance matrix between the magnitude and phase. The estimates of the uncertainty in the magnitude and phase are shown in Figure B-8. The uncertainty estimates agree well with each other except for at 1.65, 2.70, and 4.90 kHz, where one of the microphone locations corresponds to a node in the standing wave pattern. When this occurs, one of the microphones is measuring a small acoustic pressure, and the signal is dominated by the measurement noise. The value of the FRF will theoretically tend towards zero if the output microphone is at the node and will tend towards infinity if the input microphone is at the node. In both cases, the uncertainty in the FRF becomes large. The average difference between the two estimates of the simultaneous confidence intervals is 10% for the magnitude and 11% for the phase angle, and the maximum difference is 0.04 for the magnitude and 0.05 degrees for the phase angle. Given the small number of records, these differences are deemed small enough to validate the multivariate uncertainty analysis.

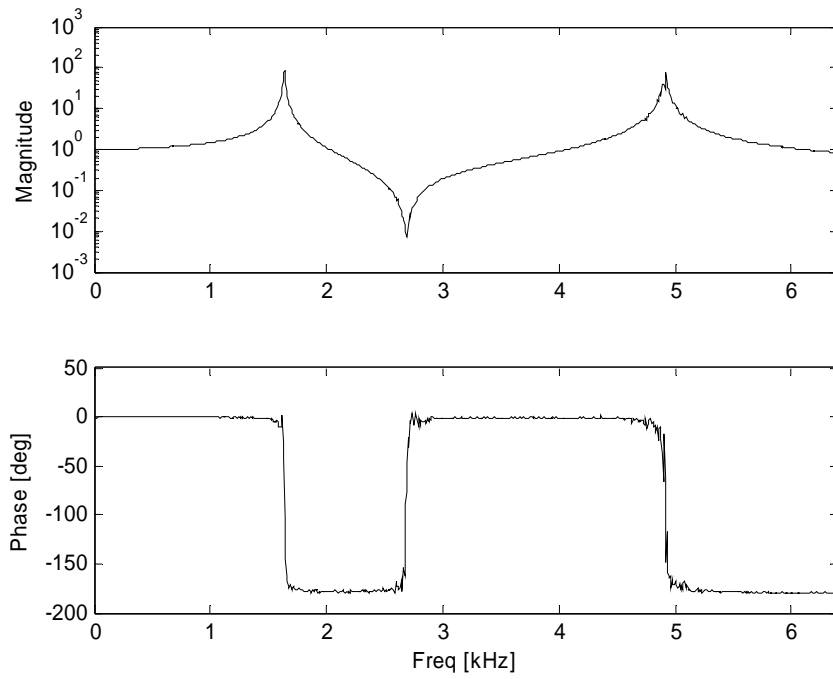


Figure B-7: The experimentally measured FRF between the two microphones.

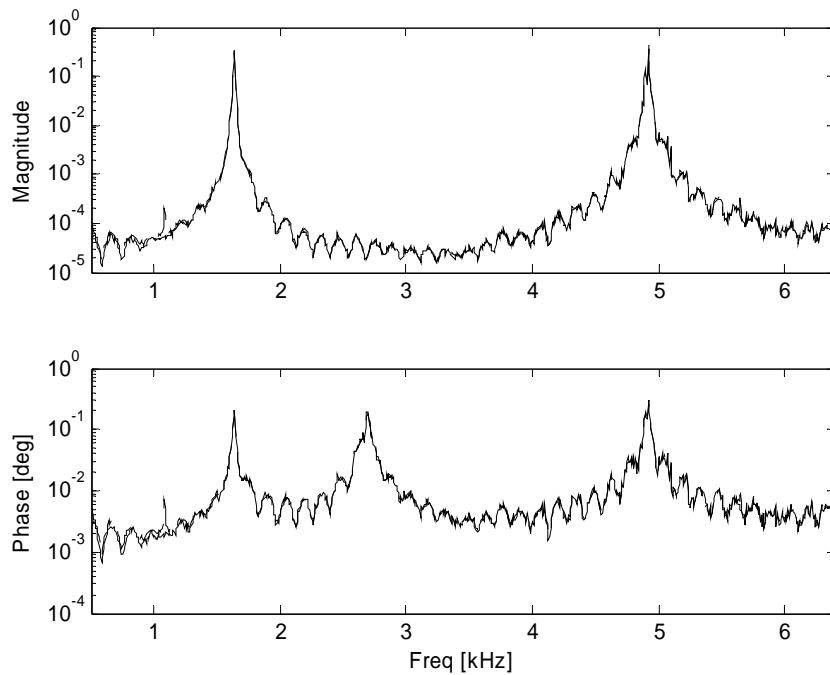


Figure B-8: Comparison for the uncertainty estimated by the multivariate method and by the direct statistics. — Direct statistics, - - Multivariate method. The two methods to estimate the uncertainty are essentially indistinguishable.

B.5 Conclusions

An experimental measurement consists of two parts, an estimate of the measured quantity and an estimate of the uncertainty. The uncertainty allows users to determine whether or not the estimate is accurate enough for their needs. Classical methods for uncertainty analysis are restricted to scalar quantities and are not applicable to complex-valued FRF estimates, an important quantity in linear, time-invariant dynamic systems. The multivariate method extends the techniques of the classical method to problems with any number of variates or dimensions. This paper applies the multivariate method to the nonparametric measurement of the FRF. Two system models were considered, one with only noise in the output signal and the other with uncorrelated noise sources in both the input and output signals. The sample covariance matrices were derived for both cases for the spectral density estimates. The results showed that, in the first model, all required information is contained in the measurement of the input and output signals, while the second model required an extra measurement to estimate the power spectra of the two noise signals. The sample covariance matrices were then propagated to the magnitude and phase of the FRF. For the first model, the derived expressions were identical to published expressions in Bendat and Piersol [1]. The second model was verified by numerical simulations, which showed that the multivariate method yielded uncertainty estimates consistent with the direct computation of the statistics from the sample records.

Finally, this appendix demonstrated the multivariate method on real experimental data involving the frequency response estimation between two microphones in an acoustic waveguide. The estimate of the uncertainty by the multivariate method yielded consistent results with the direct computation of the statistics from the sample records.

The results demonstrate that the multivariate method can be applied to experimental data that are multivariate in nature and provide reliable estimates of measurement uncertainty.

APPENDIX C
FREQUENCY RESPONSE FUNCTION BIAS UNCERTAINTY ESTIMATES

C.1 Bias Uncertainty

The bias uncertainty is the part of the total uncertainty that is constant for every measurement (Coleman and Steele 1999). For an example with ten length measurements of a rod, the bias uncertainty would be the accuracy of the ruler since the accuracy of the ruler did not change during the ten measurements. Sources of bias uncertainty are more complex for the FRF than just the accuracy of a ruler. Three sources of bias uncertainty for the FRF are the total accuracy of the analog-to-digital converter, spectral leakage due to the finite frequency resolution of discrete-time spectral analysis, and time delays that may be present between the two measurement channels. The bias uncertainty due to the accuracy of the analog-to-digital converter can be minimized by using the proper range for the device with regards to the input signal, thus maximizing the significant number of bits. In most cases where the range has been adjusted, the bias uncertainty because of the accuracy of the analog-to-digital converter can be neglected. The bias uncertainty due to a time delay in the output signal as compared to the input signal has been developed by Seybert and Hamilton (Seybert and Hamilton 1978) and by Schmidt (Schmidt 1985). Physically, a time delay in one of the measurement channels compared to the other is an effect of a phase mismatch between the responses of the two measurement channels, including phase mismatches in the transducers. Both papers concluded that the bias error is dependent on the parameter τ/T , where τ is the time delay and T is the record length. Thus the bias error can be minimized by keeping the time delay short as compared to the

record length. Schmidt also stated that the time delay bias error is a function of the window function used and gives expressions for a rectangular window and an arbitrary window (Schmidt 1985).

The bias uncertainty due to spectral leakage is more difficult to quantify than any other uncertainty source for the FRF. The FRF is computed through the use of ensemble averaging and a FFT algorithm. The advantage to this procedure is the ability to use digital computers for the processing, but the disadvantage is that the signal must be approximated. Only discrete samples and finite record lengths can be used in the computation. This gives rise to the finite frequency resolution in the estimate for the FRF, and in the coherence as well as for other spectral measurements. The bias uncertainty can be minimized through the use of properly designed window functions, but there still is a necessity to estimate a value for the bias uncertainty. Bendat and Piersol (Bendat and Piersol 2000) and Schmidt (Schmidt 1985) have derived expressions for the bias uncertainty of the FRF and coherence functions for the cases with a continuous window function and white noise excitation, but there are no expressions given for other excitation signals other than white noise. A particularly useful signal is a periodic random noise signal. This signal is designed specifically for an FFT analyzer that will be measuring the output signal of a linear system. The periodic random noise signal is a summation of discrete tones or frequencies which also are exact bin frequencies for the FFT analyzer. This allows for the signal to be periodic within a single record and allows for the use of a rectangular or boxcar window. Spectral leakage is not possible since no frequency content exists in frequencies other than the bin frequencies, therefore eliminating any bias uncertainty in the FRF at the exact bin frequencies. There

still would be a bias uncertainty in the FRF as a result of insufficient frequency resolutions, which would limit the ability to resolve fine scale detail in the FRF, such as peaks in the response for resonant absorbers, for example the SDOF liner discussed earlier. Usually, sufficient frequency resolution can be achieved through an iterative process, but still a properly designed input signal and window function should be used to avoid bias error due to spectral leakage.

To illustrate the conclusion that no bias error due to spectral leakage is present when a properly designed periodic random input signal is used, numerical simulations are preformed. These simulations first choose an analytical form for the FRF of the system model and a bandwidth for the analysis. Next, the remainder of the FFT analysis parameters are chosen and the input periodic random signal is constructed. The output signal of the modeled system is then computed by using the input signal and the analytical FRF model. The output signal and the input signal are then reduced to estimate the FRF. The estimated FRF is then compared to the analytical FRF at the bin frequencies and a root-mean-square (rms) error estimate is made for the magnitude and phase from the two FRFs to provide a representative number of the averaged error in the estimate of the FRF at each bin. This will help to illustrate the order of magnitude for the error and thus to illustrate whether or not bias error is present. Next, a nonlinear least-squares fit is used to estimate the parameters of the FRF from the simulated data. In most cases the estimated parameters would have a residual imaginary part that is over four orders of magnitude smaller than the real part. This residual imaginary is neglected since the parameters of the FRF are known to be real-valued.

The analysis parameters are chosen with consideration to the experimental goals for acoustic impedance testing. The bandwidth of interest is from 0 to 20 kHz. To accommodate the bandwidth and maintain an integer bin width, the sampling frequency chosen is 65.536 kHz with 4,096 points used per FFT block. This provides a frequency resolution of 16 Hz, which is small enough to distinguish the small scale detail of the FRF, including resonant peaks. The Nyquist frequency for this sampling frequency is 32.768 kHz, which is beyond the required 20 kHz for the bandwidth. The data in the range from 20 kHz to the Nyquist frequency is not used in the computation of the rms errors and for the nonlinear least-squares fit since it is beyond the bandwidth of interest.

The first system model chosen is a second-order system represented by a spring-mass-damper system. The analytical expression for the FRF for this model is

$$H = \frac{1}{k} \frac{1}{1 - \left(\frac{f}{f_n}\right)^2 + j2\xi\left(\frac{f}{f_n}\right)}, \quad (\text{B.49})$$

where f is the frequency, f_n is the natural frequency, ξ is the damping ratio and k is the spring constant. Evaluating equation (B.49) for $f = 0$ shows that $H(f = 0) = 1/k$ and the spring constant can easily be found from the DC response of the system.

Therefore in these simulations the FRF has been normalized by the DC response in order to isolate the parameters responsible for the dynamic response. Thus the form for the FRF used in these simulations is

$$\frac{H}{H(f = 0)} = \frac{1}{1 - \left(\frac{f}{f_n}\right)^2 + j2\xi\left(\frac{f}{f_n}\right)}. \quad (\text{B.50})$$

For these simulations, the natural frequency is varied in ten steps from 12 kHz to 12.008 kHz. The first chosen frequency corresponded exactly to a bin frequency and the last

chosen frequency corresponded to exactly halfway in between two bin frequencies. The damping ratio is chosen to be 0.01 in order to prevent the response from becoming too large at the natural frequency, which prevents numerical problems. The results for the ten simulations are given in Table C-1. The estimated natural frequencies and damping ratios matched the true values, and the rms errors for magnitude and phase were on the order of 10^{-12} and 10^{-13} , respectively. Both of the rms errors are on the order of numerical accuracy that can be expected from an FFT-based algorithm. The results show that bias error is not present.

Table C-1: Simulation results for the second-order system.

f_n [Hz]	ξ	est f_n [Hz]	est ξ	RMS Error	
				magnitude	phase [rad]
12000.0	0.01	12000.0	0.010	1E-12	5E-13
12000.8	0.01	12000.8	0.010	2E-12	5E-13
12001.6	0.01	12001.6	0.010	1E-12	5E-13
12002.4	0.01	12002.4	0.010	1E-12	5E-13
12003.2	0.01	12003.2	0.010	1E-12	5E-13
12004.0	0.01	12004.0	0.010	2E-12	5E-13
12004.8	0.01	12004.8	0.010	1E-12	5E-13
12005.6	0.01	12005.6	0.010	2E-12	5E-13
12006.4	0.01	12006.4	0.010	1E-12	5E-13
12007.2	0.01	12007.2	0.010	1E-12	5E-13
12008.0	0.01	12008.0	0.010	1E-12	5E-13

Any real measurement of the FRF would also be influenced by random noise that would not be periodic within the record length. If a rectangular window is used this would lead to spectral leakage of the random noise component. To understand how this would affect the results for the previous simulations, another simulation is performed, but this time a small random noise signal is added to the output signal before the computations of the estimated FRF. For this case a single natural frequency of 12.008 kHz is chosen and the damping ratio is left at 0.01. Only a single time record is used so

that the effective number of averages is one. The random noise signal that is added to the output signal has a total variance of 0.1 units-squared. This yielded a signal-to-noise ratio (SNR) of approximately 40-50 dB for each bin based on the output signal for the flat response region in the FRF before the resonance peak.

The results for the simulation are shown in Figure C-1. The figure shows that the estimated FRF is in good agreement with the analytical form of the FRF. The rms errors for the magnitude and phase of the FRF are 0.007 and 0.3 rads, respectively. This is a significant increase from the rms errors that were found before. The rms uncertainty estimates due to the random components, as described in Appendix B, are $1\text{E-}7$ and $2\text{E-}8$ radians for the magnitude and phase of the FRF, respectively. These uncertainty estimates only partially explain the increase in the rms errors, therefore the random noise did contribute a bias error because of spectral leakage. To verify the results, the

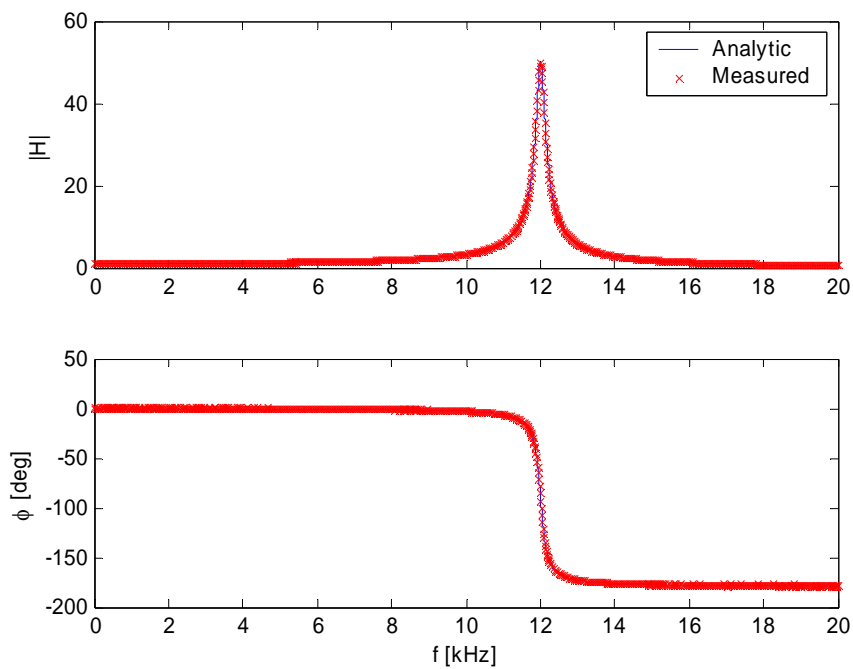


Figure C-1: FRF for the simulation with random noise.

simulation is rerun again, but this time with 1,000 spectral averages. The rms errors are $2E-4$ and $2E-4$ radians for the magnitude and phase, respectively. These results demonstrate that as the number of averages is increased, the rms error decreases as expected, since spectral averaging is known to reduce the effects of random noise. Thus spectral averages also help to reduce any spectral leakage and thus bias error due to random noise.

C.2 Conclusions

The FRF is an important estimator for the response of many engineering systems and thus its sources of error should be understood. The two major categories for uncertainty are random uncertainty and bias uncertainty. Estimates for the random uncertainty were developed in Appendix B, whereas the bias uncertainty was dealt with in this appendix. The bias uncertainty has three sources which can be eliminated, minimized, or corrected. The bias error due to the accuracy of the analog-to-digital converter can be minimized by choosing the proper range of the device to match the measured signal. The bias error due to a time delay can be minimized by keeping the time delay small compared to the record length and also can be corrected for with analytical expressions (Seybert and Hamilton 1978; Schmidt 1985). The major focus of this appendix was with the bias error due to spectral leakage. In general, there are expressions that can be used to estimate the uncertainty (Schmidt 1985; Bendat and Piersol 2000), but one special case was shown not to have any bias error. The bias error due to spectral leakage is eliminated if the input signal is a periodic within the record length.

APPENDIX D
SOUND POWER FOR WAVES PROPAGATING IN A WAVEGUIDE

This appendix documents the detailed derivation of the formulas in Chapter 4 for the power contained in the incident and reflected waves propagating in a rectangular duct.

Recall the solution to the wave equation for pressure in the frequency domain as

$$\underline{P} = \sum_m \sum_n \cos\left(\frac{m\pi}{a}x\right) \cos\left(\frac{n\pi}{b}y\right) \left(A_{mn} e^{jk_{z,mm}d} + B_{mn} e^{-jk_{z,mm}d}\right), \quad (\text{D.1})$$

and the solution for particle velocity in the d -direction as

$$\underline{U}_d = \frac{j}{\rho\omega} \frac{\partial \underline{P}}{\partial d} = \frac{j}{\rho c_0 k} \frac{\partial \underline{P}}{\partial d}. \quad (\text{D.2})$$

The derivative is given by

$$\begin{aligned} \frac{\partial \underline{P}}{\partial d} &= \sum_m \sum_n \cos\left(\frac{m\pi}{a}x\right) \cos\left(\frac{n\pi}{b}y\right) \left(jk_{z,mm} A_{mn} e^{jk_{z,mm}d} - jk_{z,mm} B_{mn} e^{-jk_{z,mm}d}\right) \\ &= \sum_m \sum_n jk_{z,mm} \cos\left(\frac{m\pi}{a}x\right) \cos\left(\frac{n\pi}{b}y\right) \left(A_{mn} e^{jk_{z,mm}d} - B_{mn} e^{-jk_{z,mm}d}\right). \end{aligned} \quad (\text{D.3})$$

Thus,

$$\underline{U}_d = -\frac{1}{\rho c_0 k} \sum_m \sum_n k_{z,mm} \cos\left(\frac{m\pi}{a}x\right) \cos\left(\frac{n\pi}{b}y\right) \left(A_{mn} e^{jk_{z,mm}d} - B_{mn} e^{-jk_{z,mm}d}\right). \quad (\text{D.4})$$

The acoustic intensity in the d -direction in the frequency domain is given by

$$I_d = \frac{1}{2} \text{Re} \left[\underline{P} \underline{U}_d^* \right]. \quad (\text{D.5})$$

Making the substitutions and simplifying,

$$I_d = \frac{1}{2} \operatorname{Re} \left[\left(\sum_m \sum_n \cos \left(\frac{m\pi}{a} x \right) \cos \left(\frac{n\pi}{b} y \right) \left(A_{mn} e^{jk_{z,mn}d} + B_{mn} e^{-jk_{z,mn}d} \right) \right) \right. \\ \left. \times \left(-\frac{1}{\rho c_0 k} \sum_m \sum_n k_{z,mn} \cos \left(\frac{m\pi}{a} x \right) \cos \left(\frac{n\pi}{b} y \right) \left(A_{mn} e^{jk_{z,mn}d} - B_{mn} e^{-jk_{z,mn}d} \right) \right)^* \right], \quad (\text{D.6})$$

$$I_d = -\frac{1}{2\rho c_0 k} \operatorname{Re} \left[\left(\sum_m \sum_n \cos \left(\frac{m\pi}{a} x \right) \cos \left(\frac{n\pi}{b} y \right) \left(A_{mn} e^{jk_{z,mn}d} + B_{mn} e^{-jk_{z,mn}d} \right) \right) \right. \\ \left. \times \left(\sum_m \sum_n k_{z,mn}^* \cos \left(\frac{m\pi}{a} x \right) \cos \left(\frac{n\pi}{b} y \right) \left(A_{mn} e^{jk_{z,mn}d} - B_{mn} e^{-jk_{z,mn}d} \right) \right)^* \right], \quad (\text{D.7})$$

$$I_d = -\frac{1}{2\rho c_0 k} \operatorname{Re} \left[\sum_m \sum_n \sum_q \sum_r k_{z,qr}^* \cos \left(\frac{m\pi}{a} x \right) \cos \left(\frac{q\pi}{a} x \right) \cos \left(\frac{n\pi}{b} y \right) \right. \\ \left. \times \cos \left(\frac{r\pi}{b} y \right) \left(A_{mn} e^{jk_{z,mn}d} + B_{mn} e^{-jk_{z,mn}d} \right) \left(A_{qr} e^{jk_{z,qr}d} - B_{qr} e^{-jk_{z,qr}d} \right)^* \right]. \quad (\text{D.8})$$

Now, integrate over the cross-section area to find the total sound power. Thus,

$$W_d(f) = \iint_S I_d dS \quad (\text{D.9})$$

$$W_d(f) = \int_{x=0}^a \int_{y=0}^b -\frac{1}{2\rho c_0 k} \operatorname{Re} \left[\sum_m \sum_n \sum_q \sum_r k_{z,qr}^* \cos \left(\frac{m\pi}{a} x \right) \cos \left(\frac{q\pi}{a} x \right) \right. \\ \left. \times \cos \left(\frac{n\pi}{b} y \right) \cos \left(\frac{r\pi}{b} y \right) \left(A_{mn} e^{jk_{z,mn}d} + B_{mn} e^{-jk_{z,mn}d} \right) \left(A_{qr} e^{jk_{z,qr}d} - B_{qr} e^{-jk_{z,qr}d} \right)^* \right] dy dx, \quad (\text{D.10})$$

$$W_d(f) = -\frac{1}{2\rho c_0 k} \operatorname{Re} \left[\sum_m \sum_n \sum_q \sum_r k_{z,qr}^* \int_{x=0}^a \cos \left(\frac{m\pi}{a} x \right) \cos \left(\frac{q\pi}{a} x \right) dx \right. \\ \left. \times \int_{y=0}^b \cos \left(\frac{n\pi}{b} y \right) \cos \left(\frac{r\pi}{b} y \right) dy \left(A_{mn} e^{jk_{z,mn}d} + B_{mn} e^{-jk_{z,mn}d} \right) \left(A_{qr} e^{jk_{z,qr}d} - B_{qr} e^{-jk_{z,qr}d} \right)^* \right]. \quad (\text{D.11})$$

Using the orthogonal condition, the two integrals are only nonzero when $m = q$ and

$n = r$. Thus the quadruple summation simplifies to a double summation as

$$W_d(f) = -\frac{1}{2\rho c_0 k} \operatorname{Re} \left[\sum_m \sum_n k_{z,mm}^* \left(\frac{a}{2} \right) \left(\frac{b}{2} \right) \left(A_{mn} e^{jk_{z,mm}d} + B_{mn} e^{-jk_{z,mm}d} \right) \right. \\ \left. \times \left(A_{mn} e^{jk_{z,mm}d} - B_{mn} e^{-jk_{z,mm}d} \right)^* \right] \quad (\text{D.12})$$

or

$$W_d(f) = -\frac{ab}{8\rho c_0 k} \operatorname{Re} \left[\sum_m \sum_n k_{z,mn}^* \left(A_{mn} e^{jk_{z,mn}d} + B_{mn} e^{-jk_{z,mn}d} \right) \times \left(A_{mn} e^{jk_{z,mn}d} - B_{mn} e^{-jk_{z,mn}d} \right)^* \right] \quad (\text{D.13})$$

Continuing to simplify

$$W_d(f) = -\frac{ab}{8\rho c_0 k} \operatorname{Re} \left[\sum_m \sum_n k_{z,mn}^* \left(A_{mn} e^{jk_{z,mn}d} + B_{mn} e^{-jk_{z,mn}d} \right) \times \left(\left(A_{mn} e^{jk_{z,mn}d} \right)^* - \left(B_{mn} e^{-jk_{z,mn}d} \right)^* \right) \right] \quad (\text{D.14})$$

$$W_d(f) = -\frac{ab}{8\rho c_0 k} \operatorname{Re} \left[\sum_m \sum_n k_{z,mn}^* \left\{ \left(A_{mn} e^{jk_{z,mn}d} \right) \left(A_{mn} e^{jk_{z,mn}d} \right)^* - \left(B_{mn} e^{-jk_{z,mn}d} \right) \left(B_{mn} e^{-jk_{z,mn}d} \right)^* \right. \right. \\ \left. \left. + \left(A_{mn} e^{jk_{z,mn}d} \right)^* \left(B_{mn} e^{-jk_{z,mn}d} \right) - \left(A_{mn} e^{jk_{z,mn}d} \right) \left(B_{mn} e^{-jk_{z,mn}d} \right)^* \right\} \right] \quad (\text{D.15})$$

$$W_d(f) = -\frac{ab}{8\rho c_0 k} \operatorname{Re} \left[\sum_m \sum_n k_{z,mn}^* \left\{ \left| A_{mn} e^{jk_{z,mn}d} \right|^2 - \left| B_{mn} e^{-jk_{z,mn}d} \right|^2 \right. \right. \\ \left. \left. + \left(A_{mn} e^{jk_{z,mn}d} \right)^* \left(B_{mn} e^{-jk_{z,mn}d} \right) - \left(A_{mn} e^{jk_{z,mn}d} \right) \left(B_{mn} e^{-jk_{z,mn}d} \right)^* \right\} \right] \quad (\text{D.16})$$

$$W_d(f) = -\frac{ab}{8\rho c_0 k} \operatorname{Re} \left[\sum_m \sum_n k_{z,mn}^* \left\{ \left(\left| A_{mn} \right| \left| e^{jk_{z,mn}d} \right| \right)^2 - \left(\left| B_{mn} \right| \left| e^{-jk_{z,mn}d} \right| \right)^2 \right. \right. \\ \left. \left. + \left(A_{mn} e^{jk_{z,mn}d} \right)^* \left(B_{mn} e^{-jk_{z,mn}d} \right) - \left(A_{mn} e^{jk_{z,mn}d} \right) \left(B_{mn} e^{-jk_{z,mn}d} \right)^* \right\} \right] \quad (\text{D.17})$$

$$W_d(f) = -\frac{ab}{8\rho c_0 k} \sum_m \sum_n \operatorname{Re} \left[k_{z,mn}^* \left\{ \left| A_{mn} \right|^2 - \left| B_{mn} \right|^2 \right. \right. \\ \left. \left. + \left(A_{mn} e^{jk_{z,mn}d} \right)^* \left(B_{mn} e^{-jk_{z,mn}d} \right) - \left(A_{mn} e^{jk_{z,mn}d} \right) \left(B_{mn} e^{-jk_{z,mn}d} \right)^* \right\} \right] \quad (\text{D.18})$$

At this point, an assumption regarding the wavenumber is needed. This derivation progresses under the assumption of isentropic flow, thus the wavenumber is real-valued and Eq. (D.14) can be simplified further. First, consider the following case:

$$\begin{aligned}
z_1^* z_2 - z_1 z_2^* &= (x_1 + jy_1)^* (x_2 + jy_2) - (x_1 + jy_1)(x_2 + jy_2)^* \\
&= (x_1 x_2 + y_1 y_2 + jx_1 y_2 - jx_2 y_1) - (x_1 x_2 + y_1 y_2 - jx_1 y_2 + jx_2 y_1), \\
&= x_1 x_2 + y_1 y_2 + jx_1 y_2 - jx_2 y_1 - x_1 x_2 - y_1 y_2 + jx_1 y_2 - jx_2 y_1 \\
&= 2j(x_1 y_2 - x_2 y_1)
\end{aligned} \tag{D.19}$$

which is purely imaginary. This is of the same form as the last two terms in the summation in Eq. (D.14). Thus, taking the real part of those terms results in zero contribution to the sum and Eq. (D.14) is simplified to

$$W_d(f) = -\frac{ab}{8\rho c_0 k} \sum_m \sum_n k_{z, mn} (|A_{mn}|^2 - |B_{mn}|^2), \tag{D.20}$$

which can easily be broken into the incident and reflected components as

$$W_i(f) = \frac{ab}{8\rho c_0 k} \sum_m \sum_n k_{z, mn} |A_{mn}|^2 \tag{D.21}$$

and

$$W_r(f) = \frac{ab}{8\rho c_0 k} \sum_m \sum_n k_{z, mn} |B_{mn}|^2. \tag{D.22}$$

To satisfy the first law of thermodynamics, the inequality, $W_r \leq W_i$, must hold.

APPENDIX E
MODAL DECOMPOSITION METHOD NUMERICAL ERROR STUDY

The main sources of error for the MDM are the signal-to-noise ratio, microphone phase mismatching, and uncertainties in the measurement of the microphone locations and the temperature. The frequency scaling of the uncertainty in the MDM is also important, as the goal of the MDM is to extend the frequency range of acoustic impedance testing. To this end, numerical studies are made of the effects of the individual error sources and the frequency scaling of the total error. These studies are done for the waveguide described in the paper and for a sound-hard termination modeled by a reflection coefficient matrix

$$\mathbf{R}^{true} = \begin{bmatrix} 0.99 & 0.01 & 0.01 & 0.01 \\ 0.01 & 0.95 & 0.01 & 0.01 \\ 0.01 & 0.01 & 0.95 & 0.01 \\ 0.02 & 0.01 & 0.01 & 0.90 \end{bmatrix} e^{j2^\circ}. \quad (\text{E.1})$$

Along with the chosen value of \mathbf{R}^{true} , four different vectors of incident complex modal amplitudes are chosen as

$$\begin{aligned} \{A\}_1^{true} &= \begin{bmatrix} 12 \\ 0.5 \\ 0.5 \\ 0.5 \end{bmatrix} e^{j(-77.4^\circ)}, \{A\}_2^{true} = \begin{bmatrix} 12 \\ 1.6 \\ 0.5 \\ 0.5 \end{bmatrix} e^{j(-7.2^\circ)}, \\ \{A\}_3^{true} &= \begin{bmatrix} 12 \\ 0.5 \\ 1.6 \\ 0.5 \end{bmatrix} e^{j(21.6^\circ)}, \{A\}_4^{true} = \begin{bmatrix} 12 \\ 0.5 \\ 0.5 \\ 1.6 \end{bmatrix} e^{j(50.4^\circ)}, \end{aligned} \quad (\text{E.2})$$

with all amplitudes given in Pascals. The reflected modal amplitudes are computed using Equation (4.9). The data are then used to calculate time-series data based on Equations (2.2) and (2.5). The time-series data are then processed using the MDM. The power contained in each error-free and noise-free signal is given in Table E-1. The ambient temperature used for the error studies is 27.7 C, thus the cut-on frequencies for the higher-order modes are 6.83 kHz for the (1,0) and (0,1) modes and 9.66 kHz for the (1,1) mode.

Table E-1: Power in Pa² for all signals from all simulation sources.

<u>Signal</u>	<u>Source 1</u>	<u>Source 2</u>	<u>Source 3</u>	<u>Source 4</u>
(x_1, y_1, d_1)	158.5	143.0	136.8	146.2
(x_2, y_2, d_1)	198.1	224.1	181.1	212.5
(x_3, y_3, d_1)	200.4	218.8	226.6	187.0
(x_4, y_4, d_1)	190.6	167.1	208.4	204.6
(x_1, y_1, d_2)	262.1	270.9	274.5	232.6
(x_2, y_2, d_2)	285.4	273.3	294.8	318.6
(x_3, y_3, d_2)	241.2	233.1	229.7	212.9
(x_4, y_4, d_2)	289.1	302.5	280.7	322.5

The root-mean-square (rms) normalized error between the true values of the complex modal amplitude and the calculated values and between elements of the calculated reflection coefficient matrix and \mathbf{R}^{true} is used as the test metric to gauge the success of the MDM. The rms normalized error is defined separately for the magnitude and phase as

$$\varepsilon_m = \sqrt{\frac{1}{\sigma} \sum_{m=0}^M \sum_{n=0}^N \left(\left(\frac{|A_{mn}^{calc}| - |A_{mn}^{true}|}{|A_{mn}^{true}|} \right)^2 + \left(\frac{|B_{mn}^{calc}| - |B_{mn}^{true}|}{|B_{mn}^{true}|} \right)^2 \right)} \quad (\text{E.3})$$

and

$$\varepsilon_p = \sqrt{\frac{1}{\sigma} \sum_{m=0}^M \sum_{n=0}^N \left(\left(\frac{\angle A_{mn}^{calc} - \angle A_{mn}^{true}}{\angle A_{mn}^{true}} \right)^2 + \left(\frac{\angle B_{mn}^{calc} - \angle B_{mn}^{true}}{\angle B_{mn}^{true}} \right)^2 \right)}, \quad (\text{E.4})$$

for the complex modal coefficients and as

$$\varepsilon_{|\mathbf{R}|} = \sqrt{\frac{1}{\sigma^2} \sum_{m=0}^{\sigma} \sum_{n=0}^{\sigma} \left(\frac{|R_{mn}^{calc}| - |R_{mn}^{true}|}{|R_{mn}^{true}|} \right)^2} \quad (\text{E.5})$$

and

$$\varepsilon_{\angle \mathbf{R}} = \sqrt{\frac{1}{\sigma^2} \sum_{m=0}^{\sigma} \sum_{n=0}^{\sigma} \left(\frac{\angle R_{mn}^{calc} - \angle R_{mn}^{true}}{\angle R_{mn}^{true}} \right)^2}, \quad (\text{E.6})$$

for the reflection coefficient matrix. The numerical studies are performed at a frequency of 12 kHz to avoid pressure nodes for the microphone locations listed in Section 3.4.1 of this dissertation. For the error-free/noise-free simulation, the rms normalized error in the modal coefficients is on the order of 10^{-14} for the magnitude and 10^{-13} for the phase, and for the reflection coefficient matrix the rms normalized error is on the order of 10^{-13} for

the magnitude and 10^{-11} for the phase. The results offer a baseline for comparison to the studies with perturbations introduced to model the error sources.

E.1 Signal-to-Noise Ratio

To test the sensitivity of the MDM to noise in the measurement signals, white noise is added to the simulated data signals. The power in the noise component is varied from 10^{-4} to 1 Pa^2 to yield a range of signal-to-noise ratios (SNR) representative of realistic values. The results for the rms normalized error for the modal coefficients are shown in Figure E-1, and Figure E-2 shows the results for the reflection coefficient matrix. To better model an actual experiment, averaging of the measured complex acoustic pressure is added to the routine. For this simulation, the noise power is fixed at 10^{-2} Pa^2 and the number of averages is varied from no averages to 10,000 averages. The results in Figure E-3 for the complex modal amplitudes and in Figure E-4 for the reflection coefficient matrix show that the rms normalized error can be significantly reduced with the use of large numbers of averages.

E.2 Microphone Phase Mismatch

The phase mismatch between the microphones is studied by introducing a phase offset into one of the microphone signals and then processing the data. The measurement location chosen is the microphone located at (x_4, y_4, d_2) . The phase offset applied is varied from 0.01 to 10 degrees. The results for the complex modal coefficients are given in Figure E-5, and Figure E-6 shows the results for the reflection coefficient matrix. The results show that a phase offset of order unity increases the error in the phase of the reflection coefficient, but reliable estimates of the complex modal amplitudes and the reflection coefficient can be obtained within an order of magnitude of 10^0 . If the

application of the data requires higher accuracy, the microphones should be phase calibrated before use.

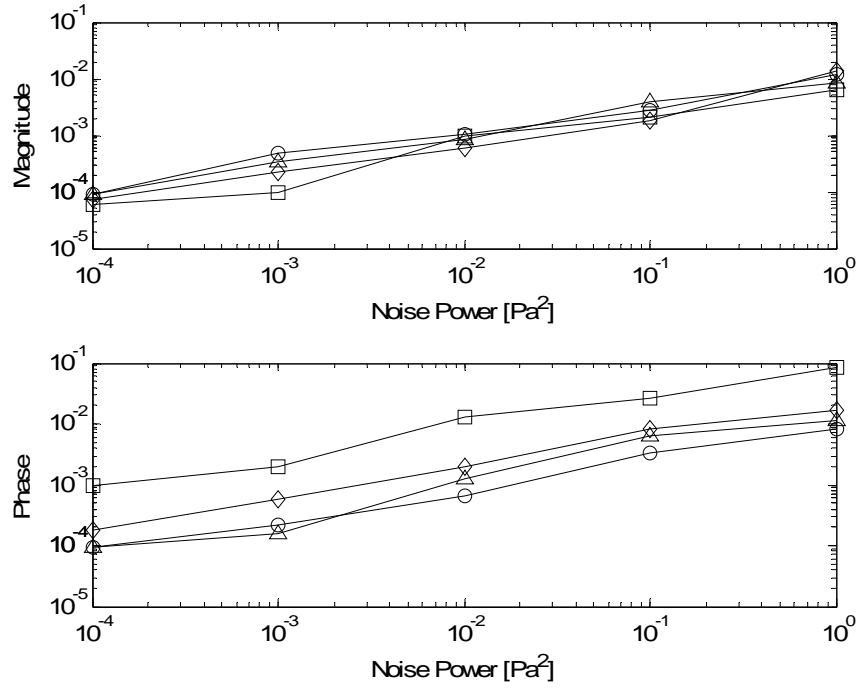


Figure E-1: The rms normalized error for the modal coefficients versus noise power added to the signals. —○— Source 1, —□— Source 2, —◇— Source 3, —△— Source 4.

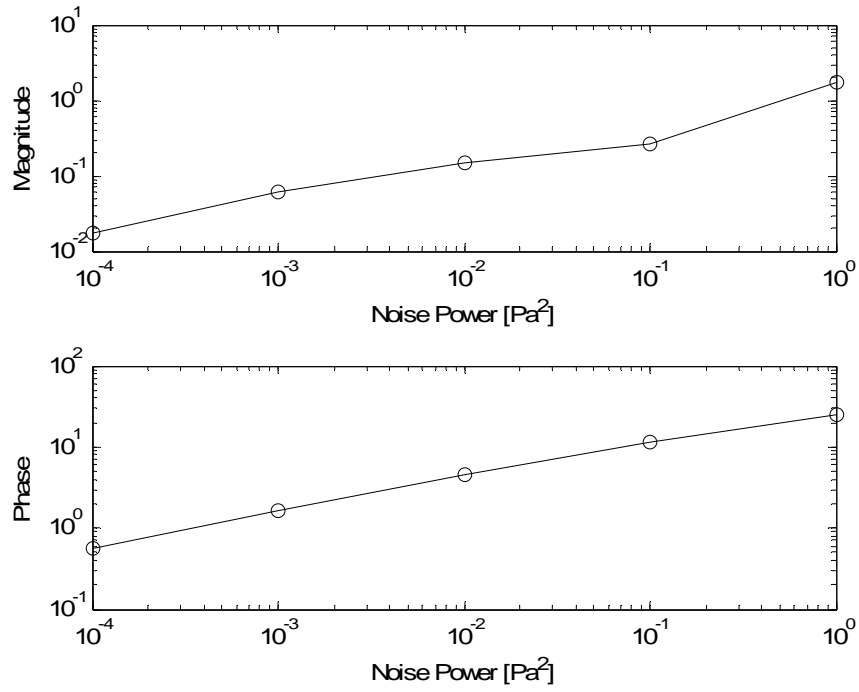


Figure E-2: The rms normalized error for the reflection coefficient matrix versus noise power.

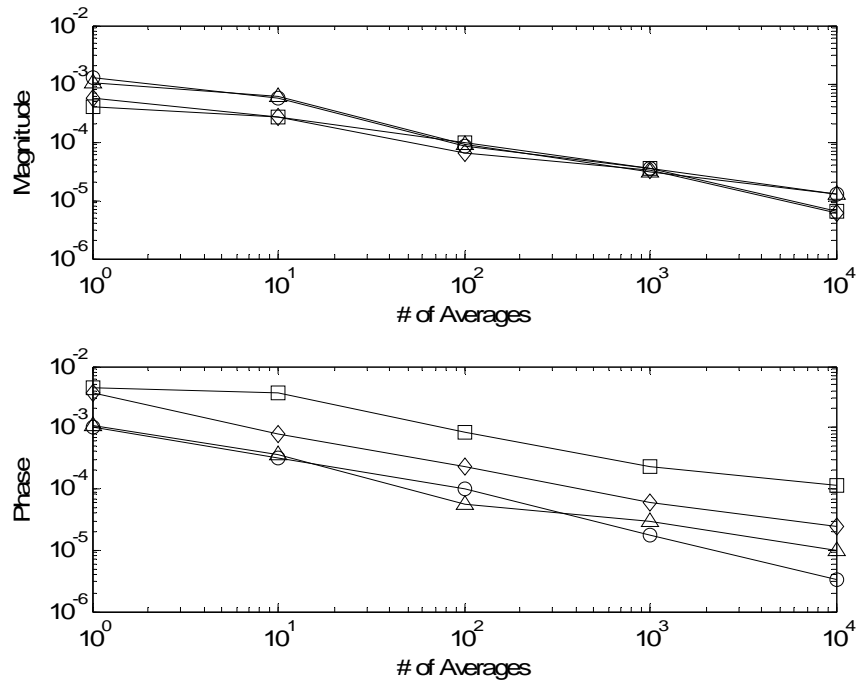


Figure E-3: The rms normalized error versus the number of averages for a noise power of 0.01 Pa^2 . —○— Source 1, —□— Source 2, —◇— Source 3, —△— Source 4.

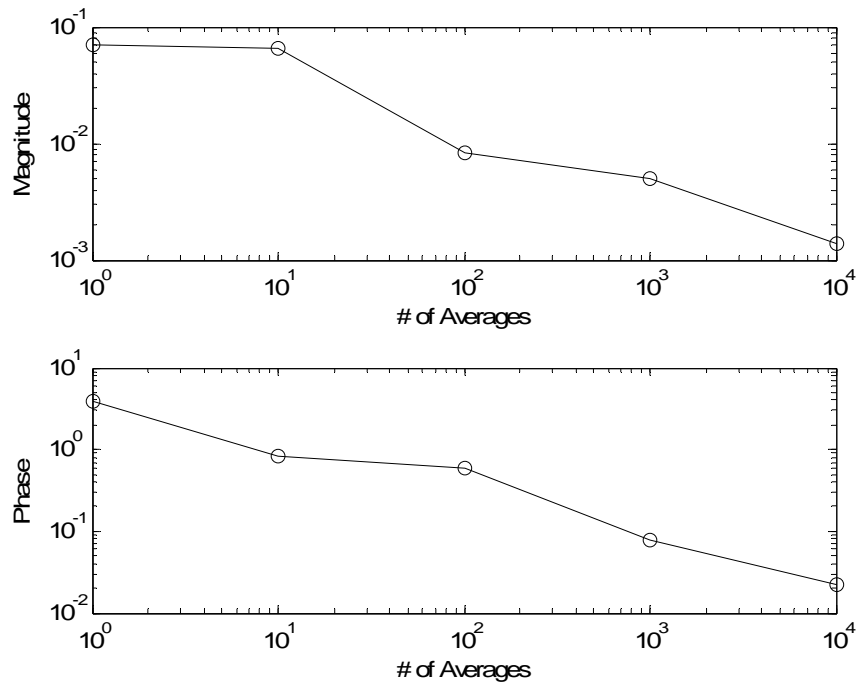


Figure E-4: The rms normalized error for the reflection coefficient versus the number of averages for a noise power of 0.01 Pa^2 .

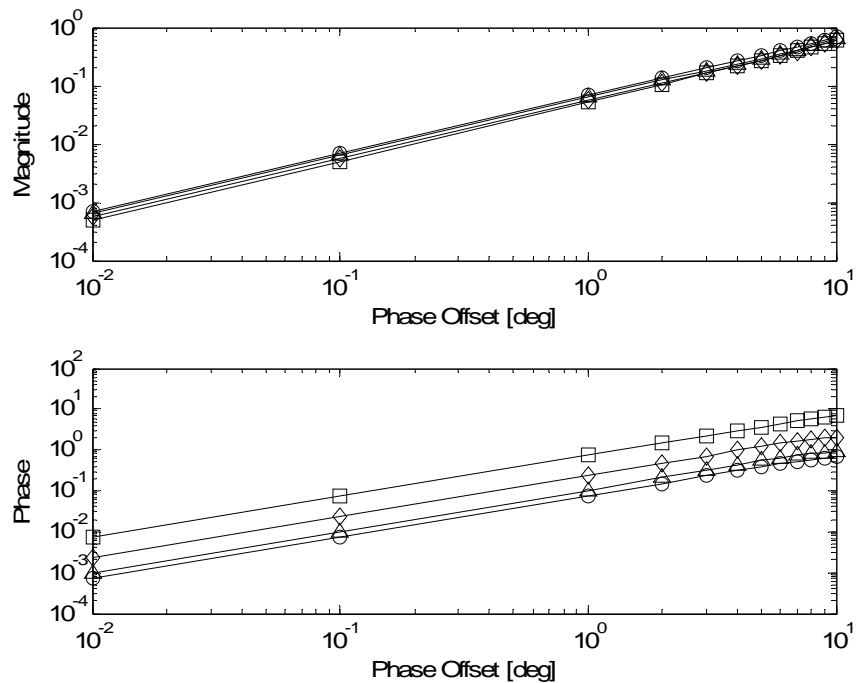


Figure E-5: The rms normalized error for the modal coefficients versus a phase error applied to microphone 4 in group 2 for each source. \circ Source 1, \square Source 2, \diamond Source 3, \triangle Source 4.

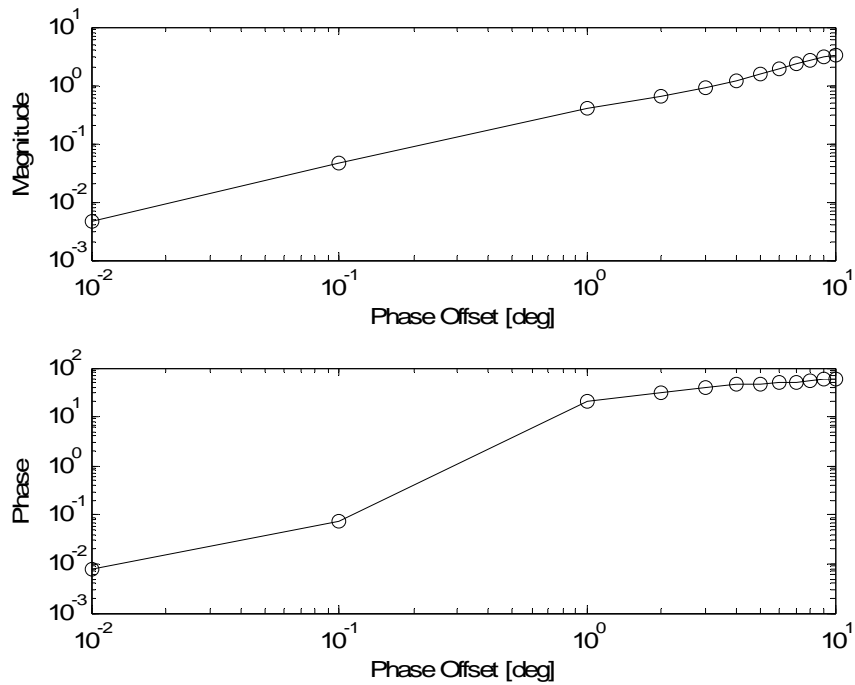


Figure E-6: The rms normalized error for the reflection coefficient matrix versus a phase error applied to microphone 4 in group 2 for all sources.

E.3 Microphone Locations

Error in the location of the microphone measurements is studied by applying an error to one of the microphone locations before data reduction with the MDM. The applied location error is varied from 0.001 to 1 mm and is applied to the microphone located at (x_1, y_1, d_1) . The results for the rms normalized error are shown in Figure E-7 for the complex modal amplitudes and in Figure E-8 for the reflection coefficient matrix. The error in the phase of both the complex modal amplitudes and the reflection coefficient matrix is larger than in the magnitude. Physically, this is realistic, as a location error can also be modeled as a phase error for propagating waves. Combined with studies of the uncertainty in the TMM, this error source for the MDM will be a strong function of frequency.

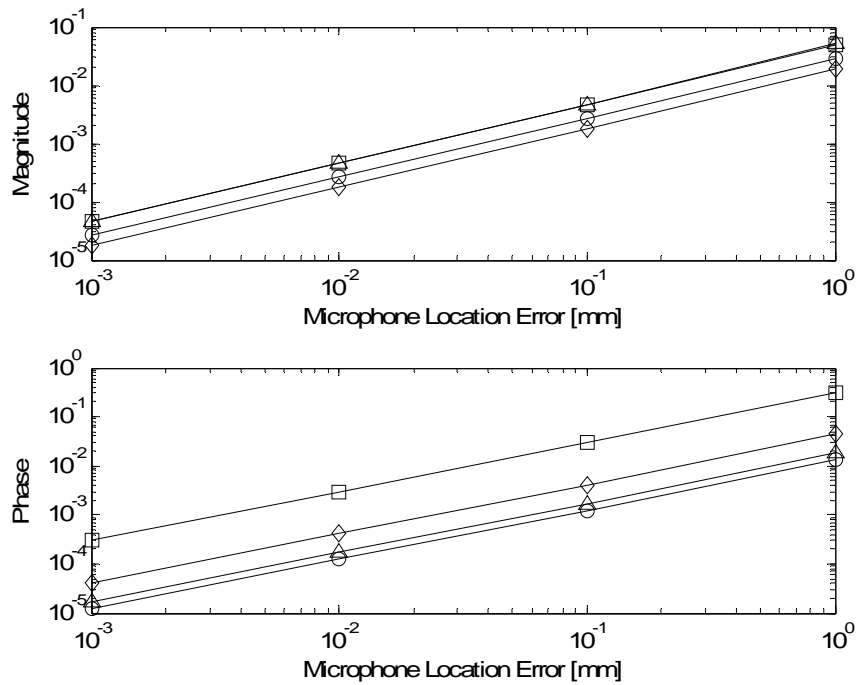


Figure E-7: The rms normalized error for the modal coefficients versus a microphone location error applied to microphone 1 in group 1 for each source. —○— Source 1, —□— Source 2, —◇— Source 3, —△— Source 4.

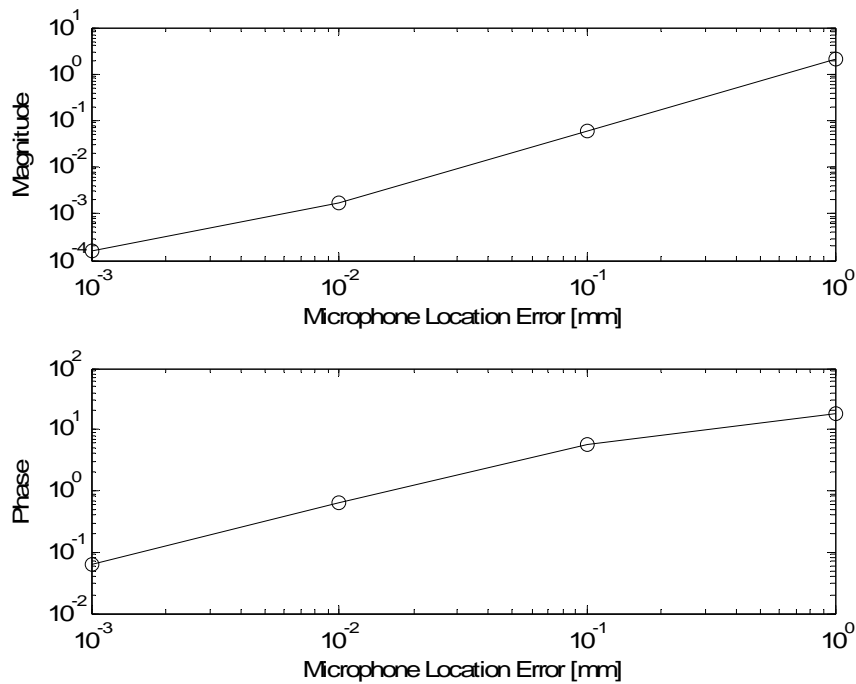


Figure E-8: The rms normalized error for the reflection coefficient matrix versus a microphone location error applied to microphone 1 in group 1 for all sources.

E.4 Speed of Sound

The last error source studied individually is errors in the estimate for the speed of sound. Under the assumption of lossless acoustics with an ideal gas, the speed of sound is solely related to the temperature via the isentropic speed of sound equation

$$c_0 = \sqrt{\gamma R_{gas} T}, \quad (E.7)$$

where γ is the ratio of specific heats, R_{gas} is the ideal gas constant, and T is the absolute temperature. With these assumptions and this equation, studying the error in the speed of sound is reduced to studying the error in the measurement of temperature. This is done by applying a perturbation to temperature before processing with the MDM. The perturbation is varied from 0.01 to 10 K and the results are given in Figure E-9 for the complex modal amplitudes and in Figure E-10 for the reflection coefficient matrix. The

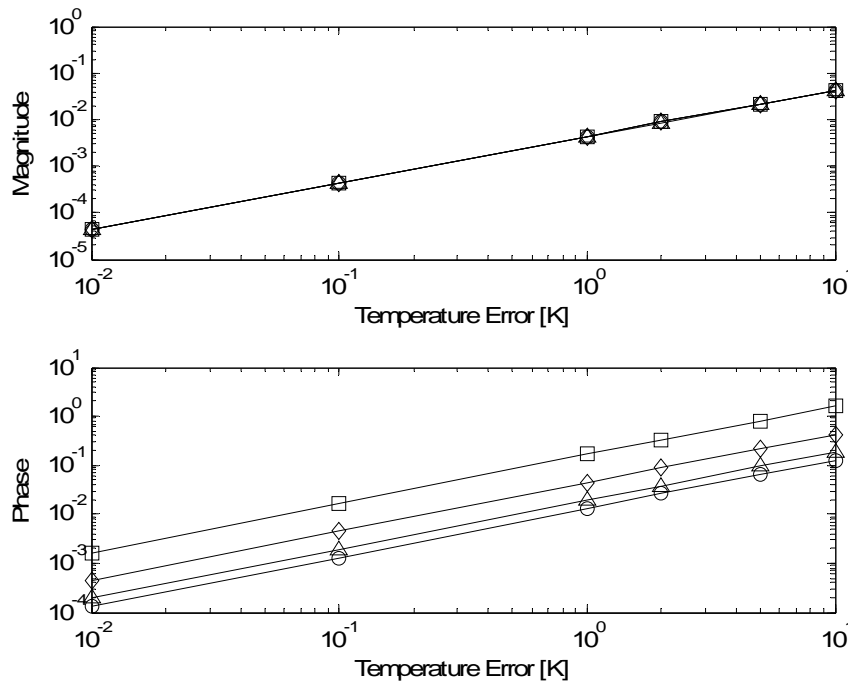


Figure E-9: The rms normalized error for the modal coefficients versus a temperature error. —○— Source 1, —□— Source 2, —◇— Source 3, —△— Source 4.

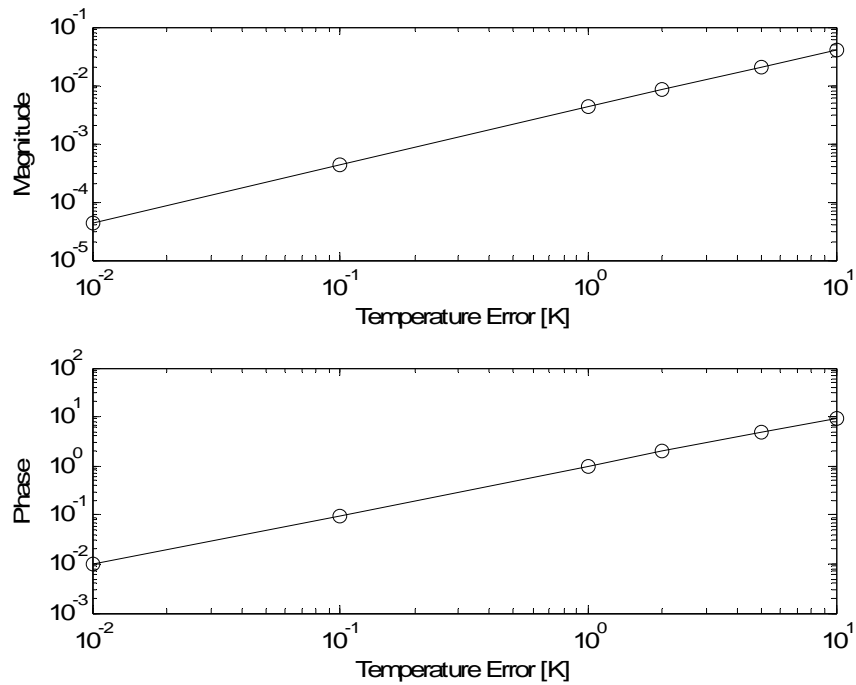


Figure E-10: The rms normalized error for the reflection coefficient matrix versus a temperature error.

E.5 Frequency

Knowledge of the frequency scaling of the error sources is desirable, since the MDM is not applied only to a single frequency. For this study, the error in the input measurements is held constant and the simulation is swept across the frequency range of 1 to 12 kHz in steps of 1 kHz. The errors used in this study are designed to resemble uncertainty levels to which an actual experimental measurement may be subject. The noise power added to the signals is $10^{-2} Pa^2$, processed with 1,000 averages. The applied phase offset is 0.1 degree, the applied location error to a single microphone location is 0.01 mm, and the applied temperature error is 1 K. The results are shown in Figure E-11 for the complex modal amplitudes and in Figure E-12 for the reflection coefficient

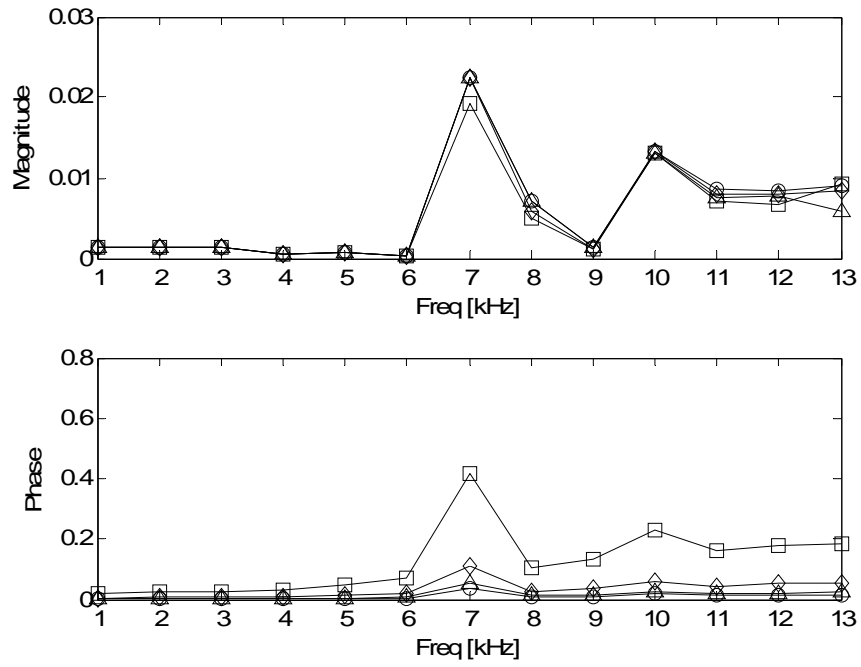


Figure E-11: The rms normalized error for the modal coefficients versus frequency.
 —○— Source 1, —□— Source 2, —◇— Source 3, —△— Source 4.

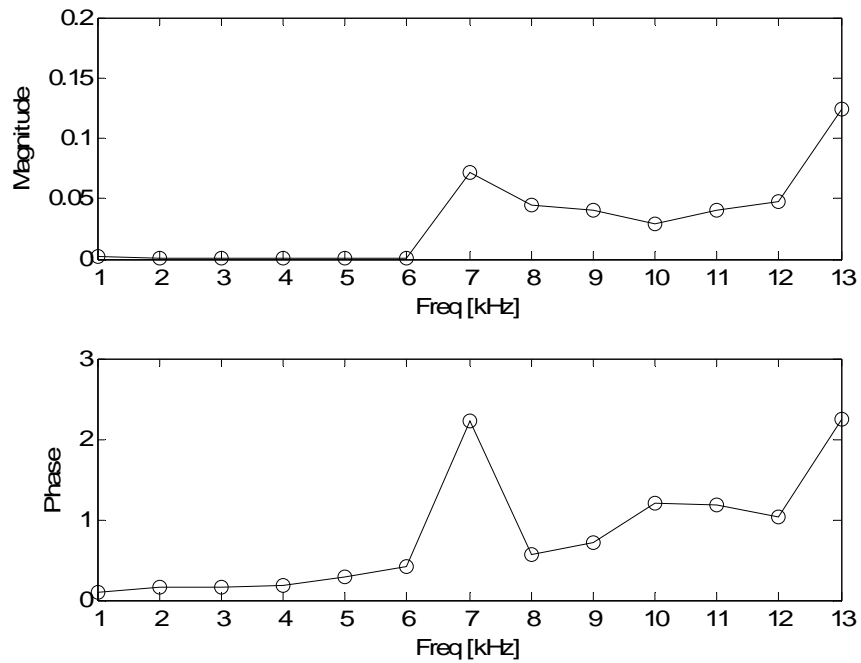


Figure E-12: The rms normalized error for the reflection coefficient matrix versus frequency.

matrix. The results for the frequency ranges of 1 to 6 kHz only have plane wave propagation, whereas higher-order modes are present in the remaining frequency ranges. The results show that the rms normalized error increases dramatically in the vicinity of a cut-on frequency.

E.6 Conclusions

The results for the error study presented here show that the MDM has the potential to provide accurate and reliable results for acoustic impedance measurements, except near the cut-on frequencies. The actual experimental uncertainty values will still be needed for experimental data to concisely define the accuracy of any measurements made with this technique and to evaluate it compared to the requirements of the application. The accuracy of the results from the MDM could be improved upon by increasing the accuracy of the measurement instruments. The largest improvements to the accuracy can be had from improvements in the measurements of the microphone locations and temperature and from improvements in the phase matching between the microphones. The temperature measurement can be improved by calibrating the measurement device before use to achieve uncertainties on the order of 0.1 K, the microphone location measurements can be improved by using a high resolution measurement system to measure the locations, and the phase matching of the microphones can be improved by phase calibrating before use. Since this error study was performed with simulated time-series data, the interesting behavior of the rms error near the cut-on frequencies is due to the data reduction algorithm. Further studies are necessary to determine the exact cause of the rise in the rms error.

APPENDIX F
AUXILIARY GRAPHS

This appendix presents auxiliary data graphs from the experimental measurements of the different specimens.

F.1 CT65

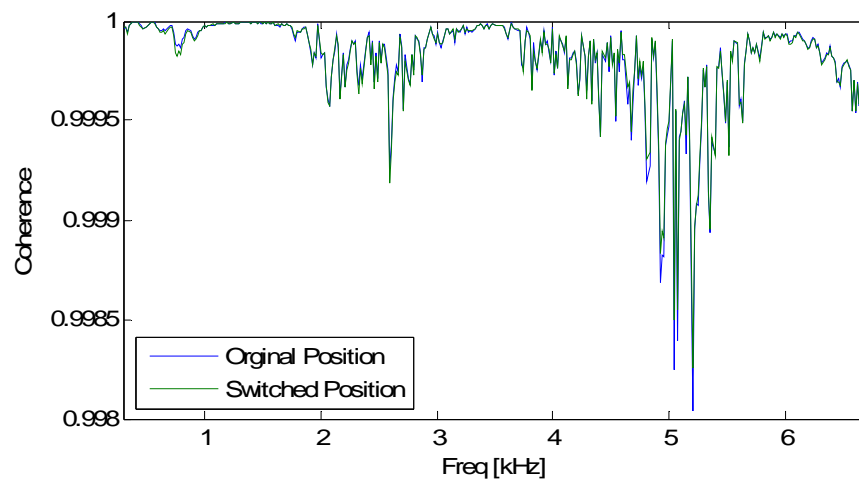


Figure F-1: Ordinary coherence function for the TMM measurement of CT65.

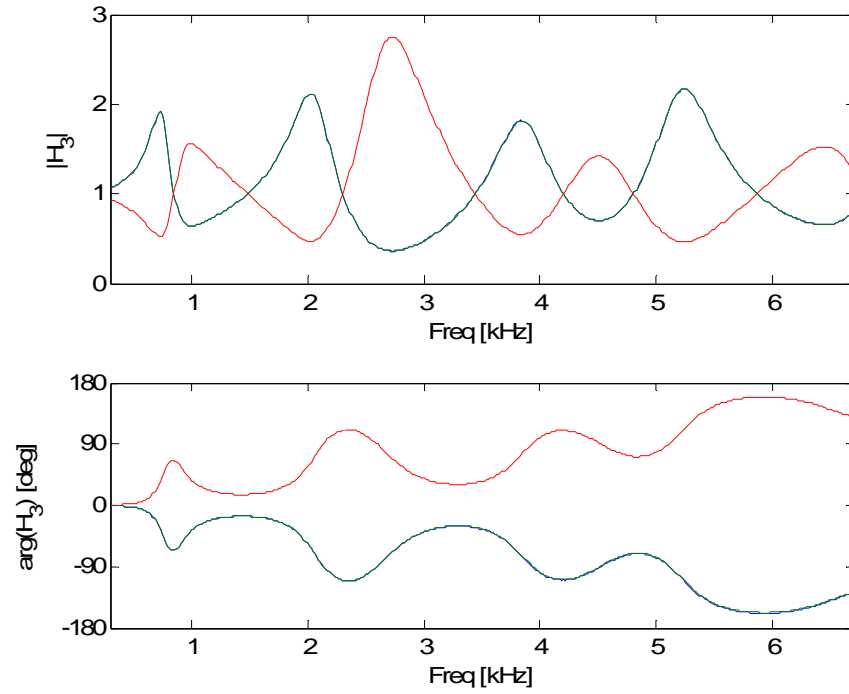


Figure F-2: The measured FRF for CT65 for the TMM. — Averaged, — Original, and — Switched.

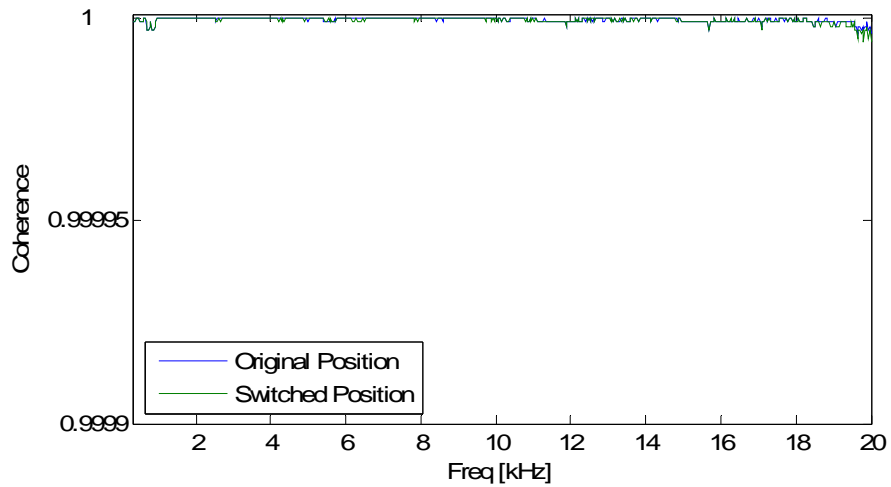


Figure F-3: Ordinary coherence function for the high frequency TMM measurement of CT65.

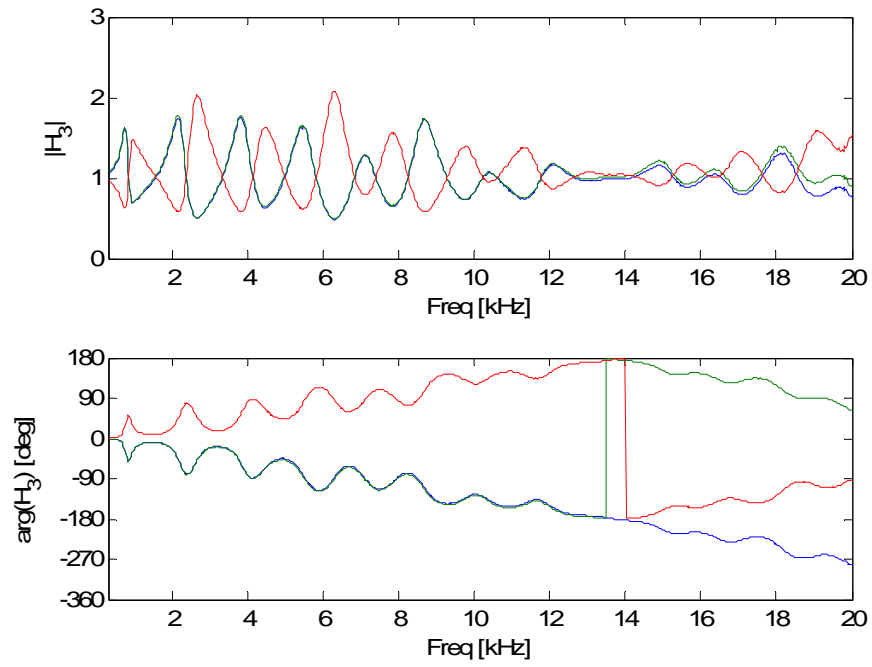


Figure F-4: The measured FRF for CT65 for the high frequency TMM. — Averaged, — Original, and — Switched.

F.2 CT73

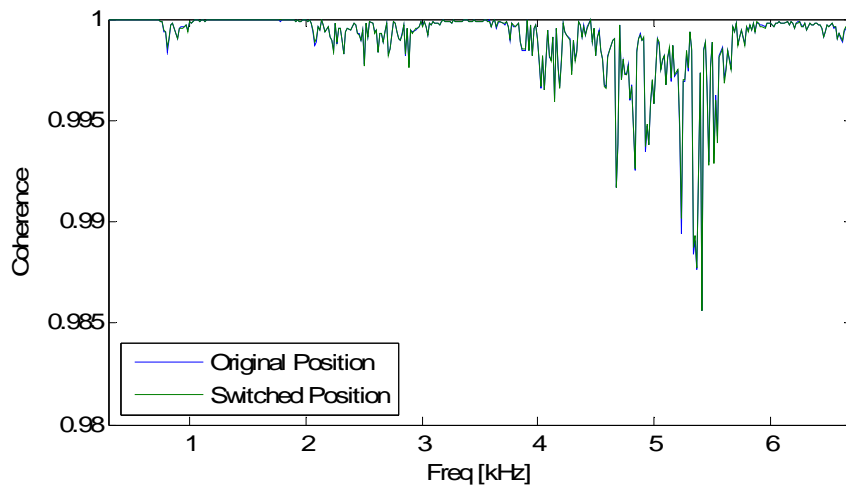


Figure F-5: Ordinary coherence function for the TMM measurement of CT73.

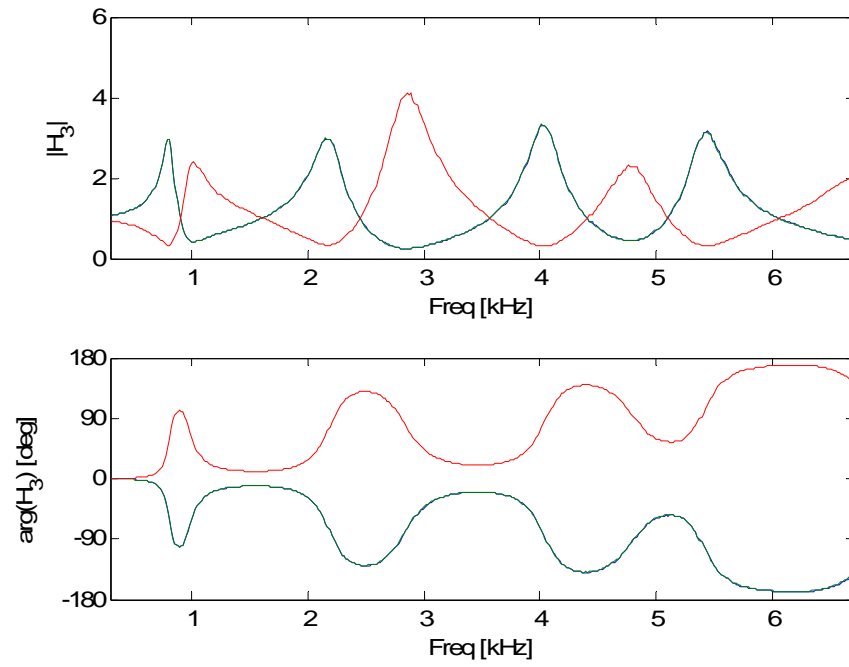


Figure F-6: The measured FRF for CT73 for the TMM. — Averaged, — Original, and — Switched.

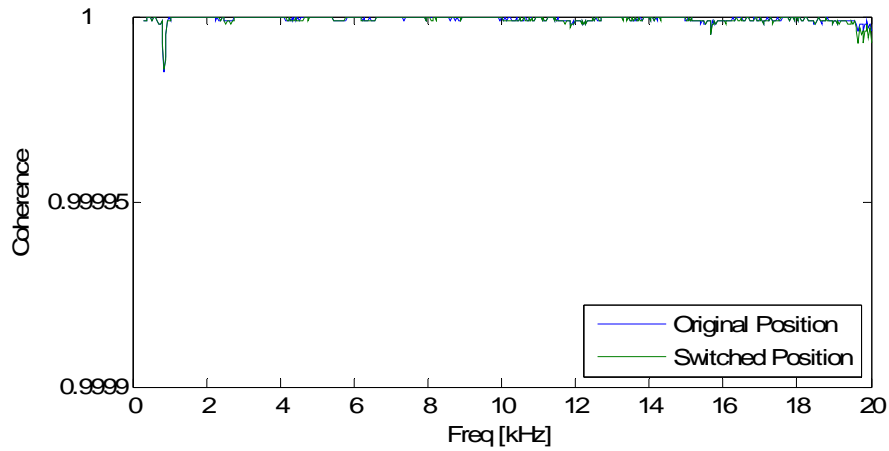


Figure F-7: Ordinary coherence function for the high frequency TMM measurement of CT73.

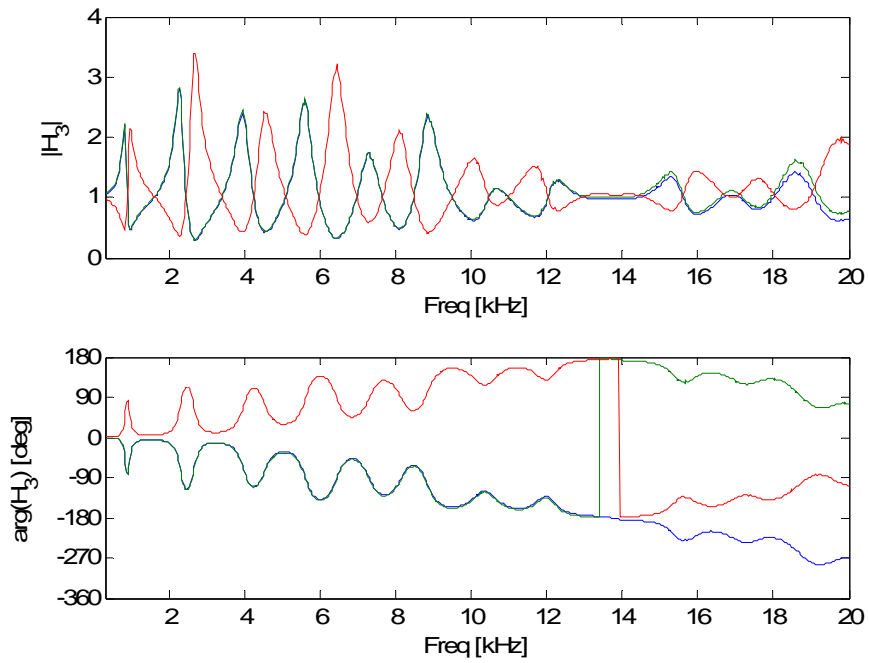


Figure F-8: The measured FRF for CT73 for the high frequency TMM. — Averaged, — Original, and — Switched.

F.3 Rigid Termination

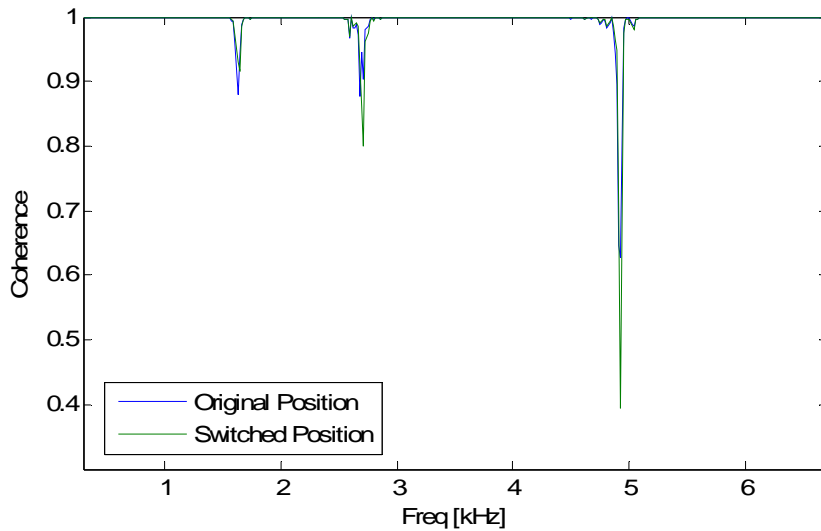


Figure F-9: Ordinary coherence function between the two microphones for the TMM measurement of the rigid termination.

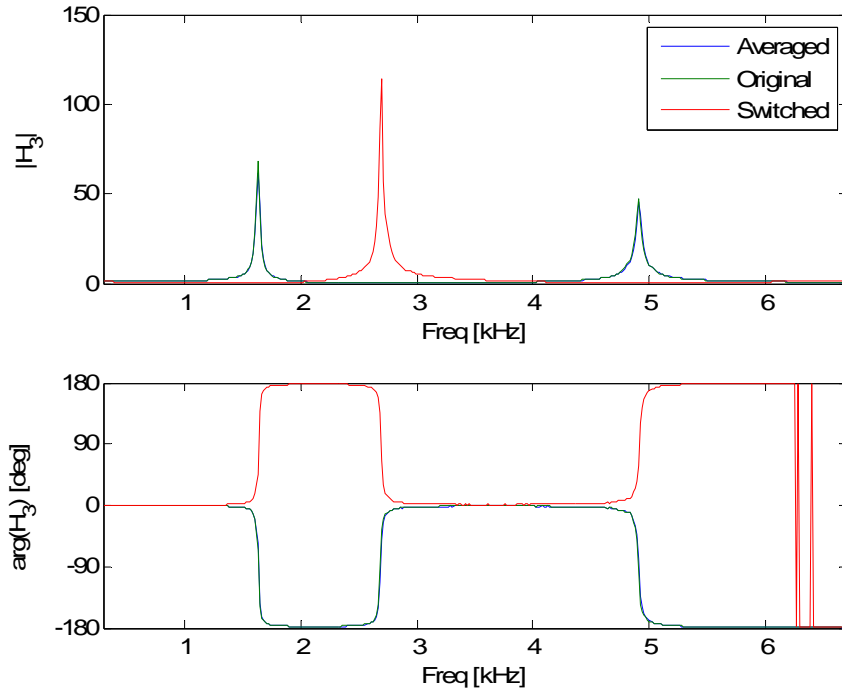


Figure F-10: The measured FRF for the rigid termination for the TMM.

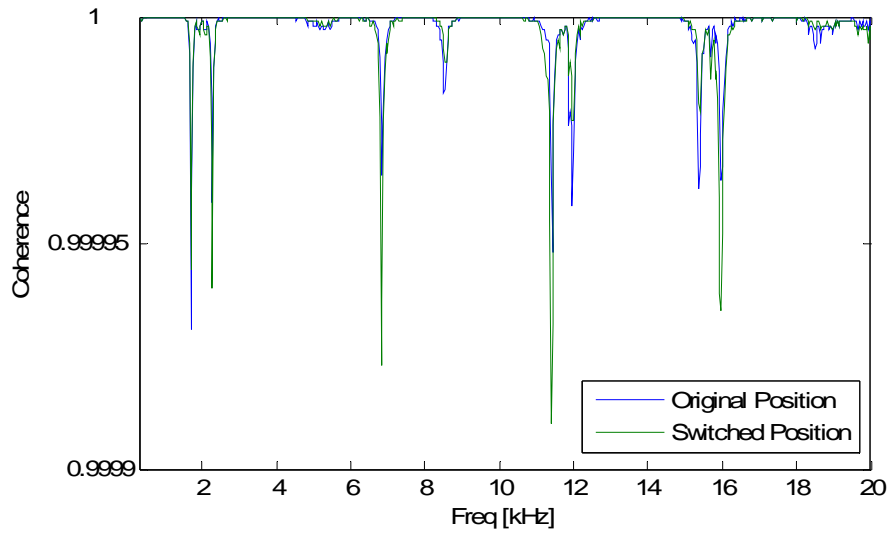


Figure F-11: Ordinary coherence function for the high frequency TMM measurement of the rigid termination.

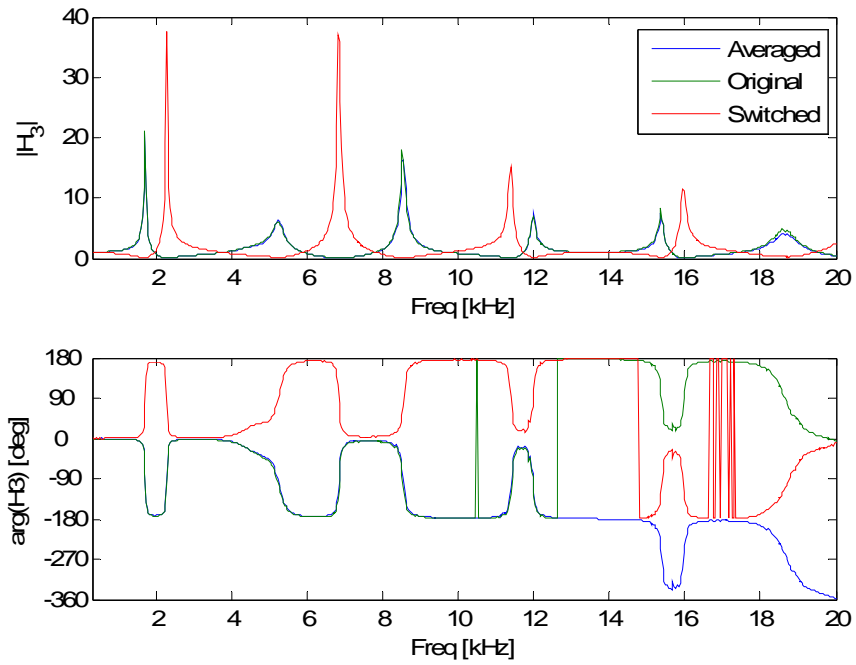


Figure F-12: The measured FRF for the rigid termination for the high frequency TMM.

F.4 SDOF Liner

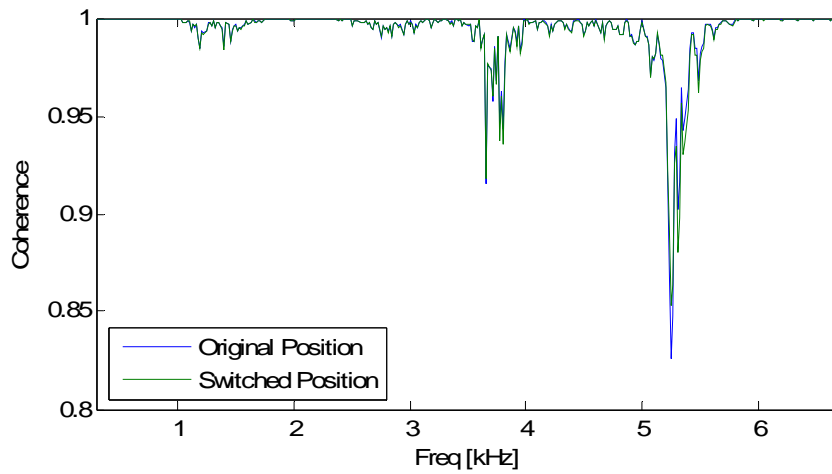


Figure F-13: Ordinary coherence function for the TMM measurement of the SDOF specimen.

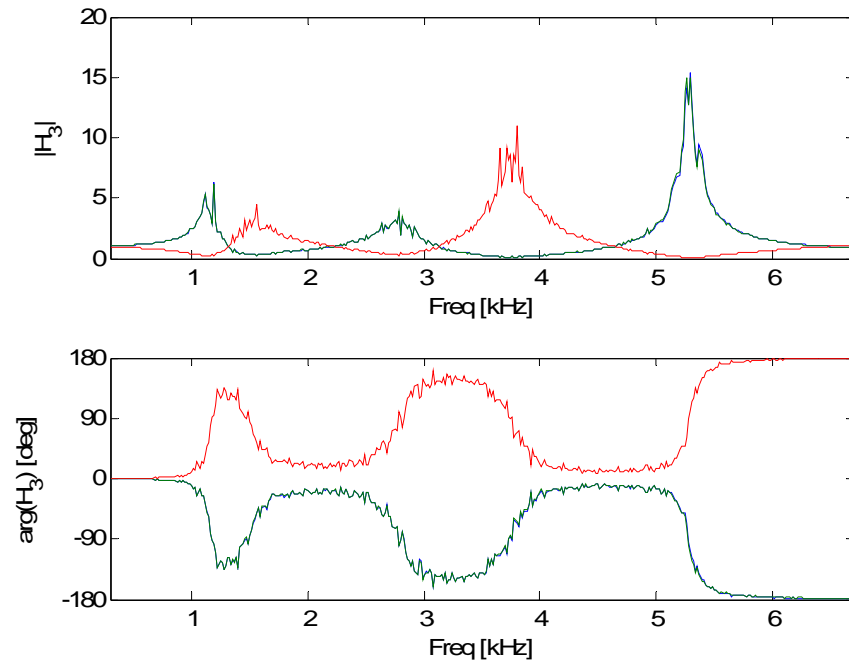


Figure F-14: The measured FRF for the SDOF specimen for the TMM.

APPENDIX G COMPUTER CODES

G.1 TMM Program Files

G.1.1 TMM Program Readme File

The file format for the input files for tmmv5.m are given in this document. Both of the files are to be tab delimited text files. Note the convention that microphone 1 is the microphone farther from the test specimen and microphone 2 is the microphone closer to the test specimen. The first file is to contain the data on the experimental setup (from LabVIEW) as such:

tube number (0 = 1 inch PWT, 1 = 8.5 mm PWT)
of effective averages
mic location 2 [m] (closer to the specimen)
uncertainty in mic location 2
number of measurements of l
mic spacing [m]
uncertainty in mic spacing
number of measurements of s
Temp [C]
uncertainty in Temp [C]
number of measurements of T
press [kPa]
uncertainty in press [kPa]
number of measurements of P

The second file is to contain the measured data. Each entry should be a column array with each column containing the following information in the given order (from Pulse). The uncertainty analysis used in the tmmv4.m code assumes that there is no biased error in the measurement of the frequency responsefunction. This is done by

using a periodic or pseudo random signal for the source. Gmm and Gnn are estimates of the noise spectrum from microphone 1 and 2 respectively.

freq[Hz] Gxxo Gyyo Cxyo Qxyo Re[TFo] Im[TFo] coho Gxxs Gyys Cxys Qxys Re[TFs]
Im[TFs] cohs Gmm Gnn SPLref[dBspl]

G.1.2 Pulse to MATLAB Conversion Program

```
% pulsereadv6.m
%
% Todd Schultz      9/2/2005
%
%
% This program is designed to call the BKfiles.m script generated from
the
% B&K Pulse system to read in the data files and then to assign useful
% variable names to the required data from the tmmv6.m script file.
Then
% the data is saved to the current directory in a mat file formate for
use
% by the tmmv6 script.
%
% Inputs
% This file must be run in the same folder as the BKfiles.m and the
text data files.
% Must pull of the frequency array, frequency response for both the
original and switched and
% the coherence for both the original and switched and the reference
sound pressure level.
%
% Outputs
% f = frequency array [Hz]
% w = angular frequency array [rad/s]
% navg = effective number of spectral averages
% Gxxo = power spectrum of mic 1
% Gyyo = power spectrum of mic 2
% Cxyo = co-spectrum
% Qxyo = quad-spectrum
% Gxyo = Cxyo+j*Qxyo;
% h12o = frequency response function with the mics in the original
position
% coho = coherence with the mics in the original position
% Gxxs = power spectrum of mic 1
% Gyys = power spectrum of mic 2
% Cxys = co-spectrum
% Qxys = quad-spectrum
% Gxys = Cxys+j*Qxys;
% h12s = frequency response function with the mics in the switched
position
% cohs = coherence with the mics in the switched position
% Gmm = noise power spectrum of mic 1
% Gnn = noise power spectrum of mic 2
% splref = SPL at the reference mic [dB re 20*10^-6 Pa]
```

```

%% Program

%% call BKfiles.m to retrieve the data
BKFiles
%pause(1)

%% extract the required data

splrefo = Group3.Function3.DatasetSection.Data.';
splrefs = Group4.Function3.DatasetSection.Data.';
splref = (splrefo + splrefs)/2;

navg = Group3.Function1.SpecialSection.Tags.AverageNumber;
f = Group3.Function1.DatasetSection.X_axis;
w = 2*pi*f;

Gxxo = Group3.Function1.DatasetSection.Data.';
Gyyo = Group3.Function2.DatasetSection.Data.';
Gxyo = Group3.Function5.DatasetSection.Data.';
Cxyo = real(Gxyo); Qxyo = imag(Gxyo);
coho = Group3.Function4.DatasetSection.Data.';
h12o = Group3.Function6.DatasetSection.Data.';

Gxxs = Group4.Function1.DatasetSection.Data.';
Gyys = Group4.Function2.DatasetSection.Data.';
Gxys = Group4.Function5.DatasetSection.Data.';
Cxys = real(Gxys); Qxys = imag(Gxys);
cohs = Group4.Function4.DatasetSection.Data.';
h12s = Group4.Function6.DatasetSection.Data.';

Gmm = Group8.Function1.DatasetSection.Data.';
Gnn = Group8.Function2.DatasetSection.Data.';

clear BKFileNames BKIndex Group3 Group4 Group5 Group6 Group7 Group8

%% Resize the data arrays
I = find(f>=300 & f<=20000);
f = f(I);
w = w(I);
Gxxo = Gxxo(I); Gyyo = Gyyo(I); Gxyo = Gxyo(I); Cxyo = Cxyo(I);
Qxyo = Qxyo(I); coho = coho(I); h12o = h12o(I);
Gxxs = Gxxs(I); Gyys = Gyys(I); Gxys = Gxys(I); Cxys = Cxys(I);
Qxys = Qxys(I); cohs = cohs(I); h12s = h12s(I);
Gmm = Gmm(I); Gnn = Gnn(I); splref = splref(I);

%% save data to mat file for convience later
save pulsedata f w Gxxo Gyyo Gxyo Cxyo Qxyo coho h12o Gxxs Gyys Gxys Cxys Qxys
cohs h12s Gmm Gnn splref

```

G.1.3 TMM Main Program

```

%%%%%%%%%%%%%%%%%%%%%%%%%%%%%%%%%%%%%%%%%%%%%%%%%%%%%%%%%%%%%%%%%%%%%%%%
%%%%
%% tmmv6.m
%
% Two Microphone Method
% Todd Schultz 9/2/2005
%          v6 4/27/2006 *updated uncertainty calculation for
magnitude
%          and phase of R for the Monte Carlo method
% This file imports the data from the correct sources and preforms the
% calculations to estimate the reflection coefficient and normalized
acoustic
% impedance and the corresponding uncertainties.  This code assumes
that
% there is no bias error in the measurement of the frequency response
% function.  This is done by using a periodic random signal as the
source.
%
% Assumptions: 1. exp(jwt) sign convention
%              2. no mean flow
%              3. mic 1 is farther from the sample
%              4. mic 2 is closer to the sample
%              5. no bias error for H12
%
% trig = logical trigger for dispersion and attenuation
%              0 = off (analytical method used for the uncertainty of
r)
%              1 = on (attenuation and dispersion are not accounted
for
%              in the uncertainty analysis which still uses
the
%              analytical method)
% trig_uncert = logical trigger for the uncertainty method
%              0 = linear multivariate method (Doesn't account for
attenuation and dispersion.)
%              1 = Monte Carlo simulation assuming normal output
distribution
%              2 = Monte Carlo simulation with arbitrary output
distribution
%
%%%%%%%%%%%%%%%%%%%%%%%%%%%%%%%%%%%%%%%%%%%%%%%%%%%%%%%%%%%%%%%%%%%%%%%%
%%%%
clear all; close all; pack;

%% Input file names
disp('Did you run pulseradv6 or is the data in the proper text file
format?')
disp('0 = pulseradv6')
disp('1 = text file')
trig_pulse = input('Choose now.\n');
fname1 = input('Input the file name for the experimental setup
information file.\n','s');
if trig_pulse == 1
    fname2 = input('Input the file name for the data file.\n','s');

```

```

end
fname3 = input('Input the file name for the output file (no
extension).\n','s');
pic = input('Press 0 if you would like the figures saved or press 1
otherwise.\n');
disp('Input whether dispersion and dissipation should be accounted
for.')
disp('0 = NO dispersion and dissipation')
disp('1 = Dispersion and dissipation included')
trig = input('Choose now.\n');
disp('Input the method for the uncertainty estimates.')
disp('0 = Linear multivariate method (Doesn't included dispersion and
dissipation)')
disp('1 = Monte Carlo simulation assuming normal output distribution')
disp('2 = Monte Carlo simulation assuming arbitrary output
distribution')
trig_uncert = input('Choose now.\n');
disp('Thank you. Your answers are being computed now.')

% trig_pulse = 1
% fname1 = 'inputjsv1.txt'
% fname2 = 'ideal40db.txt'
% fname3 = 'ideal40'
% pic = 0
% trig = 0
% trig_uncert = 2

iter = 25000;           % number of iterations

%% Read in experimental setup information
A = dlmread(fname1, '\t');           % Read in set up file
tube = A(1);                         % Tube number
navg = A(2);                         % Number of averages used
l = A(3);                             % mic location closer to the
specimen [m]
Ul = A(4);                           % standard Uncertainty in d [m]
nl = A(5);                           % # of measurements of l
s = A(6);                             % mic spacing [m]
Us = A(7);                           % standard Uncertainty in s [m]
ns = A(8);                           % # of measurements of s
tatm = A(9)+273.15;                  % Atmospheric temperature [K]
(input units are [C])
Utatm = A(10);                      % standard Uncertainty in Tatm
[K] or [C]
nT = A(11);                          % # of temperature measurements
patm = A(12)*1000;                   % Atmospheric pressure [Pa]
(input units are [kPa])
Upatm = A(13)*1000;                  % standard Uncertainty in Patm
[Pa] (input units are [kPa])
nP = A(14);                          % # of pressure measurements
clear A;

switch trig_pulse
case 0                               % Read pulse data file
    load pulsedata
    % Define the cross-spectrums

```

```

    Gxyo = Cxyo+j*Qxyo;
    Gxys = Cxys+j*Qxys;
case 1
    A = dlmread(fname2, '\t');
    f = A(:,1);
    w = 2*pi*f;
[rad/s]
    Gxxo = A(:,2);
    Gyyo = A(:,3);
    Cxyo = A(:,4);
    Qxyo = A(:,5);
    Gxyo = Cxyo+j*Qxyo;
    h12o = A(:,6)+j*A(:,7);
Original
    coho = A(:,8);
    Gxxs = A(:,9);
    GyyS = A(:,10);
    Cxys = A(:,11);
    Qxys = A(:,12);
    Gxys = Cxys+j*Qxys;
    h12s = A(:,13)+j*A(:,14);
switched
    cohS = A(:,15);
    Gmm = A(:,16);
spectrum for mic1 [Pa^2]
    Gnn = A(:,17);
spectrum for mic2 [Pa^2]
    splref = A(:,18);
[dBspl]
    clear A;
end

tic

%% Constants
% Cross-section width, l [m]
switch tube
    case 0
        dtube = 0.02544;
        Udtube = 0.00003;
dimension
    case 1
        dtube = 0.0085;
        Udtube = 0.001;
dimension
    case 2
        dtube = 4*0.0127;
end

%% Compute the uncertainty of h12o
SHo = zeros([2 2 length(f)]);
for ii = 1:length(f)
    SHo(:, :, ii) =
H3uncert(Gxxo(ii), Gyyo(ii), Gxyo(ii), Gmm(ii), Gnn(ii), h12o(ii), navg);
end

```

```

%% Compute the uncertainty of h12s
SHs = zeros([2 2 length(f)]);
for ii = 1:length(f)
    SHs(:, :, ii) =
H3uncert(Gxxs(ii), Gyys(ii), Gxys(ii), Gmm(ii), Gnn(ii), h12s(ii), navg);
end

%% Calculate averaged frequency response function
h12m = sqrt(abs(h12o)./abs(h12s));
phi = 0.5*(unwrap(angle(h12o))-unwrap(angle(h12s)));
h12 = h12m.*exp(i.*phi);      % h12 will be passed to the subroutine
tmm_sub.m

% Calculate the standard uncertainty in the frequency response function
SH = zeros([2,2,length(f)]);
for ii = 1:length(f)
    SH(:, :, ii) = have_div(h12o(ii), SHo(:, :, ii), h12s(ii), SHs(:, :, ii));
end

%% Call tmm_sub.m to carry out the caclutations
[r,z,k,SWR] = tmm_subv6(w,l,s,h12,tatm,patm,dtube,trig);
% Save the outputdata
save outputdata f k r z

%% Uncertainty Computations
switch trig_uncert
    case 0
        % Linear multivariate uncertainty
        analysis
            % Initialize variables for the loops
            SR = zeros([2 2 length(f)]);
            SZ = zeros([2 2 length(f)]);
            % Call the tmm_rv4 and tmm_zv5 to compute the uncertainties
            for ii = 1:length(f)
                SR(:, :, ii) =
tmm_rv5(w(ii),k(ii),l,s,h12(ii),r(ii),Ul,Us,Utatm,SH(:, :, ii),trig);
                SZ(:, :, ii) = tmm_zv5(r(ii),SR(:, :, ii),trig);
            end

            % Estimate the coverage factor kcf
            p = 2;          % # of variates
            % First estimate the effective # of degrees of freedom
            nu = zeros(length(f),1);
            nux = [navg nl ns nT]-1;
            Snew = zeros([p p length(nux)]);
            for ii = 1:length(f)
                Snew(:, :, 1) = SH(:, :, ii);
                Snew(:, :, 2) = [Ul^2 0; 0 0];
                Snew(:, :, 3) = [Us^2 0; 0 0];
                Snew(:, :, 4) = [Utatm^2 0; 0 0];
                nu(ii) = nu_eff(Snew,nux);
                if nu(ii) == 0
                    disp('Try again!')
                    break
                end
            end
            end
            kcf = sqrt((nu*p./(nu+1-p)).*finv(0.95,p,nu+1-p));

```

```

    % Estimate the uncertainty bounds on the real and imaginary
parts of
    % the reflection coefficient and normalized acoustic impedance
    URr = kcf.*sqrt(squeeze(SR(1,1,:)));
    URi = kcf.*sqrt(squeeze(SR(2,2,:)));
    UZr = kcf.*sqrt(squeeze(SZ(1,1,:)));
    UZi = kcf.*sqrt(squeeze(SZ(2,2,:)));

    % Convert from rectangular form to polar form
    SRpolar = rect_to_polar(r,SR);

    % Estimate the uncertainty bounds on the polar form of
    % the reflection coefficient
    URm = kcf.*sqrt(squeeze(SRpolar(1,1,:)));
    URp = kcf.*sqrt(squeeze(SRpolar(2,2,:)));

    % Save the multivariate uncertainty data
    save mv_uncertainty URr URi URm URp UZr UZi SR SRpolar SZ kcf

    case 1 % Monte Carlo simulation assuming a
normal output distribution
        %iter = 25000; % number of iterations
        tmm_mcv6 % Performs Monte Carlo simulations and
saves the data

        % compute the magnitude and phase

        % compute the coverage factor
        nu = iter-1;
        p = 2;
        kcf = sqrt((nu*p./(nu+1-p)).*finv(0.95,p,nu+1-p));

        % compute the covariance of the magnitude and phase for each
frequency
        % compute the covariance of the real and imaginair parts of Z
for each
        % frequency
        SR = zeros([2,2,length(f)]);
        SRpolar = zeros([2,2,length(f)]);
        SZ = zeros([2,2,length(f)]);

        for ii = 1:length(f)
            SR(:, :, ii) = cov(real(r_data(:,ii)), imag(r_data(:,ii)));
            SRpolar(:, :, ii) =
cov(abs(r_data(:,ii)), angle(r_data(:,ii)));
            SZ(:, :, ii) = cov(real(z_data(:,ii)), imag(z_data(:,ii)));
        end

        % Estimate the uncertainty bounds on the real and imaginary
parts of
        % the reflection coefficient and normalized acoustic impedance
        URr = kcf.*sqrt(squeeze(SR(1,1,:)));
        URi = kcf.*sqrt(squeeze(SR(2,2,:)));
        URm = kcf.*sqrt(squeeze(SRpolar(1,1,:)));

```

```

    URp = kcf.*sqrt(squeeze(SRpolar(2,2,:)));
    UZr = kcf.*sqrt(squeeze(SZ(1,1,:)));
    UZi = kcf.*sqrt(squeeze(SZ(2,2,:)));

% Save the Monte Carlo uncertainty data
save mcnormal_uncertainty URr URi URm URp UZr UZi SR SRpolar SZ
kcf

case 2 % Monte Carlo simlaton assuming an
arbitrary distribution
% For this case, the uncertainty is given as a lower and upper
% limit range. This is done aviod an assumption regarding the
% symmetry of the distribution.
%iter = 25000; % number of iterations
cilevel = 0.95; % desired level for the CI's
bins = 40; % number of bins to use to estimate the
pdf
cbins = 100; % number of contours to use
tmm_mcv6 % Performs Monte Carlo simulations and
saves the data

% Initialize variables
URr = zeros(length(f),2);
URi = zeros(length(f),2);
URm = zeros(length(f),2);
URp = zeros(length(f),2);
UZr = zeros(length(f),2);
UZi = zeros(length(f),2);

probrri = zeros(length(f),1);
probrmp = zeros(length(f),1);
probrz = zeros(length(f),1);

xrri = cell(length(f),1);
% xrmv = cell(length(f),1); % v6 change
xz = cell(length(f),1);

for ii = 1:length(f)
% compute the Confidence intervals
[probrri(ii),x] = numericCI([real(r_data(:,ii))
imag(r_data(:,ii))],cilevel,bins,cbins);
xrri{ii} = x;
URr(ii,1) = min(x(:,1)); URr(ii,2) = max(x(:,1));
URi(ii,1) = min(x(:,2)); URi(ii,2) = max(x(:,2));

% v6 changes here
% Old way of mag/phase uncertainty (not consistant with
with
% how I quote the nominal value.
% [probrmp(ii),x] = numericCI([abs(r_data(:,ii))
angle(r_data(:,ii))],cilevel,bins,cbins);
% xrmv{ii} = x;
% URm(ii,1) = min(x(:,1)); URm(ii,2) = max(x(:,1));
% URp(ii,1) = min(x(:,2)); URp(ii,2) = max(x(:,2));
% New way

```

```

xamp = sqrt(x(:,1).^2+x(:,2).^2);
xphase = atan2(x(:,2),x(:,1));
URm(ii,1) = min(xamp); URm(ii,2) = max(xamp);
URp(ii,1) = min(xphase); URp(ii,2) = max(xphase);

    [probbz(ii),x] = numericCI([real(z_data(:,ii))
imag(z_data(:,ii))],cilevel,bins,cbins);
    xz{ii} = x;
    UZr(ii,1) = min(x(:,1)); UZr(ii,2) = max(x(:,1));
    UZi(ii,1) = min(x(:,2)); UZi(ii,2) = max(x(:,2));
end

    % Save the Monte Carlo uncertainty data
    save mcarbitrary_uncertainty URr URi URm URp UZr UZi probrrri
probrmp probz xrri xz

end

% Write the data to text file
fname_out = [fname3 '.out'];
fid=fopen(fname_out,'w');
switch trig_uncert
    case {0,1}
        fprintf(fid,'F[Hz] \t SPLref \t SWR[dB] \t Rmag \t +/-Rmag \t
Rpha[deg] \t +/-Rpha[deg] \t Resist \t +/-Resist \t React \t +/-React
\r');
        fprintf(fid,'%7.2f\t %5.1f\t %5.1f\t %9.5f\t %9.5f\t %9.5f\t
%9.5f\t %9.5f\t %9.5f\t %9.5f\t %9.5f\r',...

[f';splref';abs(SWR)';abs(r)';URm';(180*angle(r)/pi)';(180*URp/pi)';rea
l(z)';UZr';imag(z)';UZi']);
    case 2
        fprintf(fid,'F[Hz] \t SPLref \t SWR[dB] \t Rmag \t lowerRmag \t
upperRmag \t Rpha[deg] \t lowerRpha[deg] \t upperRpha[deg] \t Resist \t
lowerResist \t upperResist \t React \t lowerReact \t upperReact \r');
        fprintf(fid,'%7.2f\t %5.1f\t %5.1f\t %9.5f\t %9.5f\t
%9.5f\t %9.5f\t %9.5f\t %9.5f\t %9.5f\t
%9.5f\t %9.5f\t %9.5f\t %9.5f\t %9.5f\r',...

[f';splref';abs(SWR)';abs(r)';URm(:,1)';URm(:,2)';(angle(r)*180/pi)';(U
Rp(:,1)*180/pi)';(URp(:,2)*180/pi)';real(z)';UZr(:,1)';UZr(:,2)';imag(z
)';UZi(:,1)';UZi(:,2)']);
end
fclose(fid);

toc

%% Plots
% Plot the coherence for the two TF
figure (1)
    set(gcf,'paperorientation','landscape')
    set(gcf,'paperposition',[0.25 0.25 10.5 8.0])
    plot(f/1000,coho,f/1000,cohs)
    xlim([f(1) f(end)]/1000)

```

```

xlabel('Freq [kHz]');
ylabel('Coherence');
title('Coherence of the Two Measured Transfer Functions')
legend('Original Position','Switched Position')
%axis tight
%grid on

% Plot the two frequency response functions
figure(2)
set(gcf,'paperorientation','landscape')
set(gcf,'paperposition',[0.25 0.25 10.5 8.0])
h1=subplot(2,1,1);
h2=subplot(2,1,2);
subplot(2,1,1); plot(f/1000,h12m,f/1000,abs(h12o),f/1000,abs(h12s))
subplot(2,1,2);
plot(f/1000,180.*phi./pi,f/1000,180.*angle(h12o)./pi,f/1000,180.*angle(
h12s)./pi)
subplot(h1);
xlim([f(1) f(end)]/1000)
ylabel('|H_3|');
xlabel('Freq [kHz]');
title('Frequency Response Function')
legend('Averaged','Original','Switched')
%axis tight
%grid on
subplot(h2);
xlim([f(1) f(end)]/1000)
ylabel('arg(H_3) [deg]');
xlabel('Freq [kHz]');
%axis tight
%grid on

% Plot the reflection coefficient
figure (3)
set(gcf,'paperorientation','landscape')
set(gcf,'paperposition',[0.25 0.25 10.5 8.0])
h1=subplot(2,1,1);
h2=subplot(2,1,2);
subplot(2,1,1); plot(f/1000,abs(r))
subplot(2,1,2); plot(f/1000,180.*angle(r)./pi)
subplot(h1);
xlim([f(1) f(end)]/1000)
ylabel('|R|');
xlabel('Freq [kHz]');
title('Reflection Coefficient')
%axis tight
%grid on
subplot(h2);
xlim([f(1) f(end)]/1000)
ylabel('\phi [deg]');
xlabel('Freq [kHz]');
%axis tight
%grid on

% Plot the reflection coefficient with uncertainty
figure (4)

```

```

set(gcf,'paperorientation','landscape')
set(gcf,'paperposition',[0.25 0.25 10.5 8.0])
h1=subplot(2,1,1);
h2=subplot(2,1,2);
switch trig_uncert
    case {0,1}
        subplot(2,1,1); errorbar(f/1000,abs(r),URm)
        subplot(2,1,2);
errorbar(f/1000,180.*angle(r)./pi,180.*URp./pi)
    case 2
        subplot(2,1,1);
plot(f/1000,abs(r),f/1000,URm(:,1),'r',f/1000,URm(:,2),'r')
        subplot(2,1,2);
plot(f/1000,180.*angle(r)./pi,f/1000,URp(:,1)*180./pi,'r',f/1000,URp(:,
2)*180/pi,'r')
    end
subplot(h1);
xlim([f(1) f(end)]/1000)
ylabel('|R|');
xlabel('Freq [kHz]');
title('Reflection Coefficient')
%axis tight
%grid on
subplot(h2);
xlim([f(1) f(end)]/1000)
ylabel('\phi [deg]');
xlabel('Freq [kHz]');
%axis tight
%grid on

% Plot the normalized impedance
figure (5)
set(gcf,'paperorientation','landscape')
set(gcf,'paperposition',[0.25 0.25 10.5 8.0])
h1=subplot(2,1,1);
h2=subplot(2,1,2);
subplot(2,1,1); plot(f/1000,real(z))
subplot(2,1,2); plot(f/1000,imag(z))
subplot(h1);
xlim([f(1) f(end)]/1000)
ylabel('\theta');
xlabel('Freq [kHz]');
title('Normalized Acoustic Impedance')
%axis tight
%grid on
subplot(h2);
xlim([f(1) f(end)]/1000)
ylabel('\chi');
xlabel('Freq [kHz]');
%axis tight
%grid on

% Plot the normalized impedance with uncertainty
figure (6)
set(gcf,'paperorientation','landscape')
set(gcf,'paperposition',[0.25 0.25 10.5 8.0])

```

```

h1=subplot(2,1,1);
h2=subplot(2,1,2);
switch trig_uncert
    case {0,1}
        subplot(2,1,1); errorbar(f/1000,real(z),UZr)
        subplot(2,1,2); errorbar(f/1000,imag(z),UZI)
    case 2
        subplot(2,1,1);
plot(f/1000,real(z),f/1000,UZr(:,1),'r',f/1000,UZr(:,2),'r')
    subplot(2,1,2);
plot(f/1000,imag(z),f/1000,UZI(:,1),'r',f/1000,UZI(:,2),'r')
end
subplot(h1);
xlim([f(1) f(end)]/1000)
ylabel('\theta');
xlabel('Freq [kHz]');
title('Normalized Acoustic Impedance')
%axis tight
%grid on
subplot(h2);
xlim([f(1) f(end)]/1000)
ylabel('\chi');
xlabel('Freq [kHz]');
%axis tight
%grid on

% Plots
%%%%%%%%%%%%%%%%%%%%%%%%%%%%%%%%%%%%%%%%%%%%%%%%%%%%%%%%%%%%%%%%%%%%%%%%
% Save the MatLab figures
if pic == 0
    h=figure(1);
        saveas(h,'coherence.fig')
    h=figure(2);
        saveas(h,'frf.fig')
    h=figure(3);
        saveas(h,'r.fig')
    h=figure(4);
        saveas(h,'runcert.fig')
    h=figure(5);
        saveas(h,'z.fig')
    h=figure(6);
        saveas(h,'zuncert.fig')
end

% end
%%%%%%%%%%%%%%%%%%%%%%%%%%%%%%%%%%%%%%%%%%%%%%%%%%%%%%%%%%%%%%%%%%%%%%%%

```

G.1.4 TMM Subroutine Program

```

function [r,z,k,SWR] = tmm_subv6(w,l,s,Hl2,tatm,patm,dtube,trig);
%%%%%%%%%%%%%%%%%%%%%%%%%%%%%%%%%%%%%%%%%%%%%%%%%%%%%%%%%%%%%%%%%%%%%%%%
% tmm_subv6.m
%
% Todd Schultz 7/29/02 revised 4/15/2005
%

```

```

% This matlab program calculates the acoustical impedance of a sample
% based on the Two Microphone Method. A trigger is given to allow the
% user to turn on or off the corrections for dispersion and
% attenuation.
% Assumptions: 1. exp(jwt) sign convention
%               2. no mean flow
%               3. mic 1 is farther from the sample
%               4. mic 2 is closer to the sample
%%%%%%%%%%%%%%%%%%%%%%%%%%%%%%%%%%%%%%%%%%%%%%%%%%%%%%%%%%%%%%%%%%%%%%%%
%
% Inputs
% w = vector of test angular frequencies [rad/s]
% s = spacing between microphones [m]
% Us = uncertainty in s [m]
% l = location of mic closer to the specimen [m]
% H12 = vector of the frequency response function [Parms]
% tatm = atmospheric temperature [K]
% patm = atmospheric pressure [Pa]
% dtube = tube cross-section dimension [m]
% trig = logical trigger for dispersion and attenuation
%        0 = off (analytical method used for the uncertainty of
%        r)
%        1 = on (attenuation and dispersion are not accounted
%        for
%           in the uncertainty analysis which still uses
%           the
%           analytical method)
%
% Outputs
% r = vector of the reflection coefficients
% k = wavenumber vector used for the calculation of R

%% Variable definitions
global gamma Rair c0

%% Constants
% Hydraulic diameter for square duct [m]
HD = dtube;
% Gas Constant for air [J/(kg*K)]
Rair = 287;
% Ratio of specific heats for air
gamma = 1.4;
% Specific heat at constant pressure for air [J/(kg*K)]
cp = 3.5*Rair;
% Atmospheric density [kg/m^3]
rhoatm = patm./(Rair.*tatm);
% Atmospheric speed of sound [m/s]
c0 = sqrt(gamma.*Rair.*tatm);
% Fluid properties look up (data take from Fundamentals of Heat
% and Mass Transfer, 4th ed.)
% mu_alpha=matrix of temps of the table data (c 1) [K],
% the absolute viscosity (c 2) [(N*s)/m^2]
% and the thermal diffusivity (c 3) [m^2/s]
table = [100 71.10e-7 2.54e-6;
         150 103.4e-7 5.84e-6;

```

```

200 132.5e-7 10.3e-6;
250 159.6e-7 15.9e-6;
300 184.6e-7 22.5e-6;
350 208.2e-7 29.9e-6;
400 230.1e-7 38.7e-6];
% Interpolate the values for mu and alpha from table
mu_alpha = interp1(table(:,1),table(:,2:3),tatm, '*cubic');
% Prandtl Number
Pr = mu_alpha(:,1)./(rhoatm.*mu_alpha(:,2));
% Heat conduction coefficient [W/(m*K)]
kappa = cp*mu_alpha(:,1)./Pr;

%% Calcate the attenuation constants
% Viscothermal attenuation [1/m]
bv =
(sqrt(2)/(HD))*(w./c0).*(sqrt(mu_alpha(:,1)./(rhoatm.*w))).*(1+(gamma-
1)./sqrt(Pr)));
% Tube speed of sound (taken from DTB)
ct = c0.*(1-(sqrt(2)/HD).*sqrt(mu_alpha(:,1)./(rhoatm.*w))).*(1+(gamma-
1)./sqrt(Pr)));

%% Wave number [1/m] (use trigger for dispersion and attentuation)
switch trig
case 0
k = w./c0;
case 1
k = w./ct;
k = k - j*bv;
end

% Reflection
coefficient%%%%%%%%%%%%%%%%%%%%%%%%%%%%%%%%%%%%%%%%%%%%%%%%%%%%%%%%%%%%%%%%%%%%%%%%%%
r = exp(j*2*k*(1+s)).*(H12-exp(-j*k*s))./(exp(j*k*s)-H12);

% Normalized Acoustic Impedance
z = (1.+r)./(1.-r);

% Standing Wave Ratio
SWR = 20*log10((1+abs(r))./(1-abs(r)));

%
end%%%%%%%%%%%%%%%%%%%%%%%%%%%%%%%%%%%%%%%%%%%%%%%%%%%%%%%%%%%%%%%%%%%%%%%%%%
%%

```

G.1.5 TMM Subroutine for the Analytical Uncertainty in R

```

function SR = tmm_rv6(w,k,l,s,H12,r,Ul,Us,Utatm,SH,trig);
%%%%%%%%%%%%%%%%%%%%%%%%%%%%%%%%%%%%%%%%%%%%%%%%%%%%%%%%%%%%%%%%%%%%%%%%%%
% tmm_rv6.m
%
% Todd Schultz 4/15/2005
%
% This matlab program calculates the estimate for the uncertainty
% using analytical methods. A trigger is given to allow the user to

```

```

% turn on or off the corrections for dispersion and attenuation.
% Assumptions: 1. exp(jwt) sign convention
%               2. no mean flow
%               3. mic 1 is farther from the sample
%               4. mic 2 is closer to the sample
%%%%%%%%%%%%%%%%%%%%%%%%%%%%%%%%%%%%%%%%%%%%%%%%%%%%%%%%%%%%%%%%%%%%%%%%
%
% Inputs
% w = vector of test angular frequencies [rad/s]
% k = wavenumber vector used for the calculation of R
% s = spacing between microphones [m]
% Us = uncertainty in s [m]
% l = location of mic closer to the specimen [m]
% Ul = uncertainty in d [m]
% H12 = vecotr of the frequency response function [Parms]
% SH = covariance matrix for the FRF [Parms^2]
% tatm = atmospheric temperature [K]
% Utatm = uncertainty in atmospheric temperature [K]
% trig = logical trigger for dispersion and attenuation
%         0 = off (analytical method used for the uncertainty of
r)
%         1 = on (attenuation and dispersion are not accounted
for
%           in the uncertainty analysis which still uses
the
%           analytical method)
% r = vector of the reflection coefficients
%
% Outputs
% Sr = covariance matrix for the reflection coefficient

% Variable definitions
global gamma Rair c0
Hr = real(H12);
Hi = imag(H12);

% wavenumber derivative
dkdT = -k.*gamma.*Rair./(2*c0.^2);

% Partial derivatives of the reflection coefficient
% common factor in derivatives
Dem = 1+Hr^2+Hi^2-2*Hr*cos(k*s)-2*Hi*sin(k*s);

dRrdHr = (2*cos(k*(2*l+s))-2*Hr*cos(2*k*(l+s)))/Dem -
(2*Hr*cos(k*(2*l+s))-cos(2*k*l)-(Hr^2+Hi^2)*cos(2*k*(l+s)))*(2*Hr-
2*cos(k*s))/Dem^2;
dRrdHi = -2*Hi*cos(2*k*(l+s))/Dem - (2*Hr*cos(k*(2*l+s))-cos(2*k*l)-
(Hr^2+Hi^2)*cos(2*k*(l+s)))*(2*Hi-2*sin(k*s))/Dem^2;
dRrdl = -2*k*imag(r);
dRrds = -2*k*(Hr*sin(k*(2*l+s))-
(Hr^2+Hi^2)*sin(2*k*(l+s))+real(r)*(Hr*sin(k*s)-Hi*cos(k*s)))/Dem;
dRrdk = (-
2*Hr*(2*l+s)*sin(k*(2*l+s))+2*l*sin(2*k*l)+(Hr^2+Hi^2)*(2*l+2*s)*sin(2*
k*(l+s)))/Dem - (2*Hr*cos(k*(2*l+s))-cos(2*k*l)-
(Hr^2+Hi^2)*cos(2*k*(l+s)))*(2*Hr*s*sin(k*s)-2*Hi*s*cos(k*s))/Dem^2;

```

```

dRidHr = (2*sin(k*(2*l+s))-2*Hr*sin(2*k*(l+s)))/Dem -
(2*Hr*sin(k*(2*l+s))-sin(2*k*l)-(Hr^2+Hi^2)*sin(2*k*(l+s)))*(2*Hr-
2*cos(k*s))/Dem^2;
dRidHi = -2*Hi*sin(2*k*(l+s))/Dem - (2*Hr*sin(k*(2*l+s))-sin(2*k*l)-
(Hr^2+Hi^2)*sin(2*k*(l+s)))*(2*Hi-2*sin(k*s))/Dem^2;
dRidl = 2*k*real(r);
dRids = 2*k*(Hr*cos(k*(2*l+s))-(Hr^2+Hi^2)*cos(2*k*(l+s))-
imag(r)*(Hr*sin(k*s)-Hi*cos(k*s)))/Dem;
dRidk = (2*Hr*(2*l+s)*cos(k*(2*l+s))-2*l*cos(2*k*l)-
(Hr^2+Hi^2)*(2*l+2*s)*cos(2*k*(l+s)))/Dem - (2*Hr*sin(k*(2*l+s))-
sin(2*k*l)-(Hr^2+Hi^2)*sin(2*k*(l+s)))*(2*Hr*s*sin(k*s)-
2*Hi*s*cos(k*s))/Dem^2;

% Form the Jacobian matrix
J = [dRrdHr dRrdHi dRrdl dRrds dRrdk*dkdT;
     dRidHr dRidHi dRidl dRids dRidk*dkdT];

% Form the input covariance matrix
Sx = [SH(1,1) SH(1,2) 0 0 0;
      SH(2,1) SH(2,2) 0 0 0;
      0 0 Ul^2 0 0;
      0 0 0 Us^2 0;
      0 0 0 0 Utatm^2];

% Compute the covariance of the reflection coefficient
SR = J*Sx*J';

%
end%%%%%%%%%%%%%%%%%%%%%%%%%%%%%%%%%%%%%%%%%%%%%%%%%%%%%%%%%%%%%%%%%%%%%%%%%%%%%%%%%%%%%%%%%%%%%%%%%%%%%%%%%%%%%%%%%%%%%%%%%%%%%%%%%%%%%%%%%%%%%%%%
%
```

G.1.6 TMM Subroutine for the Analytical Uncertainty in Z

```

function SZ = tmm_zv6(r,Sr,trig);
%%%%%%%%%%%%%%%%%%%%%%%%%%%%%%%%%%%%%%%%%%%%%%%%%%%%%%%%%%%%%%%%%%%%%%%%
% tmm_zv6.m
%
% Todd Schultz 5/1/2005
%
% This matlab program calculates the estimate for the uncertainty
% using analytical methods. A trigger is given to allow the user to
% turn on or off the corrections for dispersion and attenuation.
% Assumptions: 1. exp(jwt) sign convention
%              2. no mean flow
%              3. mic 1 is farther from the sample
%              4. mic 2 is closer to the sample
%%%%%%%%%%%%%%%%%%%%%%%%%%%%%%%%%%%%%%%%%%%%%%%%%%%%%%%%%%%%%%%%%%%%%%%%
%
% Inputs
% r = vector of the reflection coefficients
% Sr = sample covariance matrix for R
% trig = logical trigger for dispersion and attenuation
%       0 = off (analytical method used for the uncertainty of
r)
```

```

%           1 = on (attenuation and dispersion are not accounted
for
%           in the uncertainty analysis which still uses
the
%           analytical method)
%
% Outputs
% SZ = covariance matrix for the normalized acoustic impedance

% Variable definitions
Rr = real(r);
Ri = imag(r);

% Partial derivatives of the normalized acoustic impedance
% common factor in derivatives
Dem = ((1-Rr).^2+Ri.^2).^2;

dthetadRr = 2*((1-Rr).^2-Ri.^2)./Dem;
dthetadRi = -4*Ri.*(1-Rr)./Dem;
dxidRr = 4*Ri.*(1-Rr)./Dem;
dxidRi = 2*((1-Rr).^2-Ri.^2)./Dem;

% Form the Jacobian matrix
J = [dthetadRr dthetadRi;
     dxidRr    dxidRi];

% Compute the covariance of the reflection coefficient
SZ = J*Sr*J';

%
end%%%%%%%%%%%%%%%%%%%%%%%%%%%%%%%%%%%%%%%%%%%%%%%%%%%%%%%%%%%%%%%%%%%%%%%%%%
%
```

G.1.7 TMM Subroutine for the Monte Carlo Uncertainty Estimates

```

% tmm_mcv6.m
%
% Todd Schultz          9/2/2005
%
% This program takes the data from the tmmv6 program and carries out a
% Monte Carlo simulatio. The output is the array of random data that
% is to
% be processed with other file to determine the statistics.

% Initialize Monte Carlo variables
r_data = zeros(iter,length(f));
z_data = zeros(iter,length(f));

ld = zeros(iter,1);
sd = zeros(iter,1);
td = zeros(iter,1);
hd = zeros(iter,length(f));
```

```

if trig == 1
    pd = zeros(iter,length(f));
    dtube = zeros(iter,length(f));
end

% pertub the values
ld = l + Ul*randn(iter,1);
sd = s + Us*randn(iter,1);
td = tatm + Utatm*randn(iter,1);
if trig == 1
    pd = patm + Upatm*randn(iter,1);
    dtubed = dtube + Udtube*randn(iter,1);
end

for ii = 1:length(f)
    junk = mvgrnd([0;0],SH(:, :, ii), iter);
    hd(:, ii) = real(h12(ii))+junk(:,1)+j*(imag(h12(ii))+junk(:,2));
end
clear junk

% Carry out the Monte Carlo simulations
switch trig
case 0
    % no dissipation and dispersion
    for jj = 1:iter
        [r_data(jj,:),z_data(jj,:),k,SWR] =
tmm_subv6(w,ld(jj),sd(jj),hd(jj,:).',td(jj),patm,dtube,trig);
    end
case 1
    % with dissipation and dispersion
    for jj = 1:iter
        [r_data(jj,:),z_data(jj,:),k,SWR] =
tmm_subv6(w,ld(jj),sd(jj),hd(jj,:).',td(jj),pd(ii),dtube(ii),trig);
    end
end

% Save the Monte Carlo simulation data
switch trig
case 0
    save mc_data r_data z_data ld sd td hd
case 1
    save mc_data r_data z_data ld sd td hd pd dtubed
end

```

G.2 Uncertainty Subroutines

G.2.1 Frequency Response Function Uncertainty

```

function [varargout] = H3uncert(Gxx,Gyy,Gxy,Gmm,Gnn,H,nrec)
% H3uncert.m
%
% Todd Schultz      4/14/2005
%
% This program computes the random uncertainty in the frequency reponse
% function estimate.  This program is for when the FRF is estimated
% using
% H3.  H3 = sqrt(H1*H2) where H1 = Gxy/Gxx and H2 = Gyy/Gyx

```

```

% The input signal is assumed to be deterministic and
% that the noise on the signal does not pass through the system.  Both
% noise signals are assumed to be Gaussian and uncorrelated with
% eachother.
%
% Usage: [varargout] = H3uncert(Gxx,Gyy,Gxy,Gmm,Gnn,H,nrec)
%
% Inputs
% Gxx = power spectrum of the input signal
% Gyy = power spectrum of the output signal
% Gxy = cross spectrum between the input and output signals
% Gmm = estimate of the input noise power spectrum
% Gnn = estimate of the output noise power spectrum
% H = estimate of the FRF
% nrec = number of spectral averages
%
% Outputs
% SH = sample covariance matrix for H

% Relationships
Cxy = real(Gxy);
Qxy = imag(Gxy);

% Sample Covariance matrix for the spectrums
Sx = [Gmm.*(2.*Gxx-Gmm)          0          Gmm.*Cxy
      Gmm.*Qxy;
      0          Gnn.*(2.*Gyy-Gnn)      Gnn.*Cxy
      Gnn.*Qxy;
      Gmm.*Cxy      Gnn.*Cxy      (Gnn.*Gxx+Gmm.*Gyy-
      Gmm.*Gnn)/2          0;
      Gmm.*Qxy      Gnn.*Qxy          0
      (Gnn.*Gxx+Gmm.*Gyy-Gmm.*Gnn)/2];
Sx = Sx/nrec;

% Derivative for the real and imaginary parts of H
dHrdGxx = -sqrt(Gyy/Gxx)*Cxy/(2*Gxx*sqrt(Cxy^2+Qxy^2));
dHrdGyy = Cxy/(2*sqrt(Gxx*Gyy*(Cxy^2+Qxy^2)));
dHrdCxy = sqrt(Gyy/Gxx)*Qxy^2./((Cxy^2+Qxy^2)^(3/2));
dHrdQxy = -sqrt(Gyy/Gxx)*Cxy*Qxy/((Cxy^2+Qxy^2)^(3/2));

dHidGxx = -sqrt(Gyy/Gxx)*Qxy/(2*Gxx*sqrt(Cxy^2+Qxy^2));
dHidGyy = Qxy/(2*sqrt(Gxx*Gyy*(Cxy^2+Qxy^2)));
dHidCxy = -sqrt(Gyy/Gxx)*Cxy*Qxy/((Cxy^2+Qxy^2)^(3/2));
dHidQxy = sqrt(Gyy/Gxx)*Cxy.^2/((Cxy^2+Qxy^2)^(3/2));

% Define the Jacobian matrix
J = [dHrdGxx dHrdGyy dHrdCxy dHrdQxy;
     dHidGxx dHidGyy dHidCxy dHidQxy];

% Compute the sample covariance matrix of H
SH = J*Sx*J';

if nargout == 1
    varargout = {SH};
elseif nargout == 2

```

```

    varargout = {SH Sx};
end

```

G.2.2 Averaged FRF Uncertainty

```

function [SHave] = have_div(Ho,SHo,Hs,SHs)
% have.m
%
% Todd Schultz      4/14/2005
%
% This program computes the random uncertainty in the averaged
frequency
% reponse function estimate. This programs works when the FRFs are
% averaged by division. Have = sqrt(Ho/Hs) Also, this programs is set to
% handle only one frequency at a time.
%
% Usage: [SHave] = have_div(Ho,SHo,Hs,SHs)
%
% Inputs
% Ho = original FRF
% SHo = sample covariance matrix for the original estimate of the FRF
% Hs = switched FRF
% SHs = sample covariance matrix for the switched estimate of the FRF
%
% Outputs
% SHave = sample covariance matrix for Have

% Useful variables
Hor = real(Ho);
Hoi = imag(Ho);
Hsr = real(Hs);
Hsi = imag(Hs);

theta = (atan2(Hoi,Hor)-atan2(Hsi,Hsr))/2;

% Derivatives for Have
dHrdHor =
(Hor*cos(theta)+Hoi*sin(theta))/((Hsr^2+Hsi^2)^(1/4)*2*(Hor^2+Hoi^2)^(3/4));
dHrdHoi = (Hoi*cos(theta)-
Hor*sin(theta))/((Hsr^2+Hsi^2)^(1/4)*2*(Hor^2+Hoi^2)^(3/4));
dHrdHsr = (-Hsr*cos(theta)-
Hsi*sin(theta))*(Hor^2+Hoi^2)^(1/4)/(2*(Hsr^2+Hsi^2)^(5/4));
dHrdHsi = (-
Hsi*cos(theta)+Hsr*sin(theta))*(Hor^2+Hoi^2)^(1/4)/(2*(Hsr^2+Hsi^2)^(5/4));

dHidHor = (-
Hoi*cos(theta)+Hor*sin(theta))/((Hsr^2+Hsi^2)^(1/4)*2*(Hor^2+Hoi^2)^(3/4));
dHidHoi =
(Hor*cos(theta)+Hoi*sin(theta))/((Hsr^2+Hsi^2)^(1/4)*2*(Hor^2+Hoi^2)^(3/4));

```

```

dHidHsr = (Hsi*cos(theta)-
Hsr*sin(theta))*(Hor^2+Hoi^2)^(1/4)/(2*(Hsr^2+Hsi^2)^(5/4));
dHidHsi = (-Hsr*cos(theta)-
Hsi*sin(theta))*(Hor^2+Hoi^2)^(1/4)/(2*(Hsr^2+Hsi^2)^(5/4));

% Define the Jacobian matrix
J = [dHrdHor dHrdHoi dHrdHsr dHrdHsi;
     dHidHor dHidHoi dHidHsr dHidHsi];

% Define input covariance matrix
Sx = [SHo zeros(2);
     zeros(2) SHs];

% Compute covariance matrix for the Have
SHave = J*Sx*J';

```

G.2.3 Effective Number of degrees of Freedom

```

function nu = nu_eff(S,nux)
%
% Todd Schultz          5/2/2005
%
% This program is designed to compute the effective number of degrees
of
% freedom for the multivariate uncertainty propagation to estimate the
% coverage factor. This program uses the trace method but constrains
the
% minimum number of effective degrees of freedom to be at least as much
as
% the minimum number of the input values.
% Reference: Willink and Hall, "A classical method for uncertainty
analysis
% with multidimensional data." Metrologia, 2002, 39, p361-369.
%
% Usage nu = nu_eff(S,nux)
%
% Inputs
% S = 3 dimensional array of the covariance matrices for all input
% variables S(x,y,z) S(x,y) = covariance matrix for variable z
% nux = vector degrees of freedom for each input variable nux(z)
%
% Output
% nu = effective number of degrees of freedom for the output variable
%
% Determine the number of variates and variables
[x,y,z] = size(S);

if x == y
    p = x;          % number of variates
else
    disp('Sample covariance matrices must be square.')
    return
end

```

```

m = z;           % number of input variables

% Compute the numerator
num = 0;
for jj = 1:p
    for kk = jj:p
        num = num + sum(S(jj,jj,:))*sum(S(kk,kk,:))+sum(S(jj,kk,:))^2;
    end
end

% Compute the denominator
den = 0;
for jj = 1:p
    for kk = jj:p
        d = 0;
        for ii = 1:m
            d = d + (S(jj,jj,ii)*S(kk,kk,ii) + S(jj,kk,ii)^2)/nux(ii);
        end
        den = den + d;
    end
end

% Compute the effective number of degrees of freedom
nu = num/den;
nu = floor(nu);

% Check that nu is greater than min(nux)
nu = max([min(nux) nu]);
% Check that nu is less than sum(nux)
nu = min([nu sum(nux)]);

```

G.2.4 Numeric Computation of Bivariate Confidence Regions

```

function [prob,x,vp] = numericCI(z,p,bins,cbins,vin)
% numericCI.m
% Todd Schultz      9/1/2005
%
% This program is designed to take a set of data from a bivariate Monte
% Carlo simulation and determine the p% confidence region.  This is
% done
% purely numerically and makes no assumptions about the underlying
% distribution of the data.  First, the data is used to generate a
% bivariate probability density function and to compute a certain
% number of
% constant probability density contours.  The pdf is then integrated
% over
% the contours to determine the total propability.  The two contours
% that
% bound the desired probability level are linearly interpolated to
% determine the desired confidence interval.  The estimate pdf is
% smoothed
% to help "average out" any irregularities due to the limited sample
% data.
%

```

```

% Usage: [prob,x] = numericCI(z,p,bins,cbins)
%
% Inputs:
% z = matrix of the Monte Carlo simulation data
%     (Should be n rows by 2 columns)
% p = desired probability level for the confidence region
% bins = number of bins to used in estimating the pdf
%     (20 is too few, 35 seems to work well for 25,000 points)
% cbins = number of contour levels used to estimat the pdf contours
%
% Output:
% prob = probability of the region inside the found contour
% x = matrix of the vertices that define the confidence interval when
%     connected with straight lines
%     (m rows by 2 columns)

% Check the size of input data
[m,n] = size(z);
if n ~= 2
    disp('Input matrix does not have enough columns!')
    return
end

% Compute the bivariate pdf
% pdf = pdf, c = grid locations of the pdf values
[pdf,c] = bivariate_pdf(z,bins,1);
dz1 = c{1}(2)-c{1}(1);
dz2 = c(ISO-10534-2:1998)(2)-c(ISO-10534-2:1998)(1);
[X, Y] = meshgrid(c{1},c(ISO-10534-2:1998)); % Grid locations
in matrix form

% Smooth the pdf
pdf_old = pdf;
H = fspecial('disk',2);
pdf = imfilter(pdf,H,'replicate');

% ptest = sum(sum(pdf))*dz1*dz2
% max(max(pdf))
% min(min(pdf))
% figure
%     set(gcf,'paperorientation','landscape')
%     set(gcf,'paperposition',[0.25 0.25 10.5 8.0])
%     [X, Y] = meshgrid(c{1},c(ISO-10534-2:1998));
%     contourf(X,Y,pdf,vin)
%     colorbar
%     %axis equal
%     xlabel('x1')
%     ylabel('x2')
%     title('Bivariate PDF')

% Compute a set of iso-probability density lines
% Cmatrix = contour matrix
Cmatrix = contours(X,Y,pdf,cbins);

```

```

% Pick a contour and integrate the pdf to determine the probability
pr = 100; % Initialize the loop variable
v = 0;
xy = [];
ii = 0; % Initialize loop counter
while pr >= p
    ii = ii + 1; % Increase the loop counter
    % Save the old values
    v_old = v;
    xy_old = xy;
    pr_old = pr;
    % Select the contour
    [v,xy] = contourline(Cmatrix,ii);
    % Find all points of the pdf with a value greater than or equal to
the
    % value of the contour line
    K = find(pdf >= v);
    pr = sum(pdf(K))*dz1*dz2; % Compute the probability inside the
contour
end

% Interpolate between v and v_old to estimate contour value that should
% represent the p level CI and compute the contour
vp = interp1([pr_old pr],[v_old v],p,'linear');
Cmatrix = contours(X,Y,pdf,[v_old vp v]);
[v,xy]=contourline(Cmatrix,2);

% Check the probability
K = find(pdf >= v);
pr = sum(pdf(K))*dz1*dz2;
if pr > p*(1+0.02) | pr < p*(1-0.02)
    disp('Proper contour was not found. Try again with more bins.')
end

% Define the output variables
x = xy; % Contour definition
prob = pr; % Probability of the contour

% End

```

G.2.5 Analytical Propagation of Uncertainty from Rectangular Form to Polar Form

```

function Spolar = rect_to_polar(A,Srect)
% rect_to_polar.m
%
% Todd Schultz          6/6/2005
%                      edited 3/15/2006
%
% This program is designed to convert a bivariate uncertainty estimate
for
% a complex number from rectangular form to polar form.
%
% Usage: Spolar = rect_to_polar(A,Srect)
%
% Inputs

```

```

% A      = vector of the complex numbers
% Srect = sample covariance matrices for the complex numbers in
rectangular
%        form (real,imag,measurement number)
%
% Outputs
% Spolar = sample covariance matrices for the complex numbers in polar
form

% Constants
n = length(A);

xr = real(A);
xi = imag(A);

% Loop to iterate the list of numbers
S = zeros(2,2,n);
for ii = 1:n
    % Jacobian matrix
    J = [xr(ii)/sqrt(xr(ii)^2+xi(ii)^2)  xi(ii)/sqrt(xr(ii)^2+xi(ii)^2);
        -xi(ii)/(xr(ii)^2+xi(ii)^2)   xr(ii)/(xr(ii)^2+xi(ii)^2)];
    % propagate the sample covariance matrix
    S(:, :, ii) = J*Srect(:, :, ii)*J';
end
Spolar = S;

% end function

```

G.3 Multivariate Statistics Subroutines

G.3.1 Computation of Bivariate PDF

```

function [pdf,c] = bivariate_pdf(x,k,pl)
%%
% Todd Schultz          6/11/2005
%
% This function is designed to compute the bivariate probability
density
% function of a bivariate random variabe.  The pdf is first computed as
a
% histogram, then normalized and plotted.
%
% Usage: [pdf] = bivariate_pdf(x,k,pl)
%
% Inputs:
% x = n times 2 matrix containing the bivariate data, n is the number
of
% data points
% k = number of divisions to break up the two axes in for the pdf
approximation [x y]
% pl = logical trigger to dispaly the plot (0=yes, 1=no)
%
% Output:
% pdf = computed pdf values

```

```

% c = grid locations of the pdf values

%% Constants
[n,p] = size(x);

%% Compute the histogram
[pdf,c] = hist3(x,[k k]);
% Normalized the histogram to compute the pdf
dx1 = c{1}(2)-c{1}(1);
dx2 = c(ISO-10534-2:1998)(2)-c(ISO-10534-2:1998)(1);
pdf = pdf/n/dx1/dx2;
pdf = pdf'; % transpose the matrix for plotting and
consistency

if pl == 0
    % Plot the pdf
    figure
        set(gcf,'paperorientation','landscape')
        set(gcf,'paperposition',[0.25 0.25 10.5 8.0])
        [X, Y] = meshgrid(c{1},c(ISO-10534-2:1998));
        contourf(X,Y,pdf)
        colorbar
        %axis equal
        xlabel('x1')
        ylabel('x2')
        title('Bivariate PDF')
end

```

G.3.2 Numerical Computation of Constant PDF Contours

```

function [v,xy] = contourline(C,n)
% contourline.m
% Todd Schultz 8/31/2005
%
% contourline extracts the nth set of vertices from the output of
% contourc.m. This set of vertices defines the nth contour line that
now
% can be used for other purposes.
%
% Usage: [v,xy] = contourline(C,n)
%
% Inputs
% C = output from contourc
% n = nth contour to extract
%
% Output
% v = contour value
% xy = m x 2 matrix containg the ordered vertices of the contour

% Find out how many contours there are total and where they start
ncon = 1;
jj = 1;
while ncon < size(C,2)

```

```

        conmark(jj) = ncon;           % record where each contour
starts
        value(jj) = C(1,ncon);       % record the value of each
contour
        nvert(jj) = C(2,ncon);       % record the number of vertices

        ncon = ncon + nvert(jj) + 1; % compute the start of the next
contour
        jj = jj + 1;                 % increase the counter
end

% pick the desired contour line
v = value(n);
xy = C(:,conmark(n)+1:conmark(n)+nvert(n))';

% end

```

G.3.3 Multivariate Normal Random Number Generator

```

% Multivariate Normal Random Generator

function f = mvgrnd(m,sigma,n)

% m is the mean column vector
% sigma is the variance-covariance matrix
% n is the number of iterations

U = chol(sigma);
% Cholesky decomposition. U is an upper triangular matrix

d = length(m);

for i = 1:n
    y(i,1:d) = m' + randn(1,d)*U;
end
f = y;

```

G.4 Modal Decomposition Programs

G.4.1 Pulse to MATLAB Conversion Program

```

%% mdm_pulse4.m
%
% Todd Schultz      v1  5/20/2005
%                   v4  12/2/2005
%
% Version 4: The output of the Pulse system is assumed to be the time
%           series data for all eight microphones and for all 4 sources and
the
%           background noise measurements. BKFiles is no longer used due
to

```



```

df = 1/(nfft*dt);           % Desired frequency resolution [Hz]
T = dt*nfft;               % Spectrum period
npoints = 4096000;         % Expected points per signal
nave = 1000;               % Desired number of averages
noverlap = 0;              % Desired overlap
win = ones(nfft,1);        % Desired rectangular window

fstart = 300;              % Lowest frequency of interest [Hz]
fstop = 13500;             % Highest frequency of interest [Hz]

save('fftsettings','span','fs','dt','nfft','df','T','npoints','nave','noverlap','win','fstart','fstop')

%% Signal number to mic name converter
% signal 1 == g1m1        (a/4,0,d1)
% signal 2 == g1m2        (a,a/4,d1)
% signal 3 == g1m3        (3a/4,a,d1)
% signal 4 == g1m4        (0,3a/4,d1)
% signal 5 == g2m1        (a/4,0,d2)
% signal 6 == g2m2        (a,a/4,d2)
% signal 7 == g2m3        (3a/4,a,d2)
% signal 8 == g2m4        (0,3a/4,d2)

%% Load background noise data
%[NoiseTime,Info,errmsg] = readuff(['fnoise '.uff']);
%clear all
[NoiseTime,Info,errmsg] = readuff(['fnoise '.uff']);

if length(NoiseTime) ~= 16
    disp(['Error reading file ' fnoise '.uff.'])
    disp('Please try again.')
    break
end

% Extract time series
g1m1 = NoiseTime(ISO-10534-2:1998).measData;
g1m2 = NoiseTime(ISO-10534-2:1998).measData;
g1m3 = NoiseTime{6}.measData;
g1m4 = NoiseTime{8}.measData;
g2m1 = NoiseTime{10}.measData;
g2m2 = NoiseTime{12}.measData;
g2m3 = NoiseTime{14}.measData;
g2m4 = NoiseTime{16}.measData;

% Clear extra data
clear NoiseTime Info errmsg

% Compute auto-spectrums
[Gg1m1,f] = pwelch(g1m1,win,noverlap,nfft,fs);
I = find(f >= fstart & f <= fstop);
Gg1m1 = Gg1m1(I)*df;    f = f(I);

[Gg1m2,f] = pwelch(g1m2,win,noverlap,nfft,fs);
Gg1m2 = Gg1m2(I)*df;    f = f(I);

```

```

[Gg1m3,f] = pwelch(g1m3,win,noverlap,nfft,fs);
Gg1m3 = Gg1m3(I)*df;    f = f(I);

[Gg1m4,f] = pwelch(g1m4,win,noverlap,nfft,fs);
Gg1m4 = Gg1m4(I)*df;    f = f(I);

[Gg2m1,f] = pwelch(g2m1,win,noverlap,nfft,fs);
Gg2m1 = Gg2m1(I)*df;    f = f(I);

[Gg2m2,f] = pwelch(g2m2,win,noverlap,nfft,fs);
Gg2m2 = Gg2m2(I)*df;    f = f(I);

[Gg2m3,f] = pwelch(g2m3,win,noverlap,nfft,fs);
Gg2m3 = Gg2m3(I)*df;    f = f(I);

[Gg2m4,f] = pwelch(g2m4,win,noverlap,nfft,fs);
Gg2m4 = Gg2m4(I)*df;    f = f(I);

% Save the data
save(fnoise,'f','Gg1m1','Gg1m2','Gg1m3','Gg1m4','Gg2m1','Gg2m2','Gg2m3',
,'Gg2m4','-compress')

% Clear the time series data
clear g1m1 g1m2 g1m3 g1m4 g2m1 g2m2 g2m3 g2m4

%% Compute the standard uncertainty of the FFTs
% The uncertainty is for single-sided FFTs only and the real and
imaginary
% parts are assumed to be uncorrelated. The standard uncertainty in
the
% real and imaginary parts are identical.
uGg1m1 = zeros(2,2,length(f)); uGg2m1 = zeros(2,2,length(f));
uGg1m2 = zeros(2,2,length(f)); uGg2m2 = zeros(2,2,length(f));
uGg1m3 = zeros(2,2,length(f)); uGg2m3 = zeros(2,2,length(f));
uGg1m4 = zeros(2,2,length(f)); uGg2m4 = zeros(2,2,length(f));

for ii = 1:length(f)
    uGg1m1(:, :, ii) = (T/(4*nave))*Gg1m1(ii)*eye(2);
    uGg1m2(:, :, ii) = (T/(4*nave))*Gg1m2(ii)*eye(2);
    uGg1m3(:, :, ii) = (T/(4*nave))*Gg1m3(ii)*eye(2);
    uGg1m4(:, :, ii) = (T/(4*nave))*Gg1m4(ii)*eye(2);

    uGg2m1(:, :, ii) = (T/(4*nave))*Gg2m1(ii)*eye(2);
    uGg2m2(:, :, ii) = (T/(4*nave))*Gg2m2(ii)*eye(2);
    uGg2m3(:, :, ii) = (T/(4*nave))*Gg2m3(ii)*eye(2);
    uGg2m4(:, :, ii) = (T/(4*nave))*Gg2m4(ii)*eye(2);
end

% Save the uncertainty data
save([fnoise
'uncertainty'],'uGg1m1','uGg1m2','uGg1m3','uGg1m4','uGg2m1','uGg2m2','uGg2m3',
'uGg2m4')

% Prepare for the next file

```

```

clear Gg1m1 Gg1m2 Gg1m3 Gg1m4 Gg2m1 Gg2m2 Gg2m3 Gg2m4
clear uGg1m1 uGg1m2 uGg1m3 uGg1m4 uGg2m1 uGg2m2 uGg2m3 uGg2m4
pack;

%% Read in the remaining files and compute the FFTs
for ii = 1:n_source
    [MeasTime,Info,errmsg] = readuff([fname{ii} '.uff']);

    if length(MeasTime) ~= 16
        disp(['Error reading file ' fname{ii} '.uff.'])
        disp('Please try again.')
        %break
    end

    % Extract time series
    glm1 = MeasTime(ISO-10534-2:1998).measData;
    glm2 = MeasTime(ISO-10534-2:1998).measData;
    glm3 = MeasTime{6}.measData;
    glm4 = MeasTime{8}.measData;
    g2m1 = MeasTime{10}.measData;
    g2m2 = MeasTime{12}.measData;
    g2m3 = MeasTime{14}.measData;
    g2m4 = MeasTime{16}.measData;

    % Clear unwanted data
    clear MeasTime Info errmsg

    % Resize time series data into FFT blocks
    glm1 = reshape(glm1,nfft,nave);
    PG1M1 = fft(glm1,nfft,1)/nfft;
    PG1M1 = mean(PG1M1(I),2); % Convert to single-sided FFT

    glm2 = reshape(glm2,nfft,nave);
    PG1M2 = fft(glm2,nfft,1)/nfft;
    PG1M2 = mean(PG1M2(I),2); % Convert to single-sided FFT

    glm3 = reshape(glm3,nfft,nave);
    PG1M3 = fft(glm3,nfft,1)/nfft;
    PG1M3 = mean(PG1M3(I),2); % Convert to single-sided FFT

    glm4 = reshape(glm4,nfft,nave);
    PG1M4 = fft(glm4,nfft,1)/nfft;
    PG1M4 = mean(PG1M4(I),2); % Convert to single-sided FFT

    g2m1 = reshape(g2m1,nfft,nave);
    PG2M1 = fft(g2m1,nfft,1)/nfft;
    PG2M1 = mean(PG2M1(I),2); % Convert to single-sided FFT

    g2m2 = reshape(g2m2,nfft,nave);
    PG2M2 = fft(g2m2,nfft,1)/nfft;
    PG2M2 = mean(PG2M2(I),2); % Convert to single-sided FFT

    g2m3 = reshape(g2m3,nfft,nave);
    PG2M3 = fft(g2m3,nfft,1)/nfft;
    PG2M3 = mean(PG2M3(I),2); % Convert to single-sided FFT

```

```

g2m4 = reshape(g2m4,nfft,nave);
PG2M4 = fft(g2m4,nfft,1)/nfft;
PG2M4 = mean(PG2M4(I),2);           % Convert to single-sided FFT

% Clear time series
clear g1m1 g1m2 g1m3 g1m4 g2m1 g2m2 g2m3 g2m4

% Save FFTs to mat file

save(fname{ii},'f','PG1M1','PG1M2','PG1M3','PG1M4','PG2M1','PG2M2','PG2M3','PG2M4','-compress')

% Prepare for next data set
clear PG1M1 PG1M2 PG1M3 PG1M4 PG2M1 PG2M2 PG2M3 PG2M4
pack

end

toc

% End Program

```

G.4.2 MDM Main Program

```

%% mdmv4.m
%
% Todd Schultz      v1  9/12/2005
%                   v2  10/6/2005
%                   v3  10/27/2005
%                   v4  12/2/2005
%
%
% Version 4 changes: added Monte Carlo simulation option for
uncertainty
% analysis.  Input uncertainties are assumed to be Gaussian.
%
% Version 3 changes: updated solution method for determining the
pressure
% amplitudes and the reflection coefficient matrix.  I now use all
% available data and use either Gaussian elimination for a
deterministic
% system or a least-squares fit for an over determined system.  This
% appears to have smoothed out the data around cut-on frequencies.
%
% This program is design to carry out the data reduction for the MDM
% acoustic impedance testing method.  The spectral data is retrieved
from
% the mat files exported by the Pulse system  from the measurement of
the
% four independent sources and the two set up text files
% are read in directly.  The first set up file contains a 8 by 3 matrix
of
% the microphone locations with respect to the X-, Y-, and D-axis, an

```

```

% 8 by 3 matrix with the uncertainties of the microphone locations.
The
% second text file contains an array with the information about the
% waveguide used and the atmospheric temperature and pressure and
% uncertainties. The first element is the waveguide number, second
element
% is the effective number spectral averages, the third element is
% temperature, fourth element is the uncertainty in temperature, fifth
% element pressure, sixth element is the is the uncertainty in
pressure.
% Waveguide number: 0 = large waveguide (1 inch by 1 inch)
%                   1 = small waveguide (8.5 mm by 8.5 mm)
% A +jwt sign convention is used through this program.
%
clear all; close all; clc; pack;
tic

%% Input set up file names.
% fnmic = input('Input the file name for the microphone location set up
information file.\n','s');
% fnenv = input('Input the file name for the enviromental set up
file.\n','s');
% n_source = input('Input the number of independent sources
measured.\n');
% fndata = cell(n_source,1);
% fndata{1} = input('Input the file name for the first source mat
file.\n','s');
% for ii = 2:n_source
%     fndata{ii} = input('Input the file name for the next source mat
file.\n','s');
% end
% fsave = input('Input the file name to save the data in.\n','s');
% fsave_mc = input('Input the file name to save the uncertainty
estimates to.\n','s');
% pic = input('Press 0 if you would like the figures saved or press 1
otherwise.\n');
% trig = input('Press 0 for NO uncertainty analysis or press 1 for a
Monte Carlo uncertainty analysis.\n','s');
% if trig == 1
%     % funcert = input('Input the file name for the FFT uncertainty
estimates.\n','s');
% end

fnmic = 'C:\Documents and Settings\Todd\My
Documents\Matlab\mdm\version4\xydmic.txt';
fnenv = 'shmdm.txt';
fndata = {'noplake';'top';'left';'topleft'};
% fndata = {'noplake';'top';'left';'topleft';'tri'};
n_source = length(fndata);
% fsave = 'mdmCT65';
fsave = 'junk1';
% fsave_mc = 'mdmCT65_mc';
fsave_mc = 'junk2';
pic = 0;
trig = 0;
% funcert = 'backgrounduncertainty';

```

```

funcert = 'junk3';

%% Data analysis constants
n_mc = 1000; % # of Monte Carlo iterations to use

%% Read in Pulse data and rename variables to allow all data sets to be
% loaded. The frequency range is already taken care of in
mdm_pulsev4.m.
PG1M1_s = cell(n_source,1); PG1M2_s = cell(n_source,1); PG1M3_s =
cell(n_source,1); PG1M4_s = cell(n_source,1);
PG2M1_s = cell(n_source,1); PG2M2_s = cell(n_source,1); PG2M3_s =
cell(n_source,1); PG2M4_s = cell(n_source,1);
for ii = 1:n_source
    load(fndata{ii})
    PG1M1_s{ii} = PG1M1; PG1M2_s{ii} = PG1M2; PG1M3_s{ii} = PG1M3;
PG1M4_s{ii} = PG1M4;
    PG2M1_s{ii} = PG2M1; PG2M2_s{ii} = PG2M2; PG2M3_s{ii} = PG2M3;
PG2M4_s{ii} = PG2M4;
end

clear PG1M1 PG1M2 PG1M3 PG1M4 PG2M1 PG2M2 PG2M3 PG2M4

%% Read in microphone locations.
A = dlmread(fnmic, '\t'); % Read in set up file
XYD = A(1:8,:); % Microphone locations [m]
UXYD = A(9:16,:); % standard Uncertainty in Mic
locations [m]
nXYD = 35; % # of measurements
clear A;

%% Read in experimental setup information
A = dlmread(fnenv, '\t'); % Read in set up file
tube = A(1); % Tube number
navg = A(2); % Number of averages used
l = A(3); % mic location closer to the
specimen [m]
Ul = A(4); % standard Uncertainty in d [m]
nl = A(5); % # of measurements of l
s = A(6); % mic spacing [m]
Us = A(7); % standard Uncertainty in s [m]
ns = A(8); % # of measurements of s
tatm = A(9)+273.15; % Atmospheric temperature [K]
(input units are [C])
Utatm = A(10); % standard Uncertainty in Tatm
[K] or [C]
nT = A(11); % # of temperature measurements
patm = A(12)*1000; % Atmospheric pressure [Pa]
(input units are [kPa])
Upatm = A(13)*1000; % standard Uncertainty in Patm
[Pa] (input units are [kPa])
nP = A(14); % # of pressure measurements
clear A;

%% Constants

```

```

% Cross-section width, l [m]
switch tube
    case 0
        dtube = 0.02544;           % 1 in square tube
        Udtube = 1.5e-5;          % standard uncertainty in tube
    dimension
        ndtube = 30;
        ab = [dtube dtube];       % ab(1)=a=x-axis, ab(2)=b=y-axis
    case 1
        dtube = 0.0085;           % Old 8.5 x 8.5 mm tube
        Udtube = 3.8e-5;          % standard uncertainty in tube
    dimension
        ndtube = 30;
        ab = [dtube dtube];       % ab(1)=a=x-axis, ab(2)=b=y-axis
end

% Air properties and wavenumber
gamma = 1.4;                      % ratio of specific heats for
air                                  air
Rair = 287;                        % gas constant for air
[J/(kg*K)]
c0 = sqrt(gamma*Rair*tatm);        % speed of sound [m/s]
rho = patm/(Rair*tatm);           % density of air [kg/m^3]
k = 2*pi*f/c0;                    % wavenumber [1/m]

% Cut-on frequencies for the higher-order modes
% x-axis is rows, y-axis is columns
M_max = ceil(2*ab(1)*max(f)/c0);
N_max = ceil(2*ab(2)*max(f)/c0);
[N,M] = meshgrid(0:N_max,0:M_max);
fco = (c0/(2*pi))*sqrt((M*pi/ab(1)).^2+(N*pi/ab(2)).^2);
fco_sort = reshape(fco,size(fco,1)*size(fco,2),1);
fco_sort = sort(fco_sort);

I = find(max(f) >= fco_sort);
I = find(fco_sort(I(length(I))) == fco);
[N_max,M_max] = size(fco(I));
[N,M] = meshgrid(0:N_max,0:M_max);
fco = (c0/(2*pi))*sqrt((M*pi/ab(1)).^2+(N*pi/ab(2)).^2);
fco_sort = reshape(fco,size(fco,1)*size(fco,2),1);
fco_sort = sort(fco_sort);

%%
In = cell(N_max+1,M_max+1);
for nn = 0:N_max
    for mm = 0:M_max
        In{nn+1,mm+1} = find(f > fco(nn+1,mm+1));
    end
end

% Call mdm_sub.m to carry out computations of the wave mode
coefficients.
% Will have to carry out the computations in a loop, once per
frequency.
% A,B = {(0,0),(1,0),(0,1),(1,1)}
% Initialize variables

```

```

A = cell(n_source,length(f));    B = cell(n_source,length(f));
kz = cell(length(f),1);

for ii = 1:length(f)
    floop = f(ii);
    for jj = 1:n_source
        GM =
[PG1M1_s{jj}(ii);PG1M2_s{jj}(ii);PG1M3_s{jj}(ii);PG1M4_s{jj}(ii);PG2M1_
s{jj}(ii);PG2M2_s{jj}(ii);PG2M3_s{jj}(ii);PG2M4_s{jj}(ii)];
        [AA,BB,kkz] = mdm_subv4(f(ii),GM,ab,XYD,c0,fco);
        A{jj,ii} = AA;
        B{jj,ii} = BB;
        kz{ii} = kkz;
    end
end

%% Compute the incident and reflected power for each source
% W = ((a*b)/(8*rho*c0*k))*sum(kzmn*abs(Amn)^2)
Wi = zeros(n_source,length(f));
Wr = zeros(n_source,length(f));
alpha = zeros(n_source,length(f));

for ii = 1:length(f)
    for jj = 1:n_source
        Amn = A{jj,ii};
        Bmn = B{jj,ii};
        kzmn = kz{ii};
        Wi(jj,ii) =
(ab(1)*ab(2)/(8*rho*c0*k(ii)))*sum(kzmn.*abs(Amn).^2);
        Wr(jj,ii) =
(ab(1)*ab(2)/(8*rho*c0*k(ii)))*sum(kzmn.*abs(Bmn).^2);
        alpha(jj,ii) = 1-(Wr(jj,ii)/Wi(jj,ii));
    end
end

%% Construct the A and B matrices and compute the reflection
coefficient
% matrix, acoustic impedance, and specific acoustic impedance
% Initialize the variable R (mode order 00 10 01 11)
R = zeros([M_max,N_max,length(f)]);
Zac = zeros(length(A{1,length(f)}),1);
Zspac = zeros(length(A{1,length(f)}),1);
A_cond = zeros(length(f),1);

for ii = 1:length(f)
    len = length(A{1,ii});                % # of modes to resolve

    A_matrix = [A{1,ii}];
    B_matrix = [B{1,ii}];
    for jj = 2:n_source
        A_matrix = [A_matrix A{jj,ii}];
        B_matrix = [B_matrix B{jj,ii}];
    end
    % check the rank of A (should equal 4)
    A_rank = rank(A_matrix);
    A_cond(ii) = cond(A_matrix);
end

```

```

R_temp = B_matrix/A_matrix;

% Store results in final variables
R(1:len,1:len,ii) = R_temp;
Zac(1:len,ii) = (1+diag(R_temp))./(1-diag(R_temp)); % Acoustic
impedance ratio
Zspac(1:len,ii) = Zac(1:len,ii)./sqrt(1-
(fco_sort(1:len)/f(ii)).^2); % Specific acoustic impedance ratio

end

%% Save the results
save(fsave,'f','fco','kz','A','B','R','Zac','Zspac','A_cond','Wi','Wr',
'alpha','-compress');

%% Plotting functions
mdm_plotv4

toc
tic

%% Monte Carlo simulation for uncertainty estimates
if trig == 1
% Prepare workspace
close all
clear AA A_1 A_2 A_3 A_4 A_cond A_matrix A_rank Amn Atemp
clear BB B_1 B_2 B_3 B_4 B_cond B_matrix B_rank Bmn Btemp
clear I In In00 In10 In01 In11 M N R_temp Wi Wr
clear floop h h1 h2 h3 h4 h5 h6 h7 h8 ii jj mm kz kkz kzmn

load(funcert) % Load FFT uncertainties
pack

pause(0.1)

% Initialize variables to save the output in
A_mc = cell(n_source,length(f),n_mc);
B_mc = cell(n_source,length(f),n_mc);
R_mc = zeros([M_max,N_max,length(f),n_mc]);
Zac_mc = zeros(length(A{1,length(f)}),n_mc);
Zspac_mc = zeros(length(A{1,length(f)}),n_mc);
%A_cond_mc = zeros(length(f),n_mc);

PG1M1_s_mc = PG1M1_s; PG1M2_s_mc = PG1M2_s; PG1M3_s_mc = PG1M3_s;
PG1M4_s_mc = PG1M4_s;
PG2M1_s_mc = PG2M1_s; PG2M2_s_mc = PG2M2_s; PG2M3_s_mc = PG2M3_s;
PG2M4_s_mc = PG2M4_s;

for ii = 1:length(f)

for kk = 1:n_mc
% Perturb input quantities by a random amount given by
their
% uncertainty distribution

```

```

tاتم_mc = tاتم + Utاتم*randn(1);
patم_mc = patم + Upatم*randn(1);
ab_mc = ab + Udtube*randn(1,2);
XYD_mc = XYD + UXYD.*randn(8,3);

% for ii = 1:length(f)
    for jj = 1:n_source
        junk =
mvgrnd([real(PG1M1_s{jj}(ii));imag(PG1M1_s{jj}(ii))],uGg1m1(:, :, ii),1);
        PG1M1_s_mc{jj}(ii) = junk(1)+j*junk(2);

        junk =
mvgrnd([real(PG1M2_s{jj}(ii));imag(PG1M2_s{jj}(ii))],uGg1m2(:, :, ii),1);
        PG1M2_s_mc{jj}(ii) = junk(1)+j*junk(2);

        junk =
mvgrnd([real(PG1M3_s{jj}(ii));imag(PG1M3_s{jj}(ii))],uGg1m3(:, :, ii),1);
        PG1M3_s_mc{jj}(ii) = junk(1)+j*junk(2);

        junk =
mvgrnd([real(PG1M4_s{jj}(ii));imag(PG1M4_s{jj}(ii))],uGg1m4(:, :, ii),1);
        PG1M4_s_mc{jj}(ii) = junk(1)+j*junk(2);

        junk =
mvgrnd([real(PG2M1_s{jj}(ii));imag(PG2M1_s{jj}(ii))],uGg2m1(:, :, ii),1);
        PG2M1_s_mc{jj}(ii) = junk(1)+j*junk(2);

        junk =
mvgrnd([real(PG2M2_s{jj}(ii));imag(PG2M2_s{jj}(ii))],uGg2m2(:, :, ii),1);
        PG2M2_s_mc{jj}(ii) = junk(1)+j*junk(2);

        junk =
mvgrnd([real(PG2M3_s{jj}(ii));imag(PG2M3_s{jj}(ii))],uGg2m3(:, :, ii),1);
        PG2M3_s_mc{jj}(ii) = junk(1)+j*junk(2);

        junk =
mvgrnd([real(PG2M4_s{jj}(ii));imag(PG2M4_s{jj}(ii))],uGg2m4(:, :, ii),1);
        PG2M4_s_mc{jj}(ii) = junk(1)+j*junk(2);
    end % n_source loop jj
% end % frequency loop ii

% Perturbed speed of sound and wavenumber
c0_mc = sqrt(gamma*Rair*tاتم_mc); % speed of
sound [m/s]
rho_mc = patم_mc/(Rair*tاتم_mc); %
density of air [kg/m^3]
k_mc = 2*pi*f/c0_mc; %
wavenumber [1/m]

%% Call mdm_sub.m to carry out computations of the wave
mode coefficients.

```

```

% Will have to carry out the computations in a loop, once
per frequency.
% A,B = {(0,0),(1,0),(0,1),(1,1)}

% for ii = 1:length(f)
    floop = f(ii);
    for jj = 1:n_source
        GM =
[PG1M1_s_mc{jj}(ii);PG1M2_s_mc{jj}(ii);PG1M3_s_mc{jj}(ii);PG1M4_s_mc{jj}
}{ii);PG2M1_s_mc{jj}(ii);PG2M2_s_mc{jj}(ii);PG2M3_s_mc{jj}(ii);PG2M4_s_
mc{jj}(ii)];
        [AA,BB,kkz] =
mdm_subv4(f(ii),GM,ab_mc,XYD_mc,c0_mc,fco);
        A_mc{jj,ii,kk} = AA;
        B_mc{jj,ii,kk} = BB;
    end
% end

%% Construct the A and B matrices and compute the
reflection coefficient
% matrix, acoustic impedance, and specific acoustic
impedance
% Initialize the variable R (mode order 00 10 01 11)

% for ii = 1:length(f)
    len = length(A{1,ii}); % # of modes to
resolve

    A_matrix = [A_mc{1,ii,kk}];
    B_matrix = [B_mc{1,ii,kk}];
    for jj = 2:n_source
        A_matrix = [A_matrix A_mc{jj,ii,kk}];
        B_matrix = [B_matrix B_mc{jj,ii,kk}];
    end
    % check the rank of A (should equal 4)
    %A_rank = rank(A_matrix);
    %A_cond_mc(ii,kk) = cond(A_matrix);
    R_temp = B_matrix/A_matrix;

    % Store results in final variables
    R_mc(1:len,1:len,ii,kk) = R_temp;
    Zac_mc(1:len,ii,kk) = (1+diag(R_temp))./(1-
diag(R_temp)); % Acoustic impedance ratio
    Zspac_mc(1:len,ii,kk) = Zac_mc(1:len,ii,kk)./sqrt(1-
(fco_sort(1:len)/f(ii)).^2); % Specific acoustic impedance ratio

% end % end for frequency loop ii

end % end for Monte Carlo loop kk

end % end for frequency loop ii

%% Save Monte Carlo data
save([fsave
'_MCdata'], 'f', 'A_mc', 'B_mc', 'R_mc', 'Zac_mc', 'Zspac_mc', '-compress')

```



```

%% Find the maximum mode numbers that are needed
[M,N] = find(f >= fco); % mode
number indices
M = M-1; N = N-1; %
convert to mode numbers
n_modes = length(M); %
Number of modes to include

%% Define augmented amplitude vector
GMaug = [real(GM); imag(GM)]; %
Augmented amplitude vector

%% Define the required microphone locations for a deterministic system
x = XYD(:,1);
y = XYD(:,2);
d = XYD(:,3);

%% Calculate the z-axis wavenumbers
kz = sqrt((w./c0).^2-(M*pi/a).^2-(N*pi/b).^2);

%% Construct the coefficient matrix L
Lr = zeros(length(d),2*n_modes);
Li = zeros(length(d),2*n_modes);
for ii = 1:n_modes
    Lr(:,ii) = cos(M(ii)*pi*x/a).*cos(N(ii)*pi*y/b).*cos(kz(ii)*d);
    Lr(:,ii+n_modes) = cos(M(ii)*pi*x/a).*cos(N(ii)*pi*y/b).*cos(-
kz(ii)*d);

    Li(:,ii) = cos(M(ii)*pi*x/a).*cos(N(ii)*pi*y/b).*sin(kz(ii)*d);
    Li(:,ii+n_modes) = cos(M(ii)*pi*x/a).*cos(N(ii)*pi*y/b).*sin(-
kz(ii)*d);
end
Laug = [Lr -Li;Li Lr]; % augmented [L] matrix

%% Lrtemp=[cos(kz00*d1) cos(pi*x1/a)*cos(kz10*d1)
cos(pi*y1/b)*cos(kz01*d1) cos(pi*x1/a)*cos(pi*y1/b)*cos(kz11*d1) cos(-
kz00*d1) cos(pi*x1/a)*cos(-kz10*d1) cos(pi*y1/b)*cos(-kz01*d1)
cos(pi*x1/a)*cos(pi*y1/b)*cos(-kz11*d1);
% cos(kz00*d2) cos(pi*x2/a)*cos(kz10*d2) cos(pi*y2/b)*cos(kz01*d2)
cos(pi*x2/a)*cos(pi*y2/b)*cos(kz11*d2) cos(-kz00*d2) cos(pi*x2/a)*cos(-
kz10*d2) cos(pi*y2/b)*cos(-kz01*d2) cos(pi*x2/a)*cos(pi*y2/b)*cos(-
kz11*d2);
% cos(kz00*d3) cos(pi*x3/a)*cos(kz10*d3) cos(pi*y3/b)*cos(kz01*d3)
cos(pi*x3/a)*cos(pi*y3/b)*cos(kz11*d3) cos(-kz00*d3) cos(pi*x3/a)*cos(-
kz10*d3) cos(pi*y3/b)*cos(-kz01*d3) cos(pi*x3/a)*cos(pi*y3/b)*cos(-
kz11*d3);
% cos(kz00*d4) cos(pi*x4/a)*cos(kz10*d4) cos(pi*y4/b)*cos(kz01*d4)
cos(pi*x4/a)*cos(pi*y4/b)*cos(kz11*d4) cos(-kz00*d4) cos(pi*x4/a)*cos(-
kz10*d4) cos(pi*y4/b)*cos(-kz01*d4) cos(pi*x4/a)*cos(pi*y4/b)*cos(-
kz11*d4);
% cos(kz00*d5) cos(pi*x5/a)*cos(kz10*d5) cos(pi*y5/b)*cos(kz01*d5)
cos(pi*x5/a)*cos(pi*y5/b)*cos(kz11*d5) cos(-kz00*d5) cos(pi*x5/a)*cos(-
kz10*d5) cos(pi*y5/b)*cos(-kz01*d5) cos(pi*x5/a)*cos(pi*y5/b)*cos(-
kz11*d5);
% cos(kz00*d6) cos(pi*x6/a)*cos(kz10*d6) cos(pi*y6/b)*cos(kz01*d6)
cos(pi*x6/a)*cos(pi*y6/b)*cos(kz11*d6) cos(-kz00*d6) cos(pi*x6/a)*cos(-

```

```

kz10*d6) cos(pi*y6/b)*cos(-kz01*d6) cos(pi*x6/a)*cos(pi*y6/b)*cos(-
kz11*d6);
%      cos(kz00*d7) cos(pi*x7/a)*cos(kz10*d7) cos(pi*y7/b)*cos(kz01*d7)
cos(pi*x7/a)*cos(pi*y7/b)*cos(kz11*d7) cos(-kz00*d7) cos(pi*x7/a)*cos(-
kz10*d7) cos(pi*y7/b)*cos(-kz01*d7) cos(pi*x7/a)*cos(pi*y7/b)*cos(-
kz11*d7);
%      cos(kz00*d8) cos(pi*x8/a)*cos(kz10*d8) cos(pi*y8/b)*cos(kz01*d8)
cos(pi*x8/a)*cos(pi*y8/b)*cos(kz11*d8) cos(-kz00*d8) cos(pi*x8/a)*cos(-
kz10*d8) cos(pi*y8/b)*cos(-kz01*d8) cos(pi*x8/a)*cos(pi*y8/b)*cos(-
kz11*d8);];
%
% Litemp=[sin(kz00*d1) cos(pi*x1/a)*sin(kz10*d1)
cos(pi*y1/b)*sin(kz01*d1) cos(pi*x1/a)*cos(pi*y1/b)*sin(kz11*d1) sin(-
kz00*d1) cos(pi*x1/a)*sin(-kz10*d1) cos(pi*y1/b)*sin(-kz01*d1)
cos(pi*x1/a)*cos(pi*y1/b)*sin(-kz11*d1);
%      sin(kz00*d2) cos(pi*x2/a)*sin(kz10*d2) cos(pi*y2/b)*sin(kz01*d2)
cos(pi*x2/a)*cos(pi*y2/b)*sin(kz11*d2) sin(-kz00*d2) cos(pi*x2/a)*sin(-
kz10*d2) cos(pi*y2/b)*sin(-kz01*d2) cos(pi*x2/a)*cos(pi*y2/b)*sin(-
kz11*d2);
%      sin(kz00*d3) cos(pi*x3/a)*sin(kz10*d3) cos(pi*y3/b)*sin(kz01*d3)
cos(pi*x3/a)*cos(pi*y3/b)*sin(kz11*d3) sin(-kz00*d3) cos(pi*x3/a)*sin(-
kz10*d3) cos(pi*y3/b)*sin(-kz01*d3) cos(pi*x3/a)*cos(pi*y3/b)*sin(-
kz11*d3);
%      sin(kz00*d4) cos(pi*x4/a)*sin(kz10*d4) cos(pi*y4/b)*sin(kz01*d4)
cos(pi*x4/a)*cos(pi*y4/b)*sin(kz11*d4) sin(-kz00*d4) cos(pi*x4/a)*sin(-
kz10*d4) cos(pi*y4/b)*sin(-kz01*d4) cos(pi*x4/a)*cos(pi*y4/b)*sin(-
kz11*d4);
%      sin(kz00*d5) cos(pi*x5/a)*sin(kz10*d5) cos(pi*y5/b)*sin(kz01*d5)
cos(pi*x5/a)*cos(pi*y5/b)*sin(kz11*d5) sin(-kz00*d5) cos(pi*x5/a)*sin(-
kz10*d5) cos(pi*y5/b)*sin(-kz01*d5) cos(pi*x5/a)*cos(pi*y5/b)*sin(-
kz11*d5);
%      sin(kz00*d6) cos(pi*x6/a)*sin(kz10*d6) cos(pi*y6/b)*sin(kz01*d6)
cos(pi*x6/a)*cos(pi*y6/b)*sin(kz11*d6) sin(-kz00*d6) cos(pi*x6/a)*sin(-
kz10*d6) cos(pi*y6/b)*sin(-kz01*d6) cos(pi*x6/a)*cos(pi*y6/b)*sin(-
kz11*d6);
%      sin(kz00*d7) cos(pi*x7/a)*sin(kz10*d7) cos(pi*y7/b)*sin(kz01*d7)
cos(pi*x7/a)*cos(pi*y7/b)*sin(kz11*d7) sin(-kz00*d7) cos(pi*x7/a)*sin(-
kz10*d7) cos(pi*y7/b)*sin(-kz01*d7) cos(pi*x7/a)*cos(pi*y7/b)*sin(-
kz11*d7);
%      sin(kz00*d8) cos(pi*x8/a)*sin(kz10*d8) cos(pi*y8/b)*sin(kz01*d8)
cos(pi*x8/a)*cos(pi*y8/b)*sin(kz11*d8) sin(-kz00*d8) cos(pi*x8/a)*sin(-
kz10*d8) cos(pi*y8/b)*sin(-kz01*d8) cos(pi*x8/a)*cos(pi*y8/b)*sin(-
kz11*d8);];
% Laugtemp = [Lrtemp -Litemp;Litemp Lrtemp];

%% Solve for the wave-mode coefficients
Waug = Laug\GMaug;
WM = Waug(1:2*n_modes)+j*Waug(2*n_modes+1:length(Waug));
A = WM(1:n_modes);
B = WM(n_modes+1:length(WM));

% End subroutine

```

G.4.4 MDM Plotting Subroutine

```

%% mdm_plotv4.m
%
% Todd Schultz          12/17/2005
%
% This programs carries out all the plotting functions for the MDM
codes.
% The plotting functions where removed from the base code to conserve
space
% and make it easier to edit the actual computations of the results and
% Monte Carlo simulations.

%% Plotting Functions
%% Define helper variables for plotting
In00 = find(f > fco(1,1));
In10 = find(f > fco(2,1));
In01 = find(f > fco(1,2));
In11 = find(f > fco(2,2));

A_1 = zeros(length(f),n_source); B_1 = zeros(length(f),n_source);
A_2 = zeros(length(f),n_source); B_2 = zeros(length(f),n_source);
A_3 = zeros(length(f),n_source); B_3 = zeros(length(f),n_source);
A_4 = zeros(length(f),n_source); B_4 = zeros(length(f),n_source);
for ii = 1:length(f)
    for jj = 1:n_source
        Atemp = A{jj,ii};
        Btemp = B{jj,ii};

        A_1(ii,jj) = Atemp(1);
        B_1(ii,jj) = Btemp(1);

        if length(Atemp) >= 2
            A_2(ii,jj) = Atemp(2);
            B_2(ii,jj) = Btemp(2);
        end
        if length(Atemp) >= 3
            A_3(ii,jj) = Atemp(3);
            B_3(ii,jj) = Btemp(3);
        end
        if length(Atemp) >= 4
            A_4(ii,jj) = Atemp(4);
            B_4(ii,jj) = Btemp(4);
        end
    end
end

%% Plots
pref = 20e-6;
%% Plot incident pressure amplitudes
figure(1)
    h1 = subplot(2,2,1);
    h2 = subplot(2,2,2);

```

```

h3 = subplot(2,2,3);
h4 = subplot(2,2,4);
subplot(2,2,1); plot(f(In00)/1000,20*log10(abs(A_1(In00, :))/pref))
subplot(2,2,3); plot(f(In10)/1000,20*log10(abs(A_2(In10, :))/pref))
subplot(2,2,2); plot(f(In01)/1000,20*log10(abs(A_3(In01, :))/pref))
subplot(2,2,4); plot(f(In11)/1000,20*log10(abs(A_4(In11, :))/pref))
subplot(h1)
    xlim([f(1) f(length(f))]/1000)
    xlabel({'Freq [kHz]'; '(a) Mode (0,0)'})
    ylabel('|P| [dB]')
    title('Incident Sound Pressure Levels')
    grid on
subplot(h3)
    xlim([f(1) f(length(f))]/1000)
    xlabel({'Freq [kHz]'; '(b) Mode (1,0)'})
    ylabel('|P| [dB]')
    grid on
subplot(h2)
    xlim([f(1) f(length(f))]/1000)
    xlabel({'Freq [kHz]'; '(c) Mode (0,1)'})
    ylabel('|P| [dB]')
    grid on
subplot(h4)
    xlim([f(1) f(length(f))]/1000)
    xlabel({'Freq [kHz]'; '(d) Mode (1,1)'})
    ylabel('|P| [dB]')
    grid on
    legend(fndata, 'Location', 'NorthWest')

%% Plot reflected pressure amplitudes
figure(2)
set(gcf, 'paperorientation', 'landscape')
set(gcf, 'paperposition', [0.25 0.25 10.5 8.0])
h1 = subplot(2,2,1);
h2 = subplot(2,2,2);
h3 = subplot(2,2,3);
h4 = subplot(2,2,4);
subplot(2,2,1); plot(f(In00)/1000,20*log10(abs(B_1(In00, :))/pref))
subplot(2,2,3); plot(f(In10)/1000,20*log10(abs(B_2(In10, :))/pref))
subplot(2,2,2); plot(f(In01)/1000,20*log10(abs(B_3(In01, :))/pref))
subplot(2,2,4); plot(f(In11)/1000,20*log10(abs(B_4(In11, :))/pref))
subplot(h1)
    xlim([f(1) f(length(f))]/1000)
    xlabel({'Freq [kHz]'; '(a) Mode (0,0)'})
    ylabel('|P| [dB]')
    title('Reflected Sound Pressure Levels')
    grid on
subplot(h3)
    xlim([f(1) f(length(f))]/1000)
    xlabel({'Freq [kHz]'; '(b) Mode (1,0)'})
    ylabel('|P| [dB]')
    grid on
subplot(h2)
    xlim([f(1) f(length(f))]/1000)
    xlabel({'Freq [kHz]'; '(c) Mode (0,1)'})
    ylabel('|P| [dB]')
    grid on

```

```

subplot(h4)
    xlim([f(1) f(length(f))]/1000)
    xlabel({'Freq [kHz]'; '(d) Mode (1,1)'})
    ylabel('|P| [dB]')
    legend(fndata, 'Location', 'NorthWest')
    grid on

%% Plot reflection coefficients
figure(3)
    h1=subplot(2,1,1);
    h2=subplot(2,1,2);
    subplot(2,1,1);
    plot(f(In0)/1000,squeeze(abs(R(1,1,In0))),f(In10)/1000,squeeze(abs(R(
    2,2,In10))),f(In01)/1000,squeeze(abs(R(3,3,In01))),f(In11)/1000,squeeze
    (abs(R(4,4,In11))))
        subplot(2,1,2);
    plot(f(In0)/1000,squeeze(angle(R(1,1,In0)))*180/pi,f(In10)/1000,squee
    ze(angle(R(2,2,In10)))*180/pi,f(In01)/1000,squeeze(angle(R(3,3,In01)))*
    180/pi,f(In11)/1000,squeeze(angle(R(4,4,In11)))*180/pi)
        subplot(h1);
            ylabel('|R|')
            xlim([f(1) f(length(f))]/1000)
            xlabel('Freq [kHz]')
            legend('(0,0)', '(1,0)', '(0,1)', '(1,1)')
            title('Reflection Coefficients')
            grid on
        subplot(h2);
            xlim([f(1) f(length(f))]/1000)
            ylabel('\phi [deg]')
            xlabel('Freq [kHz]')
            grid on

%% Plot mode scattering coefficients
figure(4)
    h1=subplot(4,2,1);
    h2=subplot(4,2,2);
    h3=subplot(4,2,3);
    h4=subplot(4,2,4);
    h5=subplot(4,2,5);
    h6=subplot(4,2,6);
    h7=subplot(4,2,7);
    h8=subplot(4,2,8);
    % From (0,0)
        subplot(4,2,1);
    plot(f(In10)/1000,squeeze(abs(R(2,1,In10))),f(In01)/1000,squeeze(abs(R(
    3,1,In01))),f(In11)/1000,squeeze(abs(R(4,1,In11))))
        subplot(4,2,3);
    plot(f(In10)/1000,squeeze(angle(R(2,1,In10)))*180/pi,f(In01)/1000,squee
    ze(angle(R(3,1,In01)))*180/pi,f(In11)/1000,squeeze(angle(R(4,1,In11)))*
    180/pi)

        subplot(h1);
            ylabel('|R|')
            xlim([f(1) f(length(f))]/1000)
            xlabel('Freq [kHz]')
            legend('(0,0) to (1,0)', '(0,0) to (0,1)', '(0,0) to (1,1)')

```

```

        title('Mode Scattering Coefficients')
        grid on
    subplot(h3);
        xlim([f(1) f(length(f))]/1000)
        ylabel('\phi [deg]')
        xlabel('Freq [kHz]')
        grid on

% From (1,0)
    subplot(4,2,2);
    plot(f(In10)/1000,squeeze(abs(R(1,2,In10))),f(In10)/1000,squeeze(abs(R(
3,2,In10))),f(In11)/1000,squeeze(abs(R(4,2,In11))))
    subplot(4,2,4);
    plot(f(In10)/1000,squeeze(angle(R(1,2,In10)))*180/pi,f(In10)/1000,squee
ze(angle(R(3,2,In10)))*180/pi,f(In11)/1000,squeeze(angle(R(4,2,In11)))*
180/pi)

    subplot(h2);
        ylabel('|R|')
        xlim([f(1) f(length(f))]/1000)
        xlabel('Freq [kHz]')
        legend('(1,0) to (0,0)', '(1,0) to (0,1)', '(1,0) to (1,1)')
        title('Mode Scattering Coefficients')
        grid on
    subplot(h4);
        xlim([f(1) f(length(f))]/1000)
        ylabel('\phi [deg]')
        xlabel('Freq [kHz]')
        grid on

% From (0,1)
    subplot(4,2,5);
    plot(f(In01)/1000,squeeze(abs(R(1,3,In01))),f(In01)/1000,squeeze(abs(R(
2,3,In01))),f(In11)/1000,squeeze(abs(R(4,3,In11))))
    subplot(4,2,7);
    plot(f(In01)/1000,squeeze(angle(R(1,3,In01)))*180/pi,f(In01)/1000,squee
ze(angle(R(2,3,In01)))*180/pi,f(In11)/1000,squeeze(angle(R(4,3,In11)))*
180/pi)

    subplot(h5);
        ylabel('|R|')
        xlim([f(1) f(length(f))]/1000)
        xlabel('Freq [kHz]')
        legend('(0,1) to (0,0)', '(0,1) to (1,0)', '(0,1) to (1,1)')
        title('Mode Scattering Coefficients')
        grid on
    subplot(h7);
        xlim([f(1) f(length(f))]/1000)
        ylabel('\phi [deg]')
        xlabel('Freq [kHz]')
        grid on

% From (1,1)
    subplot(4,2,6);
    plot(f(In11)/1000,squeeze(abs(R(1,4,In11))),f(In11)/1000,squeeze(abs(R(
2,4,In11))),f(In11)/1000,squeeze(abs(R(3,4,In11))))

```

```

subplot(4,2,8);
plot(f(In11)/1000,squeeze(angle(R(1,4,In11)))*180/pi,f(In11)/1000,squeeze(angle(R(2,4,In11)))*180/pi,f(In11)/1000,squeeze(angle(R(3,4,In11)))*180/pi)

```

```

subplot(h6);
ylabel('|R|')
xlim([f(1) f(length(f))]/1000)
xlabel('Freq [kHz]')
legend('(1,1) to (0,0)', '(1,1) to (1,0)', '(1,1) to (0,1)')
title('Mode Scattering Coefficients')
grid on
subplot(h8);
xlim([f(1) f(length(f))]/1000)
ylabel('\phi [deg]')
xlabel('Freq [kHz]')
grid on

```

```

%% Plot normal incident normalized acoustic impedance
figure(5)

```

```

h1=subplot(2,1,1);
h2=subplot(2,1,2);
subplot(2,1,1); plot(f(In00)/1000,real(Zac(1,In00)))
subplot(2,1,2); plot(f(In00)/1000,imag(Zac(1,In00)))
subplot(h1);
ylabel('\theta')
xlim([f(1) f(length(f))]/1000)
xlabel('Freq [kHz]')
%legend('(0,0)', '(1,0)', '(0,1)', '(1,1)')
title('Normal Incident Acoustic Impedance')
grid on
subplot(h2);
xlim([f(1) f(length(f))]/1000)
ylabel('\chi')
xlabel('Freq [kHz]')
grid on

```

```

%% Plot normalized acoustic impedance
figure(6)

```

```

h1=subplot(2,1,1);
h2=subplot(2,1,2);
subplot(2,1,1);
plot(f(In00)/1000,real(Zac(1,In00)),f(In10)/1000,real(Zac(2,In10)),f(In01)/1000,real(Zac(3,In01)),f(In11)/1000,real(Zac(4,In11)))
subplot(2,1,2);
plot(f(In00)/1000,imag(Zac(1,In00)),f(In10)/1000,imag(Zac(2,In10)),f(In01)/1000,imag(Zac(3,In01)),f(In11)/1000,imag(Zac(4,In11)))
subplot(h1);
ylabel('\theta_a_c')
xlim([f(1) f(length(f))]/1000)
xlabel('Freq [kHz]')
legend('(0,0)', '(1,0)', '(0,1)', '(1,1)')
title('Acoustic Impedance Ratio')
grid on
subplot(h2);
xlim([f(1) f(length(f))]/1000)

```

```

        ylabel('\chi_a_c')
        xlabel('Freq [kHz]')
        grid on

%% Plot normalized specific acoustic impedance
figure(7)
    h1=subplot(2,1,1);
    h2=subplot(2,1,2);
    subplot(2,1,1);
    plot(f(In00)/1000,real(Zspac(1,In00)),f(In10)/1000,real(Zspac(2,In10)),
    f(In01)/1000,real(Zspac(3,In01)),f(In11)/1000,real(Zspac(4,In11)))
    subplot(2,1,2);
    plot(f(In00)/1000,imag(Zspac(1,In00)),f(In10)/1000,imag(Zspac(2,In10)),
    f(In01)/1000,imag(Zspac(3,In01)),f(In11)/1000,imag(Zspac(4,In11)))
    subplot(h1);
        ylabel('\theta_s_p_a_c')
        xlim([f(1) f(length(f))]/1000)
        xlabel('Freq [kHz]')
        legend('(0,0)', '(1,0)', '(0,1)', '(1,1)')
        title('Specific Acoustic Impedance Ratio')
        grid on
    subplot(h2);
        xlim([f(1) f(length(f))]/1000)
        ylabel('\chi_s_p_a_c')
        xlabel('Freq [kHz]')
        grid on

%% Plot the ratio of the reflected power to the incident power for each
% source (needs to be less then one)
figure(8)
    plot(f/1000,Wr./Wi)
    ylabel('W_r/W_i')
    xlim([f(1) f(length(f))]/1000)
    xlabel('Freq [kHz]')
    legend(fndata)
    title('Ratio of Reflected Power to Incident Power')
    grid on

%% Plot the absorption coefficient
figure(9)
    plot(f/1000,alpha)
    xlim([f(1) f(end)]/1000)
    ylabel('\alpha')
    xlabel('Freq [kHz]')
    legend(fndata)
    title('Power absorption coefficient')
    grid on

%% Plot the condition number for A_matrix
figure(10)
    plot(f/1000,A_cond)
    xlim([f(1) f(length(f))]/1000)
    xlabel('Freq [kHz]');
    ylabel('Condition Number')
    title('Condition Number of Amatrix')
    grid on

```

```

%% Save the MatLab figures
if pic == 0
    h=figure(1);
        saveas(h, 'Pincident.fig')
    h=figure(2);
        saveas(h, 'Preflected.fig')
    h=figure(3);
        saveas(h, 'r.fig')
    h=figure(4);
        saveas(h, 'modescattering.fig')
    h=figure(5);
        saveas(h, 'znormal.fig')
    h=figure(6);
        saveas(h, 'zacoustic.fig')
    h=figure(7);
        saveas(h, 'zspac.fig')
    h=figure(8);
        saveas(h, 'powerratio.fig')
    h=figure(9);
        saveas(h, 'alpha.fig')
    h=figure(10);
        saveas(h, 'Rcond.fig')
end

```

G.4.5 MDM Mode Scattering Coefficients Plotting Subroutine

```

%% mdm_modev4.m
%
% Todd Schultz                2/20/2006
%
% This programs carries out the plotting of the mode scattering
% coefficients.

%% File to load
pic = 0;
fname = 'mdmsdof';
load(fname)

%% Plotting Functions
%% Define helper variables for plotting
In00 = find(f > fco(1,1));
In10 = find(f > fco(2,1));
In01 = find(f > fco(1,2));
In11 = find(f > fco(2,2));

%% Plot mode scattering coefficients
%% From (0,0)
figure(1)
    h1=subplot(2,1,1);
    h2=subplot(2,1,2);

```

```

    subplot(h1);
    plot(f(In10)/1000,squeeze(abs(R(2,1,In10))),f(In01)/1000,squeeze(abs(R(
3,1,In01))),f(In11)/1000,squeeze(abs(R(4,1,In11))))
    subplot(h2);
    plot(f(In10)/1000,squeeze(angle(R(2,1,In10)))*180/pi,f(In01)/1000,squee
ze(angle(R(3,1,In01)))*180/pi,f(In11)/1000,squeeze(angle(R(4,1,In11)))*
180/pi)

    subplot(h1);
    ylabel('|R|')
    xlim([f(In01(1)) f(end)]/1000)
    xlabel('Freq [kHz]')
    legend('from (0,0) to (1,0)', 'from (0,0) to (0,1)', 'from (0,0)
to (1,1)', 'Location', 'Best')
    title('Mode Scattering Coefficients')
    %grid on
    subplot(h2);
    xlim([f(In01(1)) f(end)]/1000)
    ylim([-180 180])
    ylabel('\phi [deg]')
    xlabel('Freq [kHz]')
    set(gca, 'YTick', -180:90:180)
    set(gca, 'YTickLabel', {'-180', '-90', '0', '90', '180'})
    %grid on

%% From (1,0)
figure(2)
    h3=subplot(2,1,1);
    h4=subplot(2,1,2);

    subplot(h3);
    plot(f(In10)/1000,squeeze(abs(R(1,2,In10))),f(In10)/1000,squeeze(abs(R(
3,2,In10))),f(In11)/1000,squeeze(abs(R(4,2,In11))))
    subplot(h4);
    plot(f(In10)/1000,squeeze(angle(R(1,2,In10)))*180/pi,f(In10)/1000,squee
ze(angle(R(3,2,In10)))*180/pi,f(In11)/1000,squeeze(angle(R(4,2,In11)))*
180/pi)

    subplot(h3);
    ylabel('|R|')
    xlim([f(In01(1)) f(end)]/1000)
    xlabel('Freq [kHz]')
    legend('from (1,0) to (0,0)', 'from (1,0) to (0,1)', 'from (1,0)
to (1,1)', 'Location', 'Best')
    title('Mode Scattering Coefficients')
    %grid on
    subplot(h4);
    xlim([f(In01(1)) f(end)]/1000)
    ylim([-180 180])
    ylabel('\phi [deg]')
    xlabel('Freq [kHz]')
    set(gca, 'YTick', -180:90:180)
    set(gca, 'YTickLabel', {'-180', '-90', '0', '90', '180'})
    %grid on

%% From (0,1)

```

```

figure(3)
    h5=subplot(2,1,1);
    h6=subplot(2,1,2);

    subplot(h5);
    plot(f(In01)/1000,squeeze(abs(R(1,3,In01))),f(In01)/1000,squeeze(abs(R(
    2,3,In01))),f(In11)/1000,squeeze(abs(R(4,3,In11))))
    subplot(h6);
    plot(f(In01)/1000,squeeze(angle(R(1,3,In01)))*180/pi,f(In01)/1000,squee
    ze(angle(R(2,3,In01)))*180/pi,f(In11)/1000,squeeze(angle(R(4,3,In11)))*
    180/pi)

    subplot(h5);
    ylabel('|R|')
    xlim([f(In01(1)) f(end)]/1000)
    xlabel('Freq [kHz]')
    legend('from (0,1) to (0,0)', 'from (0,1) to (1,0)', 'from (0,1)
to (1,1)', 'Location', 'Best')
    title('Mode Scattering Coefficients')
    %grid on
    subplot(h6);
    xlim([f(In01(1)) f(end)]/1000)
    ylim([-180 180])
    ylabel('\phi [deg]')
    xlabel('Freq [kHz]')
    set(gca, 'YTick', -180:90:180)
    set(gca, 'YTickLabel', {'-180', '-90', '0', '90', '180'})
    %grid on

%% From (1,1)
figure(4)
    h7=subplot(2,1,1);
    h8=subplot(2,1,2);

    subplot(h7);
    plot(f(In11)/1000,squeeze(abs(R(1,4,In11))),f(In11)/1000,squeeze(abs(R(
    2,4,In11))),f(In11)/1000,squeeze(abs(R(3,4,In11))))
    subplot(h8);
    plot(f(In11)/1000,squeeze(angle(R(1,4,In11)))*180/pi,f(In11)/1000,squee
    ze(angle(R(2,4,In11)))*180/pi,f(In11)/1000,squeeze(angle(R(3,4,In11)))*
    180/pi)

    subplot(h7);
    ylabel('|R|')
    xlim([f(In11(1)) f(end)]/1000)
    xlabel('Freq [kHz]')
    legend('from (1,1) to (0,0)', 'from (1,1) to (1,0)', 'from (1,1)
to (0,1)', 'Location', 'Best')
    title('Mode Scattering Coefficients')
    %grid on
    subplot(h8);
    xlim([f(In11(1)) f(end)]/1000)
    ylim([-180 180])
    ylabel('\phi [deg]')
    xlabel('Freq [kHz]')

```

```
        set(gca, 'YTick', -180:90:180)
        set(gca, 'YTickLabel', {'-180', '-90', '0', '90', '180'})
        %grid on
%% Save figures
if pic == 0
    h=figure(1);
    saveas(h, 'from00.fig')
    h=figure(2);
    saveas(h, 'from10.fig')
    h=figure(3);
    saveas(h, 'from01.fig')
    h=figure(4);
    saveas(h, 'from11.fig')
end
```

LIST OF REFERENCES

- Åbom, M. (1989). "Modal decomposition in ducts based on transfer function measurements between microphone pairs." Journal of Sound and Vibration 135(1): 95-114.
- Åbom, M. and H. Bodén (1988). "Error analysis of two-microphone measurements in ducts with flow." Journal of the Acoustical Society of America 83(6): 2429-2438.
- Akoum, M. and J. M. Ville (1998). "Measurement of the reflection matrix of a discontinuity in a duct." Journal of the Acoustical Society of America 103(5): 2463-2468.
- Arnold, D. P., T. Nishida, L. N. Cattafesta and M. Sheplak (2003). "A directional acoustic array using silicon micromachined piezoresistive microphones." Journal of the Acoustical Society of America 113(1): 289-298.
- ASTM-E1050-98 (1998). Impedance and Absorption of Acoustical Materials Using a Tube, Two Microphones and Digital Frequency Analysis System, ASTM International.
- Bendat, J. S. and A. G. Piersol (2000). Random Data. New York, John Wiley & Sons, Inc: 316-345,425-431.
- Berglund, B., T. Lindvall and D. H. Schwela, Eds. (1999). Guidelines for Community Noise. Geneva, World Health Organization.
- Bielak, G. W., J. W. Premo and A. S. Hersh (1999). "Advanced Tubrofan Duct Liner Concepts." NASA-LaRC: NASA/CR-1999-209002.
- Blackstock, D. T. (2000). Fundamentals of Physical Acoustics. New York, John Wiley & Sons, Inc.
- Bodén, H. and M. Åbom (1986). "Influence of errors on the two-microphone method for measuring acoustic properties in ducts." Journal of the Acoustical Society of America 79(2): 541-549.
- Chapra, S. C. and R. P. Canale (2002). Numerical Methods for Engineers. New York, McGraw-Hill: 231-261, 440-471.

- Chung, J. Y. and D. A. Blaser (1980). "Transfer function method of measuring in-duct acoustic properties, I-Theory, II-Experiment." Journal of the Acoustical Society of America 68(3): 907-921.
- Coleman, H. W. and W. G. Steele (1999). Experimentation and Uncertainty Analysis for Engineers. New York, John Wiley & Sons, Inc.
- Crighton, D. G. (1991). Airframe Noise. Aeroacoustics of Flight Vehicles: Theory and Practice, vol. 1. H. H. Hubbard. Hampton, VA, NASA Reference Publication 1258. Volume 1: Noise Sources: 391-447.
- Dowling, A. P. and J. E. Ffowcs-Williams (1983). Sound and Sound Sources. New York, John Wiley & Sons: 157-163.
- Eversman, W. (1970). "Energy flow criteria for acoustic propagation in ducts with flow." Journal of the Acoustical Society of America 49(6): 1717-1721.
- Franzoni, L. P. and C. M. Elliott (1998). "An innovative design of a probe-tube attachment for a (1/2)-in. microphone." Journal of the Acoustical Society of America 104(5): 2903-2910.
- Gade, S. and H. Herlufsen (1987). Windows to FFT Analysis. Technical Review 3. Brüel and Kjær.
- Golub, R. A., J. J. W. Rawls and J. W. Rusell (2005). Evaluation of the Advanced Subsonic Technology Program Noise Reduction Benefits. TM-2005-212144. Hampton, VA, NASA Langley Research Center.
- Groeneweg, J. F., T. G. Sofrin, P. R. Gliebe and E. J. Rice (1991). Turbomachinery noise. Aeroacoustics of Flight Vehicles: Theory and Practice, vol. 2. H. H. Hubbard. Hampton, VA, NASA Reference Publication 1258. Volume 1: Noise Sources: 151-209.
- Hall, B. D. (2003). "Calculating measurement uncertainty for complex-valued quantities." Measurement Science and Technology 14: 368-375.
- Hall, B. D. (2004). "On the propagation of uncertainty in complex-valued quantities." Metrologia 41: 173-177.
- Herlufsen, H. (1984). Dual Channel FFT Analysis. Technical Review 1. Nærum - Denmark, Brüel and Kjær.
- Incropera, F. P. and D. P. DeWitt (2002). Fundamentals of Heat and Mass Transfer. New York, John Wiley & Sons, Inc.

- Ingard, U. and V. K. Singhal (1974). "Sound attenuation in turbulent pipe flow." Journal of the Acoustical Society of America 55(3): 535-538.
- ISO (International Organization for Standardization)-10534-2:1998 (1998). Acoustics-Determination of Sound Absorption Coefficient and Impedance in Impedance Tubes: Part 2: Transfer-function method. International Organization for Standardization.
- ISO (International Organization for Standardization) (1995). Guide to the Expression of Uncertainty in Measurement. Geneva, International Organization for Standardization.
- Johnson, R. A. and D. W. Wichern (2002). Applied Multivariate Statistical Analysis. Upper Saddle River, NJ, Prentice Hall.
- Jones, M. G. and T. L. Parrott (1989). "Evaluation of a multi-point method for determining acoustic impedance." Mechanical Systems and Signal Processing 3(1): 15-35.
- Jones, M. G., T. L. Parrott and W. R. Watson (2003). "Comparison of acoustic impedance eduction techniques for locally-reacting liners." 9th AIAA/CEAS Aeroacoustics Conference and Exhibit, Hilton Head, South Carolina, AIAA.
- Jones, M. G. and P. E. Stiede (1997). "Comparison of methods for determining specific acoustic impedance." Journal of the Acoustical Society of America 101(5): 2694-2704.
- Jones, M. G., W. R. Watson and T. L. Parrott (2004). "Design and evaluation of modifications to the NASA Langley flow impedance tube." 10th AIAA/CEAS Aeroacoustics Conference, Manchester, United Kingdom, AIAA.
- Katz, B. F. G. (2000). "Method to resolve microphone and sample location errors in the two-microphone duct measurement method." Journal of the Acoustical Society of America 108(5): 2231-2237.
- Kerschen, E. J. and J. P. Johnston (1981). "A modal separation measurement technique for broadband noise propagating inside circular ducts." Journal of Sound and Vibration 76(4): 499-515.
- Kinsler, L. E., A. R. Frey, A. B. Coppens and J. V. Sanders (2000). Fundamentals of Acoustics. New York, John Wiley & Sons, Inc.
- Kirchhoff, G. (1869). "On the influence of thermal conduction in a gas on sound propagation." Ann. Physik Chem. 134: 177-193.

- Kline, S. J. (1985). "The purposes of uncertainty analysis." Journal of Fluids Engineering 107: 153-160.
- Kline, S. J. and F. A. McClintock (1953). "Describing uncertainties in single-sample experiments." Mechanical Engineering 75(1): 3-8.
- Kraft, R. E., J. Yu, H. W. Kwan, B. Beer, A. F. Seybert and P. Tathavadekar (2003). Acoustic Treatment Design Scaling Methods: Phase II Final Report. NASA/CR-2003-212428. Hampton, VA, NASA-Langley Research Center.
- Kraft, R. E., J. Yu, H. W. Kwan, D. K. Echternach, A. A. Syed and W. E. Chien (1999). Acoustic Treatment Design Scaling Methods. NASA/CR-1999-209120. Hampton, VA, NASA-Langley Research Center.
- Moffat, R. J. (1985). "Using uncertainty analysis in the planning of an experiment." Journal of Fluids Engineering 107: 173-178.
- Moore, C. J. (1972). "In-duct investigation of subsonic fan "rotor alone" noise." Journal of the Acoustical Society of America 51(5): 1471-1482.
- Moore, C. J. (1979). "Measurement of radial and circumferential modes in annular and circular fan ducts." Journal of Sound and Vibration 62(2): 235-256.
- Morse, P. (1981). Vibration and Sound. Sewickley, PA, Acoustical Society of America.
- Morse, P. M. and K. U. Ingard (1986). Theoretical Acoustics. Princeton, NJ, Princeton University Press.
- Motsinger, R. E. and R. E. Kraft (1991). Design and performance of duct acoustic treatments. Aeroacoustics of Flight Vehicles: Theory and Practice, vol. 2. H. H. Hubbard. Hampton, VA, NASA Reference Publication 1258. Volume 2: Noise Control: 165-206.
- Owens, R. E. (1979). Energy Efficient Engine Propulsion System-Aircraft Integration Evaluation. NASA/CR-159488. NASA.
- Pasqualini, J. P., J. M. Ville and J. F. d. Belleval (1985). "Development of a method of determining the transverse wave structure in a rigid wall axisymmetric duct." Journal of the Acoustical Society of America 77(5): 1921-1926.
- Pickett, G. F., T. G. Sofrin and R. A. Wells (1977). Method of fan sound mode structure determination. NASA-CR-135293. NASA-Lewis Research Center.
- Pierce, A. D. (1994). Acoustics: An Introduction to its Physical Principles and Applications. Woodbury, NY, Acoustical Society of America.

- Pintelon, R., Y. Rolain and W. V. Moer (2002). "Probability density function for frequency response function measurements using periodic signals." IEEE Instrumentation and Measurement Technology Conference, Anchorage, AK, IEEE.
- Pintelon, R. and J. Schoukens (2001a). System Identification: A Frequency Domain Approach. New York, IEEE: 33-68.
- Pintelon, R. and J. Schoukens (2001b). "Measurement of frequency response functions using periodic excitations, corrupted by correlated input/output errors." IEEE Transactions on Instrumentation and Measurement 50(6): 1753-1760.
- Randall, R. B. (1987). Frequency Analysis. Nærum, Denmark, Brüel and Kjær.
- Rao, S. S. (2002). Applied Numerical Methods for Engineers and Scientists. New York, Prentice Hall.
- Rayleigh, J. W. S. (1945). The Theory of Sound. New York, Dover Publications.
- Ridler, N. M. and M. J. Salter (2002). "An approach to the treatment of uncertainty in complex S-parameter measurements." Metrologia 39: 295-302.
- Rolls-Royce (1996). Noise suppression. The Jet Engine. Derby, England, Rolls-Royce plc: 199-205.
- Salikuddin, M. (1987). "Sound radiation from single and annular stream nozzles, with modal decomposition of in-duct acoustic power." Journal of Sound and Vibration 113(3): 473-501.
- Salikuddin, M. and R. Ramakrishnan (1987). "Acoustic power measurement for single and annular stream duct-nozzle systems utilizing a modal decomposition scheme." Journal of Sound and Vibration 113(3): 441-472.
- Schmidt, H. (1985). "Resolution bias errors in spectral density, frequency response and coherence function measurements, I-VI." Journal of Sound and Vibration 101(3): 347-427.
- Schoukens, J., Y. Rolain, G. Simon and R. Pintelon (2003). "Fully automated spectral analysis of periodic signals." IEEE Transactions on Instrumentation and Measurement 52(4): 1021-1024.
- Schultz, T., M. Sheplak and L. Cattafesta (2005). "Multivariate uncertainty analysis and application to the frequency response function estimate." Submitted to Journal of Sound and Vibration.

- Seybert, A. F. and J. F. Hamilton (1978). "Time delay bias errors in estimating frequency response and coherence functions." Journal of Sound and Vibration 60(1): 1-9.
- Seybert, A. F. and D. F. Ross (1977). "Experimental determination of acoustic properties using a two-microphone random-excitation technique." Journal of the Acoustical Society of America 61(5): 1362-1370.
- Seybert, A. F. and B. Soenarko (1981). "Error analysis of spectral estimates with application to the measurement of acoustic parameters using random sound fields in ducts." Journal of the Acoustical Society of America 69(4): 1190-1199.
- Smith, M. J. T. (1989). Aircraft Noise. Cambridge, Cambridge University Press.
- Taylor, B. N. and C. E. Kuyatt (1994). Guidelines for Evaluating and Expressing the Uncertainty of NIST Measurement Results. Gaithersburg, MD, National Institute of Standards and Technology.
- Tijdeman, H. (1975). "On the propagation of sound waves in cylindrical tubes." Journal of Sound and Vibration 39(1): 1-33.
- Underbrink, J. R. (2002). Aeroacoustic Phased Array Testing in Low Speed Wind Tunnels. Aeroacoustic Measurements. T. J. Mueller. New York, Springer: 165-179.
- Vold, H., J. Crowley and G. T. Rocklin (1984). "New ways of estimating frequency response functions." Sound and Vibration: 34-38.
- Weston, D. E. (1953). "The theory of the propagation of plane sound waves in tubes." Proceeds of the Physical Society of London B66: 695-709.
- White, F. M. (1991). Viscous Fluid Flow. New York, McGraw-Hill.
- Willink, R. and B. D. Hall (2002). "A classical method for uncertainty analysis with multidimensional data." Metrologia 39: 361-369.
- Yardley, P. D. (1974). Measurement of noise and turbulence generated by rotating machinery. Southampton, University of Southampton. Ph.D. dissertation.
- Zinn, B. T., W. A. Bell, B. R. Daniel and A. J. S. Jr (1973). "Experimental determination of three-dimensional liquid rocket nozzle admittances." AIAA Journal 11(3): 267-272.

BIOGRAPHICAL SKETCH

Todd Schultz was born on March 18, 1978, in Winchester, Connecticut. He graduated from Torrington High School in 1996. In the fall of that year, he entered the University of Florida to study aerospace engineering and earned his B.S. degree in May 2001. Todd was awarded the National Defense Science and Engineering Graduate Fellowship from the Department of Defense in the spring of 2001 to attend graduate school at the University of Florida the following fall. In December 2003, he earned a M.S. degree in mechanical engineering while still pursuing his Ph.D. in mechanical engineering with a focus on acoustical measurements. In the summer of 2004, Todd was awarded a Graduate Student Researchers Program Fellowship from NASA Langley Research Center to finish his dissertation research.